Tuning two dimensional Cu-based quantum spin systems

Dissertation zur Erlangung des Doktorgrades

der Naturwissenschaften

vorgelegt beim Fachbereich Physik

der Johann Wolfgang Goethe -Universität

in Frankfurt am Main

von

Pascal Puphal

aus Offenbach am Main

Frankfurt 2017

(D30)

vom Fachbereich Physik der

Johann Wolfgang Goethe - Universität als Dissertation angenommen.

Dekan: Prof. Dr. Owe Philipsen

Gutachter : Prof. Dr. Cornelius Krellner, Prof. Dr. Roser Valentí

Datum der Disputation: 10.1.2018

Contents

List of utilized physical constants

Electron mass $m_e \approx 9.109 \cdot 10^{-31}\,\mathrm{kg}$

Elementary charge/ electron charge $e \approx 1.602 \cdot 10^{-19}\,\mathrm{C}$

Bohr magneton $\mu_B = \frac{e\hbar}{2m_e} \approx 9.274 \cdot 10^{-24}\,\mathrm{J/T}$

Vacuum permeability $\mu_0 = 4\pi \cdot 10^{-7}\,\mathrm{H/m} \approx 1.257 \cdot 10^{-6}\,\mathrm{N/A^2}$

Boltzmann constant $k_B \approx 1.381 \cdot 10^{-23}\,\mathrm{J/K} \approx 8.617 \cdot 10^{-2}\,\mathrm{meV/K}$

Abbreviations

BEC: Bose Einstein condensate

BKT: Berezinskii–Kosterlitz–Thouless transition

QSL: quantum spin liquid

NMR: nuclear magnetic resonance spectroscopy

μ-SR: muon spin resonance spectroscopy

LRO: long range order

PXRD/ XRD: powder X-ray diffraction

PM: paramagnet

FM: ferromagnetism

AFM: antiferromagnetism

SEM: scanning electron microscopy

EDX: energy dispersive X-ray spectroscopy

PPMS: physical property measurment system

VSM: vibrating sample magnetometry

STA: simultaneous thermal analysis

DTA: differential thermal analysis

RPA: random phase approximation

FWHM: full width at half maximum

Introduction

This thesis deals with two classes of copper-based two dimensional quantum materials. In both classes substitutions are presented that lead to a better understanding of the physical properties and enable a controlled tuning of the system. The search for unknown topological ground states is presently of highest interest and thus was recently acknowledged by the Nobel price in 2016 to Haldane, Kosterlitz and Thouless on behalf of the foundation of a theory for low dimensional systems proving to have unconventional phase transitions accompanied by possible topological excitations.

A realization of the Berezinskii–Kosterlitz–Thouless (BKT) transition in a *two dimensional square lattice of dimers* (see figure 0.1), can be found in Han Purple $BaCuSi_2O_6$. Han Purple is a blue to purple (from red Cu_2O impurities) colour pigment, which was used already in China during the Han Dynasty (∼200 BC). This thesis presents the synthesis and analysis of a substitution series of $(Ba_{1-x}Sr_x)Cu(Si_{1-y}Ge_y)_2O_6$ and $Ba_2CuSi_2O_6Cl_2$, which both are two-dimensional magnetic systems where this BKT-transition leads to a condensate of bosonic quasi particles called triplons. The pure $BaCuSi_2O_6$ was dealed as the best candidate of such a realization of a 2D-BKT, but when a structural phase transition to a more complex phase was discovered the community lost interest in this material. However the presented substitution series and $Ba_2CuSi_2O_6Cl_2$ both have a stable structure down to lowest temperatures.

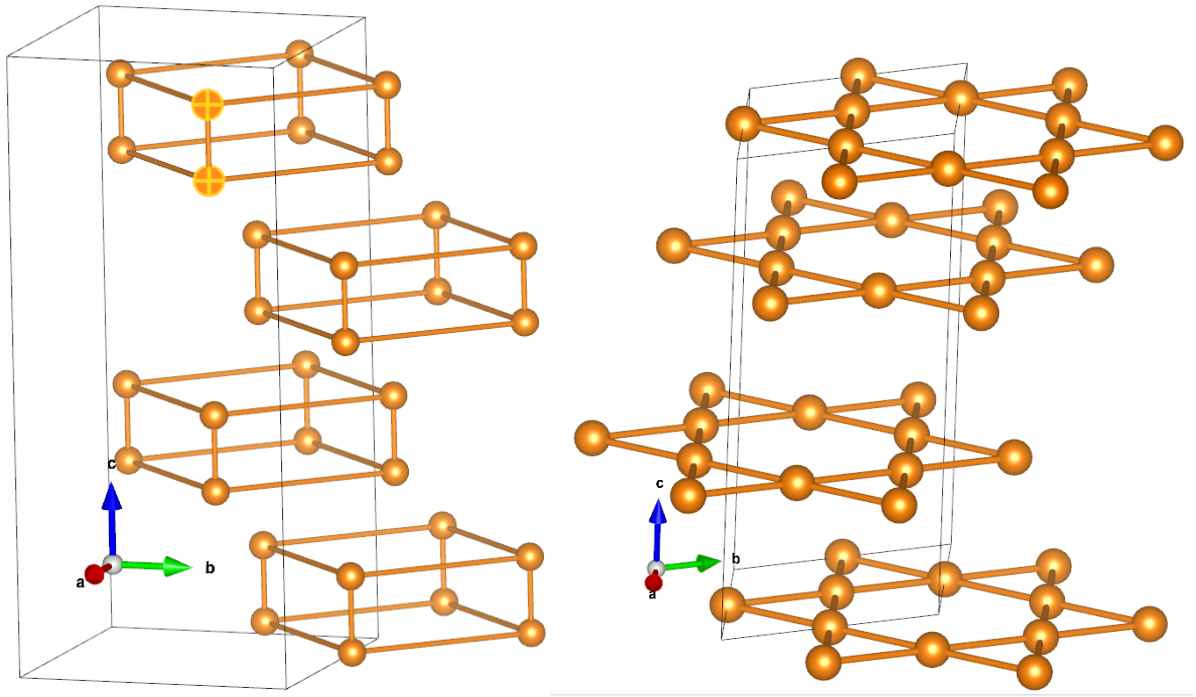

Figure 0.1: Image of seperated layers of a *two dimensional square lattice of dimers* of Cu in the $BaCuSi_2O_6$ elementary cell and layers of Cu Ions in the *two dimensional kagome lattices* in the $ZnCu_3(OH)_6Cl_2$ elementary cell.

Another topic is the search for new materials revealing a magnetic ground state presenting a quantum spin liquid (QSL). A class of material where this state is not only expected,

but also the first example has been found are those presenting a *two dimensional kagome lattice* (see figure 0.1), where the arrangement of the magnetic copper ions prevents a satisfaction of the antiferromagnetic arrangement of spins. Besides the already prominent herbertsmithite $ZnCu_3(OH)_6Cl_2$ and organic kagome materials [1], the synthetic kagome materials $Ga_xCu_{4-x}(OH)_6Cl_2$, $YCu_3(OH)_6Cl_3$ and $Y_3Cu_9(OH)_{19}Cl_8$ are presented, all exhibiting strong geometric spin frustration preventing the spins from magnetic long-range ordering (LRO) at the expected temperature. $Ga_xCu_{4-x}(OH)_6Cl_2$ is a substitution series structurally and physically similar to Zn-substitution. The $x = 1$ candidate was promised to be a dirac metal by theory and we could synthesize powder samples up to $x = 0.8$ which turn out to be a mott insulator like the Zn variant, presenting equal magnetic behaviour. Astonishing is the fact, that no trace of the additional electron could be found so far. The two Y based systems are both stoichiometric kagome materials with no Y-Cu exchange. Since the so far best candidate herbertsmithite always has some Zn-Cu exchange they present better candidates to research the excitations in a QSL state. Additionally due to really close structures these systems give us an unique example not only to study the QSL state of the so far best known example for $YCu_3(OH)_6Cl_3$, but also to understand the effect of slight release of frustration going into a strongly frustrated ordered state for $Y_3Cu_9(OH)_{19}Cl_8$.

Since the experimental results obtained in this thesis are about two different material classes of copper based magnetic systems, it thus is divided primarly in these two different topics: the two-dimensional dimer systems $BaCuSi_2O_6$ and $Ba_2CuSi_2O_6Cl_2$ and the frustrated kagome systems $Ga_xCu_{4-x}(OH)_6Cl_2$, $Y_3Cu_9(OH)_{19}Cl_8$ and $YCu_3(OH)_6Cl_3$. Following this order all materials are presented seperately beginning with a literature introduction, then the synthesis procedure, followed by structural and magnetic analysis.

1 Crystal growth

In this chapter the basics of crystallization will be sketched so that the flux-growth can be explained either in the common sense with a high melting flux for the $BaCuSi_2O_6$ systems or in the case of the hydrothermal method for the atacamite family, where water is the solvent. The information of this chapter is based on the fundamental book of reference [2].

1.1 Crystallization

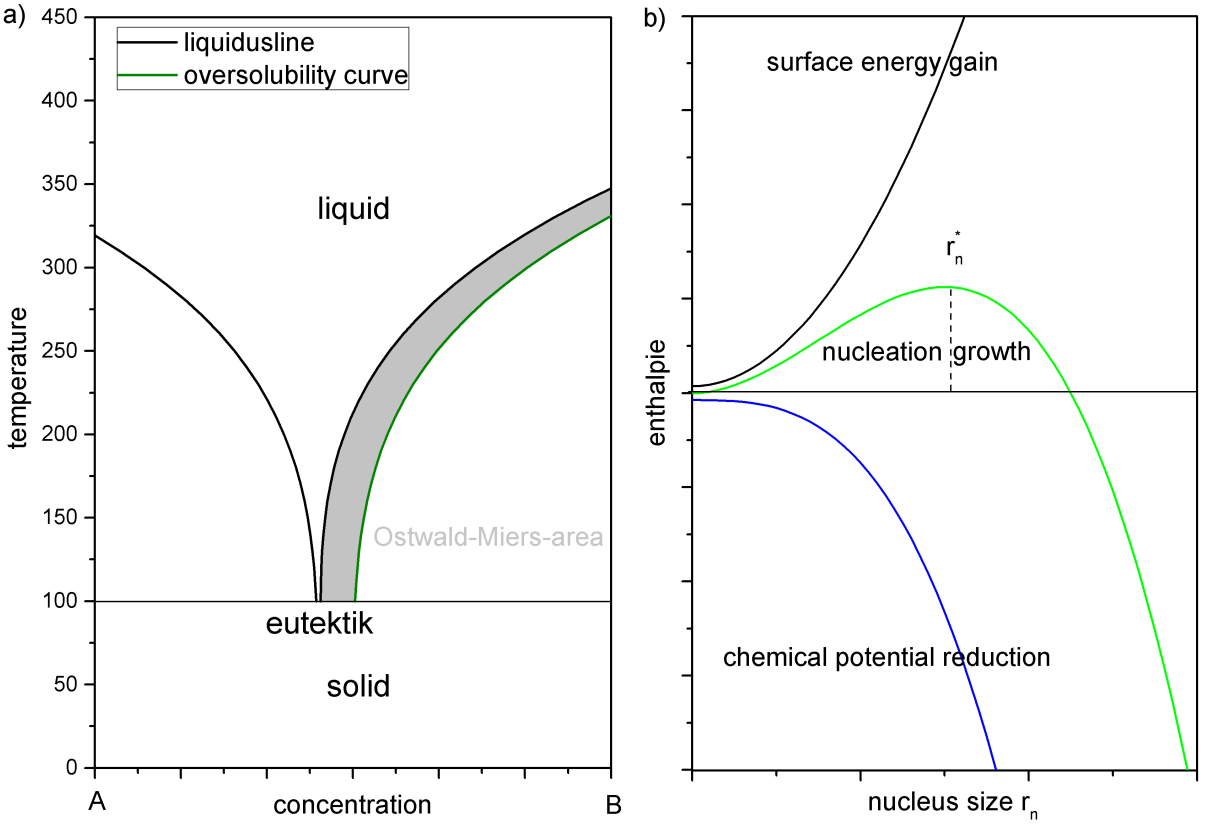

Figure 1.1: a) shows a scetch of the Ostwald-Miers-area (grey) in a binary phase diagram showing the oversolubility curve (green line) after which a nucleus may form. b) the interacting energies and the resulting curve for the nucleation formation and crystal growth are shown.

Generally crystallization occurs when we acces the solid state by a phase transition from a different state of aggregation. Ideally in a very slow manner so that the transportation processes enable a perfect arrangement of atoms in a crystal lattice. In the most simple case this is done first by a phase transition from the solid to the liquid phase either by solving the substance in a flux/solvent or by melting the substance alone. The latter makes sense for congruent melting systems. Congruent means that the composition of liquid and

crystallizing solid do not change. The congruent melting point can be found as a maximum of the liquidusline in binary phase diagrams surrounded by two eutektik minima. With a known crystallisation temperature for a congruent melting system a controlled cooling over this crystallisation temperature will be an easy way to grow single crystals. The cooling rate can be adaped to the crystallisation rate. Here, the transition from the liquid to the solid phase has to overcome the nucleation formation energy; a struggle between the nucleation volume $\sim r_n^3$ of radius r_n : nucleation radius and the nucleation surface $\sim r_n^2$ resulting in an under-cooled melt. Whereas a prepared cooled nucleus would grow directly at the crystallization temperature. This results in the so called Ostwald-Miers-area, which is a thermodynamic metastable region between the melting point of a nucleus compared to a crystal. In figure 1.1 a) a scetch of a simple binary phase diagram is shown, where a oversolubility curve (nucleus melting point) beneath the liquidus-line (true melting point) is shown. The enthalpy change can be described with the free molar enthalpy change Δg, and two constants $a_{p,G}$ σ as:

$$\Delta G \approx a_p \Delta g \cdot r_n^3 - a_G r_n^2$$

$\Delta G_n^{'} = 0 = \frac{\partial \Delta G}{\partial r_n}$ gives us a critical nucleation radius $r_n^* = \frac{2a_G}{3a_p}\Delta g$ above which the nucleus is stable. A scetch of the competing and resulting curves is shown in figure 1.1 b).

In the case of a flux/solvent the crystallization can also be reached by concentration changes via reducing the flux-amount (e.g. A = NaCl, B = H_2O), since there is a limited amount at a given temperature which the solvent can dissolve. When the saturation is reached a further reduction of flux/solvent or a cooling will result in an oversaturation and after the nucleation formation energy has been overcome a nucleus will form and grow. In the case of a growing nucleus the amount of solved substance is limited in the surrounding area. To grow, the nucleus will draw upon the sample in a radius around it, forming the so called diffusion layer where locally the amount of solved sample is reduced and will be filled up slowly by the surrounding area by diffusion. This enables the controlled growth of a single crystal with no further nucleation formation if a nucleus is prepared and given its specific solution pool area to draw from.

1.2 Sintering

Once a certain phase cannot be reached from the liquid melt and no working flux can be found it still can be accessed from a solid state reaction. Sintering is such a process using enhanced pressure and/ or temperature. Here, polycrystalline starting compounds have to be mixed well. This can be done by grinding them with a mortar and afterwards bringing the grains closely together, e.g. by pressing them to a pallet. Then an enhanced temperature ~70-90% of the lowest melting point of the involved compounds is applied for a long time. On the microscopic scale the bonds can rearrange and atoms can move due to different transport processes. The main driving force is diffusion either of the surface, the lattice, or the grain boundary. Diffusion is the random thermal movement, automatically balancing concentration differences. Macroscopically the grains build up sintering necks and thus grow together, slowly filling the empty space. This does not lead to a single crystal with a single orientation, but still inexessable polycrystalline phases can be produced and the simplicity of the method gives a fast tool to produce samples for quick characterisations.

1.3 Hydrothermal Synthesis

1.3.1 Water

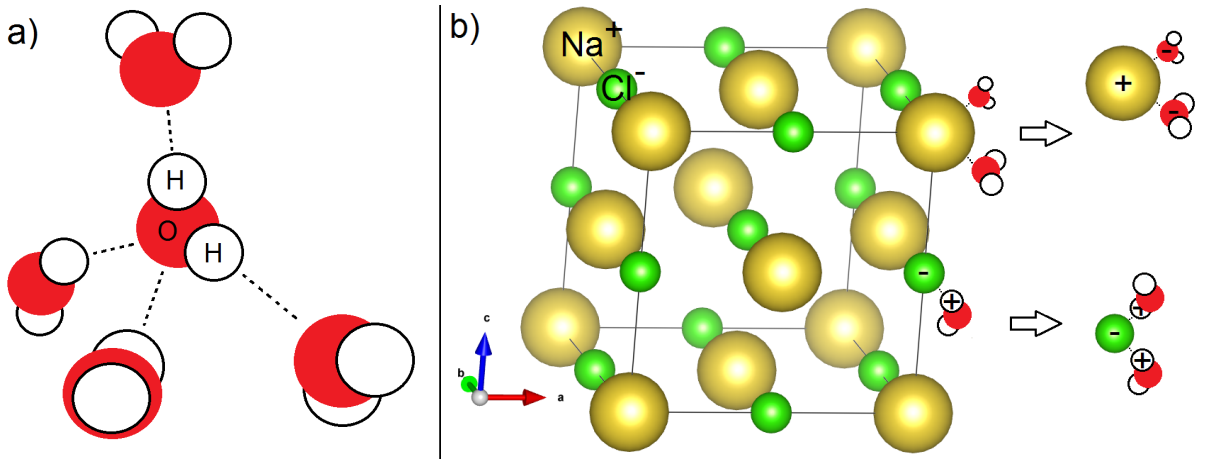

Figure 1.2: Abilites from water: a) The left image shows a scetch of the water molecules building up hydrogen bondings (dashed lines) and on the right image (b) a scetch is shown how water molecules dissolve the ionic bonding in salts.

Here we discuss the general properties of water (H_2O) as a possible solvent in our synthesis. The electronegativities is the potential to bind an electron, where the values of H and O are 2.20 and 3.44. This difference causes the electron to be closely bound to the O atom. The distance of the electron to the H atom results in an effective positive charge from the proton in the nuclei, while the oxygen sees two more electrons than the nuclei has protons resulting in a negative charge. The ionic bonding thus leads to a dipolar moment for H_2O because of the 104.45° angle arrangement of the H atoms. This gives rise to weak hydrogen bondings between water molecules shown in figure 1.2 a). In the liquid state these bonds constantly rearrange.

The polarity of the water results in the ability to dissolve salts, alcohols, acids and hydrophilic organic molecules at ambient conditions, depicted in figure 1.2 b). The negative and positive charges of the molecule interacts with the contrary charge and thus the ions of the salt-bonding. Several or a single molecule can drag away an atom from the salt-crystal and thus slowly dissolve it atom by atom.

In figure 1.3 a sketch of the p-T phase diagram of H_2O is shown. For hydrothermal setups we are interested in a special part of this phase diagram: Liquid water under pressure at temperatures between the usual boiling point at 100°C and the critical temperature at 374°C, which is called superheated water. Superheated water is a stable phase because of overpressure that raises the boiling point. The liquid water is in equilibrium with vapour at the saturated vapor pressure. The hydrogen bonds break easier, changing the properties more than usually expected by increasing temperature alone. Water becomes less polar and acts more like an organic solvent. The viscosity and surface tension of water drop and diffusivity goes up with increasing temperature. Self-ionization $2H_2O \leftrightarrows H_3O^+ + OH^-$ of water ascends with rising temperature, resulting in a higher K_W and thus a lower $pK_W = -\log K_W$ value while the pH remains neutral. Where $K_W = \left[H_3O^+\right]\left[OH^-\right]$ is the ionization constant of water, e.g. at 250°C pK_W =11 compared to 14 at 25°C. This change of properties in superheated water enables the solving of different phases than salts, in our case copper based oxydes and hydroxides and thus the crystal growth of hydroxide containing minerals (see next chapter).

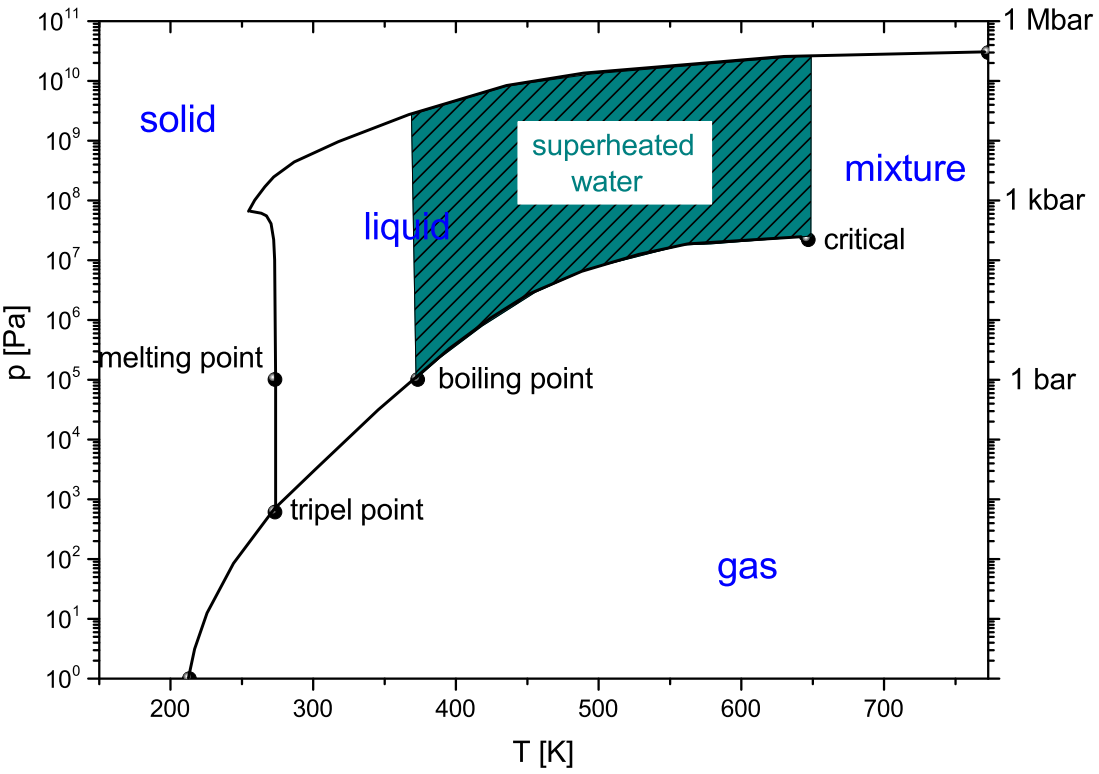

Figure 1.3: The p-T phase diagram of H_2O is shown with the superheated water region highlighted.

1.3.2 Basics on Hydrothermal Growth

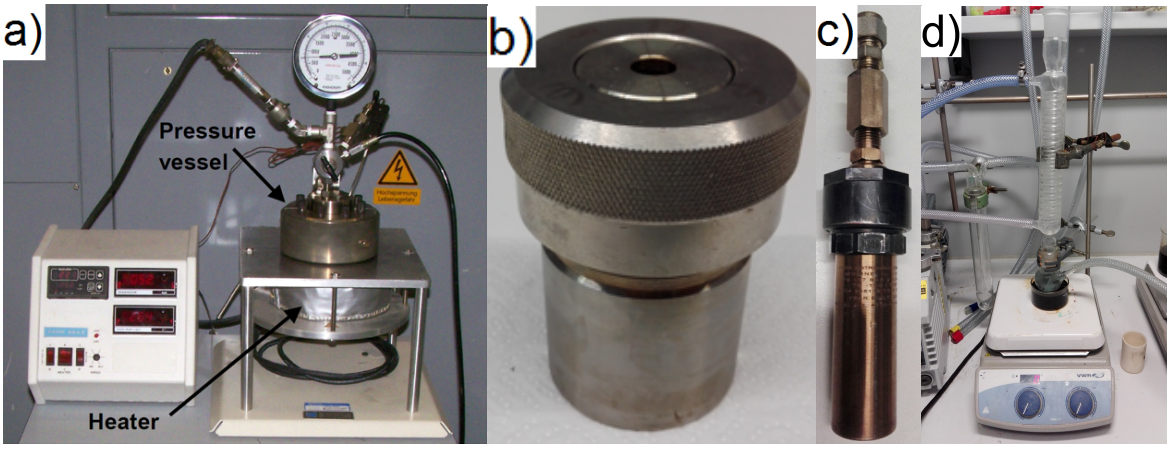

Figure 1.4: Pictures of three different types of autoclaves that were used in this thesis as well as a realization of the reflux method. a) The first is a hydrothermal Parr 4625 autoclave with a 575 ml filling capacity, sealed with a teflon sealing screwed tight by 8 x 4 cm screws. It is operated by a Parr 4842 power supply including a 982 Watlow controller going up to 300°C and 400 bar. b) The second is a Parr 4749 acid digestion vessel, sealed with a screwable head held by a simple spring. It contains a teflon liner inside with a capacity of 23 ml and due to the teflon goes up to 250°C and 125 bar. c) The third is a Parr general purpose vessel 4700 sealed by a screwable head on a teflon sealing. It has a capacity of 45 ml lasting up to 300°C and 150 bar. d) The last image shows a heating plate with an oil bath on top which heats a round-bottom flask. The solution condenses in the fractionating column and thus is regained keeping the molar ratio steady.

Hydrothermal growth is a special case of solution growth. The term describes hot salt water solutions up to the critical point of the H_2O phase diagram shown in figure 1.3. Since the water would start to evaporate, latest at its boiling point, it needs to be enclosed in an autoclave. These are stainless steel vessels with a large wall-thickness most sealed with teflon gaskets and screws or screwable heads. Some examples of autoclaves are shown in figure 1.4. The autoclave is mainly limited by its capacity of pressure endurance. The pressure dependence of filling rate and temperature is shown in figure 1.5. The plot shows that once a certain temperature is reached the pressure dependence increases drastically which might be simplified be the fact that the liquid phase starts to play a role in the pressure dependance. In our setup we are always in the lower filling rates at temperatures below 300°C (red dotted line). For a generel secure use, a rupture disk is present in all autoclaves. The disk lasts up to a certain pressure, until it breaks. The water then evaporates, preventing a complete explosion of the autoclave.

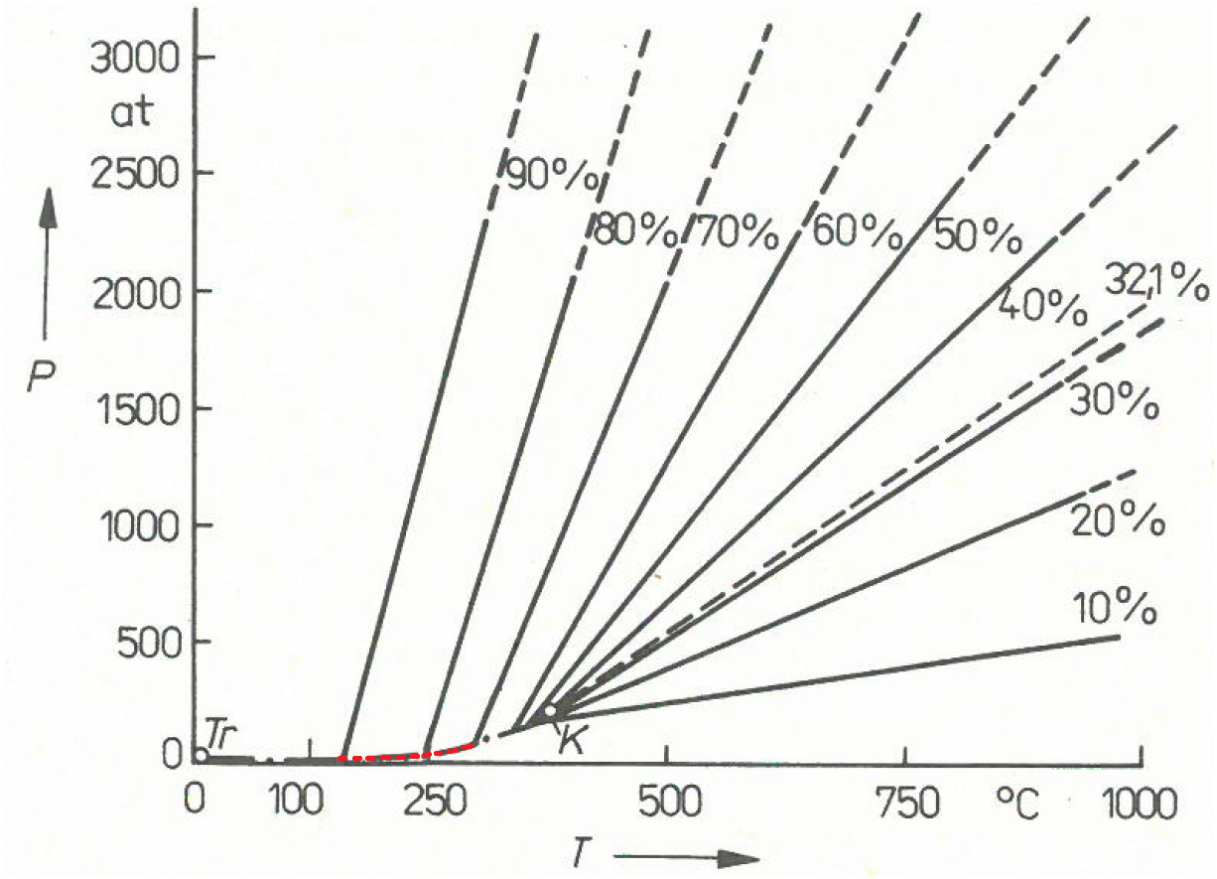

Figure 1.5: Pressure dependence of hot water at different filling rates (given in %) [2].

This experimental effort is done since the solubility is temperature dependent and increases upon heating. At some point a maximum is reached and a component starts to fall out again. An acidic or basic pH value also increases the solubility, but is generally a hindrance for nucleation. As an example the solubility of CuO is shown in figure 1.6, which is often the starting material in this thesis.

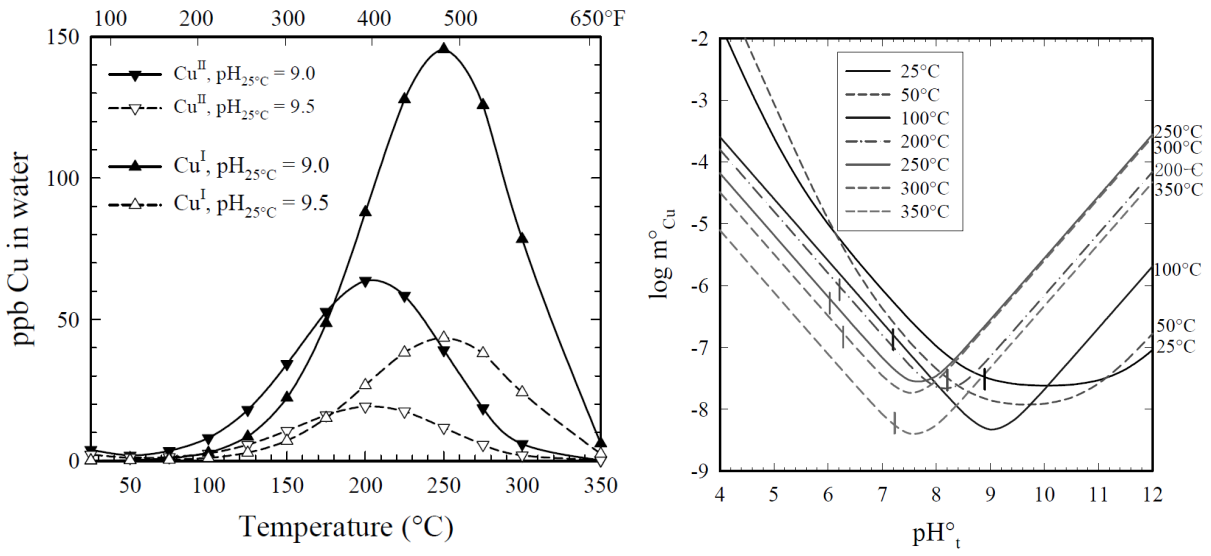

Figure 1.6: Solubility-temperature dependence of cupric oxide (CuO, Cu^{II}) and cuprous oxide (Cu_2O, Cu^{I}) at two fixed pH values of 9 and 9.5 [3]. The second image shows the solubility (m°_{Cu} in units of mol·kg^{-1} (H_2O)) of CuO in water as functions of pH_t revealing a complex T-pH behaviour [3].

Generally, hydrothermal methods can be used to grow e.g. oxide single crystals, where a salt is added as a flux to increase the solubility in hot water. The synthesis is also necessary for phases containing crystal water such as the here grown atacamite family, these can not be grown from low temperature solutions. Here, one component is the salt that will be incorporated into the structure, the other ones are metals/oxides that need to be solved at high temperatures. Due to salt in the solutions the samples have to be sealed in glass ampules, or a teflon inlay has to be used, to prevent corrosion and decay.

Experimental detail

The filling rate dependence of the pressure has a strong influnce on the large hydrothermal autoclave Parr 4625, since the heating is done by a simple hemispherical heating mantle the thermal coupling plays an important role in this mashine. The regulating thermocouple is applied on the outside of the heater. This leads to a filling rate dependant overheating of the apparatus which is at the order of 10 - 30°C. All given temperatures from this setup are the controlled temperatures measured on the inner side of the autoclave with a second thermocouple that is installed in a thin stainless steel surrounded inlet.

1.3.3 Hydrothermal growth in an external gradient

Generally, due to the sealing in this method a slow evaporation of the solution is not possible. Thus the crystallization discussed in chapter 1.1 can only be realized with a temperature gradient either realized through cooling, or as an external temperature gradient. Since cooling over a small range of temperature (e.g. 5°C) can only be done in a limited time region due to instrument limitations the resulting size of single crystals is limited. Whereas an external gradient can be held constant until all the powder is recrystallized.

The gradient can easily be realized in a tube furnace or a three-zone furnace, where either thick quartz ampules (up to 200°C) or the thin autoclaves of figure 1.4 c) are placed inside

horizontally. The crystallisation of herbertsmithite in a thick walled quartz ampule was discovered by the group of D. G. Nocera at the Massachusetts Institute of Technology (MIT) and this method is well described in reference [4]. It is a similar technique to vapor transport with the difference that we do not reach the pure gaseous phase but dissolve the phase in water: In a closed ampule a powder sample is placed at the hot part of the gradient. At this hot end the temperature is enough to dissolve the sample. Then the gradient enables a transport to the cold end by simple fluid dynamics as well as molecular diffusion resulting in a cooling of the solution until it falls out at the cold end and crystallizes.

Experimental detail

The quartz ampoules utilised in the tube furnace last up to an average temperature of 230°C in the center of the ampoule at a filling rate below 40%. Of course this value is extremely dependant on the wall thickness which was 3 mm in our case and is thinner on the sealed tip. The growth duration in a gradient is strongly solubility dependant, ranging from a few hours for CuO in high molarity Cl solutions up to a few months for reacted atacamite compounds in water.

1.3.4 Reflux synthesis

A special case of hydrothermal synthesis is the reflux method, which strictly speaking is not hydrothermal, since there is no pressure in the solution: In this case the hot salt water solution is filled in a round-bottom flask, which is placed in an oil bath and heated with either a Bunsen burner or a hot plate. On top of it a distillation column is placed, where water flows through to cool the evaporating solution down. Thus the method has a stable amount of solution and fixed molar ratio/pH value and can be used equally as the hydrothermal method. The utilised setup is shown in figure 1.4 d). The solution will reach in this process a stable temperature of 100°C due to the evaporating water. The advantage of this technique is that instead of a casual round-bottom flask, one with a guide tube inside the solution can be used, to let a gas flow into the solution (e.g. oxygen for kapellasite). However this method misses the pressure and high solution temperatures, thus yielding only microcrystalline samples.

2 Magnetism

Now that the material preparation methods have been discussed, we can look at the basics of the physical motivation for the material classes of this thesis: their magnetic ground states. This chapter introduces the fundamental concepts of magnetism applied in this thesis. From the single effects of magnetic fields on electrons we go to the case of bound electrons and the various magnetic exchange interactions will be discussed. This gives the basis to understand the role of frustration and what the resulting spin liquid state is. Afterwards the other class of materials is discussed, where a two-dimensional lattice of spin dimers creates a condensate of spin-flip quasi particles. This chapter is based on the fundamental books [5, 6].

2.1 Basic parameters: Magnetic field, Susceptibility

Generally the magnetic field strength is divided into the external field and the demagnetization field

$$H = H_e + H_d$$

but it is often only referred to as the external magnetic field. An induced internal field M is observed, when an external magnetic field H is applied. Assuming a linear relationship we can define the susceptibility as

$$\chi = \frac{M}{H} \tag{2.1}$$

The magnetic induction, so the magnetic field within matter is defined as

$$B = \mu_0 (H + M) = \mu_0 H (1 + \chi)$$

where $\mu_0 = 4\pi \cdot 10^{-7} \frac{\mathrm{N}}{\mathrm{mA}^2}$ is the magnetic field constant.

2.2 Spin interaction of electrons

The ever present movement of an electron around its atomic nucleus causes a magnetic moment of

$$\vec{m}_{orbit} = -\frac{e}{2m_e}\vec{l}$$

with the electrical charge $e \approx -1,6{\cdot}10^{-19}\,\mathrm{C}$, the mass of an electron $m_e \approx 9,11{\cdot}10^{-31}\,\mathrm{kg}$ and the angular momentum $\vec{l}$. But if one looks from the inert system of the electron, the nucleus moves around it. This causes an intrinsic moment on the electron, the so called **spin-orbit coupling (SO)**

$$E_{SO} = -\mu_B B_{SO} = -\frac{\mu_0 \mu_B^2 Z^4}{4\pi a_0^2}$$

One has to differentiate between localized (bound) and delocalized electrons (e.g. the electrons in a metal). But for this work only the first case is relevant since all materials are insulators. A bound electron can now be differentiated into the case of closed- and open electron-shells containing ions, atoms, or molecules with unpaired electrons.

2.2.1 Diamagnetism

The closed- shell materials are governed by the orbital motion through the Larmor precession following Lenz's law. Charges moving in a magnetic field experience an electromotive force. To minimize this force, they align anti-parallel with the field, producing an internal field. The susceptibility in this case is a very small constant independant of temperature:

$$\chi_{dia} = -\frac{n\mu_0 e^2}{6m_e}\left\langle r^2 \right\rangle \sim -1 \cdot 10^{-6}\mathrm{emu/mol}$$

2.2.2 Paramagnetism

The open-shell materials exhibit paramagnetism (PM), since they interact more strongly with an applied magnetic field wanting to aling parallel to it. Since thermal fluctuations prevent a field alignment of spins, the susceptibility in this case goes inversely to the temperature:

$$\chi_{curie} = \frac{C}{T} = \frac{n\mu_0\mu_B^2}{k_B T} \sim -1 \cdot 10^{-4}\mathrm{emu/mol}$$

C will be discussed on the next page. Without an external magnetic field a paramagnet behaves like a gas, since the direction of the spin vector is mainly affected by thermal fluctuations, thus rotating freely.

The magnetic moment in this case

$$M = M_s \cdot B_J \tag{2.2}$$

is described by the **Brillouin-function**

$$B_J(x) = \frac{2J+1}{J}\coth\left[\frac{2J+1}{J}x\right] - \frac{1}{2J}\coth\left[\frac{1}{2J}x\right]$$

where $J = |L \pm S| = \sqrt{j(j+1)}\hbar$ (following hund's rules) is the total angular momentum quantum number, $S = \sqrt{s(s+1)}\hbar$ the total spin quantum number and $L = \sqrt{l(l+1)}\hbar$ the total orbital angular momentum quantum number.

$$M_s = n g_J \mu_B J \tag{2.3}$$

is the saturation magnetization. g_J is the Landé g-factor for an electron is defined as

$$g_J = 1 + \frac{J(J+1) + S(S+1) - L(L+1)}{2J(J+1)} \tag{2.4}$$

and $x \equiv \mu_B B/(k_B T)$. The derivation of this law can be done with the Boltzmann distribution of the Zeeman splitted energy levels in a magnetic field.

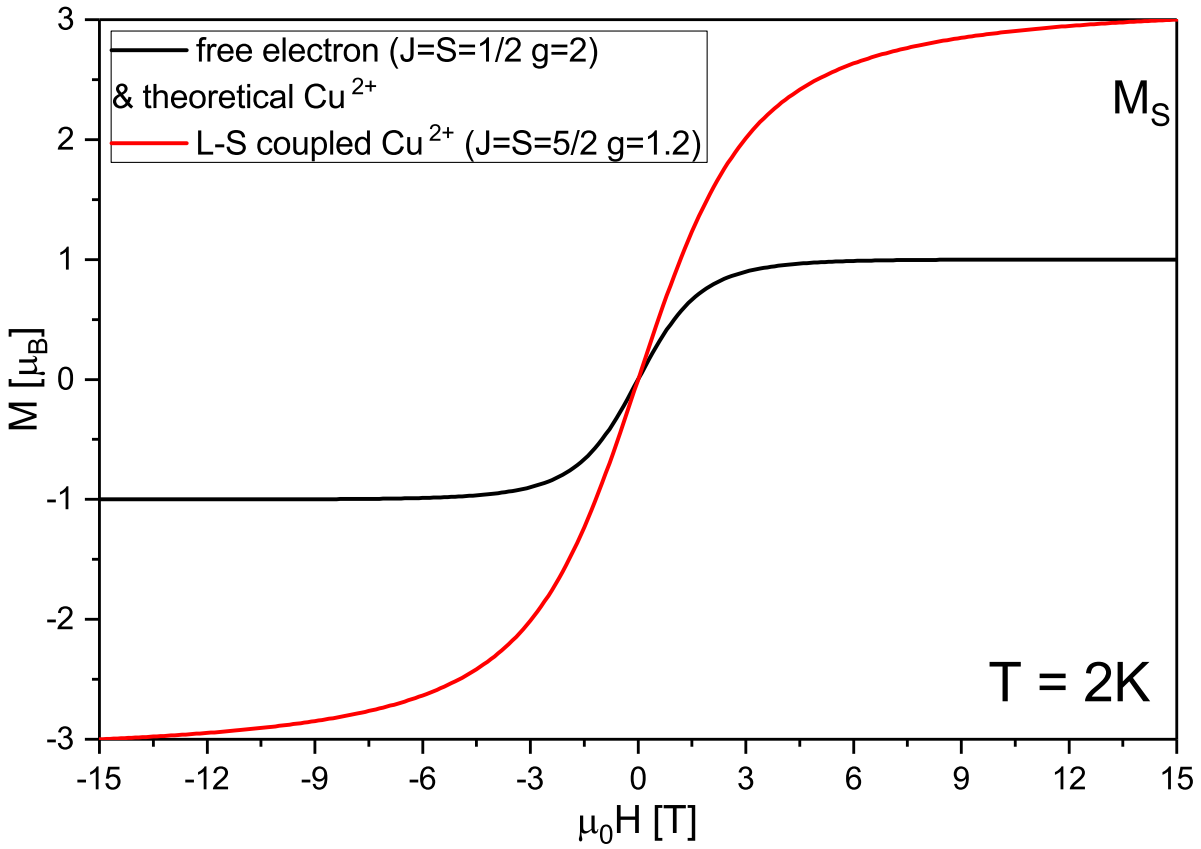

Figure 2.1: A plot of the magnetization using the Brillouin-function for a free electron and a L-S coupled Cu^{2+} state.

For small fields and high temperatures ($x \ll 1$) the approximation $\coth(x) \approx \frac{1}{x} + \frac{x}{3} - ...$ gives rise to the **Curie-law**

$$\chi = \frac{\mu_0 M}{B} \approx \frac{n \mu_0 \mu_{eff}^2}{3 k_B T} \equiv \frac{C}{T} \tag{2.5}$$

with the effective magnetic moment

$$\mu_{eff} = g_J \mu_B \sqrt{J(J+1)} \tag{2.6}$$

and the Curie constant

$$C = \frac{n\mu_0\mu_{eff}^2}{3k_B} \tag{2.7}$$

For a simple ferromagnet (FM) and an antiferromagnet (AFM) (introduced in chapter 2.4) there is a correction of an additional Weiss temperature θ_W giving the general Curie-Weiss law:

$$\chi^{-1} = \frac{T - \theta_W}{C} \tag{2.8}$$

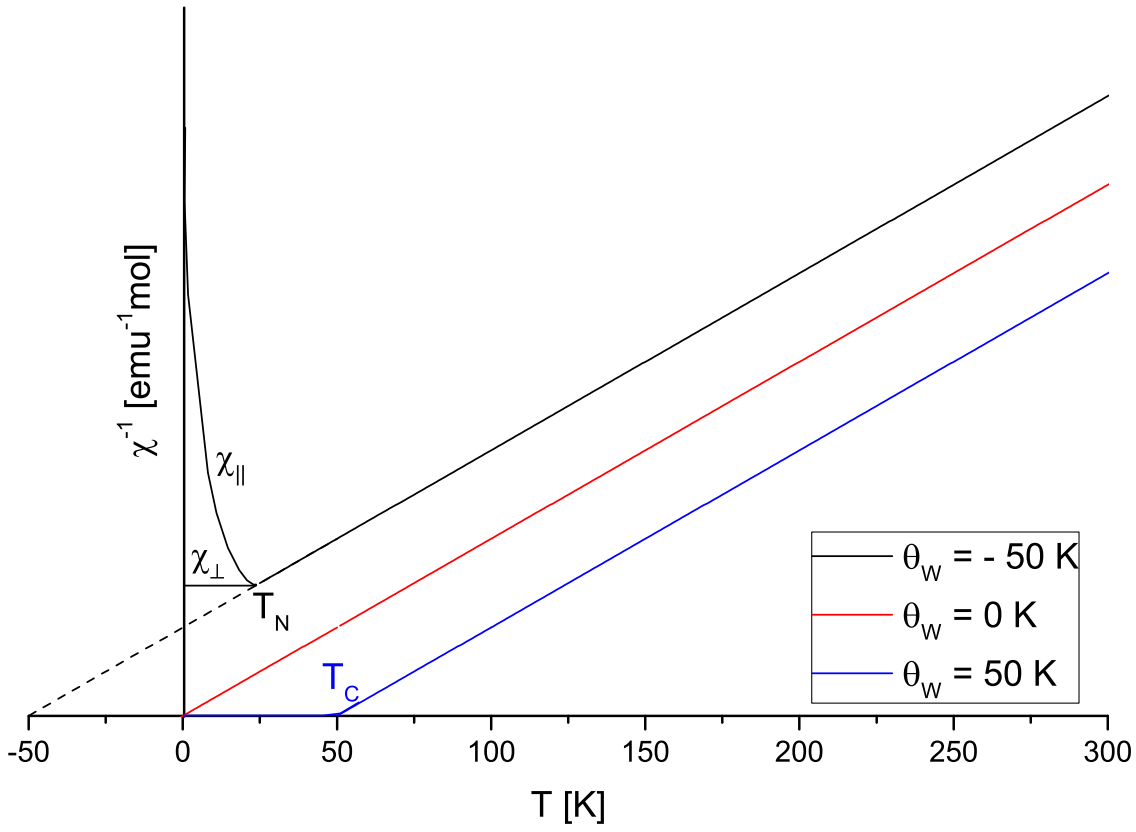

Figure 2.2: A plot of χ^{-1} vs. T showing the Curie-Weiss behavior for ferromagnetic, antiferromagnetic, and for zero coupling between ions.

Transition metals

Different are the transition metals, where the 3d-shell is exposed to strong in-homogeneous electrical fields, the **crystal electric fields** from the neighbors cause an internal Stark-effect moving the energy levels, which lifts the $2L + 1$ degeneracy. This effect is often the case for an octahedral, or a tetrahedral environment of the metal ion, where the crystal field causes a slight distortion and splits the e_g and t_{2g} levels. So an additional term has to be included into the Hamiltonian H_{CF} which quenches the orbital angular momentum leaving only the total spin S as a good quantum number.

2.2.3 Copper ions

The only magnetic ion discussed in this thesis is $\mathbf{Cu}^{2+}$, since closed shell atoms such as all ions and anions of the main groups (H^{1+}, O^{2-}, Cl^{1-}, Si^{4+}, Ge^{4+}, Sr^{2+}, Ba^{2+}) experience only diamagnetism, which is negligibly small. This only leaves the atoms Y with

the electron configuration [Kr]$4d^1 5s^2$, Zn with [Ar]$3d^{10}4s^2$ and Ga having [Ar]$3d^{10}4s^2 4p^1$, which are again with Y^{3+}, Zn^{2+} and Ga^{3+}closed shell ions.

Whereas Cu^{2+} has an electron configuration of [Ar]$3d^9$ so $l = 2$ giving us the levels of $m_s = -2, -1, 0, 1, 2$ filled with 9 electrons:

2	1	0	-1	-2
↑↓	↑↓	↑↓	↑↓	↑

So the total spin is $S = 1/2$ and the orbital angular momentum $L = |\sum m_{sl}| = 2$. The total angular momentum following Hund's rule for a more than half filled band would be $J = L + S = 5/2$, but due to a large crystal field splitting in comparison to the spin-orbit coupling for the 3d electrons L is quenched ($L = 0$) and thus the total angular momentum in this case is

$$J^{Cu^{2+}} = S = 1/2 \tag{2.9}$$

The effective moment of Cu^{2+} for the calculated $J = 5/2$ following equation 2.6 and 2.4 with $g_{J=5/2} = 1.2$ would have been $\mu_{eff}^{J=1/2} = g_J\sqrt{J(J+1)}\mu_B \approx 3.55\mu_B$, but for our $J = 1/2$ we get with $g_{J=1/2} = 2$ the theoretical value of

$$\mu_{eff}^{Cu^{2+}} = g_J\sqrt{J(J+1)}\mu_B \approx 1.73\,\mu_B \tag{2.10}$$

Also the saturation magnetization and Curie constant normalized to one copper ($n = 1$) can be calculated for Cu^{2+} using equation 2.3 and 2.7:

$$\begin{aligned} M_s^{Cu^{2+}} &= ng_J\mu_B J = 1 \cdot 2 \cdot 1/2\,\mu_B = 1\,\mu_B \\ C_{mol}^{Cu^{2+}} &= nN_A\mu_0\mu_{eff}^2/(3k_B) \approx 4.7 \cdot 10^{-6}\,\mathrm{m^3K/mol} \end{aligned} \tag{2.11}$$

The only other oxidation state of copper is $\mathbf{Cu}^{1+}$, which has a closed 3d shell and thus is nonmagnetic with $S = 0$, $L = 0$ and $J^{Cu^{1+}} = 0$.

2.3 Types of magnetic interactions

The discussed phenomena of dia- and paramagnetism are for non interacting spins. In this chapter we introduce the other types of magnetic groundstates for interacting spin systems

The magnetic interaction can be well described by the classical Heisenberg model of only next neighbour interacting spins

$$H = -\sum_{ij} J_{ij}(\vec{S_i} \cdot \vec{S_j}) \tag{2.12}$$

where

$$J_{ij} = \begin{cases} J & \text{i,j neighbors} \\ 0 & \text{else} \end{cases} \quad \& J \begin{cases} > 0 & \text{FM} \\ < 0 & \text{AFM} \end{cases}$$

describes the coupling constant between two spins, which is mostly given in eV, or K to see at which temperature the interaction overcomes the thermal fluctuations.

2.3.1 Magnetic dipole interaction

Magnetic ions behave as dipoles always inducing a really small magnetic field and thus can interact and polarize each other.

$$E_{dipol} = \frac{\mu_0}{4\pi r^3} \left| \left(\vec{m}_1 \cdot \vec{m}_2 - \frac{3}{r^3} (\vec{m}_1 \cdot \vec{r}) \cdot (\vec{m}_2 \cdot \vec{r}) \right) \right|$$

This only becomes relevant at low temperatures since the order of the magnetic dipole interaction is in a solid state only in the Kelvin region: $m \sim \mu_B$, $r \sim 10^{-10} m \rightarrow E \sim \frac{\mu_0 \mu_B^2}{4\pi r^3} \sim 10^{-23} J \sim 1K$.

2.3.2 Exchange interaction

Superexchange The most important magnetic interaction for Cu - O based magnetic materials is the Superexchange. It relies on the overlap of electronic wave functions and is mediated by a third ion, which is often oxygen and thus found mainly in isolators. The exchange is between two metallic cations where the wave functions do not directly overlap, but overlap with the orbitals of a mediator (e.g. oxygen). For a 90° Cu-O-Cu bridging angle often weak ferromagnetic coupling is found since orthogonal orbitals do not overlap, so there is no electron transfer and the exchange interaction between spins in orthogonal orbitals is a ferromagnetic potential exchange. Thus it is responsible for the Hund highest-spin rule for the free atom or ion. For a 120 - 180° Cu-O-Cu bridging angle often strong antiferromagnetic coupling is found.

According to the Goodenough-Kanamori rule, the superexchange interactions are antiferromagnetic where the virtual electron transfer is between overlapping orbitals that are each half-filled and is ferromagnetic where the virtual electron transfer is from a half-filled to an empty orbital or from a filled to a half-filled orbital.

From experimental data collection of several CuO compounds the different superexchange constants for varying bond angles could be extracted. An attempt of a fit of these summarised coupling constants is shown in figure 2.3 resulting in the equation:

$$J_z[\text{meV}] = 0.089(\phi[^\circ] - 90)^{1.66} \tag{2.13}$$

Note however that the distance of the atoms is not taken into account. It varies from 1.94 to 2 Å and thus this is only an attempt to estimate the exchange interaction, while on the inset of the second image the variation for a fixed distance is shown revealing a linear behaviour.

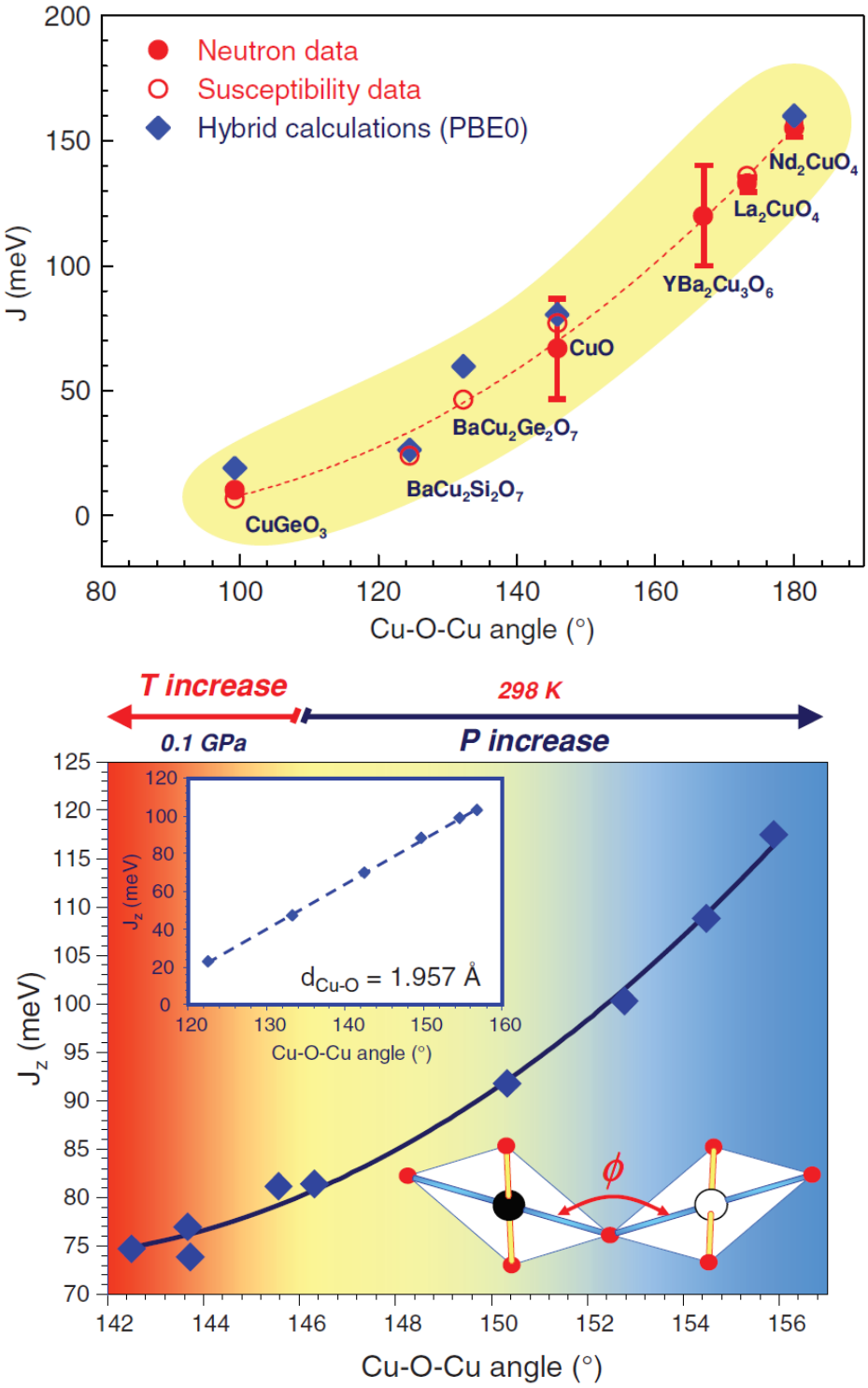

Figure 2.3: Both images show the magnetic coupling J_z from superexchange of Cu-O-Cu plotted versus the bond angle. The first plot are many Cu-O based materials fitted with a critical exponent of 1.66 and the second image is CuO under high-temperature and high-pressure. In the second figure, P and T are increasing to the right and to the left, respectively. The inset shows the evolution of J_z in CuO as a function of the Cu-O-Cu bond angle ϕ for CuO under positive and negative pressure, while keeping constant the Cu-O bond length in the CuO_4 plaquettes ($d_{Cu-O} = 1.957$ Å) [7].

Dzyaloshinskii-Morya (DM) exchange/ antisymmetric exchange The DM interaction mainly is present in systems with no inversion center in the crystal structure, since there is a low local symmetry. Furthermore it is found in systems with a high spin-orbit coupling

(SO), SO is explained in chapter 2.2. DM exchange gives an additional term to the symmetric Heisenberg model equation (2.12).

$$H = \sum_{ij} D_{ij} \left(\vec{S}_i \times \vec{S}_j \right)$$

This equation term might cause some canting of the moment or a long range modulation like a helix.

The following interactions are described for completenes, but do not play a role in the examined systems of this thesis.

Direct exchange If the electronic orbitals of neighboring magnetic ions do directly overlap as it is the case in metals, then the Pauli exclusion principle dictates that no two electrons can be in the same quantum mechanical state and forces a correlation between the electronic spin states. For fillings close to half filled band the exchange is antiferromagnetic, while for the other cases of empty and nearly filled orbitals it is ferromagnetic.

Indirect exchange (RKKY: only relevant in metals) The magnetic field induced by the magnetic moment of localized electrons polarize the spin of the conducting electrons, and transmit this polarization to neighboring magnetic ions. Whether it is ferromagnetic or antiferromagnetic is determined by the distance r of the localized moments and the band structure of the conduction electrons.

Double exchange If magnetic ions with different valence states are present the double exchange can occur, which is a stronger version of the ferromagnetic superexchange. It is only possible in the case of a high-spin configuration. Ferromagnetic coupling means that a jump in the e_g level of an up state can only occur if the lower t_{2g} state also is populated by up states.

2.4 Magnetic ground states

In this chapter the groundstates of now interacting spin systems are presented.

When all of the dominant ordering parameter terms can be satisfied, a transition into an ordered ground-state will occur, around the order of the Weiss temperature. The complexity of a lattice with 10^{23} atoms interacting with each other over different coupling constants can be simplified by the **mean field approach**. Here a moment is considered to only couple to an average magnetic mean field, which is caused by all surrounding magnetic moments. Which then can be treated like a paramagnet in an external field. So the Hamiltonian can be described by

$$H_{mf} = g\mu_B \sum_i \vec{S}_i \left(\vec{B} + \vec{B}_{mf} \right)$$

Ferromagnetism (FM) is the case of only positive coupling constants in the Heisenberg model ($J_{ij} > 0$), we see a parallel alignment of all spins below the so called Curie temperature $T_C = \theta_W > 0$. In this case, the only symmetry of the parent ion structure that is broken is the time-reversal symmetry. Due to the parallel alignment of all spins, a net magnetization is induced.

We speak of **antiferromagnetism** (AFM) if the coupling constant of the Heisenberg model is negative ($J_{ij} < 0$), the spins want to align antiparallel. At the so called Néel temperature the ordering occurs with $-T_N = \theta_W < 0$. This can be described as two sub-lattices of ferromagnets. These sub-lattices produce equal moments in opposite directions and cancel to a zero net-moment.

If two sub-lattices describe our system, where one sub-lattice of ions has a different net moment to the other, we speak of **ferrimagnetism**. This leads to an unequal cancellation between the two sub-lattices, and a finite magnetization. For this kind of magnetism at least two crystallographic distinct positions of magnetic ions have to be present and they usually show no Curie-Weiss law above T_C.

A large region of e.g. a ferromagnetic material with a constant magnetization throughout will create a large magnetic field, which requires a lot of magnetostatic energy stored in the field. To reduce this energy, the sample splits into domains. For all the cases (FM, AFM, Ferri) there can be a domain structure below the critical temperature, where separated parts show up with already aligned spins. Naturally they point into different directions canceling each other out, resulting in a vanishing net magnetization. The domains are separated by domain walls, which are a gradual reorientation of individual moments across a finite distance the so called weiss area. The domain wall thickness depends on the anisotropy energy, as well as the exchange coupling of the material, but on average spans across around 100–150 atoms.

The movement of domain walls can cause a hysteresis curve and is by itself irreversible, since if the moving magnetic field is high enough the material will remember its orientation and leave with a remanence M_r so a non zero magnetization. Following figure 2.4: the initial magnetization curve M_0 will ramp up until the saturation M_S is reached and then fall into the hysteresis loop, where the remanence can be overcome by a negative field and the material will end in a zero magnetization only if we apply the so called coercitive field H_C.

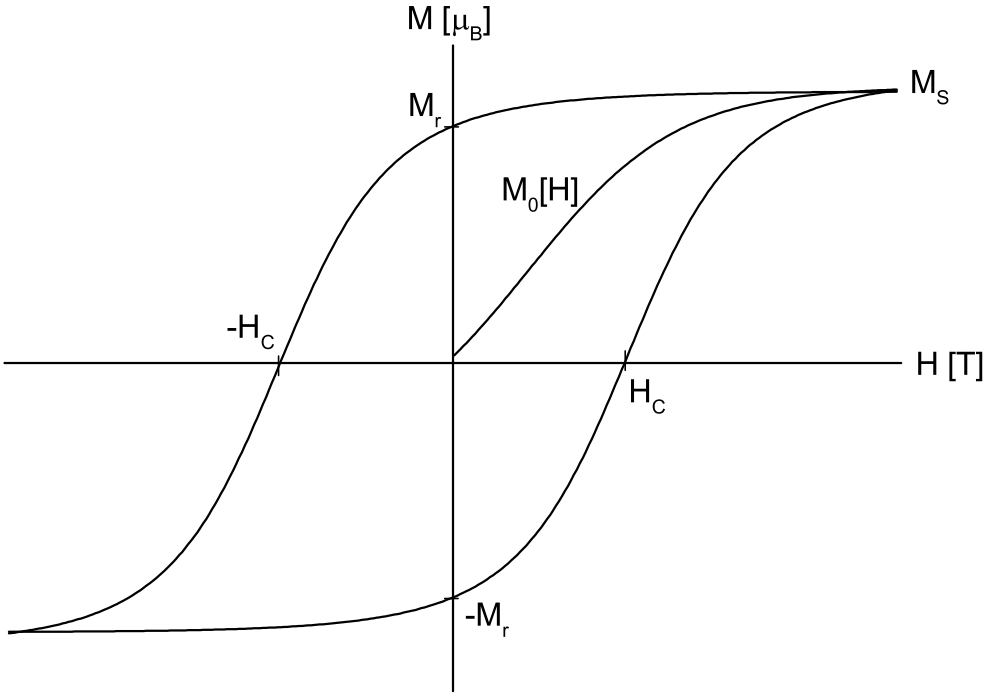

Figure 2.4: A plot of M vs. H is shown, which depicts the hysteresis process of a ferromagnet.

2.5 Geometric frustrated magnetism

In the case of the simple ground states of a FM, AFM and ferrimagnet the competing interactions (coupling constants) can be fulfilled, but there are cases where the symmetry of the underlying lattice of the magnetic ions prevents the satisfaction of all pair-wise interactions. The simplest case is a triangle of spins, where each spin has two neighboring atoms. In the case of antiferromagnetic coupling Ising spins, which are restricted to point along an axis the spins cannot order. Realized in a lattice this frustration would be for example found in a triangular lattice or in the kagome lattice (see figure 2.5). The latter is the case of the atacamite family studied in this thesis. In such a perfect lattice this geometric frustration completely prevents ordering down to lowest temperatures. One can define the parameter

$$f = \frac{\theta_W}{T_N} \tag{2.14}$$

that tells the amount of frustration in a sample.

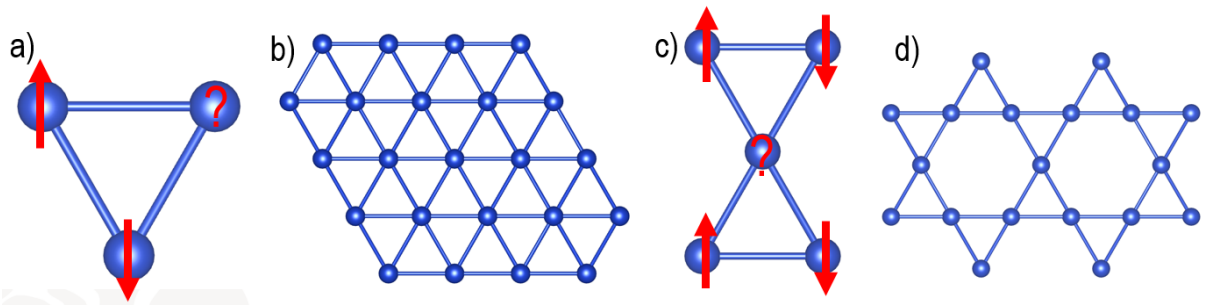

Figure 2.5: a) An image of three antiferromagnetically coupling spins in a triangle and b) it's realization in a triangular lattice. c) A spin in a fourfold antiferromagnetically coupled environment, as well as d) its realization in a kagome lattice.

The underlying ground state of highly frustrated lattices is expected to be the resonating valence bond (RVB) state. The theoretical concept of RVBs was first proposed by Anderson to describe initially the high-T_c cuprates [8]. Anderson suggested that the spins will form singlet dimers (see next chapter) at low temperatures and the ground state would be a superposition of all possible dimer configurations. This concept still has many candidates and even further neighbor pairings might be possible. Also whether the excitation to the triplet state is gapped or not is under debate. Even the microscopic image is unclear wether we have a decreasing ordered moment or a decreasing number of moments contributing, which is why we can simplify it by static/frozen - and dynamic phase parts.

In real systems as the atacamite family it is even more complex since we are not dealing with only one antiferromagnetic coupling but several couplings, thus releasing some of the frustration.

2.6 Dimers

Dimers are pairs of electrons, which each carry a spin $S = \frac{1}{2}$ and thus form a singlet ground state $S = 0 : \frac{1}{\sqrt{2}}(|\downarrow\uparrow\rangle - |\uparrow\downarrow\rangle)$ with a triplet excited state $S = 1 : \frac{1}{\sqrt{2}}(|\downarrow\uparrow\rangle + |\uparrow\downarrow\rangle)$; $|\uparrow\uparrow\rangle$; $|\downarrow\downarrow\rangle$ separated by an energy gap Δ leading to the partition function

$$Z = \sum_i e^{-\beta H_i} = 1 + e^{-\beta\Delta}\left(e^{\beta g\mu_B B} + 1 + e^{-\beta g\mu_B B}\right)$$

So the magnetization is given by

$$M = \frac{1}{\beta}\left(\partial_\beta \ln Z\right)_T = \frac{e^{-\beta\Delta}}{\beta}\beta g\mu_B \frac{\left(e^{\beta g\mu_B B} - e^{-\beta g\mu_B B}\right)}{1 + e^{-\beta J}\left(e^{\beta g\mu_B B} + 1 + e^{-\beta g\mu_B B}\right)}$$

$$\overset{\beta \ll 1}{\approx} e^{-\beta\Delta} g\mu_B \frac{\left(1 + \beta g\mu_B B - \left(1 - e^{-\beta g\mu_B B}\right)\right)}{1 + e^{-\beta\Delta}\left(\beta g\mu_B B + 1 + 1 - \beta g\mu_B B\right)} = \frac{2\beta g^2\mu_B^2 B}{e^{\beta\Delta} + 3}$$

The susceptibility for one dimer is given by

$$\chi = \frac{\partial M}{\partial H} = \frac{2g^2\mu_B^2}{k_B T\left(\exp\left(\Delta/k_B T\right) + 3\right)} \tag{2.15}$$

the Bleaney-Bowers equation with $\beta = (k_B T)^{-1}$. If we now take a lattice of dimers we will have to include the number of dimers N. To fully describe a realistic dimer system we have to add a general Curie-contribution of our paramagnetic compound and a diamagnetic contribution shown in figure 2.6. The energy gap Δ is the intradimer coupling constant J_{ij} of the previous chapter:

$$\chi_0 = \frac{Ng^2\mu_B^2}{k_B T\left(\exp\left(-J_{ij}/k_B T\right) + 3\right)} + \frac{C}{T} + \chi_d \tag{2.16}$$

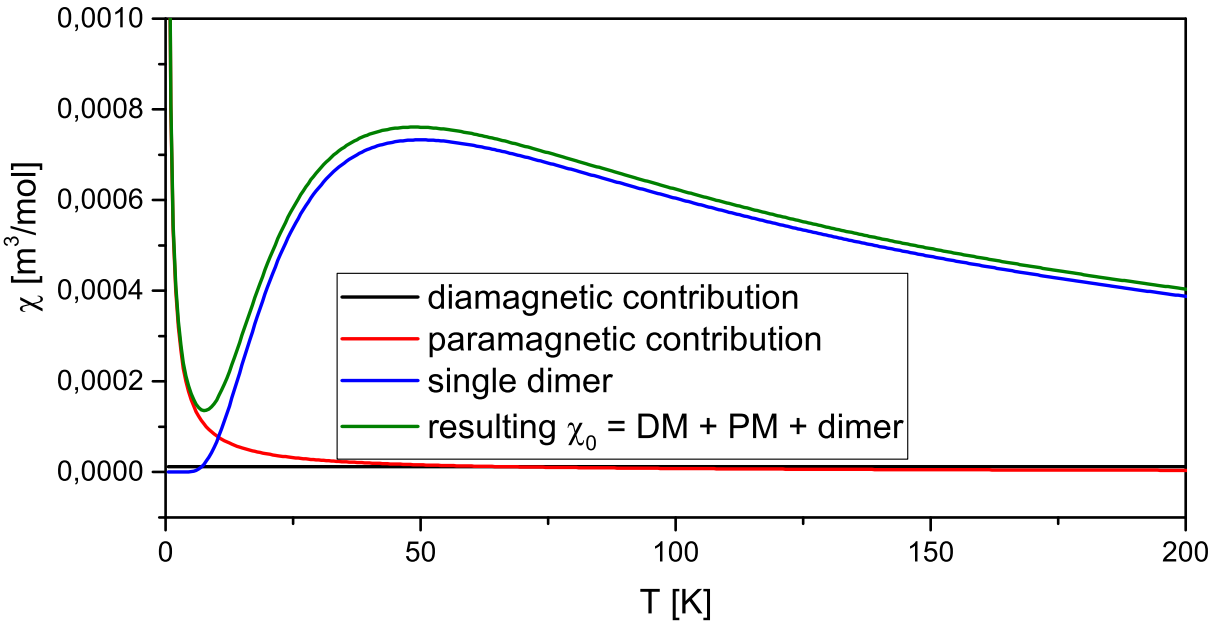

Figure 2.6: Plot of each seperate contribution and added as the χ_0 susceptibility in SI units of a dimer system.

The contribution of all nearest neighbors can be considered in a mean-field approach

(described in chapter 2.4) where the dimers are considered free of their neighbors and the coupling is applied as an external field, here all other couplings are integrated into the coupling constant J_{mf} giving the equation. Generally there are some impurities within the crystal which can be described with a paramagnetic part, where we expect for each S = 1/2 particle like Cu^{2+} a contribution of $C_{imp} = \frac{n\mu_0}{3k_B} 2\mu_B \sqrt{\frac{1}{2}(\frac{1}{2}+1)} = 4.8755 \cdot 10^{-7} \mathrm{m}^3/\mathrm{molK}$:

$$\chi = \frac{(1-i)\,\chi_0}{1 + k_B J_{MF} \left(N g^2 \mu_B^2\right)^{-1} (1-i)\,\chi_0} + i\frac{C_{imp}}{T} \tag{2.17}$$

Applying a magnetic field at lowest temperatures causes the triplet state to Zeeman split, until at a critical field H_{c_1} the energetically favored state overlaps with the ground state. In the case of $BaCuSi_2O_6$ with a magnetic field along the c direction the favored state is the $S_z = 1 = |\uparrow\uparrow\rangle$ state. The overlapping results in a linear increase in the magnetization since the spins start to flip to the favored state. This happens until at a second critical field H_{c_2} all spins are aligned and we have a field induced ferromagnet. The spinflip of a singlet state to the $|\uparrow\uparrow\rangle$ triplet state is called a triplon, which are magnons and thus bosonic quasiparticles. Bosons do not follow the fermionic exclusion principles and thus will populate all the same state. This region where the spins start to flip up is a so called Bose-Einstein-Condensate (BEC) of triplon quasi particles. In the case of a two-dimensional dimer lattice like it is the case for $BaCuSi_2O_6$ the transition to this state is called Berezinsky–Kosterlitz–Thouless (BKT) transition [9] and for a one dimensional system the state is called Luttinger Liquid (LL).

To envision this scenario a scetch was created, which is shown in figure 2.7. Where the possible spin arrangements in a dimer are shown on the left and their resulting energy levels plotted in a T-H phase diagram result in small dome between H_{c_1} and H_{c_2} of the interesting BKT phase. As mentioned the spin flips cause an increase in the magnetisation shown in an added green curve in this phase diagram.

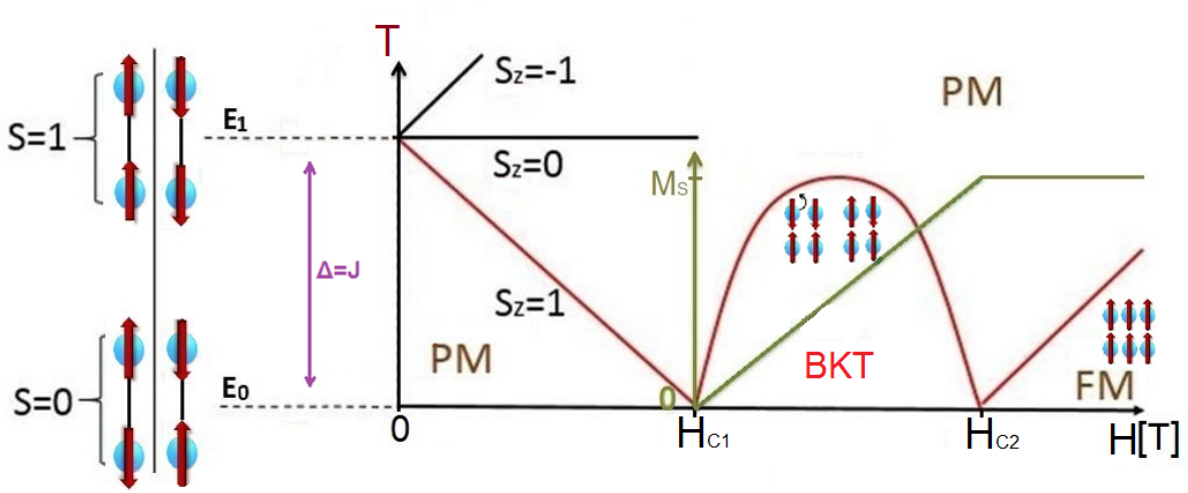

Figure 2.7: Sketch of the singlet and triplet state with its resulting energy levels to the left of a phase diagram, first depicting the Zeeman splitting. The red lines give the phase boundary of the BKT transition at the critical fields. As an inset in green the magnetization is depicted.

3 Experimental techniques

This chapter introduces the basis of all experimental techniques of analysis applied in this thesis. The logical order is based on the preparation process of new materials: for samples grown from the melt we first start with the phase diagram analysis searching for the right crystal growth parameters with the STA method and apply the knowledge to the crystal growth experiment in a furnace. Given a successful growth we then analyse the structure and thus phase purity and crystallinity of the powder/crystals with diffraction techniques. The improved diffraction measurements using synchrotron and neutron beams were performed externally at PSI and ESRF. For substituted samples the amount of substitution is best accessed using the EDX analysis of the SEM measurements giving us the stochiometry. Once the structural parameters are clear we can look into the physical properties of the system and this is best done on oriented single crystals using a Laue diffractometer to reveal anisotropies. With a physical property measurement system (PPMS) thermal properties like the heat capacity, or magnetic properties with the vibrating sample magnetometer can be analyzed. Finally local probing to understand the microscopy of magnetic materials are performed externally by the group of Philippe Mendels (Orsay) and Michael Baenitz (Dresden) using muon spin resonance ($\mu-$SR) and nuclear magnetic resonance spectroscopy

3.1 Simultaneus thermal analysis (Netzsch STA 409)

The STA method is a combination of differential thermal analysis (DTA) and thermal gravimetry (TG).

DTA measures the temperature change of a sample upon an external temperature profile. This enables us to directly measure phase transitions like the melting and crystalisation point and thus access the binary/ternary/etc. phase diagram of some systems.

The method uses two inversely coupled thermo elements. We utilized always Type S, Pt-$Pt_{0.9}Rh_{0.1}$. They measure the thermal-voltage [μV] and thus the temperature at the sample and at a reference (air) at the same time. Due to the inverse coupling the signals subtract each other and we measure the difference curve. Both sample and reference are in a furnace with a SiC heater (25°C-1500°C) and thus experience the same temperature-time-profile. The chamber can be evacuated or filled with Ar, O_2, N_2 and even a gas flow can be applied. A basis-line can be measured to rule out noises from the setup and the crucibles (Al_2O_3, Pt and SiO_2 ampules). There are always thermal flows between sample and reference and in the case of no phase transition, with a small perturbance of the symmetry of the furnace, a small temperature difference will be established. At a phase transition the local temperature of the sample will change compared to the reference, e.g. it might take heat in an endothermic reaction to change the phase and thus a positive peak will be detected as a signal.

At the same time the mass change is measured with a thermo-balance which is calibrated in the beginning. This method helps to determine the origin of the thermal signal, since in the case of a decay the outgoing gas will give us a declining mass where the differential helps us to determine the exact temperature of the phase transition. Furthermore an exact

enthalpy calculation is possible. The balance works with the substitution Balkan balance principle with electromagnetic weight compensation and is in a vacuum and shielded from the furnace by Al_2O_3 shield-plates.

3.2 Coherent-elastic scattering techniques

Diffraction refers to the coherent-elastic scattering of a wave with a periodic lattice and is a result of the interference due to the lattice. The wavelength must therefore be of the order of the atom distances $\sim 10^{-10}$m. The diffractometer is based on the Bragg equation giving the constructive interference of the order n of two light rays with the incident angle θ, normal to the diffraction plane and the wavelength λ that are reflected on the atom layers of the lattice layer indicated with the Miller indices (hkl) with the distance d:

$$n\lambda = 2d_{hkl}\sin\theta$$

The derivation of the equation can be performed easily by geometrical thoughts: We experience constructive interference when the optical path difference δ is a natural number times the wavelength $2\delta = n\lambda$. This optical path difference again constructs a right angled triangle as the opposite leg G with the lattice plane distance d_{hkl} as the hypothenuse H and our incident angle. The law of sinus then gives $\sin\theta = G/H = \delta/d_{hkl} = n\lambda/2d_{hkl}$.

Meaning that at certain angles when a lattice plane is hit there is constructive interference giving off large amounts of light which can be measured with a detector at the angle θ.

3.2.1 X-ray powder diffraction (Bruker D8-Focus, Siemens D500)

If we scan over the whole angular regime, we will see a reflex giving off more counts at the constructive angels. The whole set of reflexes is unique for each structure and compound. The amount of light interacting with the atom is dependent on many factors: the atom radius, the temperature causing the atoms to oscillate within the lattice (seeming as larger radii) and the electron density of the atom. For our laboratory experiments a flat-plate reflection geometry is used, where the powder sample is spread on grease so that statistically every orientation is present in the sample. There are different ways to scan over the angles and the two diffractometers used here work with the Bragg-Brentano geometry, where the X-ray tube is fixed, and the sample rotates with θ, while the detector rotates with 2θ. Both the Bruker and the Siemens diffractometer use a copper cathode with a nickel blind to get rid of k_β-radiation. So the resulting wavelength is $\lambda_{K_{\alpha 1}} \approx 1.5406$Å, if the K_{α_2}-line is subtracted digitally afterwards. The diffractometers use a scintillation-counter, which is a crystal transferring the light into the spectral range, which then is converted to a current pulse. In the Siemens D500 the sample is placed on a copper sample holder in a Lakeshore M-22 closed cycle refrigerator to measure in the range from 10 to 300 K.

3.2.2 Synchrotron X-ray diffraction ($\lambda = 0.77537$Å SLS-MS-PD at PSI)

If the resolution is insufficient for precise structural refinements synchrotron radiation is an improvement, where the high flux allows a good signal-to-noise ratio, with increased information content and minimal instrumental broadening. Synchrotron radiation is created in particle accelerators where electrons are accelerated close to the speed of light and kept on a circular trajectory. This is done by magnets and since electrons are charged particles

the acceleration is a change in their momentum causing them to emit electromagnetic radiation of high intensity.

The synchrotron instrument used at PSI works with the Paul-Scherrer-method, since it is also utilized for single crystal diffraction. Where the powder is enclosed in a capillary and rotated to get a statistical distribution and the detection is done using an area detector. Diamond powder is added to the sample for calibration.

The synchrotron X-ray diffraction data were collected with the SLS-MS Powder Diffractometer with a wavelength of 0.77537 Å on a powder sample enclosed in a capillary with a diameter of 0.3 mm, which was placed in a Janis flow-type cryostat (4 - 300 K). The Microstrip Mythen-II detector was used, which allowed for high counting rates while maintaining the high resolution which was essentially sample-conditioned. The typical counts of $\sim 2 \cdot 10^5$ in the strongest peaks were achieved within ~ 1 minute.

MYTHEN is one module containing 1280 p-doped silicon micro strips of 50 µm width constructed with optical lithography on n-doped silicon wafers of 300 mm-thickness, each behaving like a reverse-biased diode. The X-ray radiation is adsorbed in the silicon mainly by the photoelectric effect and creates electron–hole pairs in the silicon bulk. Under the influence of a strong electric field the holes then drift to the strips and the electrons to the back plane of the sensor consisting of a thin aluminized surface and of a np-doped layer (2 mm). Thus each X-ray photon of energy E_0 produces a charge $Q = E_0/3.6$ eV which is of the order of a few thousands of electrons and is sufficient for the front-end electronics to count each photon directly.

"The charge produced by the X-rays converting in the back plane layers recombines before drifting to the strips owing to the absence of electric field in this region, reducing the detection efficiency in particular for the low X-ray energies. For the X-rays absorbed in the depleted n-doped silicon bulk, the holes left in the valence band of the silicon crystal drift with little diffusion toward the closest strip, so that the spatial resolution is essentially defined by the 50 µm strip pitch. The efficiency of the sensor is more than 85% for X-ray energies in the range 5–10 keV and drops to about 25% at 20 keV, limited by the thickness of the silicon wafer. The readout is carried out by a 128-channel ASIC directly wirebonded to the sensor." [10]

3.2.3 Laue diffraction (Müller Mikro 91)

To orientate single crystals we shine a well collimated beam of X-rays with a wide wavelength spectrum on our single crystal with a fixed position and expose an optical video disk which then is read out using a Fujifilm FLA-7000 scanner. The method uses the fact that with a broad spectrum all necessary wavelength are present and thus constructive interference under the certain angles occurs giving off large amounts of light on certain positions. From a known crystal structure the reflection image can be reconstructed and thus we know the miller indices of the seen reflection points, enabling us to orientate the crystal. In our case we use a wolfram kathode with 12 kV and 20 mA. The optical disk is positioned in reflection at the X-ray tube, where a hole in the middle lets the incident beam pass by. The optical video disk has a BaF(Cl,Br) layer which safes the excited electrons from the X-ray beam in its F-center (a local defect). This information is read out in the scanner through luminiscence, excitating the safed electrons resulting in emitted photons due to decay. These photons are then read out using a photomultiplier.

3.2.4 Single crystal diffraction ($\lambda = 0.6972$Å BM01A SNBL and $\lambda = 0.3738$Å ID27 high pressure lab at ESRF)

For single crystals the X-rays permeate the sample and we measure the scattered area in

transmission seeing points at the constructive interference. Since we always have just one orientation present the crystal has to be two times rotated around 180° to get the full area of (hkl) reflections.

At BM01A a pylatus detector [11] is used where small Si panels create electrons from the photo effect and a direct readout method is used on each pixel (similar to MYTHEN of chapter 3.2.2). This has the advantage of no background noise, but with a too big flux the pixels can be over saturated and destroyed. The temperature was controlled by a nitrogen, helium or heat flow directly blown onto the crystal, where a stainless steel rod was used to calibrate the temperature.

In the case of the pressure cell measurement at ID27 a charge-coupled device (CCD) is used. Here again the inner photo effect separates the electrons from the area of its photodiodes and this time saves them in a potential well of a Si film until read out over the bucket-bridget device, where the electrons are moved to the borders and the voltage can be accounted to each area. To create isotropic pressures on the single crystals a diamond anvil cell is used. A sealable stainless steel mount pushes the polished plain surfaces of the diamond of 500 µm, or 250 µm on top of each other. A stainless steel gasket is manufactured with the cell: a disk is laid between the diamonds and a cavity is pressed inside, where a hole will be drilled through of half the surface area. This gives us the space for the sample, a ruby and some pressed Cu powder. Fluorescence measurement are used on the ruby to check the exact pressure and powder diffraction on the Cu gives us the temperature. After positioning the three objects, the volume is filled with the corresponding gas to ensure an isotropic pressure on the sample. The pressure is caused by a membrane that is filled with a gas, which is in our case helium to be able to measure at low temperatures. The membrane is a small space in the steel mount that presses the diamonds together. In the mount is a hole where one can see through the diamond right at the sample and access an angular range of 70°. The temperature is controlled with a helium cryostat, that has a glass-wall at the diamond positions.

3.2.5 Neutron diffraction (HRPT at PSI)

Diffraction can also be performed with a beam of neutrons instead of X-rays. Here the wavelength is dependent on their speed v. Neutrons are massive particles unlike phonons and thus they do scatter on the nuclei of the atom. Since this process is less dependent on the mass of the scattered nuclei, this technique is useful for refining light elements. The utilized neutrons can be created using a nuclear-fusion reactor and become monochromatic after the (111) reflection with a graphite single crystal. In this technique the magnetic core of the atom has an influence and thus also the magnetic structure can be accessed with refinement.

The powder diffraction experiments were carried out with two different diffraction techniques: the high-resolution powder neutron diffractometer HRPT [12] at the spallation neutron source SINQ and the Powder Diffraction station of the Materials Sciences Beamline (MS-PD) [13] at the Swiss Light Source, both at the Paul Scherrer Institute in Villigen. For the HRPT experiments, an amount of $\sim$ 1 g of powder samples was enclosed into a vanadium can with an inner diameter of 6 mm and the measurement was carried out at room temperature, as well as at 1.5 K in a ^{4}He bath cryostat with a wavelength of 1.8857 Å for $BaCuSi_2O_6$ and 1.4940 Å for the kagome systems.

3.3 SEM with EDX analysis (Zeiss DSM 940A, AMETEK EDAX Quanta400)

The Scanning-electron-microscope (SEM) uses an electron beam to analyse the surface of the material. It can reach a magnification of ∼10 nm, compared to ∼450 nm for light microscopes which are limited to the Abbe limit. The EDX detector is then used to analyse the chemical composition of this surface. To receive a focused electron beam high vacuum is necessary. The primary electrons are created using a Wolfram-hairneedle-cathode and then accelerated with a voltage of 30 kV, the position and focus of the beam is done with magnetcoils, lenses and blends. Some of the primary electrons scatter inelastically with the bound electrons of the sample and can knock them out, creating secondary backscattered electrons. The image is then created by primary and secondary electrons. The hole created in this process will be filled by electrons of higher shells sending out a characteristic X-ray light, which we detect with the Li drifted p-Si semiconductor-detector of the energy dispersive X-ray detector (EDX). Here the X-rays ionize the Si. These freed electrons create charges who will be amplified to create a voltage pulse. The position of the pulse in keV is characteristic for each element and the amount of pulses is proportional to the amount of the element.

The sample has to be conducting for this measurement, because otherwise the electrons cannot flow away from the sample and will effectively burn through it. We stick the samples on a carbon layer on top of a metal plate. For isolating samples carbon will be evaporated on top of them with a Balzers Union N318 sputtering mashine. The layer of carbon is visible in a slight blackened shining. Well prepared samples with a polished surface and carbon layer are shown in figure 3.1. The crystal edges shine brightly due to the coating and lines are burned into the carbon layer. The lightest element to measure in the EDX is carbon and the accuracy is around ∼ 2 at%, depending on the atomic number and the measurement conditions.

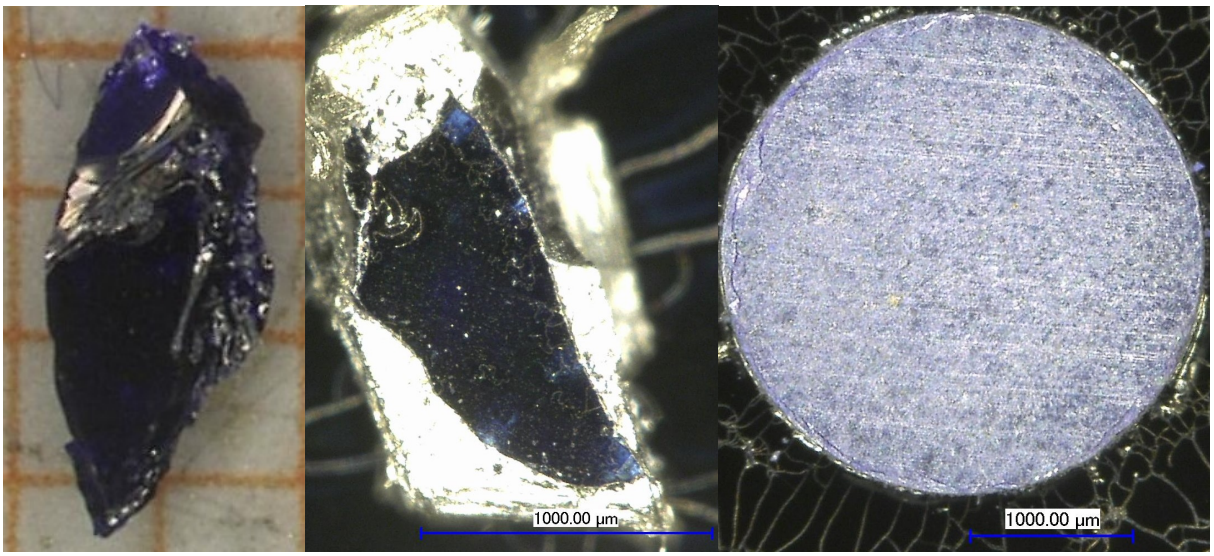

Figure 3.1: Image of a $BaCuSi_2O_6$ crystal with a polished surface before (left) and after sputtering (middle) as well as a polished pressed pallet after sputtering (right).

For optically seperable phases in combination with a diffractogram of the sample, the EDX analysis can give us nearly exact stochiometries of the powder or crystalline samples.

3.4 Physical property measurement system (Quantum Design PPMS)

The PPMS is an industrially manufactured cryostate system with different measurement applications. It is a stainless steel canister filled with liquid nitrogen (boiling point 77.355 K) on the outer shell as a thermal buffer and liquid helium (4.22 K) in the inner shell as a cooling source. Since the nitrogen and helium are liquid they will cool anything in contact to its boiling temperature while evaporating, and when pumping at the helium the pressure is reduced resulting in an effective cooling (following the phase diagram). In the center is a small chamber for the sample holders (puck), which is surrounded by a superconducting magnet, in our case going up to 9 T. With a heater on the sample holder and a pump connected to the chamber, as well as the helium room the PPMS is able to reach any temperature from 1.8 K to 350 K.

3.4.1 Heat capacity

The heat capacity is the ability of a material to save thermal energy and can be accessed by the reaction/ energy change of a sample to a temperature change. The integration over the temperature of this value gives a direct access to the change in entropy consisting of the conduction electron, vibrational and phonon degrees of freedom. In this measurement we use a platform connected by eight wires to the environment. The wires are electric contacts for a thermoelement, as well as a heater. The otherwise free floating platform ensures a thermal coupling only to the sample which is mounted with Apiezon-N a thermal well conducting grease with no phase transitions up to 250 K. For this measurement a high vacuum is applied using a shielding with activated carbon to ensure a thermally isolated measurement. The sample experiences a heating pulse while the temperature change is recorded as a function of the heating power. The phonon contribution of the specific heat can be calculated using the Debye model on a linear fit of the C/T vs T^2 curve

$$C = \beta \cdot T^3 + \ldots = \frac{12\pi^4 N_A k}{5\vartheta_D^3} T^3 + \ldots \tag{3.1}$$

where ϑ_D is the Debye temperature. This model is constructed for a single atom, so one has to multiply β by the atom number of atoms per formula unit for a real system. For our insulating systems the electron contribution is absent ($\gamma = \pi^2 N_A k^2/(2E_F) = 0$), but for the kagome systems spin liquid contributions have to be considered.

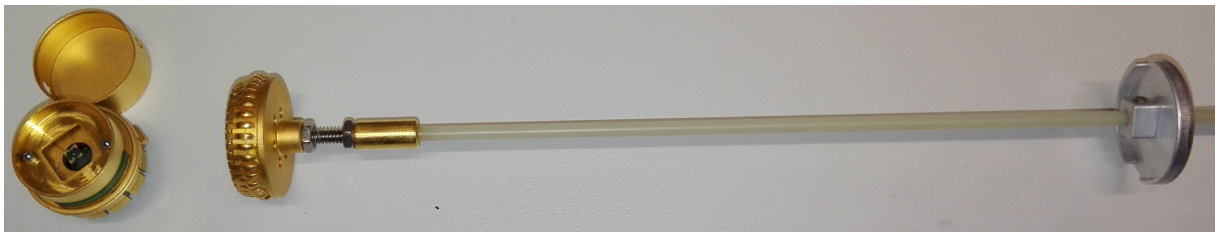

Figure 3.2: An image of the puck for heat capacity and a part of the shield with the charcoal holder from Quantum Design

3.4.2 Vibrating sample magnetometer (VSM)

This option utilizes a pickup coil puck that is surrounding the sample, so that in an applied field the magnetization of the sample can be measured indirectly by picking up the voltage

when the sample magnifies, or decreases this field. Therefore the sample is attached to a rod and moved with a motor in and out of the pickup coil. For powder samples small nonmagnetic plastic capillaries are filled and fixed in a brass holder attached to the rod. Single crystals on the other hand are glued with in ethanol solved GE-varnish to a quartz holder which is then attached to the rod. Both have only a small magnetic signal. The measured units of this application are in cgs units and are converted for comparability into SI unit:

$$\left[\frac{M\,(T)}{H}\right] = \frac{\text{emu}}{\text{Oe}} = \frac{10^{-3}\text{Am}^2}{\frac{10^3}{4\pi}\frac{\text{A}}{\text{m}}} = 4\pi \cdot 10^{-6}\text{m}^3$$

$$[M\,(H)] = \text{emu} = \frac{10^{-3}\text{Am}^2}{9.274 \cdot 10^{-24}\frac{\text{Am}^2}{\mu_B} \cdot 6.022 \cdot 10^{23}\frac{1}{\text{mol}}} \approx \frac{\mu_B}{5585}\,\text{mol}$$

The molarity is taken into account by then mutliplying these values with $m_{mol}[\text{g/mol}]/m[\text{g}]$.

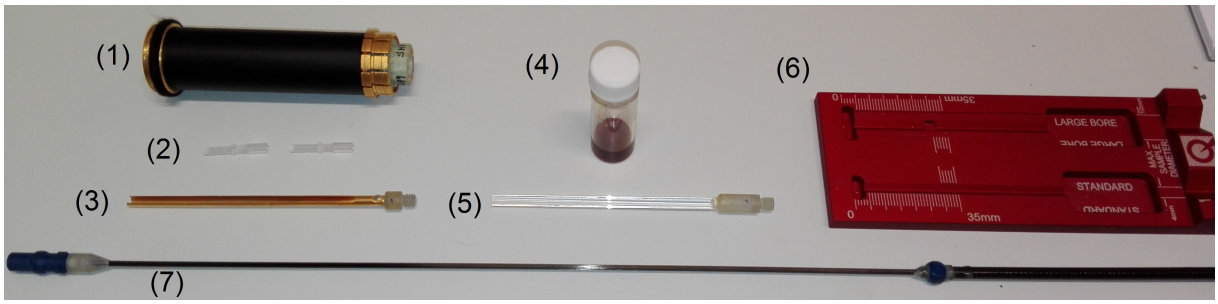

Figure 3.3: Image of the puck (1) and the different sample holders: plastic capillary (2) which will be stuck into the brass (3) and a quartz holder (5) where crystals are glued to with GE-varnish (4) for the VSM option. The optimal sample position is determined with a sample mount (6). Both sample holders are screwed onto the rod (7) which has a magnet on the top sticking it to the motor.

Pulsed field setup: High-resolution magnetization measurements were performed in a capacitor-driven pulse-field setup by Lars Postulka at the PI, Frankfurt. Experiments can be performed up to 58 T with a pulse duration of 21 ms. The setup was equipped with a ^{4}He-bath cryostat. The sample was placed in a 1266 stycast can with a diameter of 3 mm. The type of measurement is similar, but due to the pulse no sample motion is necessary.

3.5 Muon Spin Rotation/Relaxation/Resonance $\mu-$SR (GPS and LTF at PSI)

In this technique we transport a perfectly spin polarized surface muon in our sample, which then will be influenced by local fields, using a system of magnets that conserve spin polarization. Inside the sample the muon will decay after some time and send out a positron of which the spin will be detected. There are three measurement techniques: zero -, transverse - or longiturdinal field. In zero-field the spin will solely be influenced by the sample field, but with transverse field the muon-spin will turn 90° and then precess at a Larmor frequency of $\omega = \gamma H = 13.554\,\text{MHz/kG}$. The amplitude is dependent on the amount of ordering phase. From a fit the relaxation rate can be calculated. The longiturdinal mode is used to see the dynamics, since the muon senses an added vector field of the external and the local field and will only slightly precess if the local field is weak compared to the external one.

The muons are created using a beam of high energy protons (590 MeV). When these protons collide with graphite a pion is produced which is sent into a surface layer, where it lives for 26 billionths of a second and then decays into a muon of 4 MeV and an antineutrino.

The samples should cover an area of 0.5 mm x 0.5 mm and have masses above 20 mg, for the lower limit a aluminium film of 0.25 mm is placed before the beam and the sample so that the muons are slowed down. The samples are either filled in a thin aluminium foil wrapping for GPS or glued with GE-varnish to a silverblock for LTF and then surrounded by a sticking aluminiumfoil/silver attached to a copperholder. The GPS has a gas-flow cryostate going down to 1.5 K, while the LTF uses a dilution fridge with a cold finger able to reach 20 mK.

3.6 Nuclear magnetic resonance spectroscopy NMR (Bruker AVANCE-II)

The high-resolution powder NMR-spectra were recorded on $BaCuSi_2O_6$ with a Bruker AVANCE-II spectrometer attached to a 8.45 T magnet using home built MAS-NMR probes for 1.8 mm rotors at the National Institute of Chemical Physics and Biophysics in Tallinn. At room temperature spectra were recorded at 35 kHz sample spinning speed and at low temperatures they were recorded at about 30 kHz. At fast magic angle spinning (MAS) the broad NMR line of a powder sample transforms into the single peak at the isotropic value of the magnetic shift interaction [14]. If the spinning speed is less than the magnetic shift anisotropy in frequency units, then the main peak is accompanied by a number of spinning sidebands at multiples of the spinning speed value from the main peak. Although, the pattern of many spinning sidebands seems complicated, it tells us unambiguously how many inequivalent nuclear sites exist in the structure. The main purpose for using this technique here is to show, that there is only one silicon site in doped $BaCuSi_2O_6$ at room temperature and at low temperature as well, whereas the ^{29}Si MAS NMR spectrum of the parent compound shows the appearance of additional ^{29}Si resonance lines below $T < 100$ K [15].

4 Research on dimer systems

4.1 (Ba,Sr)$CuSi_2O_6$

This chapter describes the research results of the prominent dimer candidate Han Purple, $BaCuSi_2O_6$, where substitution leads to a stabilisation of the room temperature structure $I4_1/acd$. The majority of the results of this chapter were published in a Physical Review B article [16].

4.1.1 Introduction

Magnetic insulators with Cu^{2+} dimers are suitable materials to study quantum many-body effects under variable conditions. The occurrence of magnetic field-induced ordered states, which can be described as Bose-Einstein condensation (BEC) of triplons in this type of compounds provide a platform to study this ordered state in great detail, by investigating scaling laws of thermodynamic quantities [17]. The main idea behind this is that dimers of two Cu^{2+}-ions, which each carry a spin 1/2, can be mapped onto bosons to realize a BEC [18]. A prominent material where the appearance of a field-induced BEC of triplons was reported is $BaCuSi_2O_6$ [19], owing its particular structure to layers of closed rings of SiO_4 tetrahedra bridged by vertically arranged Cu^{2+} dimers which form a square lattice (see Fig. 4.1). It was proposed that frustrated inter-dimer couplings between the dimer layers lead to a dimensional crossover at the quantum phase transition from a paramagnetic to a field-induced magnetically ordered state [20]. However, it is known since 2006, that $BaCuSi_2O_6$ undergoes a first-order structural phase transition at $T \sim 100K$ from a high-temperature tetragonal to a low-temperature orthorhombic symmetry, followed by a weak incommensurability of the crystal structure [21, 23, 22] which thus leads to two different kinds of dimers in adjacent layers (see figure 4.1 first column). The impact of these two types of dimers on the peculiar properties of the reported BEC of triplons and the role of the frustration in this material are still under debate [23, 24, 25].

Mazurenko *et al.* [26] showed by performing density functional theory (DFT) calculations based on low-temperature structural data of the orthorhombic crystal structure, that the frustration between dimer layers is released due to the presence of a significant antiferromagnetic interaction between the upper site of one dimer and the bottom site of the neighbor dimer. Such a finding, backed by elastic neutron scattering data, questioned existing theories based on the presence of interlayer frustration. Recently, low-temperature high-resolution NMR (nuclear magnetic resonance) measurements [15] detected broadened ^{29}Si lines with complex line shape in the orthorhombic phase suggesting a more complex structure than originally thought, which complicates the understanding of the observed field-induced BEC of triplons at low temperatures.

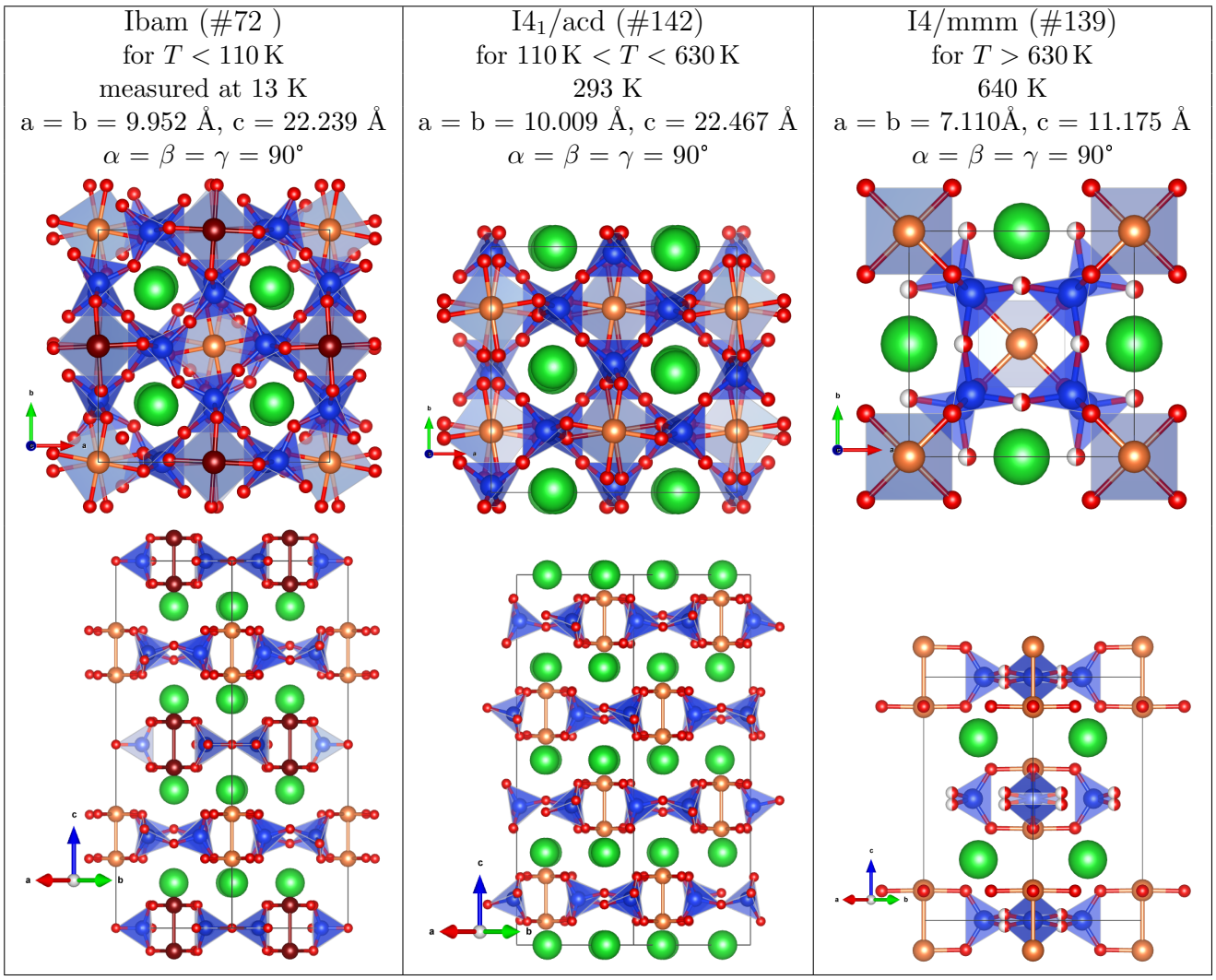

Figure 4.1: Comparison of the $BaCuSi_2O_6$ structures: orhtorhombic Ibam for low temperatures ($T < 110\,\mathrm{K}$), tetragonal $I4_1/acd$ for room temperature ($110\,\mathrm{K} < T < 630\,\mathrm{K}$) and tetragonal I4/mmm for high temperatures ($T > 630\,\mathrm{K}$). All are shown first along the c-axis and then along the (110) direction. Generally in this structure the Ba atoms in green seperate the layers of Si (blue) - O (red) tetrahedrons, which force the Cu (orange/ dark red) in the arrangement of pairs in a square lattice. With the view along (110) one can clearly see the difference of the two dimer layers: the dark red variant shows perfectly aligned SiO_4 - tetrahedrons, while the orange one is similar to the room temperature structure. Also the Cu-Cu distances vary slightly [23, 27].

To get some insight into the controversy about the role of frustration, we analyse the structural phase transition with detailed single crystal as well as powder diffraction. Furthermore we present results of a successful partial substitution of Ba by Sr as well as Si by Ge which reveals a stable tetragonal phase of $BaCuSi_2O_6$ down to the low temperature of 1.5 K of our experiment. With only one type of dimers in the structure and the absence of structural modulations down to lowest temperatures, such systems allow for the investigation of the critical properties of field-induced ordered states without having to deal with complications from the crystal structure. We further present a detailed characterization of $Ba_{1-x}Sr_xCuSi_2O_6$ based on synchrotron and neutron diffraction measurements on both single crystals and powder, NMR, thermodynamic measurements and DFT calculations and show that magnetization and susceptibility measurements for $Ba_{1-x}Sr_xCuSi_2O_6$ at $x = 0.1$ display a field-induced ordered state around 22 T.

Ibam	x/a	y/b	z/c	U_{iso}
Ba1	0.2567(5)	0.2444(5)	0.1234(3)	0.09(5)
Cu1	0	0.5	0.0624(2)	0.60(3)
Cu2	0	0	0.1893(2)	0.60(3)
Si1	0	0.2761(11)	0.25	0.29(4)
Si2	0.2773(12)	0	0.25	0.29(4)
Si3	0.0019(9)	0.7724(11)	0	0.29(4)
Si4	0.7771(13)	0.0067(9)	0	0.29(4)
O1	0.0362(5)	0.8095(5)	0.3089(3)	0.77(3)
O2	0.3054(6)	0.4622(5)	0.1891(3)	0.77(3)
O3	0.3076(5)	0.0092(5)	0.0608(3)	0.77(3)
O4	0.5123(5)	0.1918(5)	0.0626(4)	0.77(3)
O5	0.1281(6)	0.3730(5)	0.2698(2)	1.09(4)
O6	0.3454(7)	0.3454(7)	0	1.09(4)
O7	0.1042(7)	0.1043(7)	0	1.09(4)
$I4_1/acd$	x/a	y/b	z/c	U_{iso}
Ba1	0.25	0.98870(9)	0.5	0.01258(12)
Cu1	0	0.25	0.06374(3)	0.01012(16)
Si1	0.27554(11)	0.7511(2)	0.8760(4)	0.0096(3)
O1	0.1916(9)	0.7218(11)	0.8166(4)	0.0139(17)
O2	0.3725(8)	0.8786(8)	0.85939(16)	0.0226(10)
O3	0.3075(9)	0.7813(11)	0.0639(5)	0.0139(17)
I4/mmm	x/a	y/b	z/c	U_{iso}
Ba1	0	0.5	0.25	0.0242(3)
Cu1	0	0	0.12341(16)	0.0200(5)
Si1	0.2756(2)	0.2756(2)	0	0.0157(7)
O1	0.2415(14)	0.5	0.0239(18)	0.034(6)
O2	0.1916(5)	0.1916(5)	0.1209(4)	0.0392(14)

Table 4.1: Atomic positions and thermal factors of the three different structures measured at 13 K, 293 K and 640 K [23, 27] of $BaCuSi_2O_6$ shown in figure 4.1.

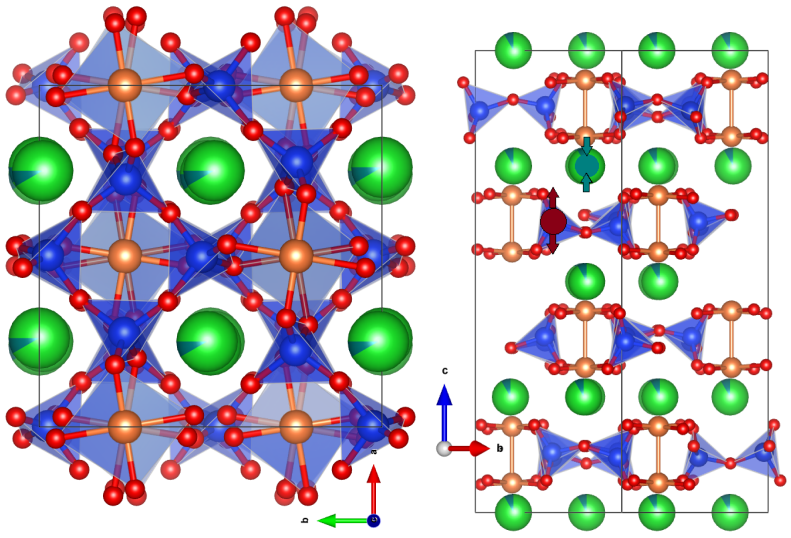

Figure 4.2: $(Ba_{1-x}Sr_x)CuSi_2O_6$ structure for $x = 0.1$ again viewed along the c-axis and the (110) direction. A cartoon of the effect of Sr (dark blue-green), as well as Ge (brown-red) on the lattice is depicted by the size of the atom as a bubble and the strain/pressure as an arrow.

4.1.2 DTA analysis

In order to investigate the conditions of the formation of the $BaCuSi_2O_6$ phase, as well as the influence of oxygen on the synthesis STA (DTA + TG) measurement was performed.

In figure 4.3 the DTA/ TG analysis of the sintering process for $BaCuSi_2O_6$ is shown both at air and in an oxygen rich atmosphere. Generally we see five obvious signals, where the first two are just structural changes of SiO_2 and $BaCO_3$. The third signal is the necessary decay of $BaCO_3$ enabling the phase formation of $BaCuSi_2O_6$ which then starts at around 1000 °C in the plateau of the mass curve in red. The fourth signal arises from the decay of CuO, after which the Ba - Si - O starts to melt and form a viscous liquid where a cooling resides in a glass formation. This prevents crystallisation from the pure melt, which is why we have to stay below 1039 °C to sinter powder samples of our compound.

The onset temperatures determined with the Netzsch software are: 576°C $\alpha\rightarrow$ β-SiO_2, 816°C $\gamma\rightarrow$ β-$BaCO_3$, main contribution ∼916°C (924.5°C with oxygen) $BaCO_3\rightarrow$ BaO + CO_2 , 1039°C (1075°C) $2CuO\rightarrow Cu_2O + \frac{1}{2}O_2$ with a mass loss of 0.6% this correspondents to 15% of CuO decaying (the total mass loss would be 4.03%), ∼1070°C (1076°C) melting and 1033°C $BaCuSi_2O_6$ crystallization.

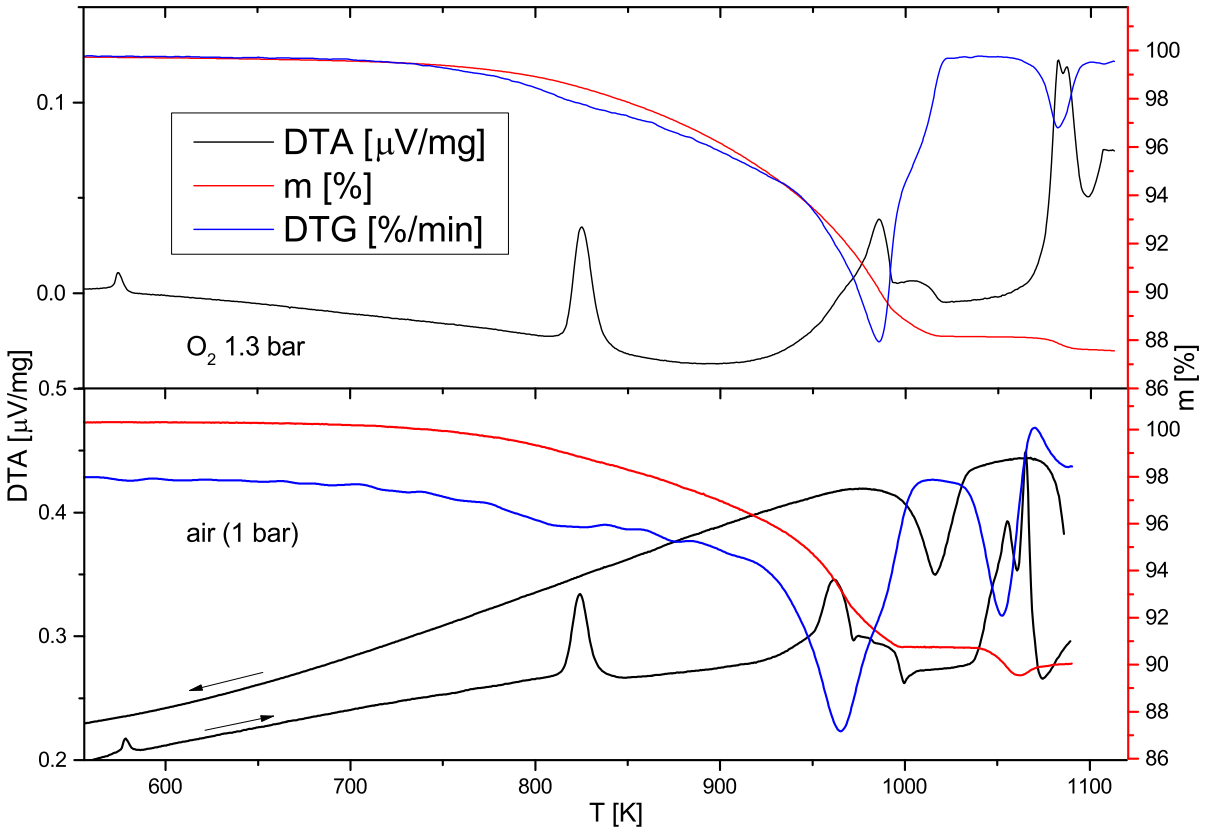

Figure 4.3: DTA/TG curve of a stoichiometric $BaCO_3$, CuO, SiO_2 mixture to create $BaCuSi_2O_6$, showing the pre-sintering process at air (lower plot) and 1.3 bar oxygen atmosphere. The derivative of the TG signal (DTG) in blue reflects the DTA signals of phase transitions with a mass loss.

The first two peaks of structural transitions are independant of the atmosphere, while the rest shifts to higher temperatures, note also the upturn of the mass in air at 1070°C, which is absent for oxygen atmosphere. This could be due to the need of oxygen during the silicate crosslinking at the creation of $BaCuSi_2O_6$ [28]. Meaning that a certain oxygen

atmosphere is necessary for the phase formation, which is also reflected in the necessity of an oxygen spending flux. Due to the overlap of the CuO decay and the formation of $BaCuSi_2O_6$ the exact onset temperature cannot be determined for the last peak.

4.1.3 Powder synthesis

Besides the obvious colour change from a grey powder mixture to a blue pigment the necessary sintering time described below was determined by PXRD.

The substitution of either $BaCO_3$ by $SrCO_3$ or SiO_2 by GeO_2 does not change the DTA signals drastically: dependent on the substitution amount the temperatures are slightly reduced. Following this observation, polycrystalline $(Ba_{1-x}Sr_x)CuSi_2O_6$ powder samples were prepared by sintering $BaCO_3$, $SrCO_3$, CuO and SiO_2 where the initial weight percentage of $BaCO_3$ was substituted by 5, 10, 20 and 30% $SrCO_3$.

substance	m[mg] $SrCO_3$	m[mg] $BaCO_3$	m[mg] CuO	m[mg] SiO_2	T [°C]
5 % Sr	18.6	471.4	200	302.1	1029
10 % Sr	37.1	446.5	200	302.1	1028
20% Sr	74.2	396.9	200	302.1	1025
30% Sr	148.5	297.7	200	302.1	1020

Table 4.2: Masses of the constituents for $(Ba_{1-x}Sr_x)CuSi_2O_6$ powder synthesis by sintering at the given temperatures of the last column.

The powder was ground and sintered in an aluminum oxide crucible at air at the given temperatures for 2 months. The process was accelerated by grinding the powder in between, leading to a better mixing of the phases. Note that higher temperatures for the 20 and 30% lead to a decay and the given temperatures are set points for a simple muffle furnace, which are not determined to the exact decree. Even after these long sintering times there is still a small amount ($< 5\%$) of impurities, which are besides the starting materials the competing pre-phase $BaCu_2Si_2O_7$ and end-phase $BaCuSi_4O_{10}$, in the silicate ring formation ($BaCu_2Si_2O_7 \rightarrow BaCuSi_2O_6 \rightarrow BaCuSi_4O_{10}$) [28]. We could not manage to synthesize compounds with Sr contents higher than 30%, but it also has to be noted that the pure $SrCuSi_2O_6$ phase has not been reported so far. Also polycrystalline $BaCu(Si_{1-y}Ge_y)_2O_6$ powder samples with 5, 10 and 20 % of the SiO_2 substituted by GeO_2 were obtained by sintering at 1027°C, 1026°C and 1025°C as well as a powder sample of both substitutions $Ba_{0.8}Sr_{0.2}Cu(Si_{0.9}Ge_{0.1})_2O_6$ which was sintered at 1025°C.

4.1.4 Crystal growth

Crucible material

The last signal in the DTA curve of figure 4.3 is the melting point. The resulting strongly viscous melt has a high wetting on the crucible surface, which is why an optimal crucible material has to have a very smooth surface. Thus Al_2O_3 and similar ceramics could not be used for the single crystal growth of $BaCuSi_2O_6$ since the crystals stick strongly to the crucible and will be damaged during the extraction process. The high melting point of this silicate thus reduces the amount of candidates as possible crucible materials strongly. In the DTA curve measured at air we see a crystallisation signal of $BaCuSi_2O_6$ since not all of the CuO did decay. This gives us a general idea of the working temperatures for crystal growth, where there are two ways to avoid the decaying of CuO: flux-growth and direct melting in a oxygen rich atmosphere. For both methods Pt crucibles are the best candidates.

Flux growth

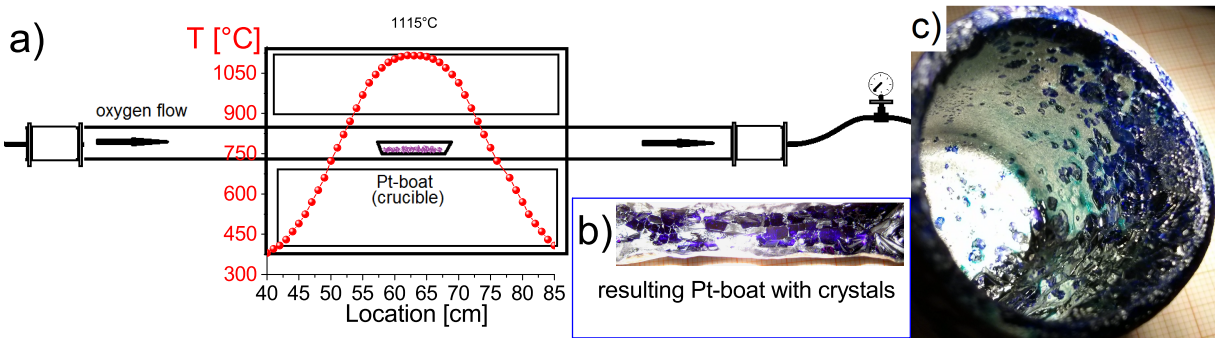

Figure 4.4: a) The sketch shows the tube furnace and its ofen profile with an applied oxygen flow at a setpoint of 1150°C plotted inside. b) As an inset a foto of a Pt-boat after the growth of $Ba_{0.9}Sr_{0.1}CuSi_2O_6$ single crystals is shown. c) A picture of a big platinum crucible after the flux growth can be seen.

$BaCuSi_2O_6$ crystals were grown in a platinum crucible with KBO_2 as well as $LiBO_2$ flux and a molar ratio of 1 : 2 (flux : powder) at 950 °C. Afterwards the Pt crucible was tilted in the furnace to remove the excess of flux, where the crystals stuck to the sides of the Pt crucible. Here similar to [29], the crystallization starts as a consequence of an oversaturation caused by evaporation and some crawling due to a wetting of the crucible. As an example of the crawling Fig. 4.4 c) shows a crucible where the crystals are not only found on the right bottom on which the crucible stood for flux removing, but also at the top of the crucible. So a decreasing of the temperature like it is done in Ref. [29] is unnecessary. It only decreases the time of growth for large amounts. Due to the viscosity of the flux-melt no signals of the crystallization could be determined in DTA measurements.

The advantage of potassium is that we could show that no flux is incorporated into the structure with simple EDX measurements on polished single crystals. We only found flux on some parts of surfaces which is already optically visible as a green phase.

Other flux attempts than the metaborates led to either cuprite or glass formation and in some cases even $BaCu_2Si_2O_7$ single crystals. For example 0.75 g $BaCuSi_2O_6$ powder with 3 g NaCl flux which was heated to 1030°C followed by slow cooling with 5 K/h to 955°C and with 0.5 K/h to 940°C gave a large yield of phase pure $BaCu_2Si_2O_7$ crystals.

Oxygen enriched atmosphere

Since the flux reacts with Sr to $SrBO_2$ the fluxgrowth cannot be applied to the substituted samples. As seen in the DTA analysis the application of oxygen shifts the CuO decay to higher temperatures, while the melting point is only slightly increased (see Fig. 4.3). Thus at some point the oxygen suppresses the decay of copper oxide $2CuO \rightarrow Cu_2O + \frac{1}{2}O_2$ even when our melt is reached as described previously in reference [19]. Single crystals of all substituted samples could be grown with $\sim$ 1 g pre-sintered powder filled in a 6 x 1 x 1 cm^3 boat-shaped platinum crucible bent from a 0.1 mm thick platinum plate. This crucible was placed in a tube furnace scetched in figure 4.4 a) with a oxygen gas flow of 1 bar (2 bar with atmosphere pressure), where a viscous melt is reached at a temperature of 1150°C, followed by a crystallization using a cooling rate of 12 K/h down to 900°C. A result of such a growth is shown a inset in figure 4.4 b). In this case the crystals can be easily extracted by carefully bending the plate [30].

Crystal shape and orientation Han Purple and its substituted single crystals grow dominantly as thin plates typical for tetragonal structures with the a = b direction along the long sides and c pointing out of the plane. Figure 4.5 shows two $BaCuSi_2O_6$ grown from flux and their corresponding Laue images, where the center point $(hkl) = (001)$ gives us the c-axis, as well as a $Ba_{0.9}Sr_{0.1}CuSi_2O_6$ crystal and the similar Laue image. The strontium substituted single crystals often are more needle shaped due to the extraction process of bending the platinum crucible, where plates tend to break.

Generally the crystal shape enables a simple orientation for measurements since the interesting dimer layers lie in the large plate, which can be seen already optically.

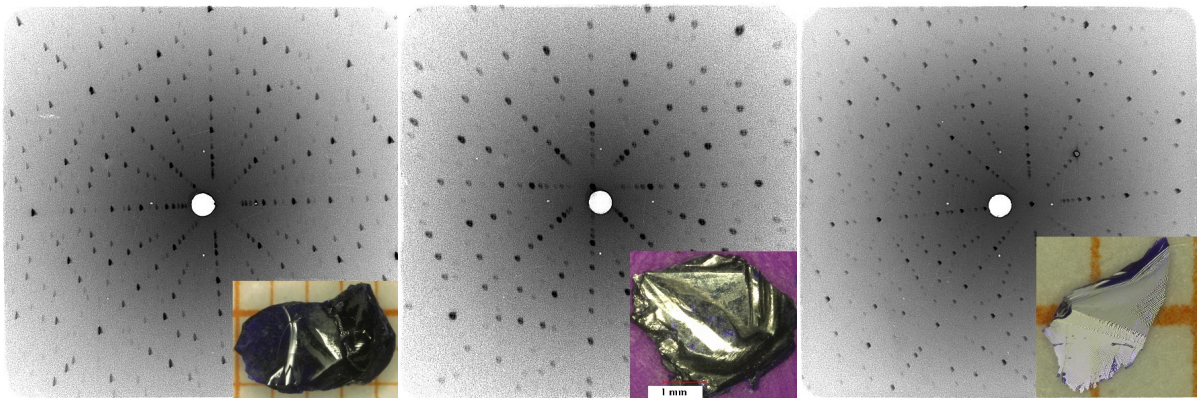

Figure 4.5: Laue diffraction images of typical $(Ba_{1-x}Sr_x)CuSi_2O_6$ crystals, which are shown as an inset.

4.1.5 Structural characterization at room temperature

We performed a refinement of the crystal structure parameters at room temperature by a combined analysis of neutron and synchrotron X-ray powder diffraction. The neutron diffraction HRPT results on 1 g of $Ba_{0.9}Sr_{0.1}CuSi_2O_6$ powder are shown for the room temperature measurement in Fig. 4.6 (black curve). The underlying refinement of the tetragonal $I4_1/acd$ structure (red curve) fits well to the measured data. Furthermore, we find a good agreement between the neutron data and the synchrotron data as shown in Table 4.3 ($x = 0.1$).

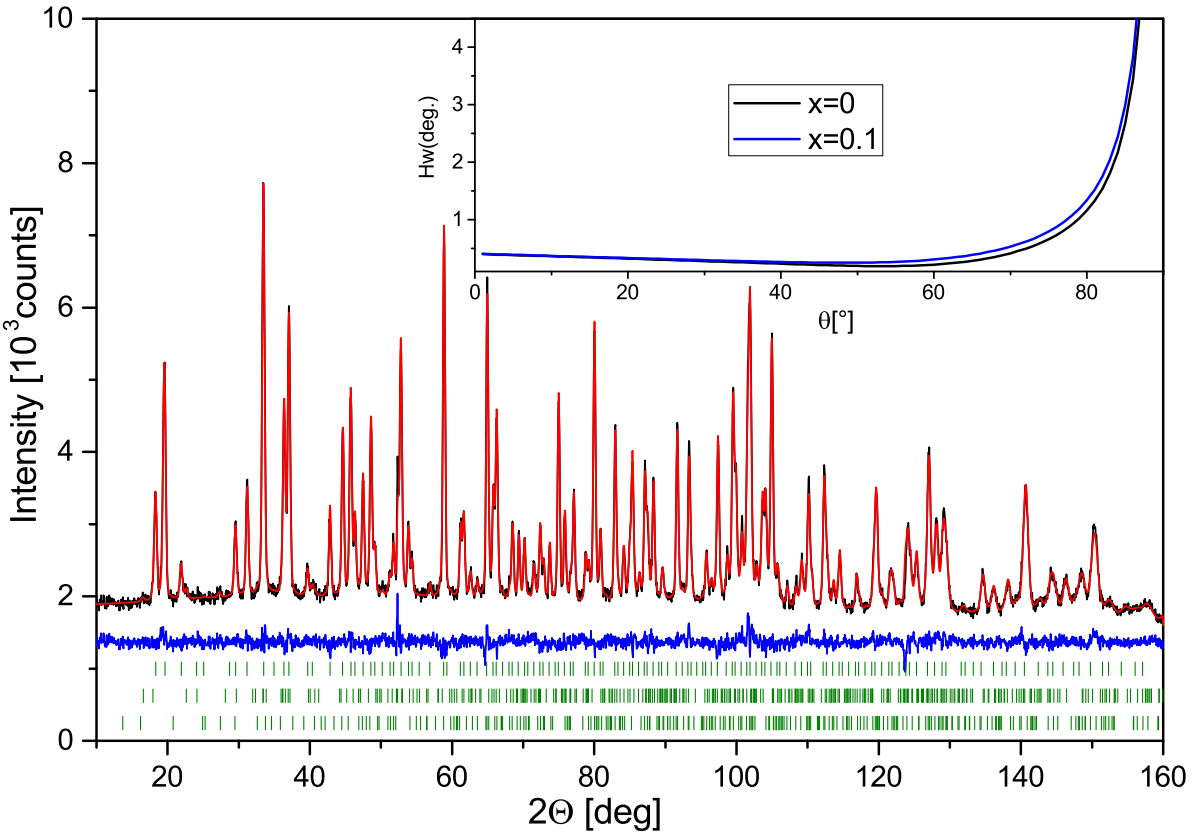

Figure 4.6: Rietveld refinement [16] of the crystal structure parameters of $(Ba_{0.9}Sr_{0.1})CuSi_2O_6$ ($x = 0.1$), based on neutron powder diffraction data at 300 K. The observed intensity (black), calculated profile (red), and difference curve (blue) are shown. The rows of ticks at the bottom correspond to the calculated diffraction peak positions of the phases (from top to bottom): $BaCuSi_2O_6$, $BaCu_2Si_2O_7$ (2.7% wt.) and $BaCuSi_4O_{10}$ (1.5% wt.). On the inset a plot of the Half width at full maximum of the neutron diffraction data of $BaCuSi_2O_6$ and $Ba_{0.9}Sr_{0.1}CuSi_2O_6$ are shown in comparison.

In addition to the sintered powder data, a crushed single crystal of $Ba_{0.9}Sr_{0.1}CuSi_2O_6$ was measured with synchrotron X-ray diffraction at room temperature and the measured data together with the refinement is shown in Fig. 4.7. We observe that the tetragonal structure is preserved at all substitution amounts of up to 30%. The ionic radius of Ba^{2+} of 143Å compared to Sr^{2+} of 127Å gives a full change of 12.6%. The unit cell dimensions decrease with increasing Sr amount.

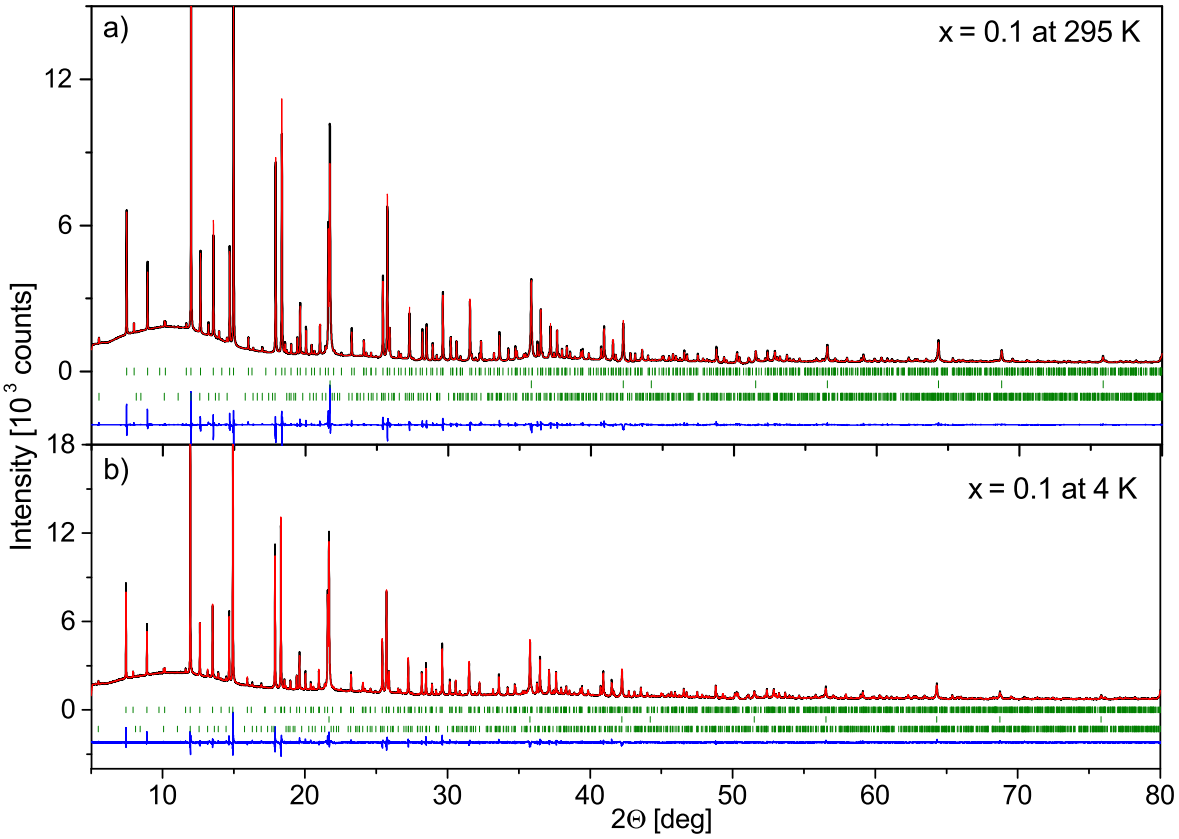

Figure 4.7: Rietveld refinement of the crystal structure parameters of a $(Ba_{0.9}Sr_{0.1})CuSi_2O_6$ ($x = 0.1$) crushed single crystal, based on synchrotron X-ray powder diffraction data at a) 295 K and b) 4 K. The rows of ticks in the middle correspond to the calculated diffraction peak positions of the phases (from top to bottom): $BaCuSi_2O_6$, diamond powder (added to reduce the absorption) and $BaCuSi_4O_{10}$ (3.4 % wt.).

This can be seen in a shift of the diffraction peaks to higher angles (see the inset in Fig. 4.8) and in the evolution of the unit cell parameters in Table 4.3. This continuous evolution evidences that the Sr is homogenously built in, replacing the larger Ba atoms. In addition, the synchrotron data in the inset of Fig. 4.8 indirectly indicate a homogeneous distribution of Sr in the material, since the FWHM (full-width at half minimum) values show no significant increase with increasing Sr content. For example, the FWHM's of the (624) peak read out from the synchrotron diffraction data shown in figure 4.8 are 0.046°, 0.050°, 0.049° and 0.051° for compounds with x = 0.05, 0.1, 0.2 and 0.3 respectively. Comparing neutron data from a $BaCuSi_2O_6$ powder to the $x = 0.1$ powder we see that introducing Sr into the structure causes a slight peak broadening, which is qualitatively indicative to the presence of microstrains in the substituted materials. To get a impression of the broadening the fullwidth at half maximum is plotted versus the scattering angle in the inset of figure 4.6. A slight indication for the microstrains, meaning the dispersion of the lattice constants, can be drawn from the U parameter of the Pseudo-Voigt profile functions in the refinement process, since $U^2_{tot} = U^2_{instr} + U^2_{microstr}$. The value for Han Purple obtained in our neutron diffraction refinement is $U_{x=0} = 0.069976$, while $U_{x=0.1} = 0.083562$ gives a enhanced value of 19.4% (while V,W are equal proving the quality of the fit). So introducing Sr into the system causes some strain, but the amount of Sr does not influence this strain further. A further effect is that a decreased thermal expansion is observed, which influences the Cu-Cu distances and the different exchange couplings J at low temperatures in Table 4.5. The lattice constant c is four times stronger influenced than a and b by the substitution and this difference increases with increasing x. Even

though Ge^{4+} has a 104% larger ionic radius than Si^{4+} (53 Å compared to 26 Å) the increase of the lattice is similar as the decrease for equal substitution of Sr since the relative ion size change is of the same order (16 compared to 27 Å).

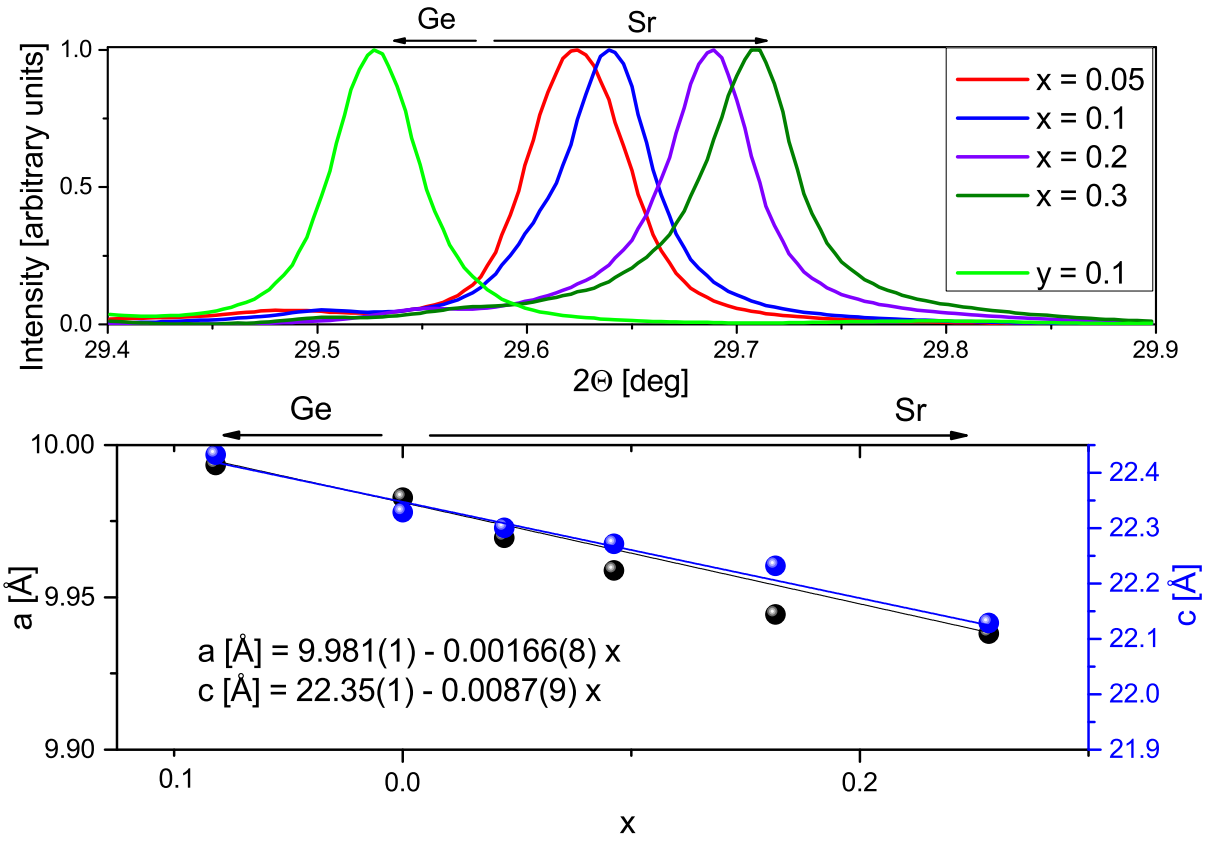

Figure 4.8: The top image shows synchrotron X-ray powder diffraction data of the (624) peak measured at 295 K of polycrystalline samples with various substitution levels. The bottom image is a plot of the lattice constants a=b, c from table 4.3 and a linear fit is performed to apply vegard's law.

The results of all refinements and of the energy dispersive X-ray spectroscopy (EDX) measurements are presented in Table 4.3 and it is apparent, that the actual Sr content slightly varies from sample to sample. As a general trend, the amount of Sr, x, in the powder is lower than the nominal one and this value further decreases in the single crystals. The occupation refinement value x is compared to the data obtained from the EDX analysis in a Zeiss DSM 940A scanning electron microscope (SEM) on both powder and single crystals. The Sr content from the EDX measurement on the powder samples seems to be slightly overestimated compared to the value from the refinement. The reason for this is possibly related to Sr-rich foreign phases such as $SrCuSi_2O_7$, which increase the amount of Sr in the EDX result, while in the refined results they are refined seperately. Also SrO impurities cannot be detected in diffraction experiments, since it decays and becomes amorphous. For clarity, we will use in the following the nominal values to describe the samples.

Nominal value	$x = 0.05$	$x = 0.1$		
Powder/ Single crystal	P	P		
x_{EDX} value	0.08(1)	0.13(1)		
Neutron/ Synchrotron	S	N [31]		S
$x_{refined}$ value	0.03	0.07		0.09
Temperature	295 K	300 K	1.5 K	295 K
$a = b$ [Å]	9.97331(2)	9.9627(3)	9.9508(2)	9.95888(2)
c [Å]	22.30826(6)	22.2774(7)	22.2815(5)	22.27168(6)
V [Å^3]	2218.93	2210.58	2205.31	2208.89

Nominal value	$x = 0.1$		$x = 0.2$	$x = 0.3$	$y = 0.1$
Powder/ Single crystal	SC		P	P	P
x_{EDX} value	0.08(2)		0.19(2)	0.33(3)	0.08(2)
Neutron/ Synchrotron	S [31]		S	S	S
$x_{refined}$ value	0.05		0.16	0.26	0.08
Temperature	295 K	4 K	295 K	295 K	295 K
$a = b$ [Å]	9.97223(2)	9.95830(5)	9.94442(1)	9.93810(3)	9.9935(1)
c [Å]	22.31379(4)	22.3246(1)	22.23223(5)	22.2129(1)	22.4325(2)
V [Å^3]	2219.08	2213.88	2198.58	2193.88	2240.33

Table 4.3: Summary of the refinement and EDX results of several samples of the series $(Ba_{1-x}Sr_x)CuSi_2O_6$ and a sample of $BaCu(Si_{1-y}Ge_y)_2O_6$. The abbreviations are as following: neutron diffraction (N), synchrotron diffraction (S), polycrystalline powder or crushed crystal (P), and single crystal sample (SC).

NMR spectroscopy at room temperature

To have a deeper insight into the distribution of Sr in the samples, room-temperature, high-resolution ^{29}Si-NMR measurements were done on the Sr-powder substitution series by Raivo Stern and Ivo Heinmaa from the National Institute of Chemical Physics and Biophysics of Tallinn. The results of the chemical shift K are depicted in Fig. 4.9 and a broadening of the main peak around $K \sim 0.05\%$ is apparent. This line broadening can be explained, assuming a random distribution of Sr on the Ba sites. In $BaCuSi_2O_6$, each silicon atom, which is the probed NMR nuclei, has two Ba nearest neighbors. For the $x = 0.1$ compound the probability to have a silicon atom with two Ba neighbors is $0.9 \cdot 0.9 = 0.81$, with one Ba and one Sr $2 \cdot 0.9 \cdot 0.1 = 0.18$, and with two Sr neighbors only $0.1 \cdot 0.1 = 0.01$, if Sr is homogeneously distributed over the Ba sites. Therefore, one would expect a peak splitting of the main ^{29}Si-NMR line into a triplet with an intensity ratio of $(0.81 : 0.18 : 0.01)$. Looking at the spectra in Fig. 4.9, such a peak splitting is indeed observed. At 10% Sr concentration the spectrum shows the main line at 0.0536 % and a shoulder at 0.0444 %. The intensity ratio of these lines is $(0.83 : 0.17)$, which is in nice agreement, with the expected splitting, although the peak with two Sr sites is below the detection limit.

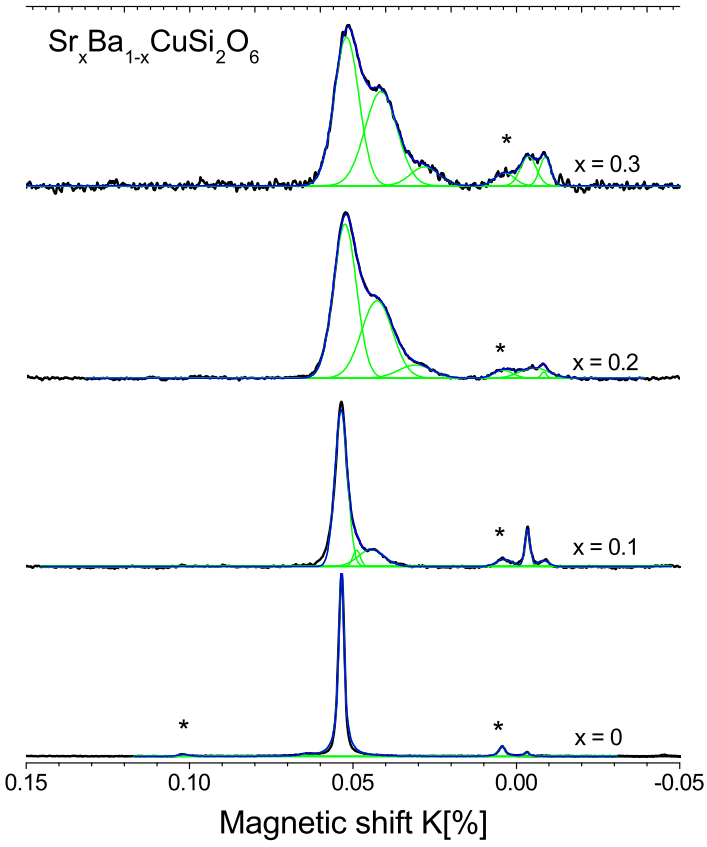

Figure 4.9: ^{29}Si MAS-NMR spectra at $T = 300\,\mathrm{K}$ with a resonance frequency of 71.5 MHz of ^{29}Si on $BaCuSi_2O_6$ (bottom spectrum) and Sr substituted $BaCuSi_2O_6$ as noted in the figure. The asterisks denote spinning side bands. Decomposition of the spectra can be seen by analyzing the green fitting curves. Homogeneous substitution of Ba by Sr is clearly reflected in the ^{29}Si MAS-NMR spectra.

The main lines in the spectrum of 20% Sr are positioned at 0.0526 %, 0.0427 % and 0.0310 % with an intensity ratio of (0.55 : 0.38 : 0.07), in rough correspondence with the expected site distribution for 0.8 and 0.2 = x of (0.64 : 0.32 : 0.04). The main lines in the spectrum of 30% Sr substituted compound are at 0.0520 %, 0.0414 % and 0.0280 %. The intensity distribution of the lines (0.51 : 0.42 : 0.07) is again in good agreement with a random distribution of Sr sites (0.49 : 0.42 : 0.09).

In summary we see no second position or preferred orientation of strontium but a homogenous random occupation on the Ba position.

4.1.6 Detailed synchrotron diffraction analysis of the structural phase transitions

We used synchrotron single crystal diffraction at various temperatures, to observe the details of the structural phase transition around 100 K. This transformation from tetragonal $I4_1/acd$ to orthorhombic Ibam is accompanied by an incommensurate modulation first described by Samulon et al. [21]. The incommensurate modulation can be seen in a fourfold of sidepeaks creating at specific reflections. In figure 4.10 a represantative area for each sample is chosen. The two pure $BaCuSi_2O_6$ crystals grown from the two different methods both show sidepeaks. Within the studies we could see that not all samples have the phase transition as well as the incommensurate modulation, but in general it can be observed at pure $BaCuSi_2O_6$ from either flux grown as well as with oxygen atmosphere as shown in the image. All $Ba_{1-x}Sr_xCuSi_2O_6$ crystals do not possess these sidepeaks, so there is no incommensurate modulation in these samples (see figure 4.10 3rd image). We have to note that at highest resolution with long counting we could resolve on some Sr substituted crystals a small misaligned second reflection on certain reflexes indicating some sort of twinning of a possible misaligned a-b-plate layer.

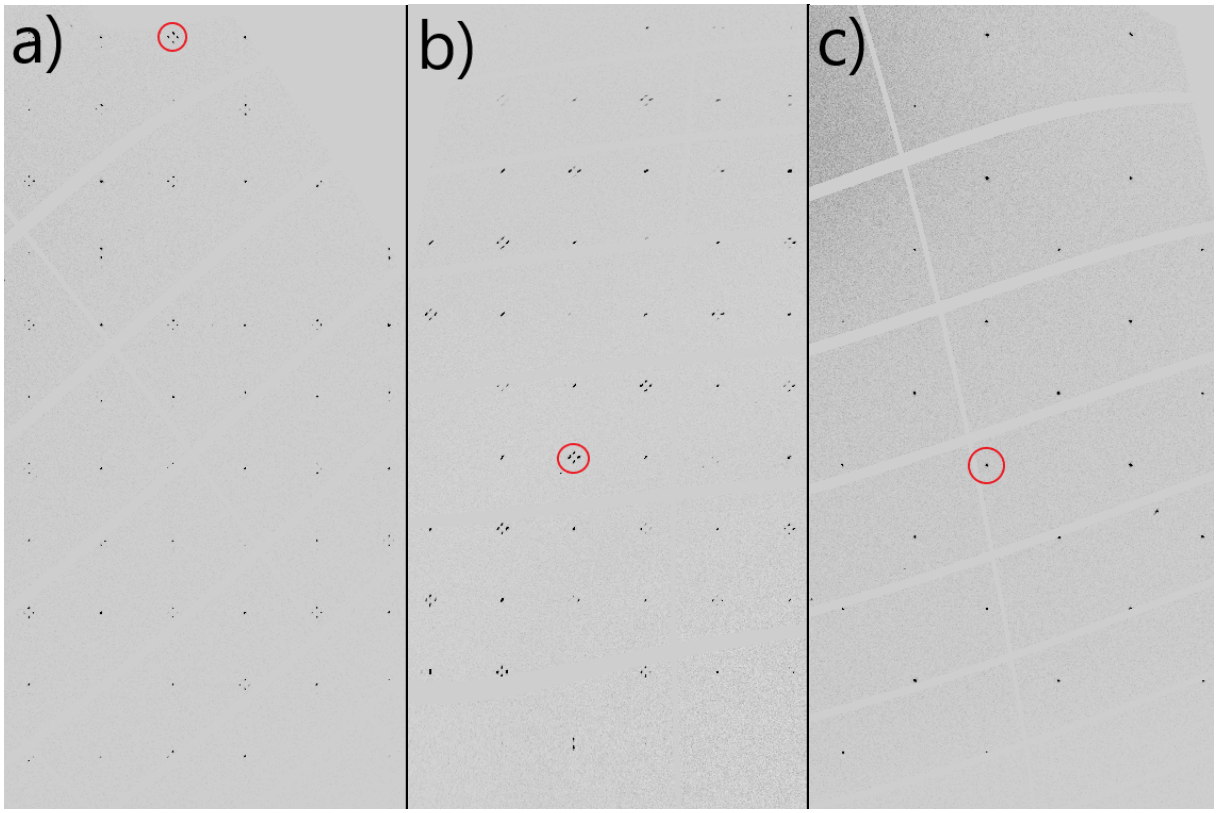

Figure 4.10: Selected parts of integrated reconstructed images done with CrysAlis of the reflections viewed along the (h k 1) direction of a) a flux grown $BaCuSi_2O_6$ single crystal, b) a single crystal grown with oxygen atmosphere and c) a $Ba_{0.9}Sr_{0.1}CuSi_2O_6$ single crystal all measured at 4 K. The red circles highlight examplary reflexes showing the presence or absence of incommensurate satellites.

In the lattice constant the structural phase transitions can be seen in a change of the volume and thus a kink when plotted against temperature, most evident in the c-axis for $BaCuSi_2O_6$. Figure 4.11 shows the lattice constants a = b, c as well as the volume V from 1.5 to 750 K of $BaCuSi_2O_6$ and $Ba_{0.9}Sr_{0.1}CuSi_2O_6$. The observed transition temperatures are 85 K and 648 K for $BaCuSi_2O_6$ and 668 K for $Ba_{0.9}Sr_{0.1}CuSi_2O_6$. In the case of $BaCuSi_2O_6$ the refinement with the I4/mmm superstructure of $I4_1/acd$ fits exactly to $V_{acd} = 4V_{mmm}$ above 648 K, but for $Ba_{0.9}Sr_{0.1}CuSi_2O_6$ the I4/mmm structure is not

correct at higher temperatures, which can be seen in an offset (see Fig. 4.11 blue points). There is also a tiny kink at 30 K for the Sr sample in the c axis. This could be the seperation of the twins described above or it is simply due to the "l-shape" of the thermal expansion since we observe no structural phase transition for this compound (see chapter 4.1.7).

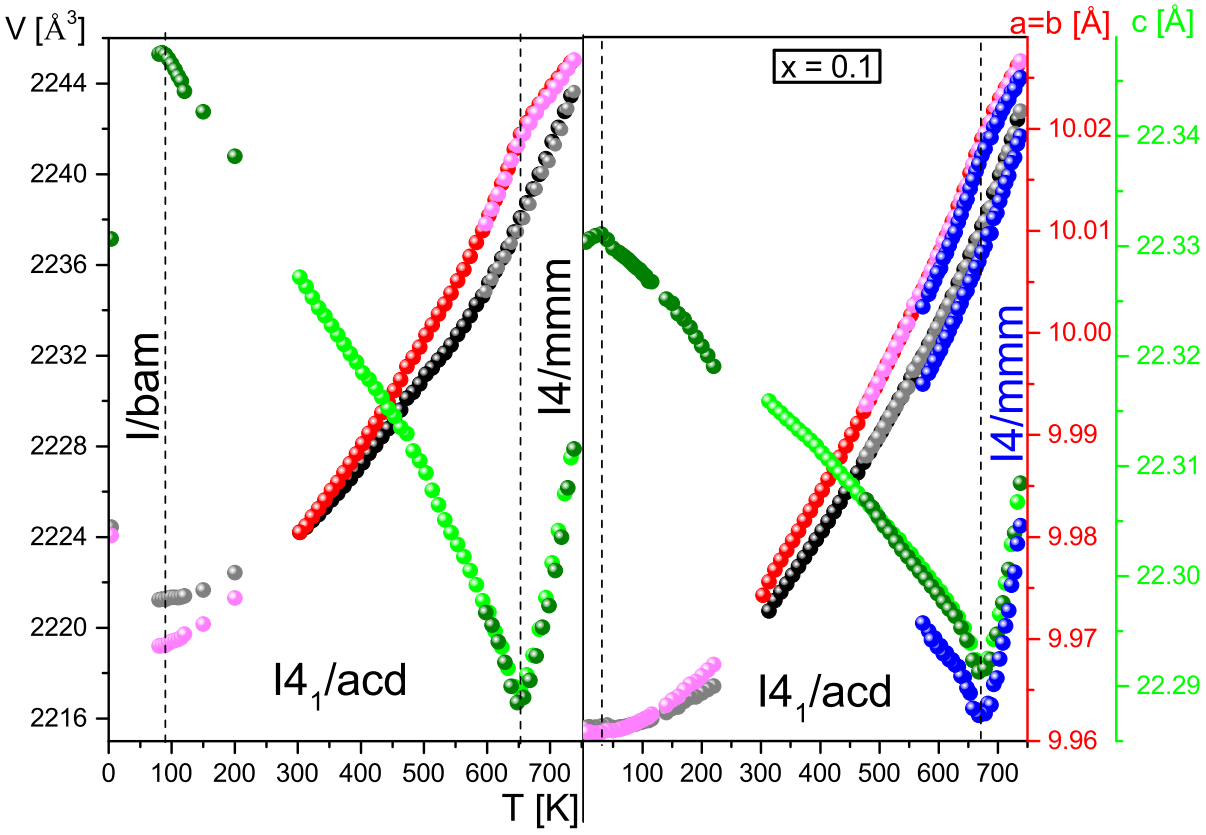

Figure 4.11: Lattice constants from Rietveld refinements at various temperatures of synchrotron powder diffraction for $BaCuSi_2O_6$ and $Ba_{0.9}Sr_{0.1}CuSi_2O_6$. The volume development of the heating cycle is given in black, while the cooling cycle (down) is given in gray. For the lattice constant a the red points describe the heating and the rose ones the down curve. The light green points are the c-axis, where the dark colour gives the cooling cycle.

4.1.7 Investigation of the absence of a structural phase transition

Now we discuss the low-temperature diffraction data obtained both in measurements on powder as well as single crystal samples with the nominal Sr concentration $x = 0.1$. The absence of a structural phase transition down to the lowest measured temperatures could be verified in neutron and synchrotron diffraction. In Fig. 4.7 b) the Rietveld refinement of the same crushed single crystal as in Fig. 4.7 a) is presented for measurements at 4 K. This data set can be well refined, using the same tetragonal crystal structure with space group $I4_1/acd$, which is observed also at room temperature. The corresponding results of the refinement are shown in Table 4.3.

Further evidence for the absence of a structural phase transition is presented in Fig. 4.12, where the temperature-dependent synchrotron data across the expected transition temperature are shown. We choose the (604) and (620) reflexes in a temperature window from 10 to 110 K to make a comparison with Ref. [23] possible, where corresponding data were shown for $x = 0$. There, a well resolved peak splitting is observed as shown for comparison in the back of Fig. 4.12. In the whole temperature region for the $x = 0.1$ sample, no peak splittings or shifts beyond the expected thermal expansion could be observed. Similar results were obtained with neutron diffraction at 1.5 K, where on a polycrystalline sample, with slightly higher Sr concentration, also no structural phase transition could be detected. The same suppression of the phase transition was observed for a 10 % Ge doped powder sample ($y = 0.1$ in Table 4.3) in synchrotron measurements in the range of 4 K $< T <$ 295 K.

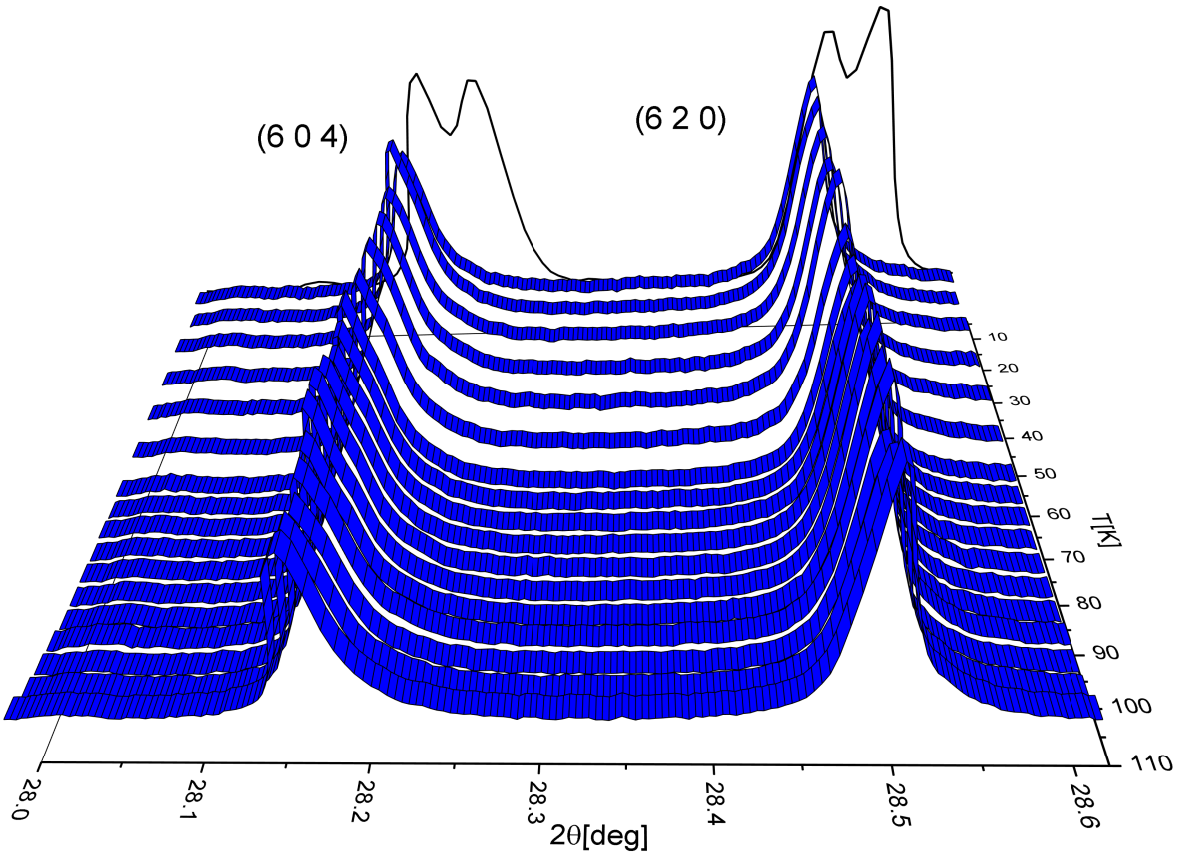

Figure 4.12: Synchrotron X-ray powder diffraction data of an $x = 0.1$ crushed single crystal from 35 to 110 K. In the back a measurement of the $x = 0$ powder at 30 K is shown (black line), demonstrating how the peak splitting due to the transition would look like (data taken from Ref. [23]). The suppression of the structural phase transition is apparent, since for $Ba_{0.9}Sr_{0.1}CuSi_2O_6$ the (604) and (620) reflexes do not split.

Low temperature NMR spectroscopy

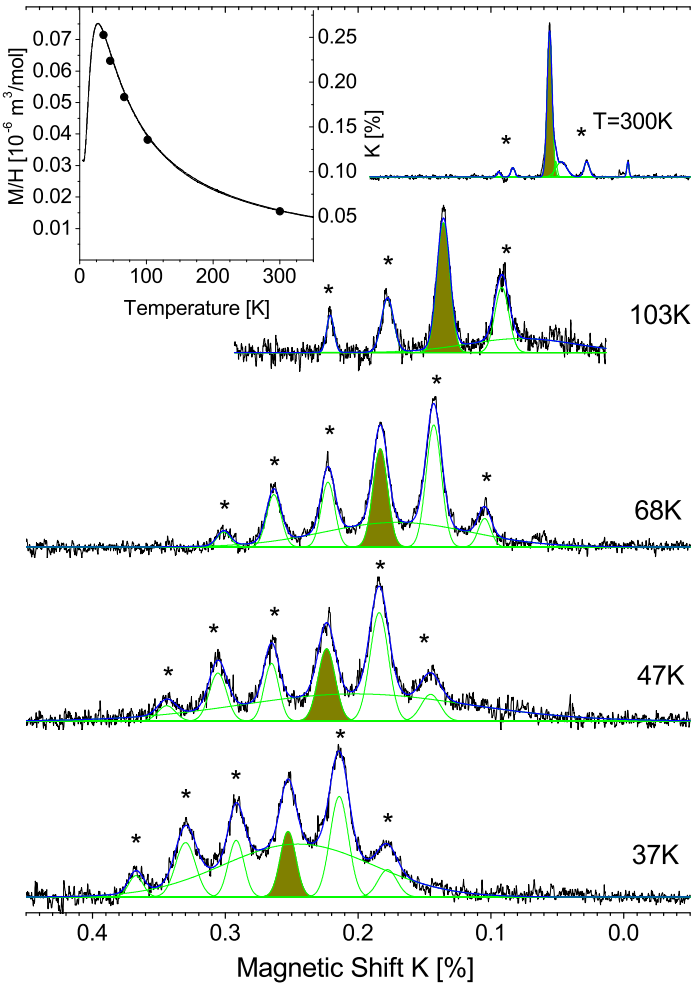

Figure 4.13: The temperature dependence of ^{29}Si MAS-NMR spectrum of $Ba_{0.9}Sr_{0.1}CuSi_2O_6$. At magic-angle spinning the NMR spectra consist of the main line at isotropic magnetic shift and of a number of spinning sidebands at multiples of the sample-spinning frequency from the main line. For clarity the main lines in the spectra are colored and the spinning sidebands are marked with asterisks. The inset shows the proportionality of the isotropic magnetic shift to the molar susceptibility measured in a PPMS on the same sample at 8.45 T. Here the susceptibility values are given by the full line and circles correspond to the isotropic shift values.

Next to the scattering experiments (sensitive to long-range structures), Raivo Stern and Ivo Heinmaa also performed cryogenic high-resolution ^{29}Si NMR which show the absence of the transition in short-range correlations. The spectra show that, unlike the case of the parent compound $BaCuSi_2O_6$, where two different ^{29}Si resonance bands were found below the phase transition at T ∼96 K [15], there is clearly only one resonance line in the studied temperature range 37 K ≤ T ≤ 300 K (see figure 4.13). With lower temperatures there is a natural line broadening due to high magnetic suscebtibility of the powder particles which is not averaged by MAS, making the structure (shoulders) caused by Sr less and less detectable. The isotropic value of the ^{29}Si magnetic hyperfine shift in the $x = 0.1$ sample at room temperature for silicon with two Ba neighbors $K = 0.0536$ % is equal to the value in pure $BaCuSi_2O_6$ ($K = 0.0535$ %). In paramagnetic compounds the isotropic magnetic shift K is proportional to the magnetic suscebtibility χ_M as: $K = \chi_M H_{hf} / (N_A g \mu_B)$ where

H_{hf} is the hyperfine field at the nucleus, N_A is the Avogadro's number, g and μ_B are the g-factor and the Bohr magneton, respectively. Equal magnetic hyperfine shifts result from equal hyperfine fields at silicon in $Ba_{0.9}Sr_{0.1}CuSi_2O_6$ and in the parent compound $BaCuSi_2O_6$.

Specific heat

A complementary measurement technique to detect first-order structural phase transitions is the heat capacity measured around the suspected phase transition. The advantages of this method are that the measurement is fast, the single crystals are kept intact and can be small (around 250 μm and down to 0.2 mg). We measured specific heat data from 10 to 130 K with heating pulses of up to 10 K in single crystals with and without strontium substitution. As a consequence of the first-order nature of the structural transition in pure $BaCuSi_2O_6$, latent heat is expected, which easily can be detected as a small plateau during a continuous heating cycle (inset of Fig. 4.14) as described in Ref. [32]. This results in a diverging specific heat at the transition temperature as evident from the large peak in the main part of Fig. 4.14 (black curve). As this is a first-order transition, we observe a small satellite peak at higher temperatures, due to hysteresis effects upon heating and cooling. This anomaly is found to be absent for Sr-substituted samples, which is exemplarily shown for one $x = 0.1$ single crystal in Fig. 4.14 (green curve).

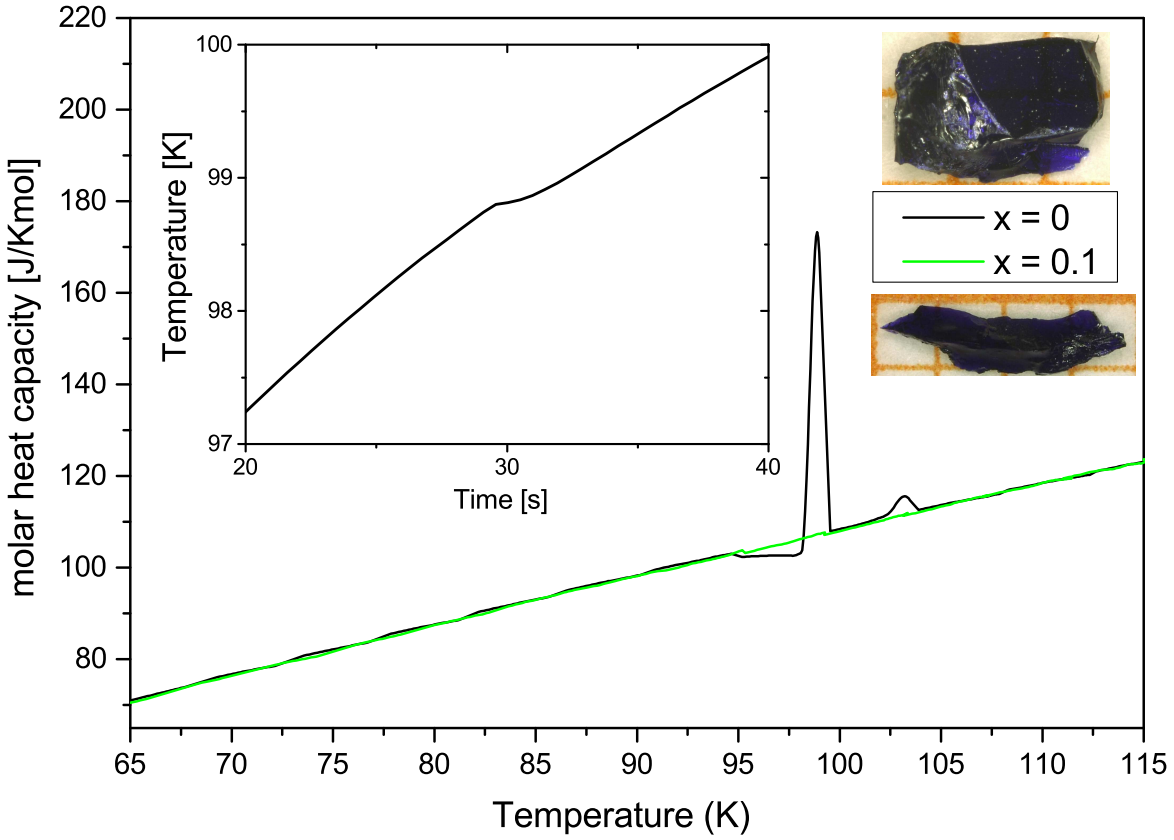

Figure 4.14: Specific heat data of a $BaCuSi_2O_6$ single crystal grown in KBO_2 flux as well as a $Ba_{0.9}Sr_{0.1}CuSi_2O_6$ single crystal grown with oxygen partial pressure. The inset shows a single heat pulse in the vicinity of the structural phase transition of the $BaCuSi_2O_6$ single crystal.

4.1.8 Single crystal diffraction under pressure

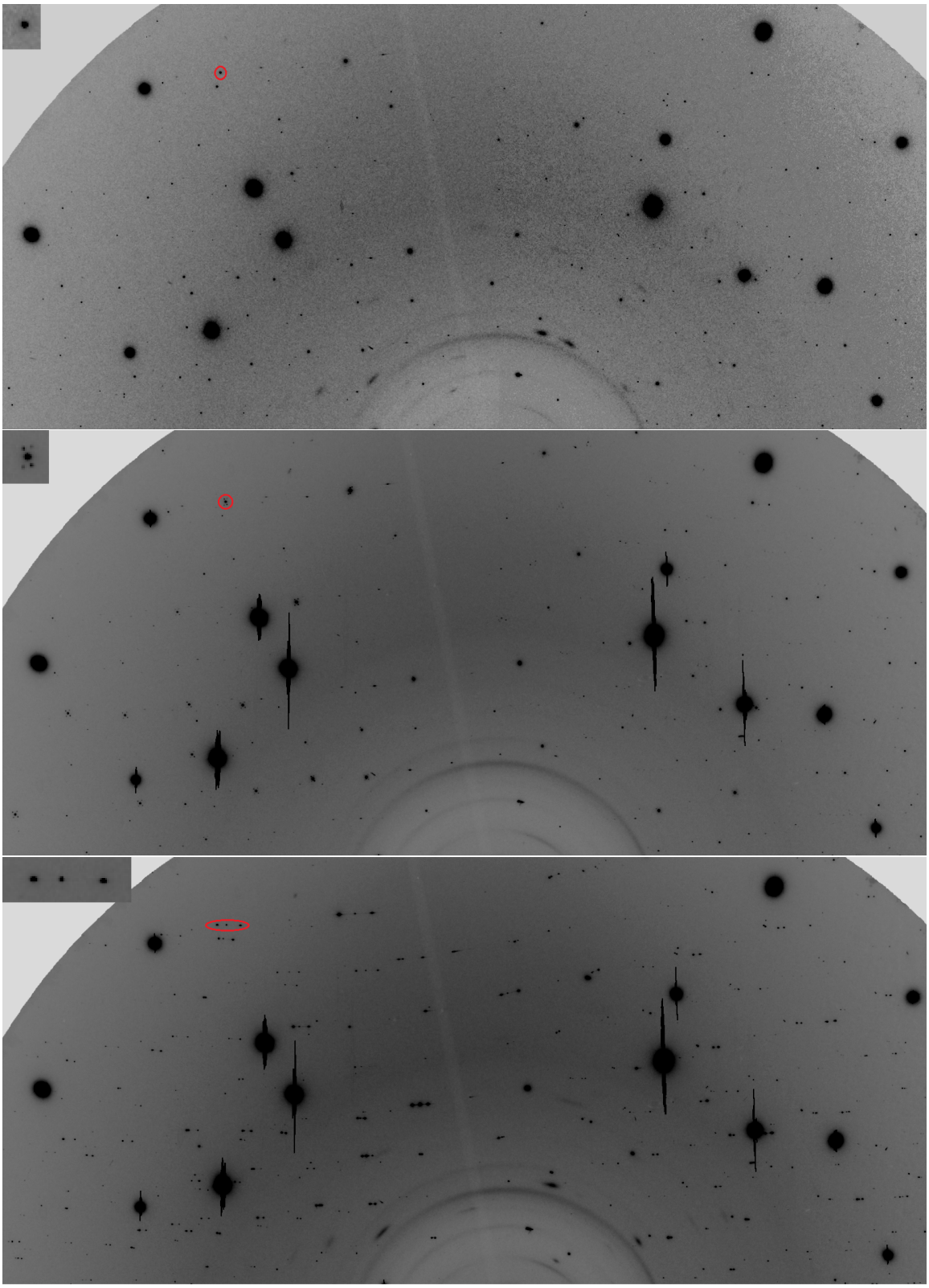

Figure 4.15: Panoramic view of the single crystal diffraction on $BaCuSi_2O_6$ under pressure at different temperatures of top: $I4_1/acd$ at 298 K and 0.52 GPa, middle: Ibam at 140 K and 0.75 GPa and bottom: at 298 K and 1.33 GPa. The thick points are reflections from the diamond and show a line when the counting is strongly oversaturated, which was necessary to get the resolution of the satellites from $BaCuSi_2O_6$. The same reflex is highlighted in red for all phases and magnified in the small upper left inset to get a good comparison.

In order to understand the effects of the chemical pressure applied to $BaCuSi_2O_6$ with Sr and Ge substitution, we applied an external pressure on small single crystals of sizes around ∼25 x 25 x 10 µm at various temperatures. The pressure was realized with a diamond anvil cell with a tip of 500 µm reaching pressures of up to 15 GPa. We could observe the low temperature phase with the incommensurate modulation not only by integrated reconstruction image as before (see figure 4.10) but also in a single measurement on a panoramic view seen in figure 4.15 due to the high flux of synchrotron radiation chosen for this experiment. Figure 4.15 shows the three relevant different phases we found when scanning the sample at different temperatures and pressures. Note that the thick reflex points are from the diamond of the pressure cell. The first image shows the $I4_1/acd$ structure observed down to 90 K at zero pressure. The second image shows the incommensurate Ibam phase at lower temperatures, where at certain reflexes four slight satellites are apparent, but better observed in a magnification. The last image shows a completely new structure at higher pressures (e.g. at 298 K starting from 1.33 GPa). In this phase we observe a maximal fourfold of reflexes spread to a line, but the reflex position stays unchanged thus keeping the supercell structure. A magnification of the important reflexes of the panoramic images is seen in the phase diagram in figure 4.16.

We tried to scetch the phase diagram of pure $BaCuSi_2O_6$ in figure 4.16. The measurement was limited by the applied beamtime at the ESRF and the duration of one data point, especially since for each new point the position had to be recalibrated due to volume changes. The three different phases are seperated by three dashed lines in the corresponding colour of their data points. For each phase a coloured magnification of a significant reflex from figure 4.15 is shown. We found the incommensurate modulation to change at higher pressures to a new phase where the twins seperate in a line. This high-pressure phase transition can be accessed from both Ibam and $I4_1/acd$ phases, but is not reversible towards the Ibam phase. It is reversible on the other hand towards the high temperature phase $I4_1/acd$, skipping the Ibam structure. The sequence of our measurement is scetched in figure 4.16 by arrows indicating also the transitions by its color. The number of the arrow corresponds to the measurement order. We started with a pressure of 0.91 GPa at 60 K ending up in the new phase of twin seperation and went back to the room temperature (arrow 1), which results in a pressure increase since we did not drain the helium gasket. Then we observed the transition to the $I4_1/acd$ phase by releasing pressure at 298 K (2). Since the helium gasket is quite sensible to changes and the realized pressure only stabilizes after some time, we still had to find the phase boundary at 298 K by increasing and releasing the pressure (3,4). The next step was to look for the low temperature incommensurate phase (5) by decreasing the temperature at 0.85 GPa. We searched for the transition to the high pressure phase from the incommensurate Ibam structure at 140 K by increasing and releasing pressure (6,7), but found it to be irreversible towards the Ibam phase. Finally we examined the reversebility towards $I4_1/acd$ at the usual transition from Ibam (8).

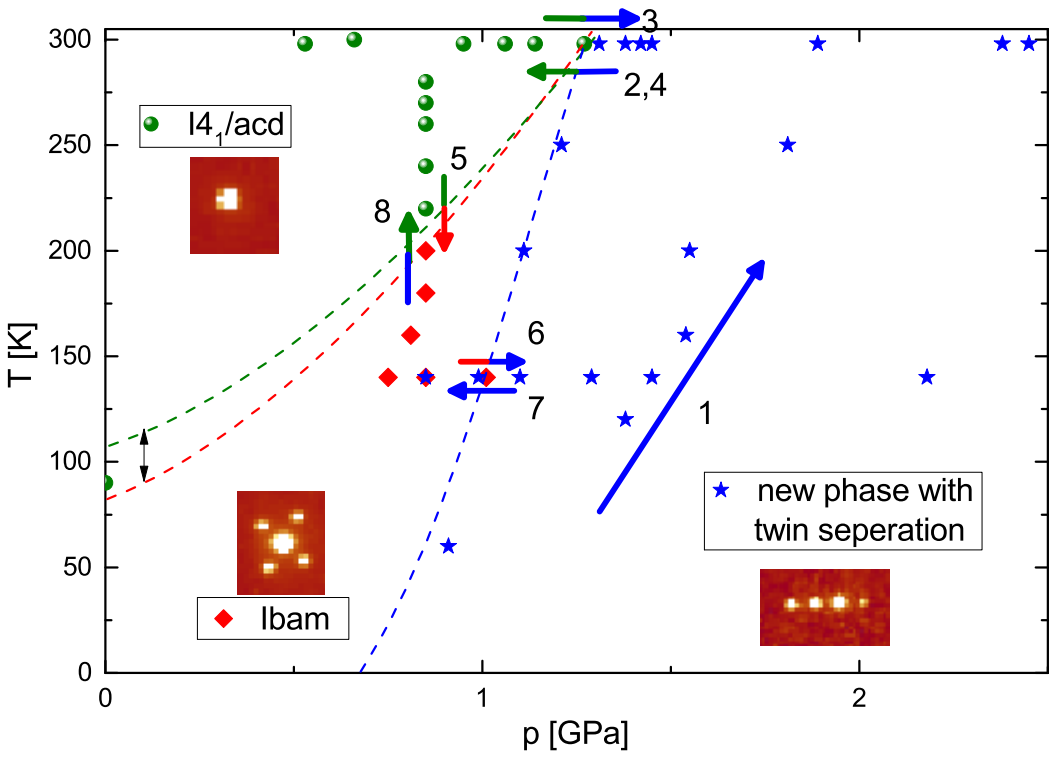

Figure 4.16: Phase diagram of a $BaCuSi_2O_6$ single crystal under pressure showing 3 phases: $I4_1/acd$ (green, no satellites), Ibam (red, four sidepeaks), a new phase (blue triangles, four points in a line). A magnification of a single reflex is shown for all three phases as an inset. The possible phase seperations are marked with a dotted line. Note that the incommensurate transition has a hysteresis and that the twin seperation induced by pressure is irreversible regarding the incommensurate phase. The sequence of measurement is marked by numbered arrows.

To conclude this chapter, also under external pressure the Ibam structure is not stable. There are two possible explanations for a stabilization of $I4_1/acd$ with Sr substitution: volume change and microstrains. Since the external pressure however leads to a new phase and thus did not reproduce the effects of substitutions, the incommensurate phase at low temperature of $BaCuSi_2O_6$ is in $Ba_{1-x}Sr_xCuSi_2O_6$ suppressed by the microstrains (see chapter 3.2.2) from the introduction of Sr into the structure.

4.1.9 Magnetic characterization

After having established that in Sr-substituted $BaCuSi_2O_6$ the structural transition into the orthorhombic structure is suppressed, the question arises, how these structural differences influence the magnetic properties at low temperatures and high magnetic fields. Here, we present magnetic susceptibility measurements on the $Ba_{1-x}Sr_xCu(Si_{1-y}Ge_y)_2O_6$ powder samples as well as single crystals down to 1.8 K together with high-field magnetization measurements on pure and x = 0.1 samples up to 50 T at 1.5 K.

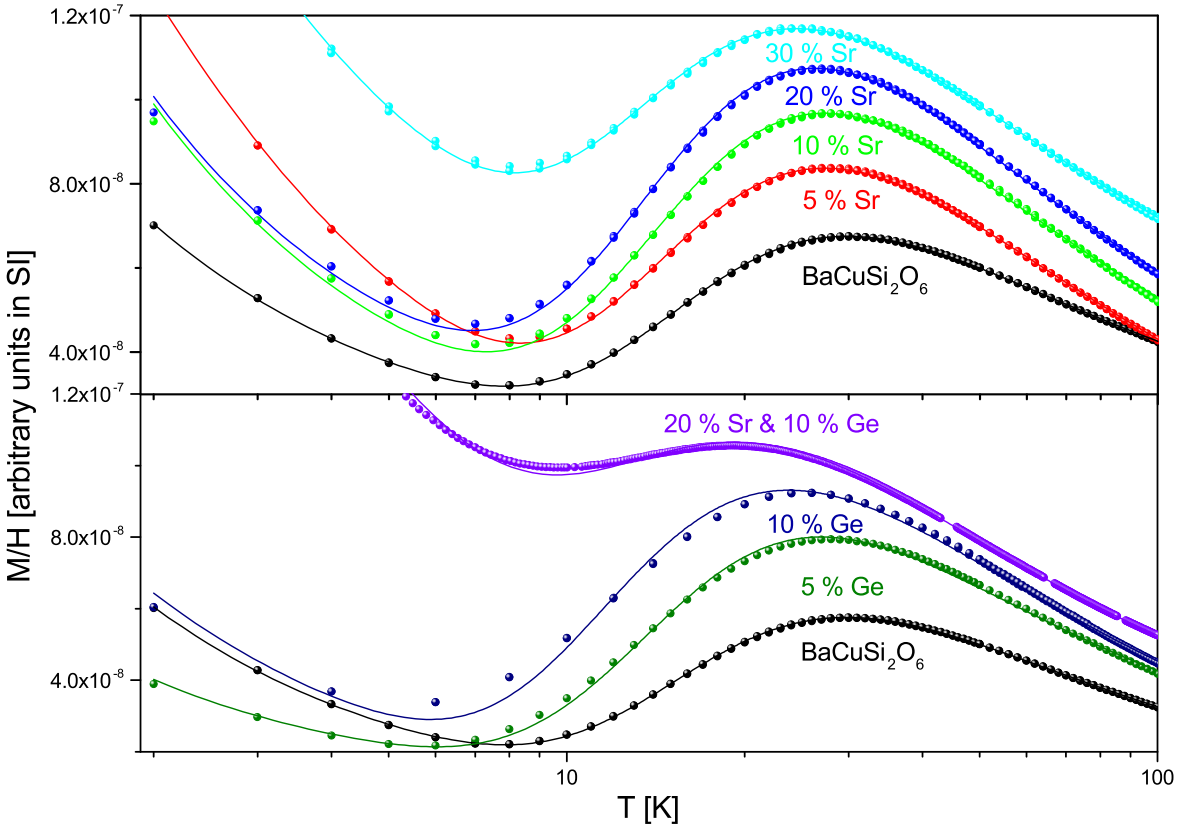

Figure 4.17: Magnetization measurements of all powder samples in comparison. A shift is applied for optical comparison. A fit of the curves with the dimer-model of eq. 2.17 reveals a decreasing J_{ij} for increasing substitution of both Sr and Ge. The values are J_{ij} [K] are given in table 4.4. The J_{MF} of powder samples varies strongly due to the dependence on the g-factor, which again is dependent on the orientation and thus is only given for single crystal measurements.

The Sr substitution decreases the unit cell and thus could increase the intradimer exchange J_{ij} but the strain from the strontium atom is between the dimer layers (see figure 4.2) and thus tears them to longer distances as can be concluded from figure 4.17, where the maximum shifts to lower values giving us smaller J values following equation 2.16 seen in table 4.4. At the same time this strain brings the dimer layers closer together resulting in an increase in J_{MF}. Ge substitution on the other hand increases the unit cell, but the pressure is in this case in between the Cu atoms of one dimer resulting in exactly the same effect on the dimers as Sr substitution. Thus the highest shift of J_{ij} can be seen in the double substitution. The paramagnetic contribution first decreases for small substitutions compared to the pure compound, but then strongly increases due to enhanced paramagnetic defects in the lattice.

substitution	pure	5% Sr	10% Sr	20% Sr	30% Sr	5% Ge	10% Ge	20% Sr 10% Ge
J_{ij}[K]	49.95(3)	47.39(4)	45.88(9)	44.18(8)	43.50(5)	44.1(1)	39.5(2)	39.67(3)

Table 4.4: Coupling constant results for different substitution

In Figure 4.18 the susceptibility and magnetic anisotropy for a $Ba_{0.9}Sr_{0.1}CuSi_2O_6$ single crystal is shown. In general the physical properties of this crystal are close to pure $BaCuSi_2O_6$ with $J = 4.45$ meV $= 51.6$ K, $J_{MF} = 0.58$ meV $= 6.7$ K [19] compared to J =48.3 K and J_{MF} =11.6 K. A linear fit of the inverse susceptibility gives a Curie-Weiss temperature $\Theta_W^{\perp} = -3.97$ K for fields perpendicular to c (black) and $\Theta_W^{||} = -13.54$ K for fields parallel to c (red). From the linear slope of the curie fit the effective moment can be derived following equation 2.7 we get $\mu_{eff}^{\perp} = 1.44\mu_B$ and $\mu_{eff}^{||} = 1.70\mu_B$. This value can be compared to a plot following equation 2.5 and 2.7 we get the dotted line in figure 4.17. The impurity amount is sample dependant and can be derived from the saturation magnetization, in this case it is ∼0.6 %. We observe in each batch similar impurity amounts ranging from 0.6 % to 16 %. It can sometimes be seen as small black dots on the surface. The impurity amount is just slightly lower for flux grown crystals and generally increases a bit with increasing substitution.

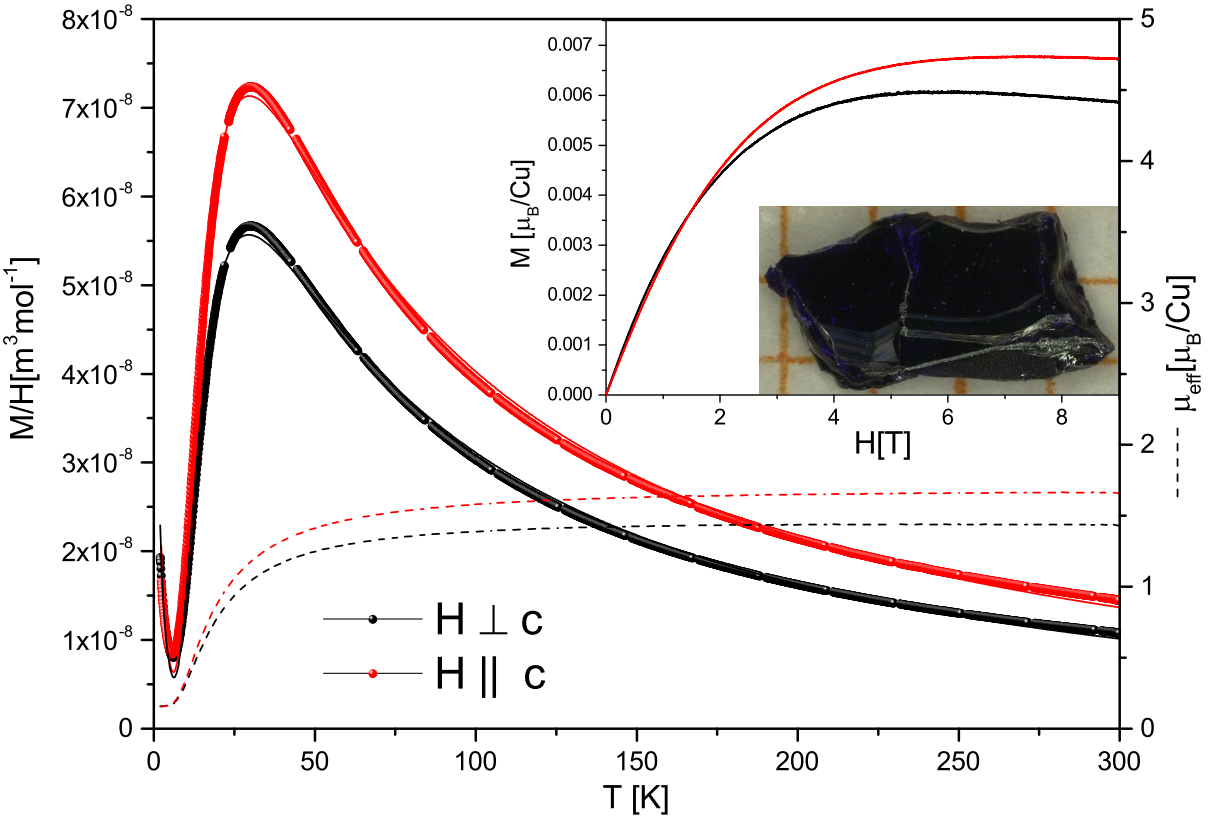

Figure 4.18: Magnetization and effective moment plots of a $Ba_{0.9}Sr_{0.1}CuSi_2O_6$ single crystal. The inset shows the magnetic field dependence of the magnetization at 2 K. The maximum gives us the impurity contribution. The plot shows the anisotropy of the $Ba_{0.9}Sr_{0.1}CuSi_2O_6$ sample which has not perceptibly changed compared to the pure compound. The curves are fitted with equation 2.17 giving us a $J = 48.3(1)$ K with $J_{MF} = 11.6(5)$ K. The dashed curve are plots of the calculated effective moments.

Pulsed field experiments

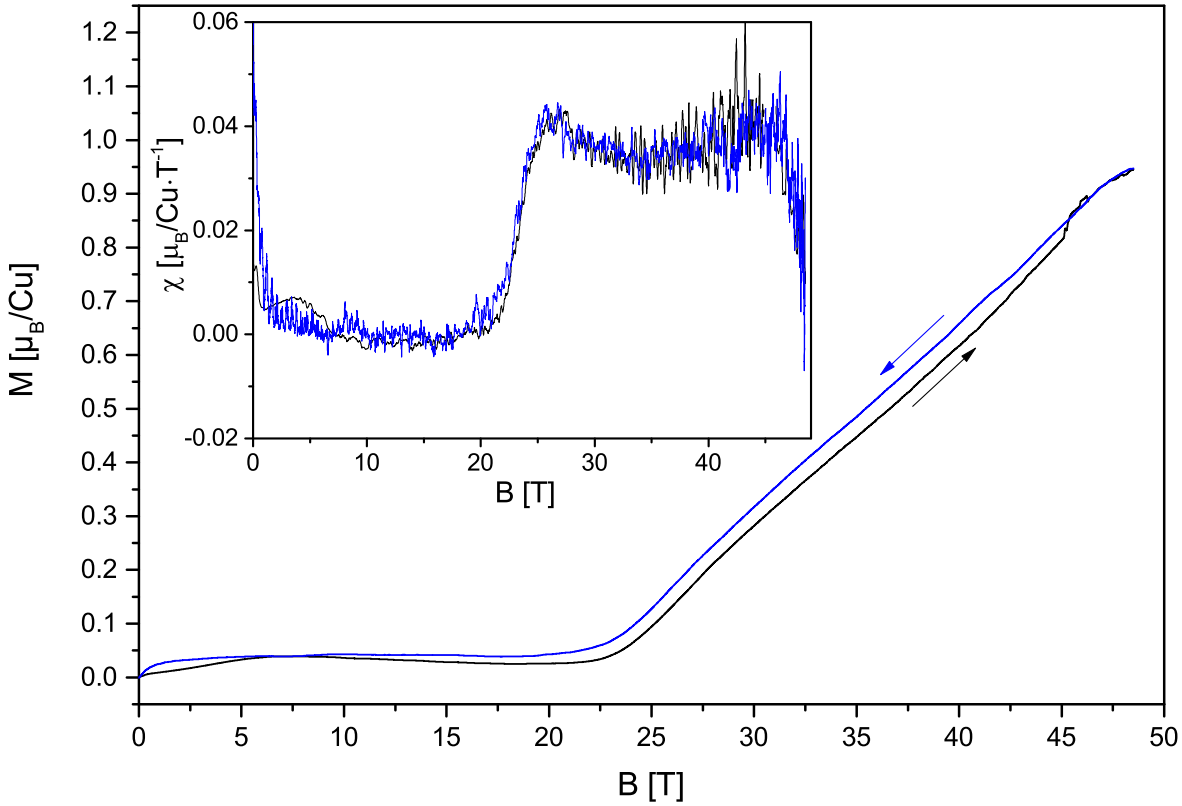

Figure 4.19: Magnetization of the $Ba_{0.9}Sr_{0.1}CuSi_2O_6$ powder sample up to 50 T measured at a bath temperature of 1.5 K. The black solid line represents the data taken during increasing field with a rise time of 8 ms whereas the blue solid line shows the magnetization with decreasing field with a decay time of 17 ms. The blue solid points are the SQUID data taken at 2 K. They follow a Brillouin function corresponding to a concentration of 5.5 % uncoupled Cu^{2+}(spin-1/2)-ions. These data are used to calibrate the pulse-field experiments and they allow a rough estimate of the magnetocaloric effect which amounts to $\Delta T \simeq +1.5$ K for the field-up curve and $\simeq$ -0.5 K for the field-down curve with respect to the bath temperature.

In Fig. 4.19 we show the results from Lars Postulka's (PI Frankfurt) measurements of the magnetization M, as a function of magnetic field up to 50 T at a He bath temperature of 1.5 K. In small fields we observe a mild increase of M which levels off at intermediate fields. We assign this to the Brillouin function of uncoupled Cu^{2+}(spin-1/2)-ions. By subtracting the corresponding contribution from the raw data we find zero magnetization up to a field of around 22 T. With further growing field, $M(B)$ increases almost linearly with B, until the saturation is reached at B_{c2} around 48 T. The small deviations between the field-up and field-down data are due to the magnetocaloric effect (MC), i.e., temperature changes due to changes of the magnetic field, in combination with the peculiar field-time characteristic of the pulse-field set up. The largest MC is expected for fields $\leq$ 5 T and around the critical fields B_{c1} and B_{c2}, with B_{c1} denoting the onset field of the field-induced order. In order to determine B_{c1}, we numerically differentiate the data and obtain the magnetic susceptibility, shown in the inset of Fig. 4.19. We define B_{c1} as the inflection point of the $\chi(B)$ curve in analogy to the criterion used in Ref. [19]. For the powder sample we obtain $B_{c1} = 23.5$ T at a temperature of about 2 K. This temperature is corrected for the MC. For a stack of single crystals (not shown here) we obtained a

slightly smaller value of 22.3 T. Since B_{c1} scales with J_{intra}/g, a slight reduction observed in B_{c1} for the single crystals would be consistent with a 10% larger g-factor for fields perpendicular to the planes even though J_{intra} is slightly (maximally 5%) enhanced. As estimated in Ref. [26] a B_{c1} around 22 T corresponds to one of the dimer layers (layer A) in the orthorhombic low-temperature phase. This layer is structurally similar to the dimer layers in the tetragonal $I4_1/acd$ structure of $BaCuSi_2O_6$.

4.1.10 Electronic structure calculations

	T (K)	J_1 (K)	J_2 (K)	J_3 (K)	J_4 (K)	J_5 (K)
N	1.5	51.6(1)	-0.27(1)	-0.41(1)	0.0(1)	7.9(1)
	300	58.6(1)	-0.27(2)	-0.35(1)	0.0(1)	8.3(1)
S	4	60.2(1)	-0.25(1)	-0.41(1)	0.0(1)	8.0(1)
	295	56.7(1)	-0.28(4)	-0.29(3)	0.0(1)	8.3(3)
$x = 0$	200	58.7(1)	-0.23(1)	-0.39(1)	0.0(1)	8.4(1)
$x = 0$ [26]	300	53	-0.3	-0.4	–	7.9

Table 4.5: Calculated exchange couplings for the $(Ba_{1-x}Sr_x)CuSi_2O_6$ structures with nominal $x = 0.1$ given in Table 1. A GGA+U functional with $U = 8$ eV and $J_H = 1$ eV is used. The abbreviations are neutron diffraction (N) and synchrotron diffraction (S). In addition, couplings for pure tetragonal $BaCuSi_2O_6$ (structure from Ref. [27]) are given in the last two lines.

In order to provide a more detailed analysis of the Cu-Cu interactions in $Ba_{0.9}Sr_{0.1}CuSi_2O_6$ beyond the J_{intra} and J_{inter} estimates from the previous section, Harald Jeschke from the Institute of Theoretical Physics in Frankfurt performed density functional theory calculations on the neutron and synchrotron diffraction refinements of 10% Sr doped $BaCuSi_2O_6$ samples (see Table 4.3, $x = 0.1$) at room and low temperatures. We employ the all electron full potential local orbital (FPLO) code [33] using a generalized gradient approximation [34] exchange and correlation functional and correct for the strong correlations on the Cu^{2+} $3d$ orbitals with the GGA+U [35] functional. We lower the symmetry of $(Ba_{1-x}Sr_x)CuSi_2O_6$ from $I4_1/acd$ to $C\,2$ in order to make eight Cu sites inequivalent and calculate the total energies of 21 distinct spin configurations for each of the four structures. Note that the isoelectronic substitution of 10% Sr^{2+} for Ba^{2+} is reflected in the calculation only by the experimentally determined lattice constants and interatomic distances but not by actual replacement of Ba sites in a supercell approach. The 21 energies can be fitted [36] against five Heisenberg exchange couplings J_i with very high accuracy, leading to very small error bars from the statistics. Note that the sub-Kelvin error bars result from the particularly well defined $S = \frac{1}{2}$ moments of Cu in $BaCuSi_2O_6$, leading to very precise mapping of the 21 DFT total energies to the Hamiltonian with five exchange couplings. The results for GGA+U interaction parameters $U = 8$ eV and $J_H = 1$ eV are given in Table 4.5. The parameters $U = 8$ eV and $J_H = 1$ eV are chosen on the upper end of the interaction parameter range $U \in [6, 8]$ eV considered in previous studies for Cu^{2+} in square-planar oxygen environment [37, 38]. The five exchange paths are visualized in Fig. 4.1.10. J_{intra} as introduced in the previous section, corresponds to J_1 while J_{inter} corresponds to a non-trivial average of interdimer Cu-Cu interactions including J_2, J_3, J_4 and J_5. In Table 4.5 we also show the calculated exchange parameters for the $x = 0$ structure at 200 K (Ref. [27]) and include the results calculated in Ref. [26] for the room-temperature tetragonal $BaCuSi_2O_6$ for comparison. We observe (i) a good agreement between our estimates and those of Ref. [26] for $x = 0$ in the tetragonal phase and (ii) a reasonably good agreement between our *ab initio*-calculated intradimer J_1 and J_{intra} obtained in the previous section. (iii) Our calculation of the Hamiltonian parameters for

the low temperature tetragonal structure of $Ba_{1-x}Sr_xCuSi_2O_6$ at nominal $x = 0.1$ show that the exchange interactions remain very similar to the couplings of the $T = 200$ K tetragonal structure of $BaCuSi_2O_6$. Clearly $Ba_{0.9}Sr_{0.1}CuSi_2O_6$, as well as the tetragonal $I4_1/acd$ $BaCuSi_2O_6$ phase display strong intradimer antiferromagnetic Cu-Cu couplings (J_1) and significant nearest-neighbor dimer top-bottom antiferromagnetic couplings (J_5) that release any type of possible frustration between dimer layers.

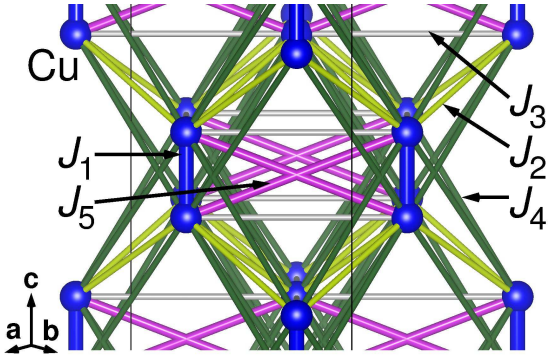

Figure 4.20: Detail of the $BaCuSi_2O_6$ unit cell with the first five exchange paths between Cu^{2+} ions. Other ions are omitted for clarity. [16]

4.1.11 Conclusions

We have experimentally confirmed the absence of a first-order tetragonal-to-orthorhombic structural phase transition in $(Ba_{1-x}Sr_x)CuSi_2O_6$ by means of powder synchrotron X-ray and neutron diffraction, NMR, thermodynamic measurements and density functional theory calculations. We find that such a phase transition is suppressed with Sr substitution. Furthermore, the unit cell volume decreases with increasing Sr content and the intradimer magnetic coupling becomes slightly reduced. Our DFT calculations for $x = 0.1$ for the tetragonal $I4_1/acd$ structures show the presence of strong antiferromagnetic Cu-Cu intradimer couplings and non-negligible antiferromagnetic nearest-neighbor dimer top-bottom antiferromagnetic couplings that avoid any kind of frustration between the dimer layers. The fact that for the germanium substituted sample the phase transition is also suppressed leaves us with a readily tunable system by varying the substitution concentrations. External pressure does not reproduce the substitution effects, but gives rise to a new phase proving that disorder suppresses the incommensurate modulation and phase transition in the case of substitution. However this new phase of a fourfold of reflexes in a line also indicates that we are not dealing with an incommensurate modulation but rather twinnings created through slightly misaligned 90° shifted layers growing on top of each other. First high-field magnetic measurements on a powder sample with $x = 0.1$ at 2 K reveal clear indications for a field-induced ordered state, similar to the observations reported for the $x = 0$ parent compound. In contrast to the parent compound, however, where the analysis of the critical properties are plagued by uncertainties related to the presence of two sorts of dimers as a consequence of the structural transition, the $x = 0.1$ material is free of this complication. Therefore, detailed high-field measurements on this new material may help to clarify the influence of structural subtleties on the critical behavior of the field-induced order. We want to mention the possibility of growing large single crystals of $Ba_{0.9}Sr_{0.1}CuSi_2O_6$ in a mirror furnace with the zone melting method under oxygen pressure to obtain large enough single crystals for inelastic neutron scattering similar to Ref. [19, 39].

4.2 $Ba_2CuSi_2O_6Cl_2$

This chapter gives an outlook on the synthesis and structure of a new material of the same class as Han Purple $BaCuSi_2O_6$, since it shows a closely related structure without any structural transitions.

4.2.1 Introduction

Following the introduction of the previous chapter on $BaCuSi_2O_6$, this material presents an excellent candidate to analyze the BKT groundstate. The advantage of $Ba_2CuSi_2O_6Cl_2$ is that we observe the same dimer-layers as in $BaCuSi_2O_6$ in a slightly changed structure. The substance $Ba_2CuSi_2O_6Cl_2$ was reported by M. Okada et al. [40] and was found as single crystals grown in a $BaCl_2$ flux. The additional $BaCl_2$ goes into the interlayer of Ba atoms and thus only further seperates the dimer layers. Here the reported critical fields are at 1.4 K $B_{c_1} = 15\,\mathrm{T}$ and $B_{c_2} = 33\,\mathrm{T}$ and the coupling in a dimer is $J_1 = 28.1\,\mathrm{K}$. We could measure not only the signal of the melting points but also a crystallisation signal in a DTA measurement and thus improve the ofen profile. Additionally we measured low temperature diffraction to show that this structure reveals no structural transitions at low temperatures.

	x/a	y/b	z/c	U_{iso}
Ba(1)	0.2715(1)	0.6230(1)	0.1093(1)	0.25(1)
Ba(2)	0	0.3917(1)	0.1045(1)	0.24(1)
Ba(3)	0.5	0.3535(1)	0.1046(1)	0.27(1)
Cl(1)	0.2512(5)	0.3562(3)	0.429(3)	0.51(2)
Cl(2)	0	0.1390(9)	0.569(4)	0.68(3)
Cl(3)	0.5	0.1244(6)	0.585(5)	0.74(3)
Cu(1)	0.2503(1)	0.3783(2)	0.1761(1)	0.17(1)
O(1)	0.1747(8)	0.4919(9)	0.1819(7)	0.24(3)
O(2)	0.3693(9)	0.4495(8)	0.1820(7)	0.26(3)
O(3)	0.1231(8)	0.6241(8)	0.2728(6)	0.21(2)
O(4)	0	0.4941(12)	0.2251(9)	0.22(4)
O(5)	0.3278(8)	0.2565(8)	0.1827(6)	0.20(2)
O(6)	0	0.2532(11)	0.2750(8)	0.19(3)
O(7)	0.1334(8)	0.2960(8)	0.1822(6)	0.20(2)
Si(1)	0.1111(4)	0.5122(3)	0.2495(3)	0.21(1)
Si(2)	0.1109(4)	0.2376(3)	0.2499(2)	0.15(1)

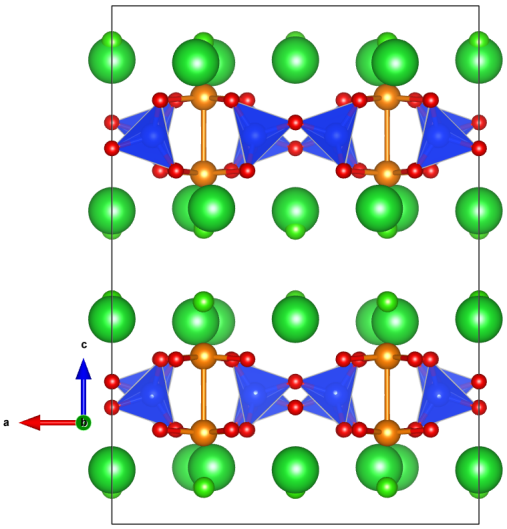

Table 4.6: Atomic positions and thermal factors of $Ba_2CuSi_2O_6Cl_2$ measured at room temperature with the structure Cmca (#64) and the lattice constants a = 13.8917(12) Å, b = 13.8563(11) Å and c = 19.6035(15) Å from reference [40]. On the right the structure along the b-axis is shown. Again in this structure the Ba atoms (big green) and Cl atoms (small green) seperate the layers of Si (blue) - O (red) tetrahedrons, which force the copper (orange/ dark red) in the rare arrangement of pairs arranged in a square lattice.

4.2.2 Synthesis

Figure 4.21 shows a DTA measurement for a detailed knowledge of the growth profile in $BaCl_2$-flux of a molar ratio of 6 : 1. Upon heating we observe 4 signals. First we see the evaporation of crystal water at 138°C (onset temperatures) of the barium salt. At 909°C the melting point of $BaCl_2$ is apparent, which is 12°C below the literature due to the

presence of additional compounds. At 950°C the dissolution of $BaCuSi_2O_6$ in the liquid $BaCl_2$ begins. And possibly at 991°C a reaction of $BaCl_2$ with the quartz ampule occurs. Upon cooling a crystallization signal of $Ba_2CuSi_2O_6Cl_2$ is observed at 1022°C which is too high for $BaCl_2$ and we do not observe the solidification of the latter because it is slowly drained by the glass due to a reaction, this is also reported in [40] and can lead to an explosion of the ampule. Similar to the flux growth of $BaCuSi_2O_6$ the reaction of the flux with the ampule leads to a slow decrease of the flux amount and thus a concentration change. So the growth can also be realized without a temperature decrease with a large enough quartz vessel absorbing the salt.

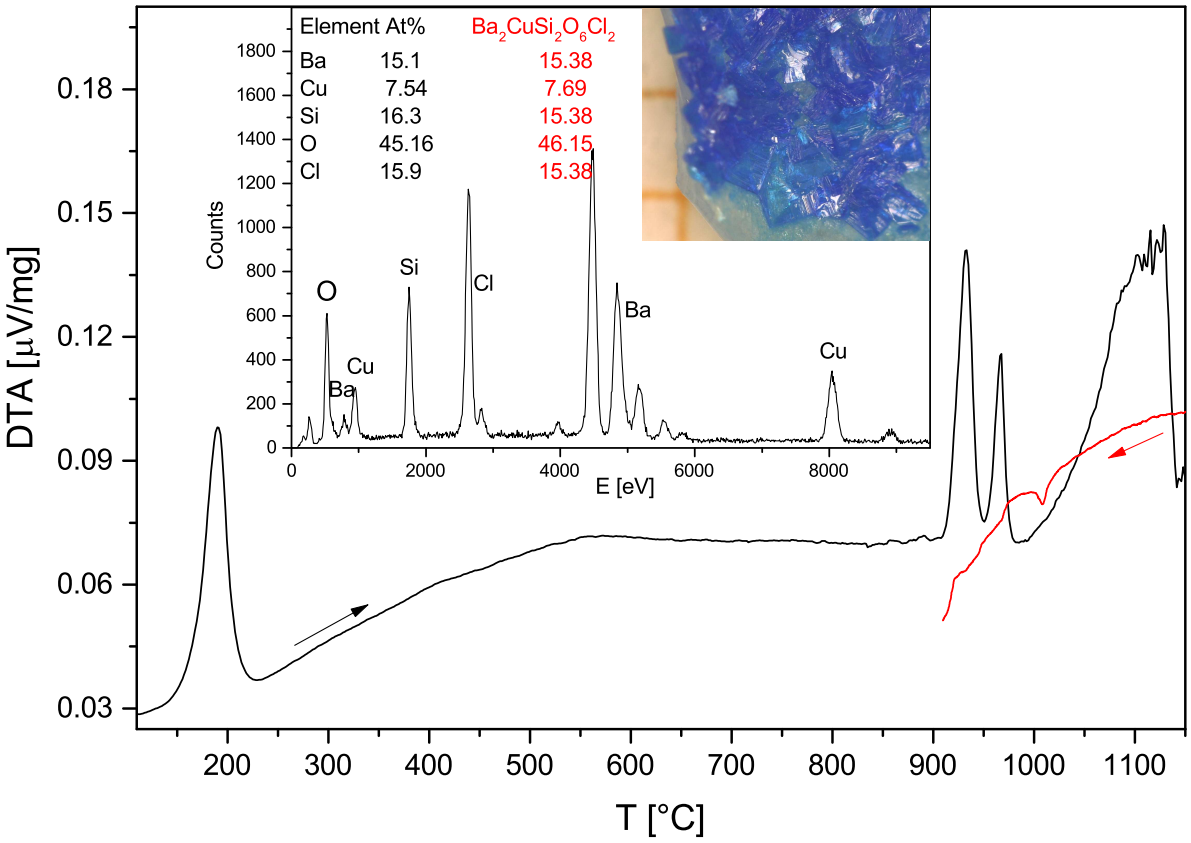

Figure 4.21: DTA measurement of a $BaCl_2$ 6 : 1 $BaCuSi_2O_6$ mixture sealed in a quartz ampule, heated up to 1150°C followed by a slow cooling with a rate of 0.2 K/min. As an inset the resulting bright blue crystals are shown and an EDX spectra of these crystals, which show a perfect $Ba_2CuSi_2O_6Cl_2$ stoichiometry.

We analyzed the bright blue single crystals of up to 1 x 1 x 0.25 mm^3 of the DTA measurement in our SEM with an EDX as shown on the inset of figure 4.21 and found a perfect agreement with reference [40].

Sr substitution

A sequential DTA run was performed with $SrCl_2$ instead of $BaCl_2$ to check for a possible substitution or creation of $BaSrCuSi_2O_6Cl_2$, the results have been confirmed by additional attempts of flux gowth and sintering. We mixed $SrCl_2$: $BaCO_3$: CuO : SiO_2 and first heated it to 950°C, then 1050°C and finally 1100°C. After each DTA curve a picture was taken shown in the inset of figure 4.22. A powder X-ray diffraction pattern is shown in the main part of figure 4.22 measured after the first and last DTA measurement. A simple refinement attempt is added in green for $Ba_2CuSi_2O_6Cl_2$ and in blue for $SrSiO_3$.

The DTA signal of the first run reveals a peak at 820°C, which can be accounted to a partial formation of $Ba_2CuSi_2O_6Cl_2$ in a $SrCl_2$ matrix (see black curve and first image in figure 4.22). But further heating leads at 980°C to an additional signal indicating a decomposition. The image of the second run, reveals a white marking around some still existing $Ba_2CuSi_2O_6Cl_2$, until finally after the third run everything is decomposed, leaving only $SrSiO_3$ and amorphous phases.

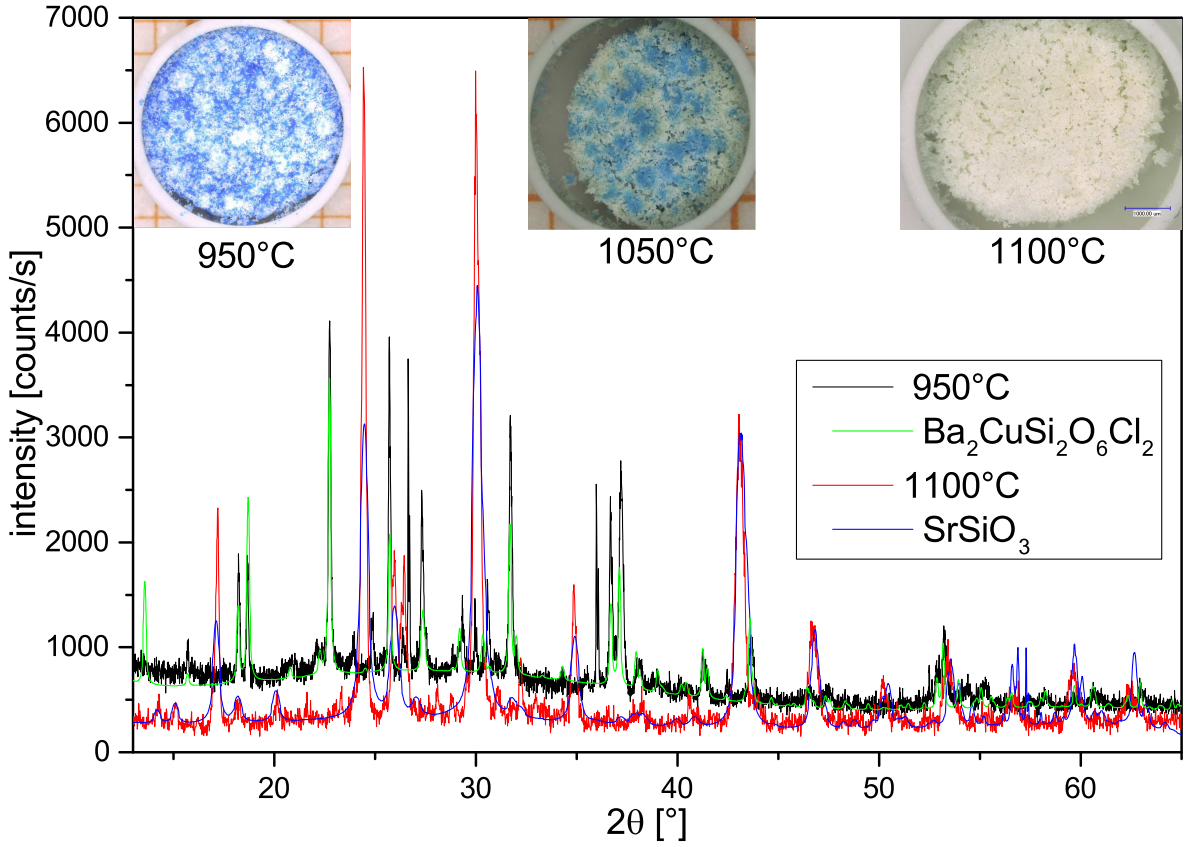

Figure 4.22: PXRD data of two DTA runs on $SrCl_2$ + $BaCO_3$ + CuO + SiO_2 measured after a profile of 950°C (black) and 1100°C (red). A refinement of $Ba_2CuSi_2O_6Cl_2$is shown in green for the first DTA run and for $SrSiO_3$ in blue for the last run. As an inset pictures of the crucible after the DTA stages are shown.

4.2.3 Low temperature properties

We produced powder samples of the compound by sintering a $BaCuSi_2O_6$ 1:1 $BaCl_2$ mixture at 1050°C for 100h. The resulting diffraction pattern is shown in figure 4.23. We also measured the same powder at 12 K with our closed cycle refridgerator and found the same structure with a really small thermal expansion typical for silicates, as can be easily seen by comparing it to the Cu peak shifting (highlighted with arrows).

Vibrating sample magnetometry measurements on powder and crystalline samples agree well with the results from reference [40]. Figure 4.23 b) shows a typical susceptibility curve where a random phase approximation fit (equation 2.17) gives a J_{intra} of 29.21(2) K with a J_{MF} = 16.7(6) K compared to 28.1 K and 17.2 K reported in reference [40]. The samples show a really low impurity content due to the growth in a self flux resulting in a negliglible Curie tail of only 0.8 % free copper spins. A previous saturation in field due to the impurities is reached at 3 T. A linear fit of the inverse susceptibility yields a Curie-Weiss temperature $\Theta_W = 8.5\,K$ and an effective moment of $\mu_{eff} = 1.44\,\mu_B$.

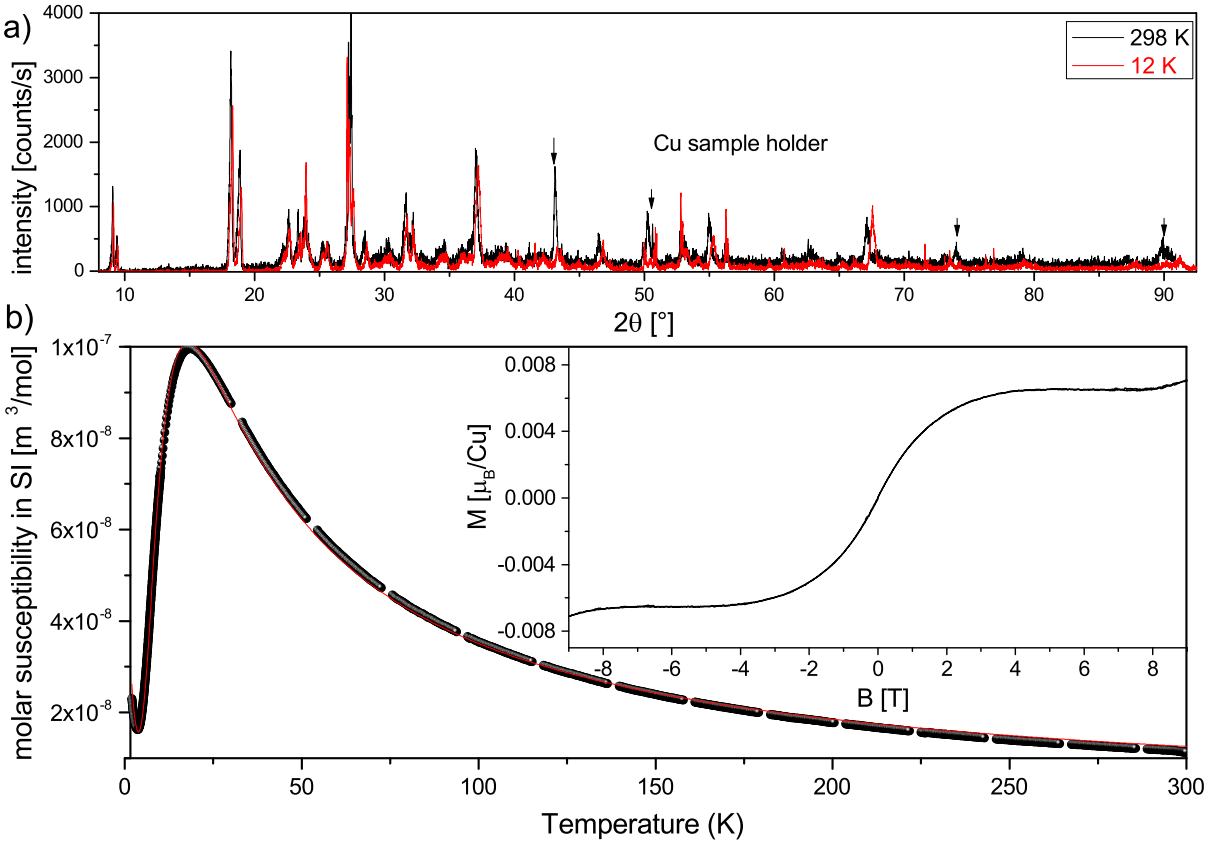

Figure 4.23: a) PXRD of $Ba_2CuSi_2O_6Cl_2$ at room temperature and 12 K. b) Effective moment plots of a $Ba_2CuSi_2O_6Cl_2$ powder sample. The inset shows the magnetic field dependence of the magnetization at 1.9 K. The maximum, before the second upturn gives us the impurity contribution. The curve is fitted with equation 2.17 giving us a $J_{intra} = 29.21(2)$ K with $J_{MF} = 16.7(6)$ K.

4.2.4 Conclusion

$Ba_2CuSi_2O_6Cl_2$ presents a system like $BaCuSi_2O_6$ and has the advantage that the structure is stable down to low temperatures. Additionally the critical fields of the BEC region are lower [40]. Strontium substitution, which could further reduce the critical fields could not be realised as shown in the DTA measurement. A successful DTA curve gives the possibilty to optimize the growth process from [40] to obtain large enough crystals to perform neutron diffraction.

5 Research on new kagome systems

Introduction

Quantum spin systems with Cu^{2+} ions are suitable materials to study quantum many-body effects under variable conditions. Prominent examples are low-dimensional materials with strong magnetic frustrations. In these systems, a quantum spin-liquid state can be realized at low temperatures which is a highly correlated state that has no static magnetic order, despite sizeable magnetic interactions [41]. Compounds with decoupled antiferromagnetic kagome layers are prototypical systems to search for an experimental realization of the quantum spin-liquid state and herbertsmithite, $ZnCu_3(OH)_6Cl_2$, has become one of the most prominent materials in recent years [42, 43, 44, 45].

Herbertsmithite is the mineral with the highest substitution of the series $Zn_xCu_{4-x}(OH)_6Cl_2$ ranging from clinoatacamite, over paratacamite, to herbertsmithite. The structures of all three compounds are shown in figure 5.2 rotated so that they can be easily compared. There are no major changes between the structures as can be seen from the point of view chosen in figure 5.2. The main difference is the choice of the unit cell, since subsequently Cu is changed to Zn and additional seperate positions have to be defined. Thus going from clinoatacamite $Cu_2(OH)_3Cl$ to paratacamite $Zn_xCu_{4-x}(OH)_6Cl_2$ the unit cell is doubled. This transition can be observed not only structurally but also by physical characterisation, since the magnetic properties change. Only clinoatacamite shows beside its dominant mainly antiferromagnetic order a magnetic transition at 18 K [46]. As an example figure 5.1 shows both a specific heat and susceptibility measurement on a slightly substituted clinoatacamite single crystal, where this magnetic transition is apparent.

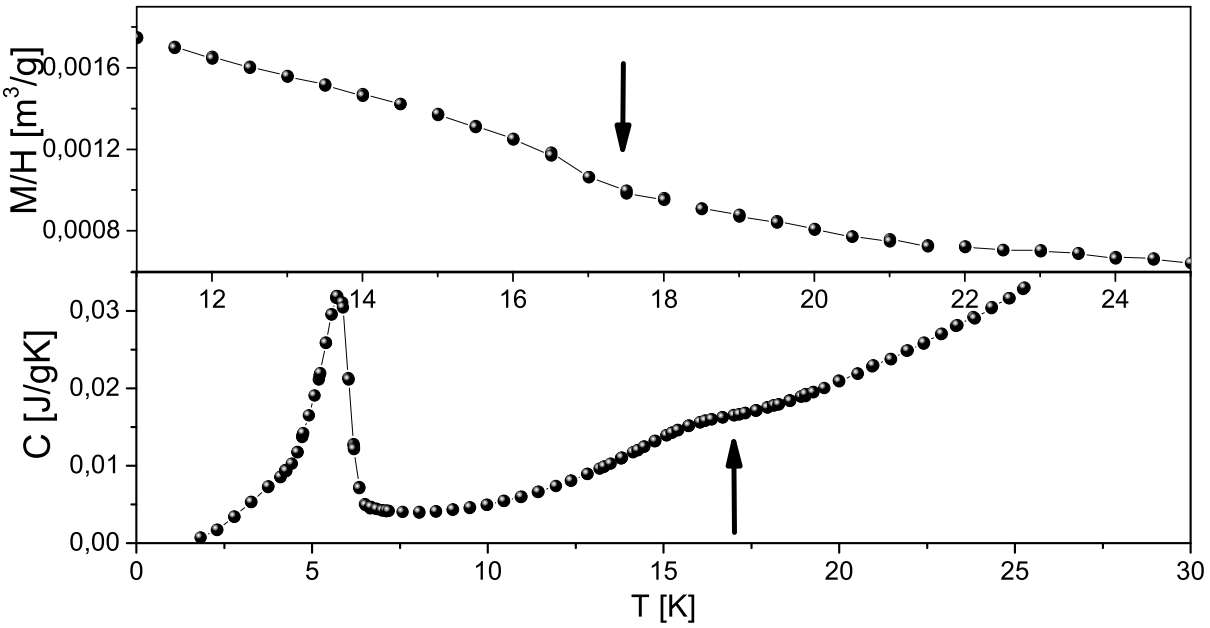

Figure 5.1: Susceptibility and specific heat of a clinoatacamite single crystal weighing 5.3 mg with the slight magnetic transition highlighted by an arrow. The transition can be seen as a slight increase for M/H and a tiny maximum in C.

clinoatacamite
$x < 0.3$
P 2_1/n, #14
measured at 294 K [47]
a = 6.123 Å, b = 6.835Å and c = 9.184Å
$\alpha = \gamma = 90°$ and $\beta = 99.577(4)°$

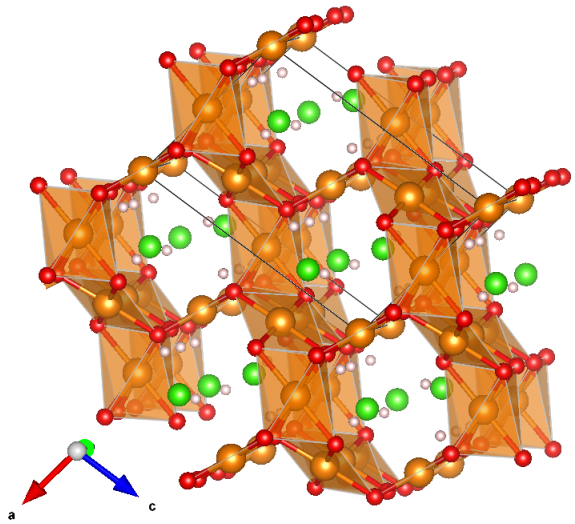

paratacamite
$0.3 \leq x < 0.6$
R$\bar{3}$H, #148
measured at 200 K [48]
a = b = 13.631 Å and c = 14.018 Å
$\alpha = \beta = 90°$ and $\gamma = 120°$

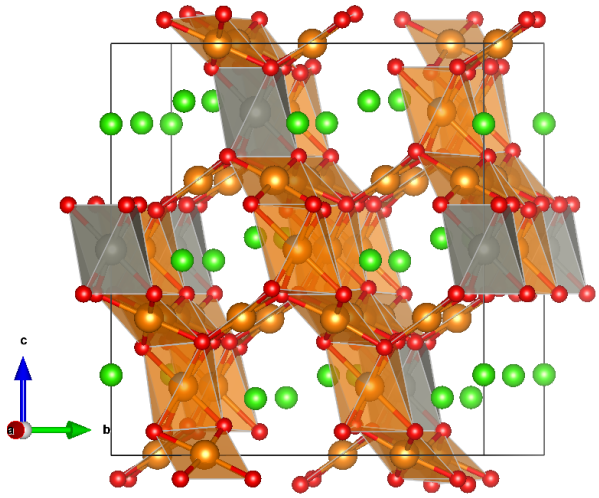

herbertsmithite
$x \geq 0.6$
R$\bar{3}$mH, #166
measured at 296 K [47]
a = b = 6.833 Å and c = 14.069 Å
$\alpha = \beta = 90°$ and $\gamma = 120°$

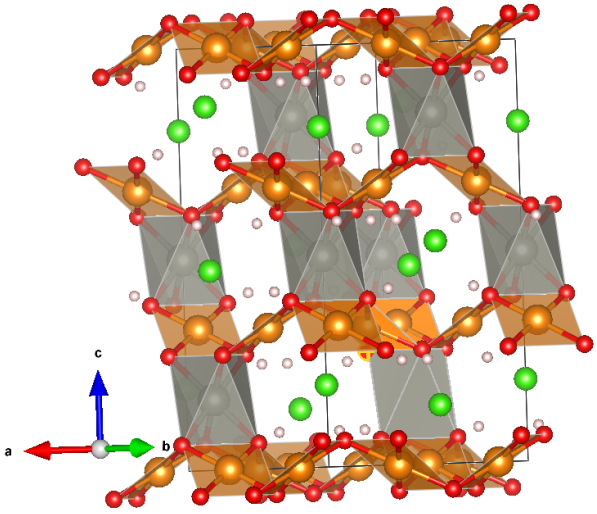

kapellasite
x ≈ 1
P$\bar{3}$m1, #164
measured at 293 K [49]
a = b = 6.330 Å and c = 5.702 Å
$\alpha = \beta = 90°$ and $\gamma = 120°$

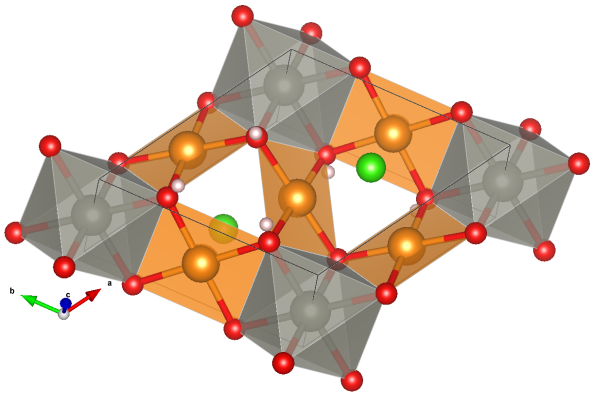

Figure 5.2: Comparison of the structures of the substitution series $Zn_xCu_{4-x}(OH)_6Cl_2$ with Cu-O and Zn-O bonding, starting with clinoatacamite for x smaller than 0.3 [47], to paratacamite for x < 0.6 [48], up to herbertsmithite at substitution values above 0.6 [47]. In comparison also the structural polymorph kapellasite is shown, where Zn is positioned on the empty spaces in the kagome layer [49]. The color identity is: Cu (orange), Zn (grey), Cl (green), O (red) and H (white). The main change is the larger unit cell for paratacamite, while we subsequently substitute Zn on the so called intersite, between the kagome layer of the CuO_4 squares.

P 2_1/n	x/a	y/b	z/c	U_{iso}
Cu1	0	0.5	0.5	0.01311(16)
Cu2	0	0	0	0.01556(17)
Cu3	0.25292(8)	0.24557(5)	0.74944(6)	0.01515(14)
Cl1	0.11236(15)	-0.00140(13)	0.30614(10)	0.0179(2)
O1	0.2809(6)	0.3056(4)	0.5432(3)	0.0241(9)
O2	0.4157(5)	-0.0056(4)	0.7679(4)	0.0230(9)
O3	0.2675(5)	0.6845(4)	0.5410(3)	0.0209(9)
H1	0.22(2)	0.202(12)	0.473(10)	0.16(3)
H2	0.23(3)	0.793(12)	0.470(10)	0.16(3)
H3	0.580(5)	-0.007(8)	0.779(17)	0.16(3)
R$\bar{3}$H	x/a	y/b	z/c	U_{iso}
Cu1	0	0	0.5	0.00762(14)
Zn1	0	0	0.5	0.00762(14)
Cu2	0.5	0.5	0.5	0.00752(10)
Zn2	0.5	0.5	0.5	0.00752(10)
Cu3	0.41437(2)	0.32881(2)	0.33136(2)	0.00919(9)
Cu4	0.41105(2)	0.57773(2)	0.33331(2)	0.00851(9)
Cl1	0	0	0.19375(8)	0.01111(18)
Cl2	0.50208(5)	0.50207(5)	0.19365(5)	0.01114(13)
O1	0.55615(14)	0.61986(13)	0.40094(12)	0.0059(3)
O2	0.55941(17)	0.43275(16)	0.39438(17)	0.0172(4)
O3	0.36360(17)	0.42837(15)	0.38526(16)	0.0145(4)
O4	0.06814(16)	0.12662(18)	0.39418(18)	0.0165(4)
H1	0.585(4)	0.678(4)	0.432(3)	0.031(8)
H2	0.586(4)	0.402(4)	0.416(4)	0.031(8)
H3	0.310(4)	0.398(4)	0.409(3)	0.031(8)
H4	0.096(4)	0.183(4)	0.412(4)	0.031(8)
R$\bar{3}$mH	x/a	y/b	z/c	U_{iso}
Zn1	0	0	0.5	0.00991(6)
Cu1	0.5	0	0	0.00906(5)
O1	0.20570(6)	-0.20570(6)	0.06117(5)	0.01043(10)
Cl1	0	0	0.19435(3)	0.01325(7)
H1	0.143(2)	-0.143(2)	0.0852(13)	0.019(5)
P$\bar{3}$m1	x/a	y/b	z/c	U_{iso}
Cu1	0.5	0	0.5	0.0264(25)
Zn1	0	0	0.5	0.0102(38)
O1	0.3567(21)	0.1783(10)	0.34033	0.0305(26)
H1	0.3979(10)	0.1989(5)	0.1849(26)	0.0847(39)
Cl1	0.3333	0.6667	0.1539(16)	0.0562(28)

Table 5.1: Atomic positions and thermal factors of the four different minerals measured at 294 K, 200 K, 296 K and 293 K. These structures are shown in figure 5.2 with the cif files from reference [47, 48, 49].

The dominant magnetic interaction in herbertsmithite is caused by Cu-O-Cu antiferromagnetic superexchange (explained in chapter 2.3.2) with an exchange energy of J$\sim$17 meV, but no magnetic long-range order has been observed down to T = 50 mK [45]. Therefore, the spin-liquid ground-state of this material could be investigated in great detail (see e.g. a recent review in [50]). One structural drawback of herbertsmithite is the intrinsic Zn-Cu-antisite disorder of up to 15% [51, 52], which makes it challenging to achieve a structurally perfect $ZnCu_3(OH)_6Cl_2$ crystal. Furthermore, the amount of antisite disorder is difficult to quantify with X-ray scattering techniques [50, 53]. Sev-

eral structural variants including polymorphism with varying intersite Cu-substitution ion mixing are common features of Cu-based kagome compounds. In fact the potential amount of unknown compounds of the atacamatie-structure is enormous. A list of the so far published compounds including the compounds described in this thesis are shown in table 5.2. Listed are if existing the mineral name its chemical formula, the substituion ion radius, structural informations including the Cu distances and angles and also the magnetic properties. The atacamite structure is quite flexible allowing many substitutions of $M_4(OH)_6H_2$ with ions M = Zn, Mg, Ni, Co, Cd, Mn, Ca, Cu, Ga and halides H = Cl, Br, NO_3, I, F as well as threevalent ions M = Y, Sm, Nd ions resulting in the formula $M_4(OH)_6H_3$ which are so far only found in the kapellasite type structure. Note that also the end-compounds without Cu exist showing the Pnam structure like $M_2(OH)_3Cl$, with M = Mg, Ni, Co, Mn. We also want to note the closely related structure of jarosite $KFe_3(OH)_6(SO_4)_2$ with a threevalent ion on the kagome layer.

Table 5.2 is divided into four large classes, where the first class are the three polymorphs atacamite, clinoatacamite and botallackite plus substitutions on the halide site. None of these material show a pure kagome layer yet since the layer seperating position is filled with a bridging copper leading to different order temperatures. A bridging structure and thus own category is paratacamite, which exists for all materials of the second class, but is only documented for Zn. As mentioned before, paratacamite is the structural step in between before reaching the herbertsmithite type structure for lower substitution values. The second class ($R\bar{3}m$) are all structural equivalents of herbertsmithite with different substitution ions instead of Zn. The third class is a different type of structure $P\bar{3}m1$ which was found in kapellasite a structural polymorph of herbertsmithite both having the formula $ZnCu_3(OH)_6Cl_2$. The structure is shown in figure 5.2 and has Zn on a new position on empty spaces in the kagome layer. As will be discussed in this thesis this structure allows also for threevalent ions, where additional (OH)/Cl have an additional position above the Zn1 place. The fourth and last group are the ones where a substitution of $x = 2$ is reached with the substitution ion (e.g. Zn) also on the kagome plane creating 1D chain systems instead of the kagome layer.

Due to the difficulties with herbertsmithite novel kagome systems with highly ordered crystal structures are essential to uncover the intrinsic properties of the kagome antiferromagnet. In addition to the material class such as herbersmithite and kapellasite with a divalent ion doping, a breakthrough would be chemical doping [50]. Mazin et al. have proposed that a correlated Dirac metal can be found in electron-doped herbertsmithite which might be realized by replacing Zn by a threevalent ion [54]. In figure 5.3 the band structure results of herbertsmithite and Ga substituted herbertsmithite are shown. In comparison to Zn the fermi level E_F is shifted up towards the crossing point (dirac point) of the bands, thus creating the first correlated dirac metal.

mineral name	formula	r_{ion}[pm]	groups	lattice	order [K]	Θ_W [K]	Cu2 [Å]	Cu1 [Å]	f	Cu1-O1-Cu1 [°]	J_z[K]
botallackite	$Cu_4(OH)_6(Cl,Br,I)_2$	181, 196, 220	P21/m	T	AF (7.2/10/14)	0.41	3.065	3.232	0	105.59	99
atacamite	$Cu_4(OH)_6Cl_2$	72	Pnma	P	AF (9)	-125	3.009	3.42	14	117.02	246
clinoatacamite	$Cu_4(OH)_6Cl_2$	72	P21/n	P	AF (6.5)	-200	3.04	3.42	30	120.21	296
brochantite	$Cu_4(OH)_6SO_4$	250	P21/n	1D	AF (7.5)	-100	3.015	3.573	13	121.3	314
rouaite	$Cu_4(OH)_6(NO_3)_2$	217	P21	T	AF (11)	-12	6.929	3.05	1	110.33	153
claringbullite	$Cu_4(OH)_6ClF$	133	P63/mmc	P	AF (17)	-33	2.737	3.337	2	117.56	254
barlowite	$Cu_4(OH)_6BrF$	196, 133	P63/mmc	P	AF (15)	-?136	2.757	3.339	9	117.21	249
paratacamite	$(Zn,Cu)_4(OH)_6Cl_2$	83	R-3m	K	AF (6)	-250	X	X	42	122.28	330
	$Ga_{0.8}Cu_{3.2}(OH)_6Cl_2$	62	R-3m	K	AF (5)	-256	5.066	3.421	55	118.88	274
tondiite	$MgCu_3(OH)_6Cl_2$	78	R-3m	K	AF (-)	-300	5.075	3.42	∞	118.76	273
gillardite	$NiCu_3(OH)_6Cl_2$	78	R-3m	K	AF, F (6)	-100	5.02	3.418	17	119.19	279
leverettite	$CoCu_3(OH)_6Cl_2$	82	R-3m	K	AF, F (3)	-40	5.096	3.421	13	119.19	279
herbertsmithite	$ZnCu_3(OH)_6Cl_2$	83	R-3m	K	AF (-)	-300	5.087	3.416	∞	118.92	275
namuwite	$(Zn,Cu)_4(OH)_6SO_4$	83	P21/a	K	AF (-)	-79	10.54	3.297	∞	108.2	128
haydeeite	$MgCu_3(OH)_6Cl_2$	78	P-3m1	K	F (4.2)	28	5.75	3.137	7	104.98	92
kapellasite	$ZnCu_3(OH)_6Cl_2$	83	P-3m1	K	F (-)	9,5	5.733	3.15	∞	105.84	101
misakiite	$MnCu_3(OH)_6Cl_2$	91	P-3m1	T	AF (10 K)	-25	5.71	3.208	3	108	125
	$SmCu_3(OH)_6Cl_3$	100	P-3m1	T	AF (18K)	-106	5.639	3.432	5	120.1	294
	$CdCu_3(OH)_6Cl_2$	103	P-3m1	K	AF (4)	45	7.012	3.261	11	106.43	108
	$NdCu_3(OH)_6Cl_3$	104	P-3m1	T	AF (20 K)	-345	5.625	3.411	19	119.3	281
centennialite	$CaCu(OH)_6Cl_2$	106	P-3m1	K	AF (5)	-56	5.76	3.324	11	107.3	117
	$YCu_3(OH)_6Cl_3$	106	P-3m1	K	AF (-)	-100	5.618	3.25	∞	117.36	251
	$Y_3Cu_9(OH)_{19}Cl_8$	106	R-3	K	AF (2.2)	-100	5.679	3.25	45	117.47	253
	$ZnCu(OH)_3Cl$	83	P21/m	1D	?	?	5.688	3.195	?	107.7	122
iyoite	$MnCu(OH)_3Cl$	91	P21/m	T	AF (29 K)	-80	5.721	3.302	3	114.12	204
	$CdCu(OH)_3Cl$	103	P21/n	1D	AF (2)	-150	6.05	3.685	75	115	216
	$SrCu(OH)_3Cl$	127	Pmn21	Trimer	AF (-)	-135	6.972	3.395	∞	119.4	283

Table 5.2: List of the atacamite family divided into four classes of structures each sorted by the size of the substitution ions. The table includes the mineral name if naturally existing, the chemical formula, the radius of the substituted ion, the structural room group, the lattice type of the magnetic ion, the resulting order and temperature, the Curie-Weiss temperature as well as the Cu arrangements and frustration. In the last row the theoretical resulting magnetic coupling following formula 2.13.

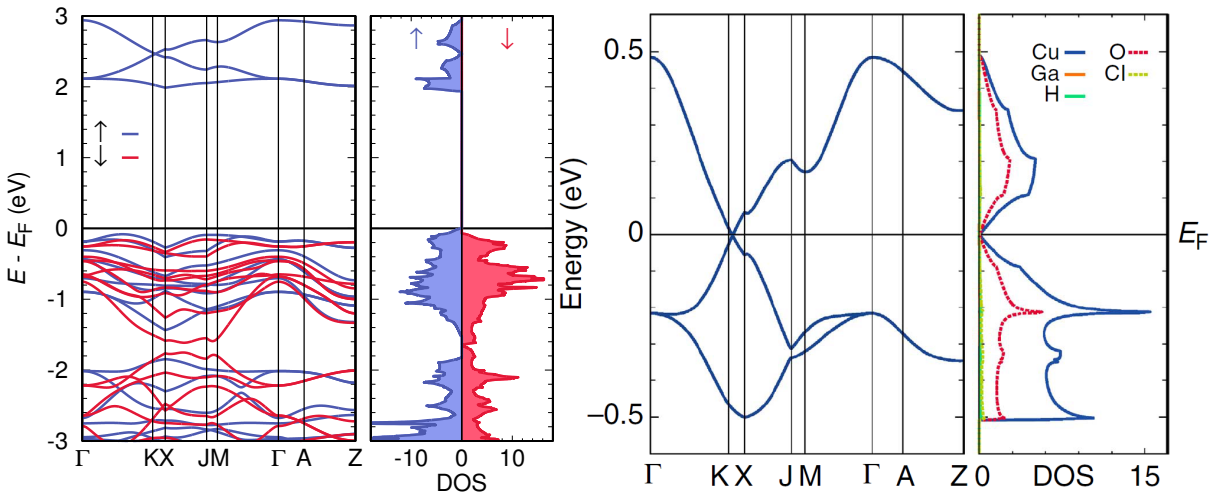

Figure 5.3: Band structure and density of states of $ZnCu_3(OH)_6Cl_2$ calculated with generalized gradient approximation (GGA) exchange correlation functional including correlation effects (data from Harald Jeschke). High-symmetry points of the $P\bar{3}m$ space group are M = ($\frac{1}{2}$,0,0), K = ($\frac{1}{3}$, $\frac{1}{3}$,0), and A = (0,0, $\frac{1}{2}$) in units of the reciprocal lattice vectors. The density of states (DOS) is given in states per electronvolt per unit cell (containing three formula units). On the right the same calculation for $GaCu_3(OH)_6Cl_2$ is shown [54].

Mazin et al. suggest $GaCu_3(OH)_6Cl_2$ as the ideal candidate for an electron doped kagome system, since even when including correlation effects to the calculation, the proposed band structure does not split as it does in herbertsmithite, but still shows the exotic phenomena of a dirac metal. Experimentally, it turned out to be challenging to synthesize samples of doped herbertsmithite. A direct doping attempt by intercalating Li into herbertsmithite does not lead to metallic behaviour, but instead strong Anderson localization of the additional charge carriers were reported [55].

In the following two chapters we present first the proposed candidate $GaCu_3(OH)_6Cl_2$, which turns out to be a mott isolator for $x < 1$ with properties very similar to herbertsmithite and a successful substitution with Y^{3+} which led to a new structure of a system more related to kapellasite, giving an ideal candidate to study spin liquid physics.

5.1 $Ga_xCu_{4-x}(OD)_6Cl_2$

5.1.1 Learning from $Zn_xCu_{4-x}(OH)_6Cl_2$

We started with the reproduction of the synthesis of Herbertsmithite single crystals with different substitutions following [4]. First a powder sample is produced from a prereaction of the starting compounds CuO, $ZnCl_2 \cdot 2H_2O$ and distilled water sealed in a duran glass ampule at air and then transferred into the hydrothermal autoclave Parr 4625. Water was added to compensate the pressure. Then it was heated up to 180-240°C, where higher temperatures lead to slightly increased substitution amounts and faster recrystallisation. In general, two days are sufficient for fully reacted samples at these temperatures. The resulting powder is then washed with distilled water and analyzed. We found a good agreement of the substitution amount controlled by tuning the molar ratio of $ZnCl_2$ with [4], but experienced that at elevated temperatures higher substitution values than $x = 1$ can be realized.

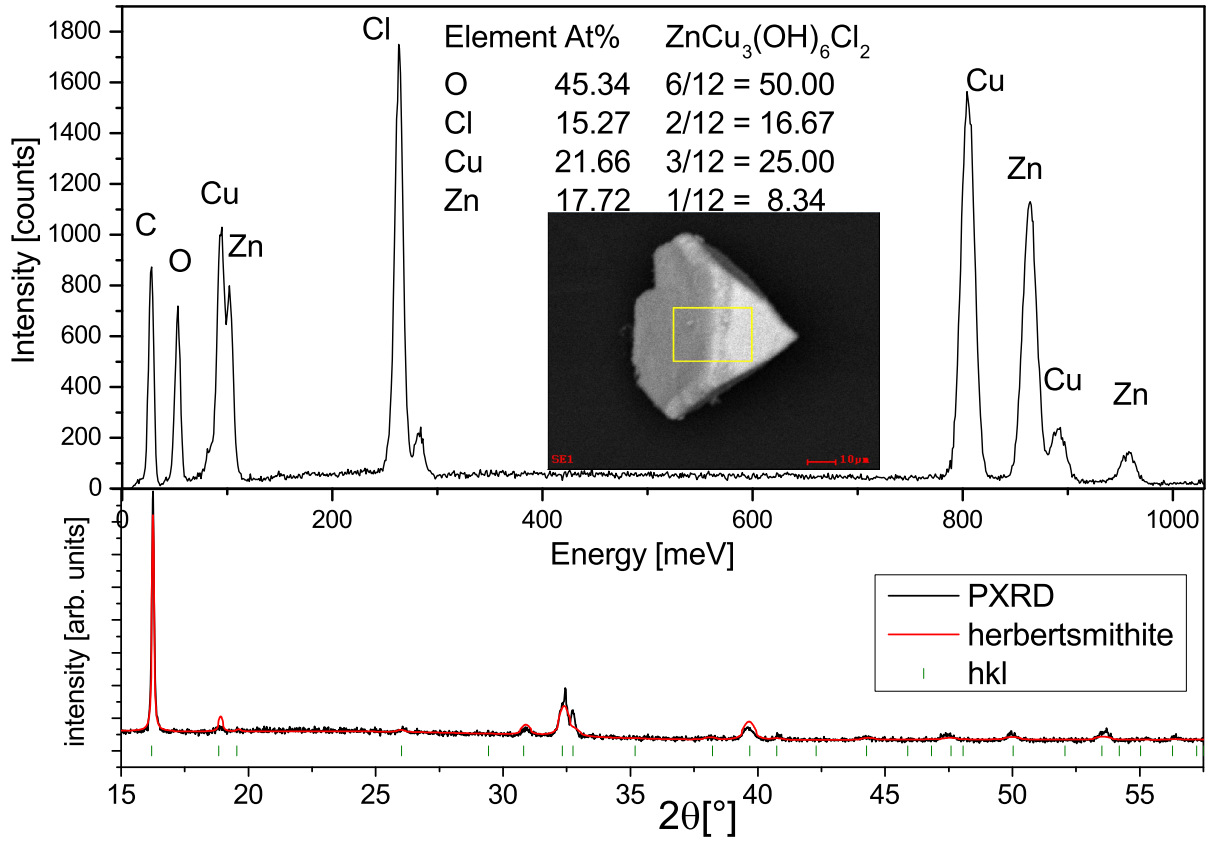

Figure 5.4: EDX analysis on a herbertsmithite single crystal of higher substitution. As an inset the REM image is shown and the measured atomic percentage is given in comparison to x = 1 herbertsmithite. Below the diffraction pattern with a simple herbertsmithite refinement is shown.

The crystal growth is then a recrystallization of the powder done with an external gradient quite similar to vapor transport: the powder is at the hot end with a temperature high enough to dissolve it. The solution is transported to the cold end through simple diffusion, where it falls out and crystallizes. This is realized by a thick walled quartz ampule placed into a tube furnace where 185°C at the hot end are optimal. Using this technique at higher temperatures and molar ratios than given in [4] we could disprove the claim that there are no Zn atoms possible on the kagome plane, since we prepared a complete batch of single

crystals with $x \approx 1.8$ (see figure 5.4) and one with $x = 1.4$still in the herbertsmithite structure.

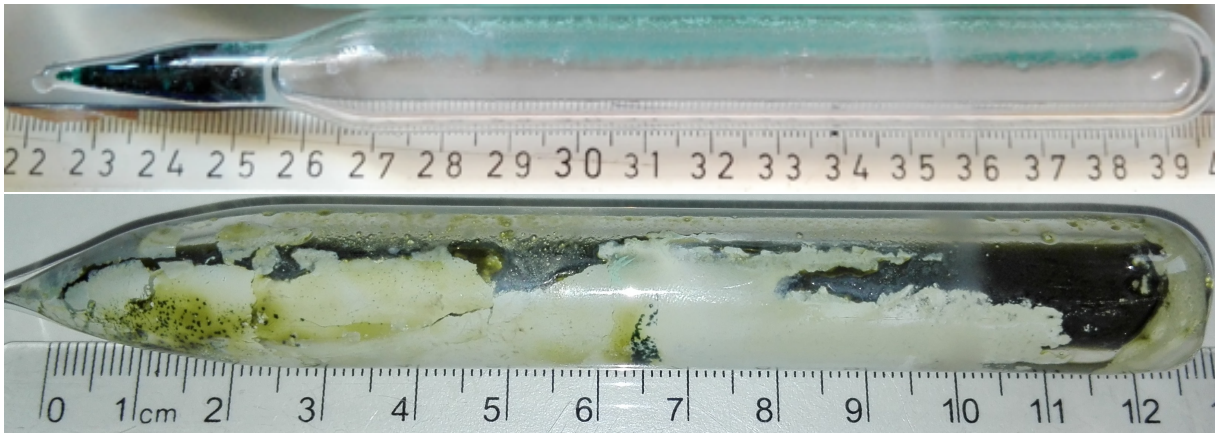

Figure 5.5: Picture of a thick quartz ampules after the growth in a tube furnace. Top: $Zn_xCu_{4-x}(OH)_6Cl_2$ regulated to 192°C, having 186°C at the hot end and 164°C at the cold end, where the whole powder is recrystallized on the left. Bottom: $Ga_xCu_{4-x}(OH)_6Cl_2$ regulated to 170°C resulting in 160°C at the hot end and 150°C at the cold end. The ampule shows a black liquid due to the high amount of $CuCl_2$ in solution and white powder of Ga_2O_3 on the bottom, where we find two zones with mainly clinoatacamite $Cu_2(OH)_3Cl$ single crystals.

Applying the same synthesis conditions to $Ga_xCu_{4-x}(OH)_6Cl_2$ results in the formation of clinoatacamite $Cu_2(OH)_6Cl_2$ and tsumgallit GaO(OH) or Ga_2O_3. The synthesis of $Ga_xCu_{4-x}(OH)_6Cl_2$ described in the next chapter could only be achieved since we experienced that the prereaction of $Zn_xCu_{4-x}(OH)_6Cl_2$ can also be performed at only 80°C, where it happens slower and shows a worse crystallinity than reactions at 180°C.

5.1.2 Synthesis

We managed to synthesize green powder samples of $Ga_xCu_{4-x}(OH)_6Cl_2$, with its color in contrast to the assumption of a dirac metal. From a detailed study we found that the phase formation of $Ga_xCu_{4-x}(OH)_6Cl_2$ happens only at low temperatures with the necessity of a surface to react on. For the synthesis we slowly dissolve CuO in a $GaCl_3$ - H_2O solution of 0.1 - 1.1 M at 90°C using the reflux method as discribed in chapter 1.3.4. For the reflux method in kapellasite [49] glass beads were used to initiate the formation of the material. For $Ga_xCu_{4-x}(OH)_6Cl_2$ this did not improve the synthesis, but it was found that $Ga_xCu_{4-x}(OH)_6Cl_2$ forms preferably on the rough surface of unreacted CuO.

$GaCl_3$ is strongly hygroscopic, so that it turns liquous at air and the reaction with water is extremely exothermal. The liquid itself is a Lewis acid and thus the solutions already heat up themselves when being mixed with water and for a controlled growth have to be cooled down again before the CuO is added. Since $GaCl_3$ is a strong Lewis acid with pH values of 1-3 in our molarity regime it already dissolves some CuO at room temperature. This leads to the formation of $CuCl_2$ and a coloration, in contrast to $ZnCl_2$where the dissolved CuO directly forms herbertsmithite and the solution stays clear. Thus a higher amount of CuO has to be used during the synthesis since otherwise the whole CuO will be dissolved. Plus we need additional CuO as a reaction-surface. A good ratio was found with 1.76 g $GaCl_3$/ $\sim$ 1 ml $GaCl_3 \cdot 6H_2O$ in 10 ml distilled water and 1.2 g CuO for 1.0 M = mol/l. The synthesis shows a good reproductivity and each molar ratio has been synthesised several times.

Deuteration

The same synthesis procedure was repeated with dehydrated $GaCl_3$ opened in a Desiccator on D_2O atmosphere. Then the reflux method at 90°C was applied to 0.72 g CuO in a 6 ml D_2O - $GaCl_3$ solution of 0.1 - 1.1 M. The resulting powder samples of $Ga_xCu_{4-x}(OD)_6Cl_2$ have the same substitution amounts for given molar ratios and show the same physical properties. Here, we present the structural and magnetic properties for 5 different Ga concentrations listed in table 5.3. For comparison, a clinoatacamite sample ($x = 0$) was prepared in a similar way.

CuO impurities

The amount of the impurity phase CuO is higher in low molarity solutions going up to 74 wt% in 0.1 M. This could be reduced however by sedimentation: The powder was shaken in distilled water and given a short time to let the CuO with a higher density (6.31g/cm^3 compared to 3.849 g/cm^3 of $Ga_xCu_{4-x}(OD)_6Cl_2$) fall down. Then the solution was decanted and filtered without the bottom part, successfully reducing the CuO amount to ~ 7 wt% for all deuterated batches except the 0.1 M since here the yield was too little after seperation. Thus we note that the $Ga_xCu_{4-x}(OD)_6Cl_2$ powder is really fine and there is always some part lost during the sedimentation process reducing the yield enormously.

Additional synthesis attempts

We were not able to obtain single crystals since higher temperatures and molar ratios already decompose the $Ga_xCu_{4-x}(OH)_6Cl_2$ samples:

We could narrow down the decomposition of $Ga_xCu_{4-x}(OH)_6Cl_2$ and thus formation temperature of GaO(OH) to temperatures above 100°C. All direct crystal growth attempts with a gradient similar to herbertsmithite gave pure clinoatacamite $Cu_2(OH)_3Cl$ crystals in a GaO(OH) matrix.
In case of higher molar ratios similar problems occur since all CuO is dissolved and again at some Ga content in the solution GaO(OH) begins to fall out.
Attempts of solution growth, where the right amount of CuO dissolved in the $GaCl_3$ Lewis acid was used only gave $CuCl_2$ single crystals in a green viscous liquid.
The utilisation of $Cu_2(OH)_3CO_3$ to increase the pH value leads to the formation of some highly viscous liquid preventing any synthesis attempts. Even in attempts with a LiCl and LiOH flux similar to [56], which prevented in this case the formation of clinoatacamite, it was not only formed but the growth yielded small single crystals. Using Ga_2O_3 or presintered Ga_2CuO_4 and $CuCl_2$ also only formed clinoatacamite and Ga-/Cu oxides. Thus $Ga_xCu_{4-x}(OH)_6Cl_2$ gives a challenging phase similar to kapellasite, which can so far only be obtained from the reflux method at low temperatures forming only powder samples.

5.1.3 EDX Analysis

The preparation process for the EDX analysis is described in chapter 3.3. Since we obtained only powder samples of $Ga_xCu_{4-x}(OD)_6Cl_2$ the analysis was performed on pressed pallets. We note that the EDX analysis on powder samples with height variations causes strong uncertainties for the measured elements. It is used as a general guide to have some insight on the substitution amount, since a refinement on a PXRD pattern of occupancies between neighbouring ions such as Ga and Cu gives no reliable values. We observed that within one batch the powder shows different substitution amounts ranging up to 2 at%,

which is taken into account in the large statistical errors in table 5.3, which is enhanced by amounts of GaO(OH) impurities. In figure 5.6 an EDX spectra is shown with the SEM image on the inset. The resulting at% are given in the figure, where we observe values in agreement with stoichiometric values of $Ga_xCu_{4-x}(OD)_6Cl_2$. We determined the average value including its resulting statistical error for oxygen and chlorine over all measured points of all substituted batches as an indication for the stoichiometry. The values O: 52(4) at% and Cl: 18(1) at% show a slight enhancement within the given instrument error, but do not yield values high enough to assume additional chlorine or hydroxil.

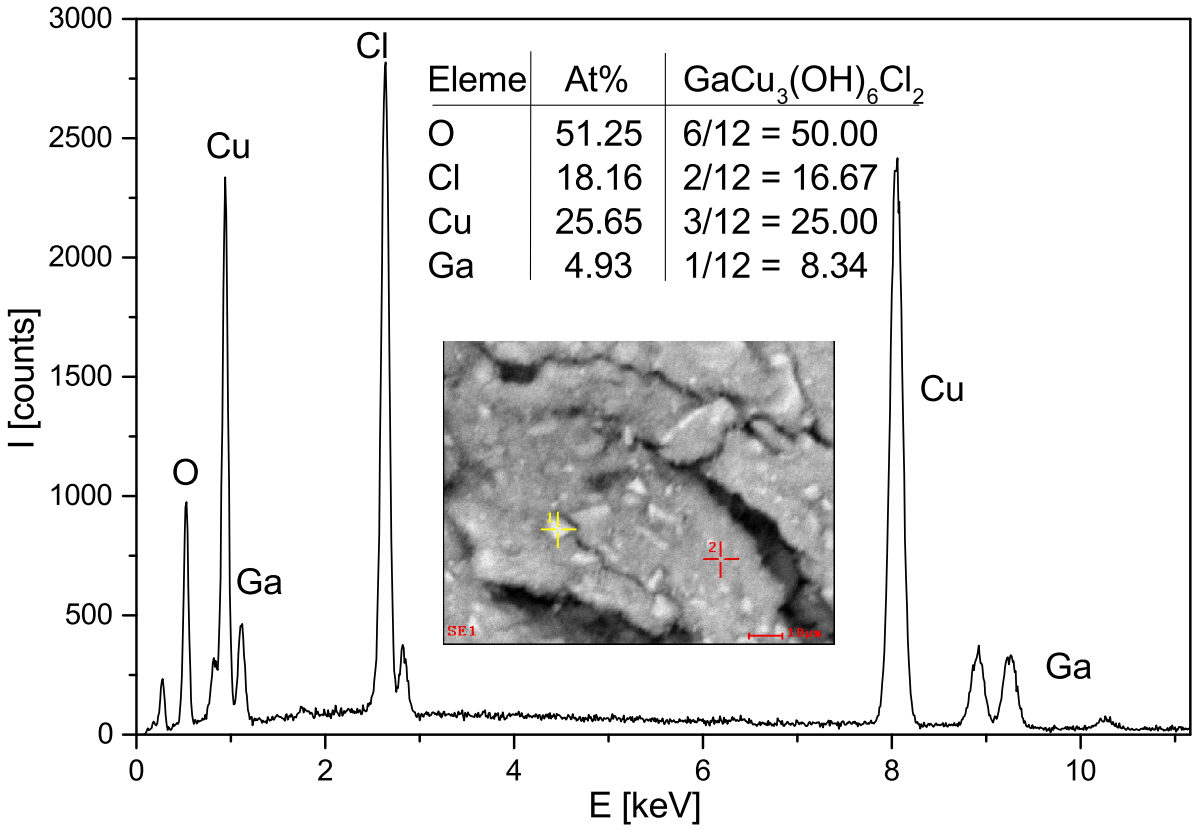

Figure 5.6: EDX analysis of a $Ga_xCu_{4-x}(OH)_6Cl_2$ sample part from the 1 M solution. In a table the measured at% are given compared to the stoichiometric values. The inset shows a SEM image in red is the measured area.

Generally we see in EDX measurements that with increasing molar ratio in the solution, also the Ga content in the powder compound increases. But even at the highest molar ratios the average Ga content in $Ga_xCu_{4-x}(OH)_6Cl_2$ stays below $x = 1$ (see table 5.3).

batch	0.0 M	0.1 M	0.2 M	0.4 M	0.7 M	1.0 M	1.1 M
x	0.00(0)	0.09(6)	0.19(4)	0.4(1)	0.47(8)	0.8(1)	0.7(2)

Table 5.3: Average results of Ga-Cu ratio in each batch explained in the substitution factor x from EDX measurements on the $Ga_xCu_{4-x}(OD)_6Cl_2$ powder series. The given errors are not instrumental but the statistical distribution.

5.1.4 Structure

The compound $Ga_xCu_{4-x}(OD)_6Cl_2$ shows similar X-ray diffraction patterns as for Zn substitutions. Thus $Ga_xCu_{4-x}(OD)_6Cl_2$ has a similar structure as shown in figure 5.2. The diffraction reflexes show a slight broadening as it was observed for $Zn_xCu_{4-x}(OH)_6Cl_2$ making it hard to differentiate clinoatacamite from herbertsmithite [53]. Since the electron density of Ga and Cu is quite close, X-ray diffraction will not be sufficient to differentiate those two atoms. Therefore, all diffraction patterns look rather similar, meaning that we observe no reflex shifting due to volume changes for different substitution values, however the amount of CuO and other phases varies.

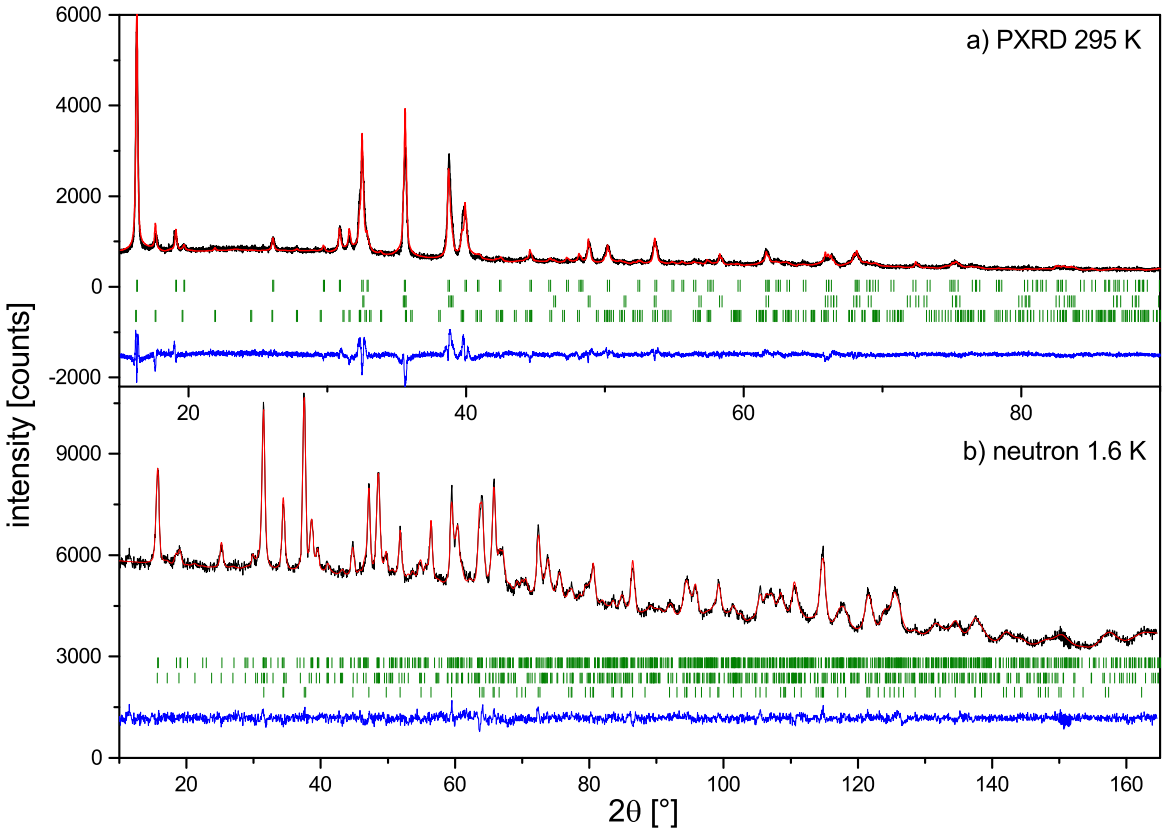

Figure 5.7: a) Rietveld refinement with a $\chi^2 = 3.8881$ of the crystal structure parameters from Cu-K_α X-ray powder diffraction data measured at $T = 295\,\mathrm{K}$. The observed intensity (black), calculated profile (red), and difference curve (blue) are shown of the 0.7 M powder sample. The rows of ticks at the bottom correspond to the calculated diffraction peak positions of the phases (from top to bottom): 58.5(4) wt% $Ga_xCu_{4-x}(OD)_6Cl_2$, 26.9(1) wt% CuO and 14.6(1) wt% atacamite. b) Rietveld refinement with a $\chi^2 = 1.5974$ of the crystal structure parameters from neutron powder diffraction data measured at $T = 1.6\,\mathrm{K}$ with a wavelenght of $\lambda = 1.49400\,\text{Å}$. The observed intensity (black), calculated profile (red), and difference curve (blue) are shown of the 1.1 M powder sample. The rows of ticks at the bottom correspond to the calculated diffraction peak positions of the phases (from top to bottom): 40.2(2) wt% $Ga_xCu_{4-x}(OD)_6Cl_2$, 48.5(2) wt% CuO and 11.3(2) wt% atacamite.

A refined PXRD of the 0.7 M batch is shown in figure 5.7 a). The goodness of the fit with the herbertsmithite structure $R\bar{3}m$ is χ^2= 3.89 with a unit cell of $a = b$ =6.83463 Å, c =13.95853 Å. In comparison to herbertsmithite ($a = b$ =6.8326(3) Å and c =14.0686(8) Å) the lattice parameters show mainly a smaller c-axis, in accordance with the Ga ion having a smaller radius then Zn. Since the c-axis is influenced stronger, it is plausible to

assume that the Ga ion mainly goes into the Cu1 position between the kagome planes. This is also underlined by the observation that during an attempt of Ga on the Cu1 position (sometimes referred to as interplane) it tends to a reasonable higher Ga occupancy while adding Ga on the Cu2 position will diverge in negative occupancies of Ga. Furthermore, also theoretical calculations suggest no Ga on the interplane Cu1-position [57]. A real refinement of the data obtained with the Bruker D8 with the Ga occupation on Cu sites set free cannot be performed due to the close properties to Cu.

Table 5.4: Structural table of the 1.1 M $Ga_xCu_{4-x}(OD)_6Cl_2$ powder sample measured at 1.6 K. The goodness of the fit with P 21/c is $\chi^2 = 1.5974$ with a unit cell of a =6.1216 Å, b =6.8213 Å, c =10.0734 Å, $\alpha = \gamma$ =90° β =116.76°.

	x/a	y/b	z/c	U_{iso}
Ga/Cu1	0.023(4)	0.752(3)	0.253(3)	0.0022(15)
Ga/Cu2	0.5	0	0	0.0022(15)
Ga/Cu3	0	0	0	0.0022(15)
O1	0.147(4)	0.005(5)	0.225(2)	0.0065(16)
O2	0.209(5)	0.317(4)	0.467(3)	0.0065(16)
O3	0.753(6)	0.215(4)	0.044(4)	0.0065(16)
Cl	0.308(2)	0.509(2)	0.1965(12)	-0.0036(17)
D1	0.311(5)	0.717(4)	0.041(3)	-0.011(3)
D2	0.210(5)	0.308(3)	0.042(3)	-0.011(3)
D3	0.307(5)	-0.019(5)	0.280(3)	-0.011(3)

Furthermore we measured neutron diffraction at 1.6 K and 295 K on the deuterated 1.1 M batch, which revealed that the optimal refinement is reached for this sample using the clinoatacamite structure. However the results are just slightly improved using $P2_1/c$ compared to $R\bar{3}mH$, since even with deuterated samples and a long counting rate the Ga position could not be refined properly using the data. The same structure was found for both temperatures, meaning that there is no structural transition down to 1.6 K apparent in this system. The neutron refinement result is shown in figure 5.7 b) and the atomic positions are given in table 5.4. The lattice parameters at 1.6 K are a =6.1216 Å, b =6.8213 Å, c =10.0734 Å, $\alpha = \gamma$ =90° and β =116.76°, while the room temperatures refinement gives a =6.079484 Å, b =6.839558 Å, c =10.109850 Å and β =116.63°. This can be compared to phase pure clinoatacamite with a =6.1226(3) Å, b =6.8346(4) Å, c =9.1841(6) Å and β =99.577(4)°. Again we observe that mainly the c-axis is influence by the substitution. However to make a clear statement on the Ga influence and position resonant X-ray diffraction on qualitative better samples regarding phase purity and crystallinity is necessary.

5.1.5 Magnetic susceptibility

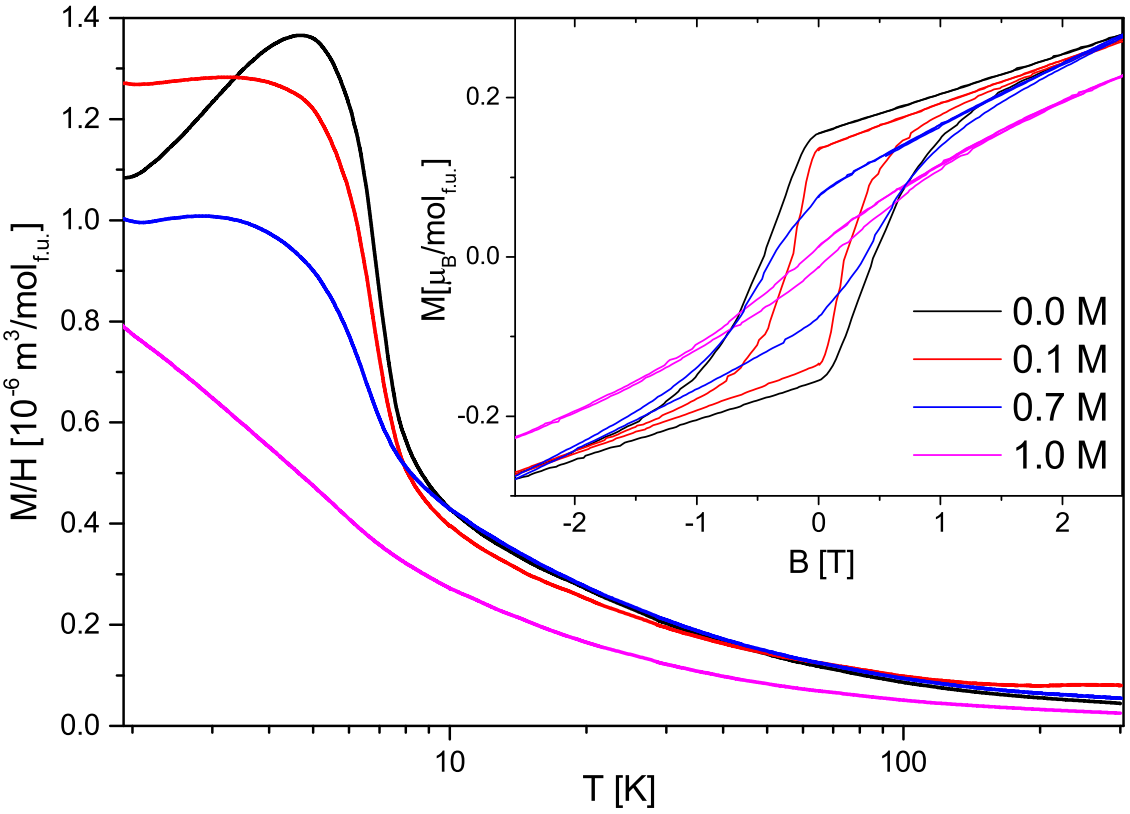

Figure 5.8: The image shows the magnetization over Magnetic field plotted against a logarithmic scale of temperature on $\sim$ 30 mg of different $Ga_xCu_{4-x}(OD)_6Cl_2$ powder samples measured at $\mu_0 H = 1$ T. On the inset the M(H) curve measured at 2 K is shown revealing a hysteresis for all powder samples.

The magnetic behaviour of the Ga-substitution series is quite similar to $Zn_xCu_{4-x}(OH)_6Cl_2$. In figure 5.8 we present the susceptibility measurements of different $Ga_xCu_{4-x}(OD)_6Cl_2$ batches. We note again that there is always some unreacted CuO in the samples and a lot in the 0.1 M sample where the segregation gave no yield and thus some of the original powder CuO containing powder was used. Refining the powder X-ray diffraction patterns with the two phase parts we determined the amount of CuO impurity in each batch and this was taken into account for the magnetization measurement by dividing by the real mass part of the $Ga_xCu_{4-x}(OD)_6Cl_2$ phase.

In the main part of figure 5.8 the susceptibility in SI per mol formular unit versus temperature shows a clear magnetic phase transition for $x = 0$ (black) at $T_N = 6.5$ K. This transition is slowly suppresses with increasing x, while T_N is nearly unchanged. This behaviour is confirmed from $M(H)$ measurements at 2 K shown in the inset of Fig. 5.8, where the same slow reduction of the frozen spin fraction is apparent. The remance values are 0.1554/ 0.1351/ 0.0802/ 0.0147 $\mu_B/\mathrm{mol_{f.u.}}$. A frozen fraction estimate can be performed by dividing the substituted sample by the first value (0 M): $\frac{M_r}{M_r^{0\,\mathrm{M}}} \approx 87\%/\ 52\%/\ 9\%$. The hysteresis loop areas of 4147/ 1468/ 2120/ 440 $\mu_B K/\mathrm{mol_{f.u.}}$ yields a too small value for the 0.1 M sample due to a high amount of CuO impurity phase as noted before. Yet we can again attempt an approach to estimate the frozen fraction by the relative change $\frac{A}{A_{0\,\mathrm{M}}} \approx 35\%\ /51\%\ /11\%$ in general good agreement with the remancence values.

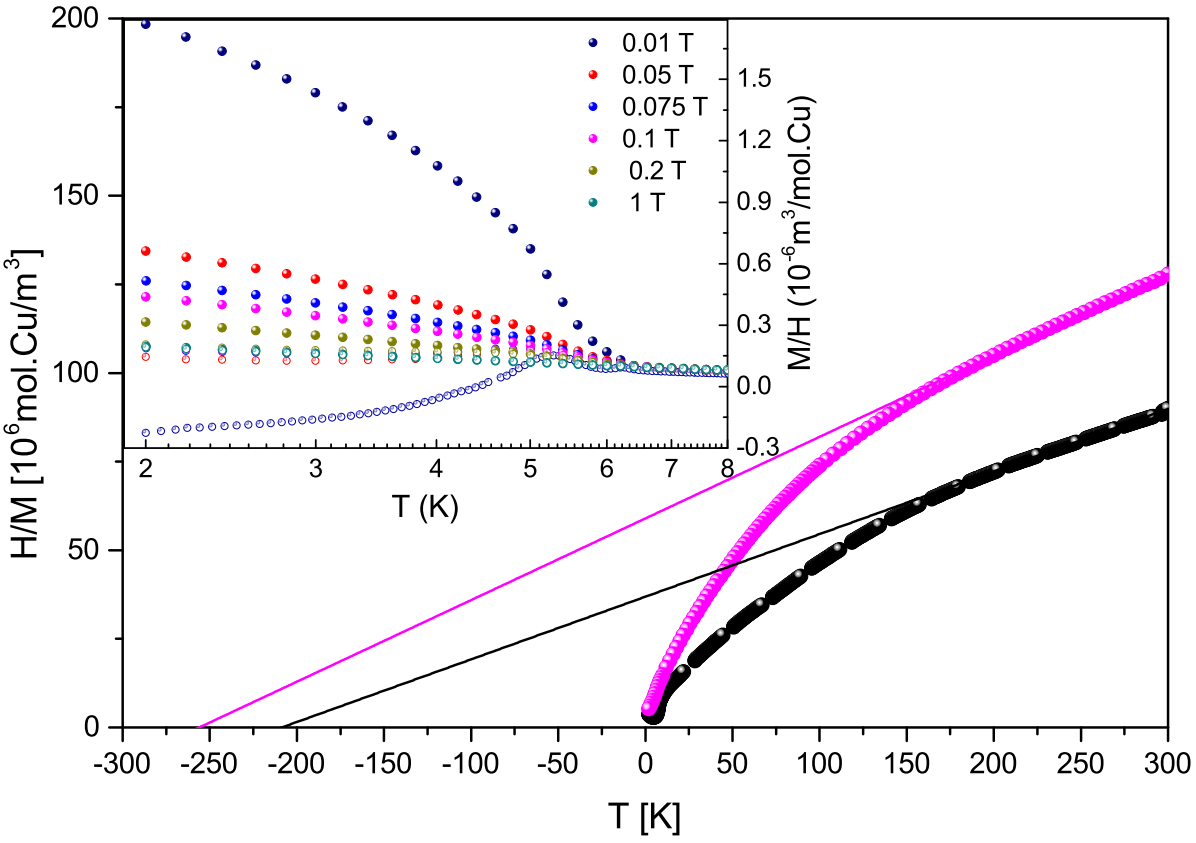

Figure 5.9: The plot displays the inverse susceptibility of the measurements on the left with an input Curie-Weiss fit. On the inset a field dependant analysis of the M(T) curve of the 1.0 M sample is shown, where the open symbols are the zerofield curve compared to the field cooled curves as full points.

Figure 5.9 shows a plot of the inverse susceptibility, which is generally quite sensible to the CuO content, since it orders antiferromagnetically at around $T_N = 230\,\mathrm{K}$ [58]. The impurity amount of CuO for the shown samples of 0.0 M and 1.0 M is 9.33 wt% and 2.9 wt%. The values were obtained by rietveld refinement. From a Curie-Weiss fit in the temperature range above 220 K wee observe an increase of the Weiss temperature with increasing substitution, as it was observed for Zn substitution [42]. However comparing equivalent x values of the two different substitution series we find a lower increase for Ga-substitution than for Zn. E.g. for $x = 0.8$ we have a Weiss temperature of $\Theta_W^{Ga} = -256$ K (see figure 5.9) compared to $\Theta_W^{Zn} = -285$ K [42]. We find an effective moment of $\mu_{eff} = 1.66\mu_B$ for the high temperature part of the 1.0 M sample, while the Curie-tail from 0 to 10 K gives an effective moment of $\mu_{eff} = 0.72\mu_B$. The resulting estimate of the amount of frozen spins is 43%, which is obtained by the ratio of the two moments. On the inset the zerofield-cooled and field cooled curves of the 1.0 M in several fields are shown, representing the hysteresis loop end at around 1 T from figure 5.8.

5.1.6 Specific heat

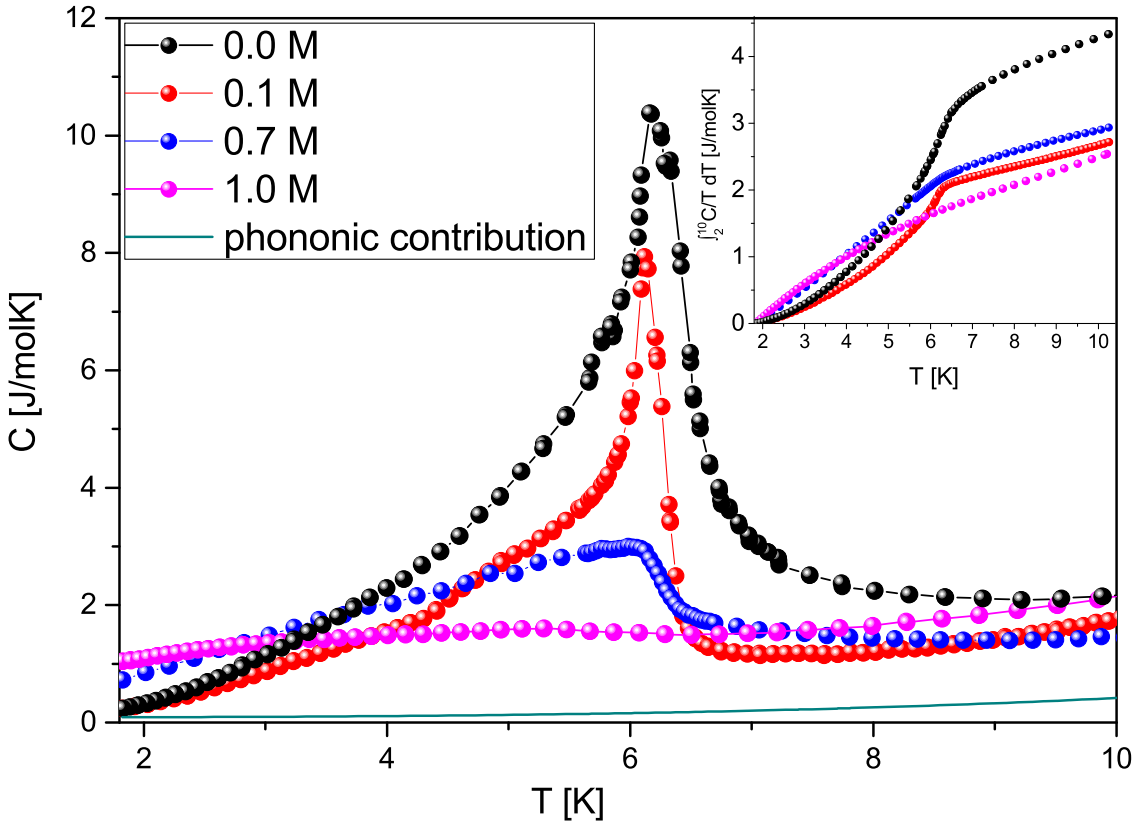

Figure 5.10: Specific heat measurements in zero field from 1.8 to 10 K on examplary batches showing a lambda shaped peak revealing the Néel order of our samples. The phononic contribution is not substracted, but shown by a turquoise line. As an inset the entropy S of the same region is shown.

Furthermore we measured the specific heat on pressed pellets of $Ga_xCu_{4-x}(OD)_6Cl_2$. The data underlines the results of the magnetization. To optimize the weak coupling in these samples we mixed apiezon N grease with powder and subtracted this contribution following Ref. [59]. We used the same measurement procedure for all shown samples to get a good comparison. For clinoatacamite ($x = 0$), we see a clear anomaly at 6.5 K indicating the Néel order of this compound [46]. With increasing amount of Ga we observe a pronounced decrease of the height of this anomaly. However, T_N is only slightly shifted to lower values with increasing x, in agreement to what was observed in the magnetization measurements (Fig. 5.8). In both measurements the strongest shift is observed in the 1.0 M sample with T_N going down to about 5 K. The phononic contribution was estimated and is similar for all samples. We utilize the 0.7 M sample fitted in the range of 9 K to 30 K. The result following equation 3.1 of a linear fit of C_{mol}/T vs. T^2 gives $\beta_0 = 0.329(4)$ mJ(mol $K^4)^{-1}$ and is plotted as a turquoise line in Fig. 5.10. This yields a Debye temperature of $\vartheta_D \approx 473$ K.

The entropy gain within the maximum in the specific heat at zero field is obtained by integration of C/T and shown on the inset of figure 5.10. We calculated the entropy of the order by subtracting a linear background to rule out spin fluctuations, which are adressed below: $S = \int_{1.8}^{10} C_{mol}/T \cdot dT - S_0 \approx 4.26 - 1.44/\,2.90 - 1.25/\,2.66 - 2.23/\,2.46 - 2.33\,\mathrm{J/molK}^2$. Thus we obtain frozen fraction estimates of $\frac{S}{S_{0\,\mathrm{M}}} \approx$56% / 15%/ 5%. The variation in comparison to the susceptibility data is reasonable since we do not adress the

moments directly and the signal becomes quite broad (going below the measured 1.8 K) for increasing doping.

A qualitative approach to estimate the change of the ordered moment can be made by the obvious value change of the maximum of the specific heat. The values of the maximum are 10.4/ 7.9/ 3.0/ 1.6 J/(molK). Again the frozen fraction can be estimated by dividing through the clinoatacamite value: $\frac{C}{C_{0\,\mathrm{M}}} \approx 72\%$ /29 % /15%. This shows that the ordered moment of the $Ga_xCu_{4-x}(OD)_6Cl_2$ is slowly reduced and a large portion of the spin degrees of freedom remain fluctuating. Note that clinoatacamite is a frustrated system and thus does not order completely. Due to these enhanced spin fluctuations the specific heat follows, after phonon substraction, a linear in T-dependence from T_N up to 10 K as can be seen in figure 5.11.

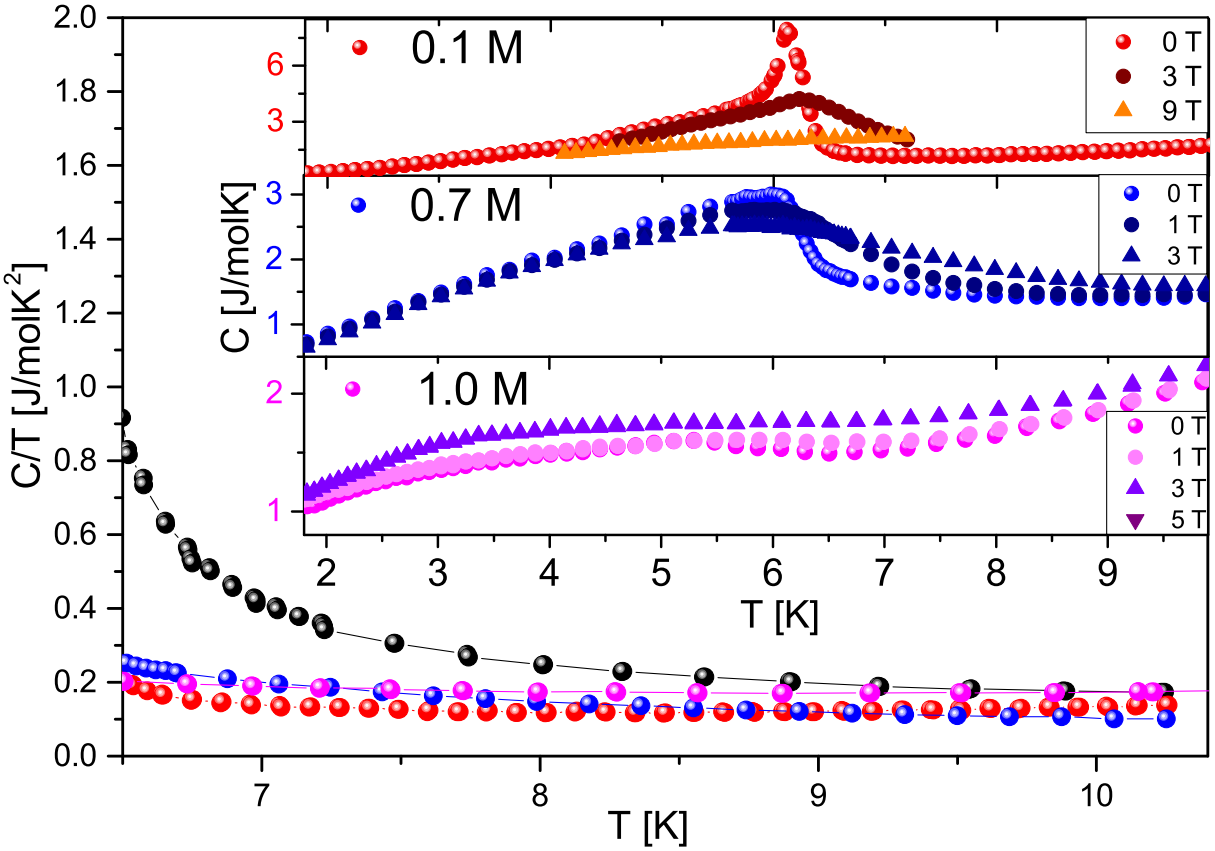

Figure 5.11: Linear in T-dependance above the Néel order of C/T. As an inset the specific heat measurements in different fields from 1.8 to 10 K on the same examplary batches show a slow washing out of the lambda shaped peak.

The field dependance of the specific heat curve shown on the inset of figure 5.11 is mainly a slow suppression realized in a broadening of the sudden ordering, since some spins are already forced into order before T_N with such large fields. The different substitutions show a similar behaviour, but the position is influenced the most in the 1.0 M sample.

5.1.7 μ−SR on deuterated $Ga_xCu_{4-x}(OD)_6Cl_2$

We measured the $Ga_xCu_{4-x}(OD)_6Cl_2$ samples on GPS at PSI in the range of 1.5 and 40 K and the 1 M sample on LTF down to 50 mK, all in zero field, transverse and longitudinal field of 50 G. An excerpt of some of the raw data of the 1.0 M sample is plotted in figure 5.12 on the inset. Even with $x = 0.8$ in the 1.0 M batch, we still see some amplitude changes and thus can again conclude that even this sample orders. In both fields from the amplitude change of the asymmetry the magnetic fraction can be extracted, meaning the amount of ordering phase (see right figure 5.12). Again we see a decrease in the ordering amount with increasing substitution, but we can see an additional transition in the magnetic fraction shape in the samples 0.9 M, 0.4 M and 0.7 M, which can be accounted to the additional AFM ordering part with the clinoatacamite $Cu_2(OH)_3Cl$ structure $P2_1/n$ at 18.1 K [46]. An additional measurement to verify this transition was performed in both specific heat and VSM measurements, where a tiny signal is visible highlighted by arrows on figure 5.2.

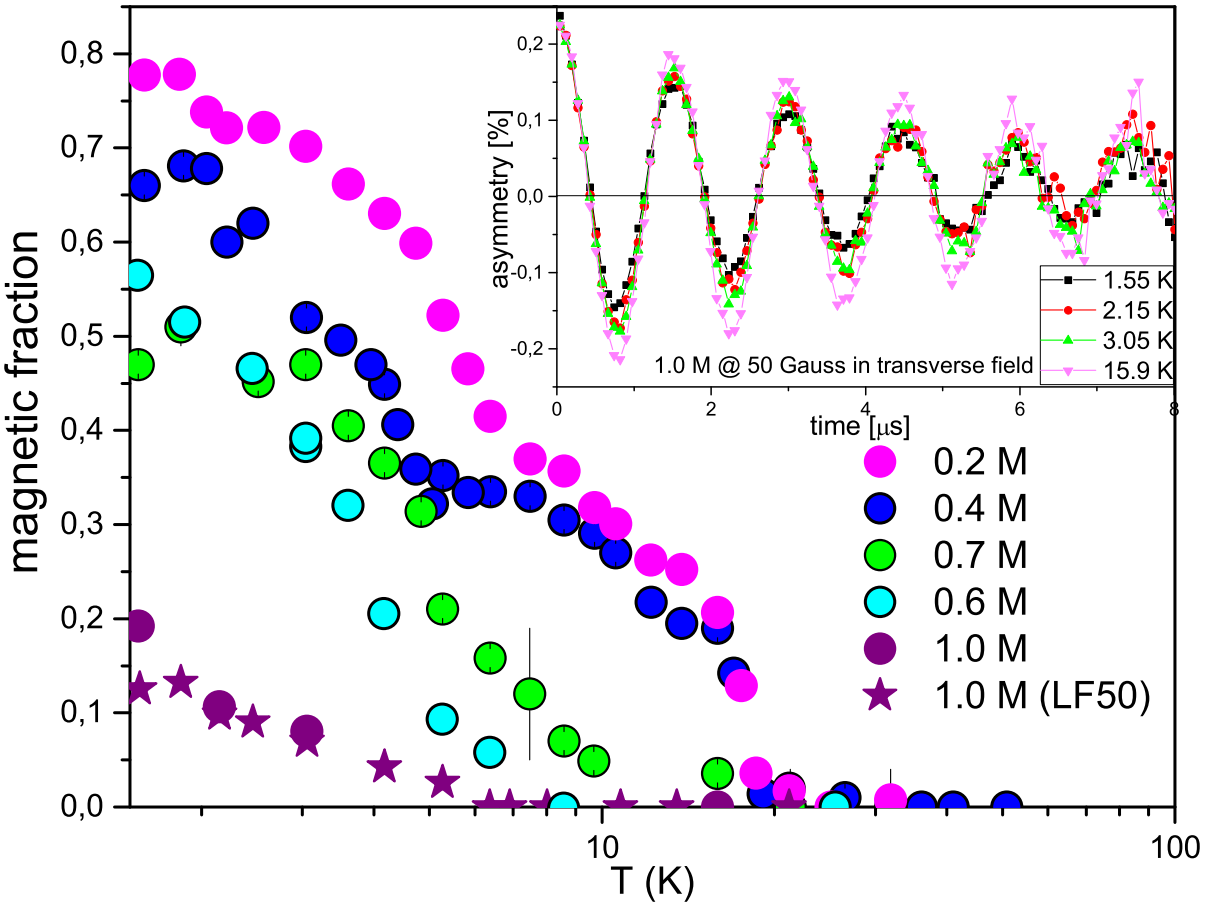

Figure 5.12: Plot of the magnetic fraction versus temperature on a logarithmic scale of different $Ga_xCu_{4-x}(OD)_6Cl_2$ powder samples obtained from a fit of the transverse field measurements. On the inset a plot of the asymmetry of the muons plotted versus the arrival time for the 1.0 M sample in transverse field at 50 G.

We sketched the phase diagram of the $Ga_xCu_{4-x}(OD)_6Cl_2$ series from the magnetic fraction results of the μ−SR data. The result is plotted in figure 5.13. In agreement with the susceptibility a completely suppressed order has yet to be observed in the series and should be at substitution values around $x \approx 0.9$. The maximal value at 0 substitution was not chosen as 100 % frozen fraction since clinoatacamite provides a frustrated system where no complete order is observed. We included the data points on the Zn substitution

series from reference [43]. The Ga phase diagram is shifted to higher substitution values as compared to $Zn_xCu_{4-x}(OD)_6Cl_2$ [43].

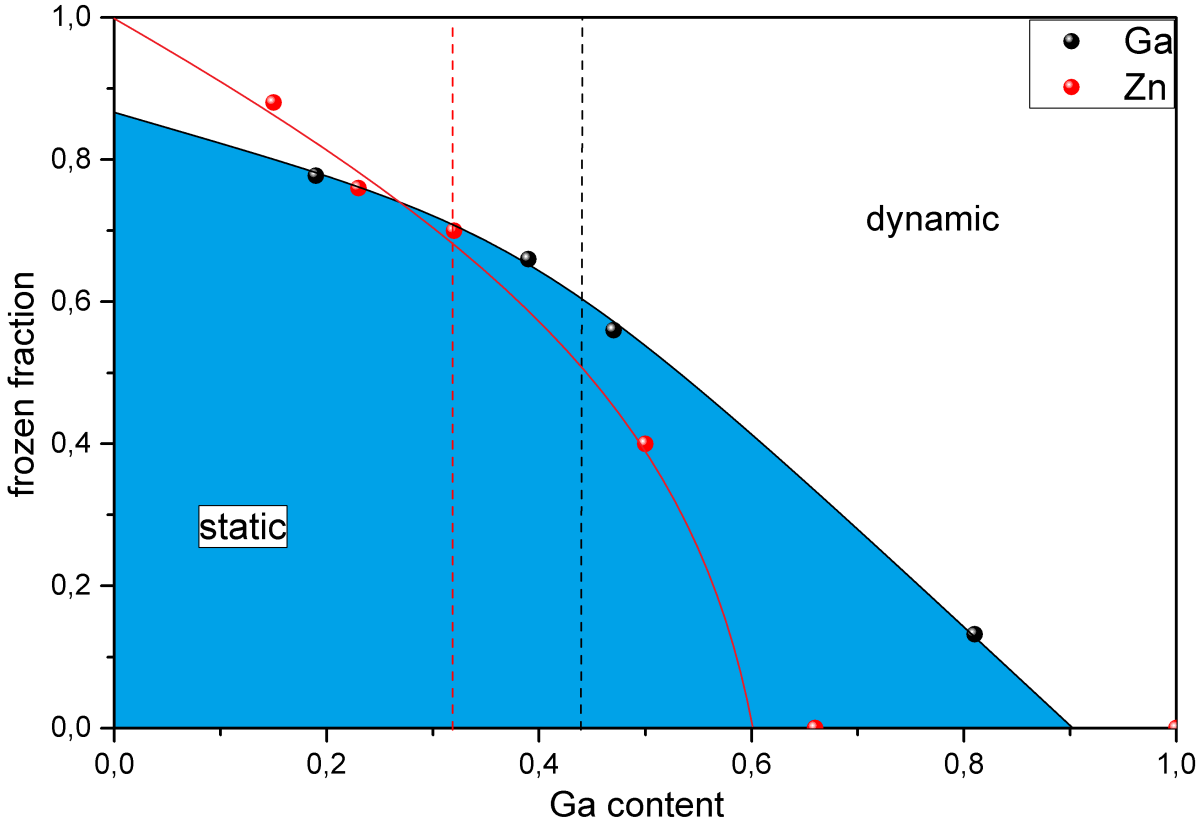

Figure 5.13: The estimated phase diagram of the magnetic/ frozen fraction versus the substitution content for $Ga_xCu_{4-x}(OD)_6Cl_2$ (black) compared to Zn substitution (red) is shown. A line was drawn which seperates the static ordered phase in blue from the dynamic spin-fluctuating one. The structural transition from clinoatacamite to paratacamite is marked by a dotted vertical line.

5.1.8 Electron doping

The main interest to understand the properties of this compound is whether there is some additional free charge compared to herbertsmithite, since if we assume the simple oxidation states of ionic bonding we get $Ga^{III}Cu_3^{II}(OH)_6^{-I}Cl_2^{-I}$ resulting in a negative charge. Resistance measurements with a Keithley multimeter show that the compound has strong isolating behaviour of several GΩ, which is also reflected in its green color. Since this result disagrees with the theoretical proposal, for $x = 1$: $GaCu_3(OH)_6Cl_2$ it is unclear where the additional electron of the threevalent Ga goes.

The charge might be balanced by a monovalent Cu^{+1} for each Ga^{3+}. If Ga goes on the Cu1 position between the kagome planes and the Cu^{1+} is formed on the neighbouring Cu1 sites the suppression of the order would be already for lower substitution values since Cu^{1+} is nonmagnetic. This is not the case since we see a slower decrease, meaning a suppression for higher x values than in Zn (see chapter 5.1.7). Additionally substitution amounts above $x = 0.5$ would have to go on the kagome plane. For this Ga^{3+} with Cu^{1+} formation for0.5¡x¡1 the order would be definately surpressed since we get either a two dimensinal (2D) or for $x = 1$ even a 1D system, such as $ZnCu(OH)_3Cl$ (see table 5.2) and perfect low dimensional systems, such as $BaCuSi_2O_6$ of the previous chapter, show no order. For $x > 0.5$ Cu^{1+} formation would have to be directly on the kagome plane resulting in a release of frustration. But in our experiment we see an increase in Θ_W, so an increasing magnetic coupling and frustration in contrast to this hypothesis.

Or it could be balanced by defect formation on the Ga site. This scenario is supported by the fact that in most EDX images the Ga content is lower than the ratio to Cu-Cl-O would incline, but it is in strong contrast to the fact that we still see order in the 1.0 M sample, since in herbertsmithite at $x = 0.8$ the order should already be suppressed and with defects on the Cu1 site less substitution would be necessary to expel Cu on the Cu1 position between the kagome layers. Furthermore in this case a broad NMR line would be the result, but the NMR lines show good full width at half maximum (FWHM) values.

Most possibly the additional electron could be bound to additional Cl or OH atoms, but we did not observe enhanced Cl values in the EDX analysis as in $Y_3Cu_9(OH)_{19}Cl_8$ and $YCu_3(OH)_6Cl_3$ [60] (see next chapter). The O content is close to the resolution edge of the EDX-detector and thus cannot be excluded with this method, however the given average values do not indicate an increase.

A different possible scenario would be an additional Ga position on the Cu1 site between the kagome layers, where additional Ga-Ga bondings balance the charge. This yields a lot of difficulties in the oxide coordination, but results only in an increase in the necessary substitution amount to suppress the order and thus would be a reasonable explanation.

The possibility of partial formation of Ga^{1+} is the last possible scenario. This is a rare scenario but can be found in Gallium dichloride Ga(I)Ga(III)Cl_4 and would explain the difficult and limited phase formation. But here the necessary amount of substitution should be the same as for Zn.

The last two scenarios cannot be excluded by our data and thus are possible candidates. Generally however the simple oxidation state picture of ionic bonding might not be the right image for this complex additionally covalent bound system as for $Y_3Cu_9O(OH)_{18}Cl_8$ and $YBa_2Cu_3O_7$.

5.1.9 Discussion

All measurements show a good agreement, that the amount of frozen spins slowly reduces with increasing substitution. A comparison of the remanence M_r, area of hysteresis A_χ, entropy S_{order} and maximum of specific heat C_{max} and their resulting frozen spin fractions is given in table 5.5. The index 0 M of these quantities denotes the value of the 0.0 M batch.

batch	0.0 M	0.1 M	0.7 M	1.0 M
substitution x (EDX)	0.00(0)	0.09(6)	0.47(8)	0.8(1)
M_r [μ_B/mol]	0.1554	0.1351	0.0802	0.0147
$M_r/M_r^{0\,\mathrm{M}}$ [%]	100	87	52	9
A_χ [$\mu_B K$/mol]	4147	1468	2120	440
$A/A_{0\,\mathrm{M}}$ [%]	100	35	15	11
S_{order} [J/molK^2]	2.82	1.65	0.43	0.13
$S/S_{0\,\mathrm{M}}$ [%]	100	56	15	5
C_{max} [J/(molK)]	10.4	7.9	3.0	1.6
$C/C_{0\,\mathrm{M}}$ [%]	100	72	29	15
magnetic fraction μ−SR [%]	100	~ 82	51	13

Table 5.5: Summary of the results of the previous chapters on the frozen/ magnetic fraction.

The μ−SR measurement gives a direct access to the magnetic fraction and thus should be taken more serious than the other values, but in general we can definately prove a continous suppression of the frozen fraction resulting in $Ga_xCu_{4-x}(OD)_6Cl_2$ to be an interesting frustrated quantum spin system to understand the effect of electron doping.

5.1.10 Conclusion

In conclusion, $Ga_xCu_{4-x}(OD)_6Cl_2$ for $x \leq 0.8$ is no dirac metal. In contrast it is a disordered quantum kagome spin system with similar properties as $Zn_xCu_{4-x}(OD)_6Cl_2$. The phase formation at low temperatures, leaves struggles and prevents the same crystal growth as for herbertsmithite. Powder samples can be obtained by reflux synthesis but no single crystal could be extracted. The green compound is a mott isolator, so the additional electron of the Ga seems to be compensated. The decrease of the Néel ordering amount observed in $Zn_xCu_{4-x}(OD)_6Cl_2$ is reproduced with Ga, but the general effect of Ga compared to Zn is lower on both the Curie-Weiss temperature as well as the suppression. The highest substitution amount is $x = 0.8$, however locally $x = 1$ substitution amounts could be reached. We observe variations of substitution within one batch in EDX, which could be caused by the height variations in the powder samples since no single crystal could be obtained for a detailed view, or more likely by varying antisite disorder between the Ga and Cu positions. Summed up $Ga_xCu_{4-x}(OD)_6Cl_2$ proves that electron doping by substitution is not an easy experimental task.

Outlook: Resonant X-ray diffraction gives the possibility to resolve the Ga position in this structure, which however requires better sample quality regarding phase purity and crystallinity. Furthermore nuclear magnetic resonance (NQR) measurements will be performed by Michael Baenitz in Dresden and might exclude/ proof wether there is Cu^{1+} present.

5.2 $Y_3Cu_9(OH)_{19}Cl_8$ and $YCu_3(OH)_6Cl_3$

The majority of the results of this chapters were published in a Journal of Materials Chemistry C article [60].

5.2.1 Introduction

In 2016, W. Sun et al. reported on a non-hydrothermal synthesis of $YCu_3(OH)_6Cl_3$ with LiOH and LiCl as pH regulating additives [56], enclosed in an autoclave to trap the crystal water. The reported structure is $P\bar{3}m1$ with one crystallographic copper position revealing a perfect two-dimensional kagome lattice. The determined crystal structure is more reminiscent to what was found in kapellasite, a structural polymorph of herbertsmithite [49]. They also show with Rietveld refinement of X-ray diffraction (XRD) data and magic angle spinning nuclear magnetic resonance (MAS-NMR) that there is no significant Y - Cu exchange. In magnetic measurements on polycrystalline samples with small amounts of impurity phases Sun et al. see no magnetic order down to 2 K. The authors report that the absence of free water in the starting mixtures has been proven to be a key factor in the formation (and preservation) of this structural variant.

In a different synthesis procedure of the Y-Cu-OH-Cl system we obtain single crystals of $Y_3Cu_9(OH)_{19}Cl_8$ from the hydrothermal method. For $Y_3Cu_9(OH)_{19}Cl_8$, we find $R\bar{3}$ as the resulting structure with two distinct copper positions and two fully occupied yttrium positions. As a consequence $Y_3Cu_9(OH)_{19}Cl_8$ presents the stoichiometric case of a slightly distorted kagome system, leading to the stabilization of magnetic order at $T_N = 2.2\,K$ but a large portion of the spin degrees of freedom remain fluctuating. Therefore, $Y_3Cu_9(OH)_{19}Cl_8$ and $YCu_3(OH)_6Cl_3$ are ideal systems to investigate the change of a spin-liquid state to a strongly frustrated AFM ordered state, by slightly releasing the frustration in a kagome lattice.

5.2.2 Synthesis of $Y_3Cu_9(OH)_{19}Cl_8$

In an attempt to form the theoretically proposed $YCu_3(OH)_6Cl_2$ similar to $GaCu_3(OH)_6Cl_2$ with the hydrothermal method, we found the new phase $Y_3Cu_9(OH)_{19}Cl_8$ with a unique structure seen in PXRD. The crystals have blue to green colour and a hexagonal shape, typical sizes are up to 1 x 1 x 0.25 mm^3. An optimization of the profile led to the following recipe where single crystals of $Y_3Cu_9(OH)_{19}Cl_8$ were prepared in the hydrothermal Parr 4625 autoclave shown in figure 1.4 a) (note the experimental advice). For the crystallization, we placed duran glass ampules filled with the solution in the autoclave and filled it with distilled water to ensure the same pressure as in the ampules. The ampules were loaded with 0.59 g Y_2O_3, 0.82 g CuO, 0.89 g $CuCl_2 \cdot 2\,(H_2O)$ and 10 ml distilled water and then sealed at air. The autoclave was heated up to 270°C in four hours and subsequently cooled down to 260°C with 0.05 K/h, followed by a fast cooling to room temperature. Afterwards, the ampules were opened and the content was filtered with distilled water, yielding some clinoatacamite and $Y_3Cu_9(OH)_{19}Cl_8$ single crystals and a closely sintered pallet on the ground.

Other growth attempts

Unlike in the synthesis of the similar compounds (herbertsmithite, $MgCu_3(OH)_6Cl_2$ tondiite [61], and $CdCu_3(OH)_6Cl_2$ [62]) there is no need to use excess Y in the growth, since the Y_2O_3 can easily be solved in chloridic solutions [63]. Attempts with an excess of YCl_3

in the solution in fact lead to a formation of $Y(OH)_3$. All changes either with pH tuning and or of the starting compounds (NaOH, YCl_3, $Cu_2(OH)_3CO_3$) led to worse results since the growth happens when the oxides are slowly solved and thus the pH value has to be nearly neutral. A recrystalisation of $Y_3Cu_9(OH)_{19}Cl_8$ with an external gradient provides difficulties due to two reasons: The recrystalisation has to be done in water since as mentioned above YCl_3 leads to $Y(OH)_3$ formation, but pure water enables the crystalisation of clinoatacamite. The high solving temperature cannot be realized with thick quartz ampules and lower temperatures (up to 220 °C) mainly cause the formation of clinoatacamite $Cu_2(OH)_3Cl$ single crystals at the tip, but some $Y_3Cu_9(OH)_{19}Cl_8$ crystals form directly next to the starting powder. Even with the above described ofen profile some clinoatacamite is formed and sometimes even included in the $Y_3Cu_9(OH)_{19}Cl_8$ crystals (see figure 5.14). Yet with a gradient growth in water heated to 240°C we also get some crystals of the same size as the above described optimal synthesis. Attempts with the thin autoclave (figure 1.4 c) in a gradient of 270°C - 230°C were unsuccessful due to a loss of the gradient from the setup, since the solution is in an ampoule inside a water filled stainless steel vessel.

Generally, only the $x = 1$ stoichiometry of $Y_xCu_{4-x}(OH)_{6.33}Cl_{2.77}$ forms and we have not observed any phase with a x-value below 1, in contrast to the other compounds of this family.

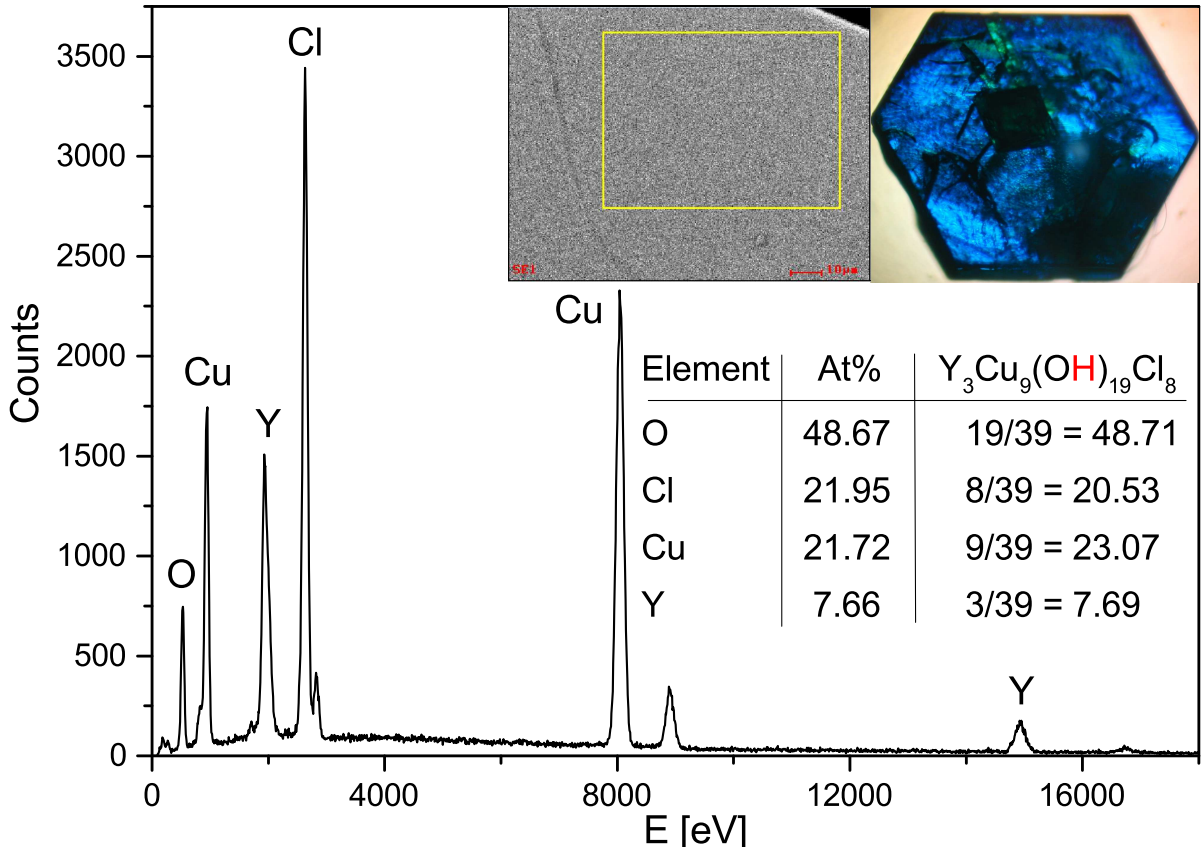

Figure 5.14: EDX analysis of a phase pure $Y_3Cu_9(OH)_{19}Cl_8$ single crystal indicating a $YCu_3(OH)_6Cl_3$ stochiometry (error $\sim$ 2 at%). The inset shows a SEM image of the measured area of the single crystal and a 1 x 1 x 0.25 mm^3 $Y_3Cu_9(OH)_{19}Cl_8$ single crystal under a polarisation microscope revealing clinoatacamite twinnings.

Crystal shape and orientation $Y_3Cu_9(OH)_{19}Cl_8$ single crystals grow dominantly as thin hexagonal plates directly revealing its structure and axis with the a = b direction along the long sides and c pointing out of the plane. Figure 5.15 shows three of the largest single crystals and their corresponding Laue images. The center point $(hkl) = (001)$ gives us the c-axis. We note again that impurity inclusions of either CuO or clinoatacamite especially in larger crystals are often the case in this kind of system, as can be seen on the images of the crystals. Thus single crystals have to be carefully selected. Since the kagome plane lies in the large area, the orientation for magnetic measurements can be don already optically.

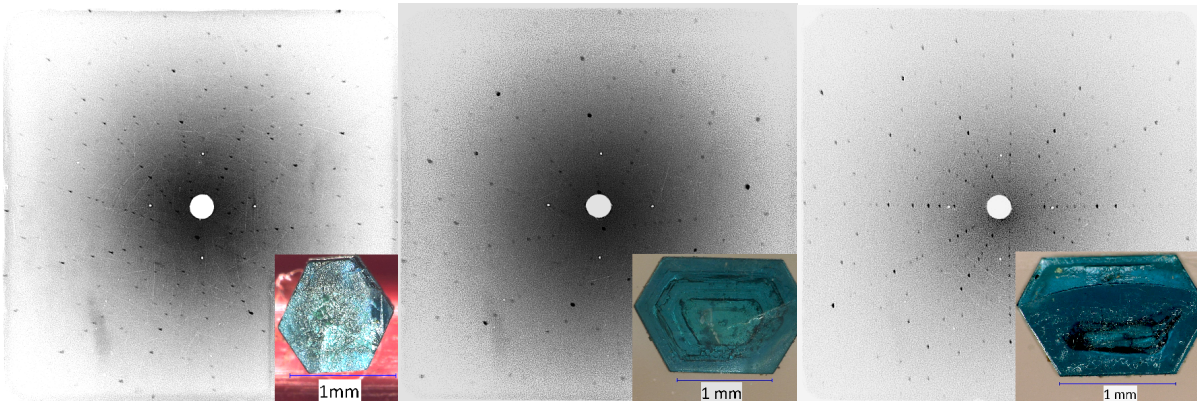

Figure 5.15: Laue diffraction images of typical $Y_3Cu_9(OH)_{19}Cl_8$ single crystals, which are shown as an inset.

$YCu_3(OH)_6Cl_3$

Furthermore to compare the magnetic ground state of the two structural variants, we have reproduced the synthesis of polycrystalline $YCu_3(OH)_6Cl_3$ with the solid state-flux method from Ref. [56], where $Y(NO_3)_3 \cdot 6H_2O$ melts at 50°C, starting to form complexes [64]. The flux of LiOH and LiCl is added to control the pH value and increase the atom mobility at enhanced temperatures. Instead of LiOH the similar NaOH of the same mole weight can be utilized to produce the sample and we found the method to work with $YCl_3 \cdot 6H_2O$ as well.

We analysed the obtained powder with laser ablation - inductively coupled plasma - mass spectrometry (LA-ICP-MS). We found only a few ppm of Lithium and could therefore exclude lithium incorporation in $YCu_3(OH)_6Cl_3$.

Another way to synthesize the $YCu_3(OH)_6Cl_3$ compound is by a real solid state sintering with the following reaction with trapped crystal water in a hydrothermal autoclave:

$$YCl_3 \cdot 3\ H_2O + 3\ CuO \overset{200°C}{\rightarrow} YCu_3(OH)_6Cl_3$$

YCl_3 normally includes six water molecules, so a drying and controlled adding of water has to be performed in advance.

In conclusion the $YCu_3(OH)_6Cl_3$ is unstable in water and will only form in a flux or from a solid state sintering.

5.2.3 Crystal structure

Michael Bolte from the Institute of Organic Chemistry of the University Frankfurt measured single crystal diffraction on a $Y_3Cu_9(OH)_{19}Cl_8$ single crystal. The data were collected at 173 K on a STOE IPDS II two-circle diffractometer with a Genix Microfocus tube with mirror optics using Mo K_α radiation ($\lambda = 0.71073$Å). The data were scaled using the frame scaling procedure in the X-AREA program system [65]. The structure was solved by direct methods using the program SHELXS [66] and refined against F^2 with full-matrix least-squares techniques using the program SHELXL-97 [66]. The H atoms bonded to O2, O3, and O4 were found in a difference map and were isotropically refined with the O-H distance restrained to 0.84(1)Å, whereas the H1 atom bonded to O1 was geometrically positioned and refined using a riding model. The crystal was twinned about (-1 0 0/1 1 0/0 0 -1) with a fractional contribution of 0.601(4) for the major domain. The space group $R\bar{3}$ was chosen, because the structure proved to be centrosymmetric (thus R3 could be excluded) and no hints for any mirror planes were detected (excluding space groups R3m and $R\bar{3}m$).

	Wyck.	x/a	y/b	z/c	U [Å^2]
Cu1	18f	0.66311(6)	0.82526(6)	0.50349(3)	0.00721(19)
Cu2	9d	0.5	1	0.5	0.0072(2)
Y1	6c	0.3333	0.6667	0.53850(4)	0.0075(2)
Y2	3b	1	1	0.5	0.0092(3)
Cl1	18f	0.66466(12)	1.00242(12)	0.61719(6)	0.0132(3)
Cl2	6c	1	1	0.33854(11)	0.0121(4)
O1	3a	0.3333	0.6667	0.6667	0.042(3)
H1	18f	0.404	0.7382	0.6561	0.063
O2	18f	0.8113(4)	0.8026(4)	0.54394(18)	0.0079(7)
H2	18f	0.813(6)	0.801(7)	0.5927(7)	0.012
O3	18f	0.5308(4)	0.6623(5)	0.55719(18)	0.0086(6)
H3	18f	0.555(6)	0.654(7)	0.6018(15)	0.013
O4	18f	0.5089(4)	0.8403(4)	0.46536(18)	0.0070(6)
H4	18f	0.492(6)	0.818(6)	0.4185(11)	0.011

Table 5.6: Crystal structure parameters of $Y_3Cu_9(OH)_{19}Cl_8$ refined from X-ray single crystal diffraction data measured at 173 K. Space group $R\bar{3}$ (# 148). The unit cell parameters are $a = b = 11.5350(8)$ Å and $c = 17.2148(12)$ Å. All positions are fully occupied except H1, which has an occupancy of 1/6.

The crystal structure of $Y_3Cu_9(OH)_{19}Cl_8$ is different from the theoretically proposed structure for electron-doped herbertsmithite [54] as well as the structure reported by [56]. The additional electron from yttrium is bound with additional Cl^-/ OH^- anions, so electron doping of herbertsmithite was not successful in this structure. In agreement with Ref. [57], the Y-atoms are not incorporated into the interlayer site but in the kagome layer. Thus, $Y_3Cu_9(OH)_{19}Cl_8$ consists of repeating kagome layers. The distances between the Cu atoms are 3.2498 Å/3.3683 Å/3.3762 Å within the layer and 5.8607 Å/ 5.6788Å between the layers. In comparison, herbertsmithite has Cu distances of 3.416 Å and 5.087 Å [53]. In Figure 5.16, the obtained crystal structure of $Y_3Cu_9(OH)_{19}Cl_8$ is shown. A comparison of the two similar structures can be made from Figure 5.16 b) and c). In contrast to $Y_3Cu_9(OH)_{19}Cl_{83}$, the $P\bar{3}m1$ structure has a partial disorder, for the two unequal Y positions, displayed as white parts of the sphere. The full occupancy of these two crystallographic Y positions in $Y_3Cu_9(OH)_{19}Cl_8$ causes the Cu-atoms to be slightly misaligned from a perfect plane. W. Sun et al. observed an increasing occupation of

these disordered yttrium-atoms with decreasing temperature showing a tendency to the R$\bar{3}$ structure when lowering the temperature [56].

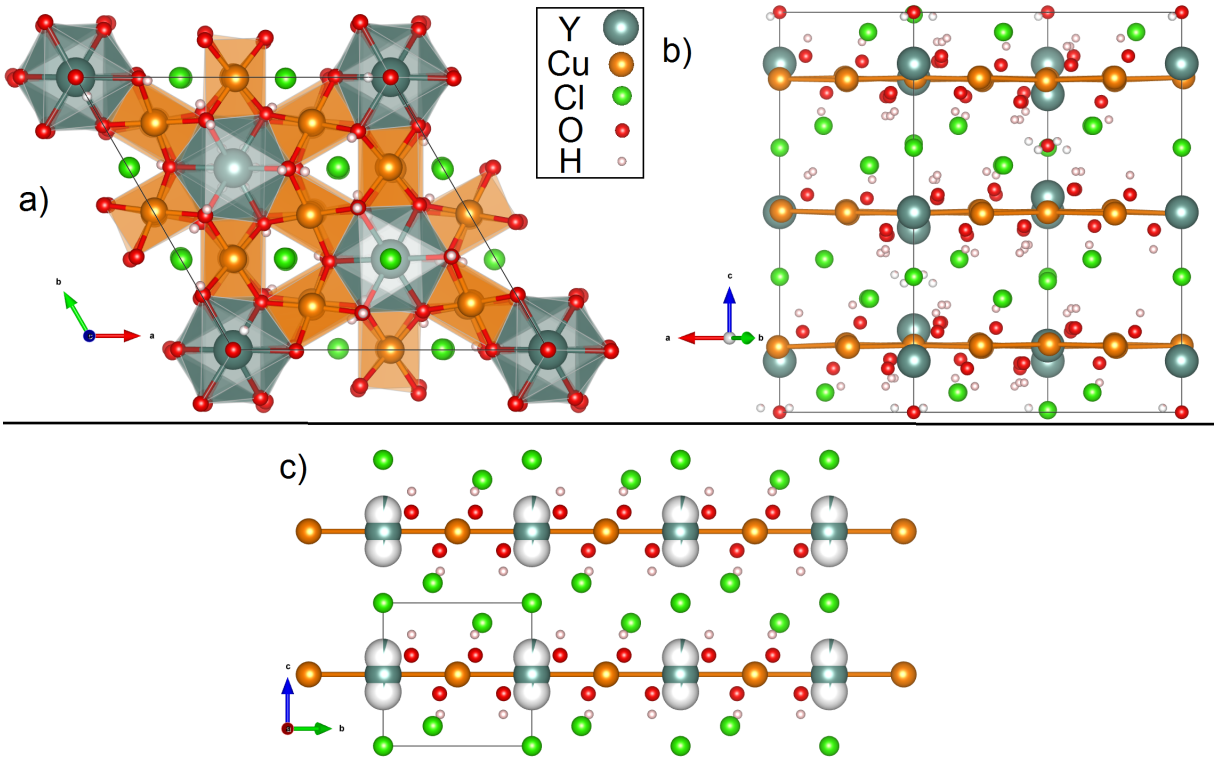

Figure 5.16: Structure model of $Y_3Cu_9(OH)_{19}Cl_8$(a,b) in comparison to $YCu_3(OH)_6Cl_3$ (c). a) Top view of the kagome layer in $Y_3Cu_9(OH)_{19}Cl_8$ crystallizing in the R$\bar{3}$ structure. b) Side view of the kagome layer in $Y_3Cu_9(OH)_{19}Cl_8$ stacked along the c-direction, where the slight buckling of the Cu-atoms due to two crystallographic positions is apparent. c) Side view of the kagome layer in $YCu_3(OH)_6Cl_3$ with the P$\bar{3}$m1 structure type [56] with a partially filled second position of Y.

A refinement plot based on the neutron powder diffraction data, at room temperature taken on 1 g of $Y_3Cu_9(OH)_{19}Cl_8$ is shown in Figure 5.17. The structure concept was obtained by the above described single crystal X-ray data and the refinement of the neutron data confirmed that structure solution. A small amount of unreacted CuO and $Cu_2(OH)_3Cl$ was observed in the large powder sample which formed due to the off-stoichiometric synthesis conditions. The unaccounted reflex part at 37° can also be ascribed to some impurity phase.

It should be noted, that neutron scattering lengths of Y and Cu are in fact very close to each other: 7.75 and 7.718 fm, which makes them practically indistinguishable in neutron refinements. We therefore concluded the stoichiometric ordering without sizable Y-Cu site exchange from the single-crystal X-ray refinement. There, the scattering cross sections for Y ($Z = 39$) and Cu ($Z = 29$) are sufficiently different.

We have used X-ray diffraction to prove the ideal cation order of the Y and Cu, and neutron diffraction to identify and precisely refine the positions of the hydrogen atoms in the structure, since the scattering contrast of hydrogen is sufficiently high in neutron diffraction (scattering length is negative, $b_H = -3.739$ fm, as opposed to +7.75, +7.718, +5.803, and +9.577 fm for Y, Cu, O, and Cl, correspondingly), which allowed for a refinement of the atomic positions of hydrogen in the structure. Using a sample produced with chemicals containing natural hydrogen (and not deuterium, as usually done for a neutron diffraction study) did of course condition a rather high background of incoherent

scattering in the pattern, thus a longer acquisition time was needed to achieve sufficient statistics for a reliable refinement. We note that using a third Cl place instead of the proposed O1 and H1 places would lead to the stoichiometry $YCu_3(OH)_6Cl_3$ similar to the structure of Ref. [56]. Neutron refinement indicates the absence of the H1 atom, thus only fully occupied O1, the result will be discussed later and we refined here first with the structure obtained by single crystal diffraction.

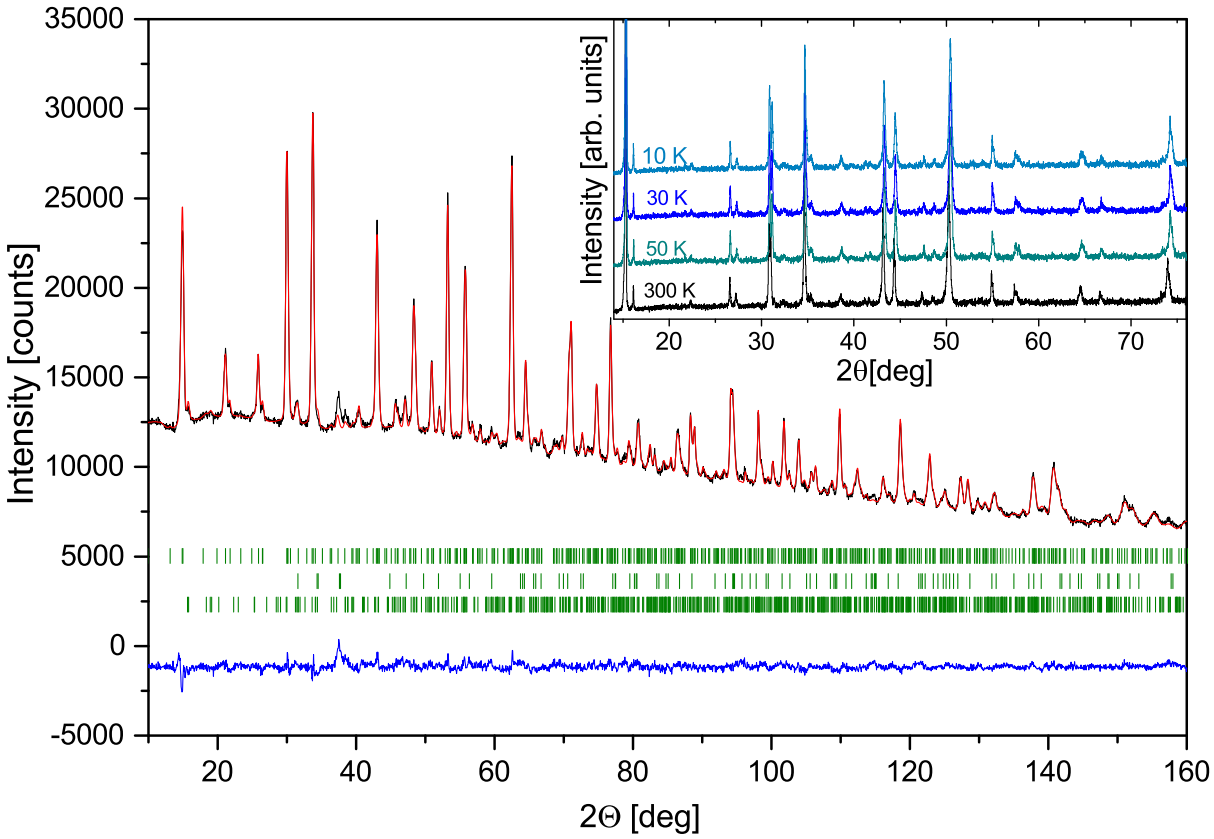

Figure 5.17: Rietveld refinement of the crystal structure parameters from neutron powder diffraction data measured at $T = 295\,\mathrm{K}$ with a wavelength of $\lambda = 1.494$Å at HRPT. The observed intensity (black), calculated profile (red), and difference curve (blue) are shown of a powder sample. The rows of ticks at the bottom correspond to the calculated diffraction peak positions of the phases (from top to bottom): $Y_3Cu_9(OH)_{19}Cl_8$, CuO 2.5(2) wt%. and $Cu_2(OH)_3Cl$ 5.8(2) wt%. Inset: Low-temperature powder X-ray diffraction at different temperatures.

The phase stability of $Y_3Cu_9(OH)_{19}Cl_8$ at various temperatures was investigated using powder X-ray diffraction (PXRD) data at 10 K - 300 K in 20 K steps. The inset in Fig. 5.17 reveals that no structural phase transition could be resolved down to 10 K.

The two structure types are further compared in Fig. 5.18, where we present PXRD data of the two Y-Cu-OH-Cl compounds. For that we have reproduced the synthesis method of Ref. [56]. From Fig. 5.18 it is obvious, that a discrimination between the two compounds can be easily done using PXRD.

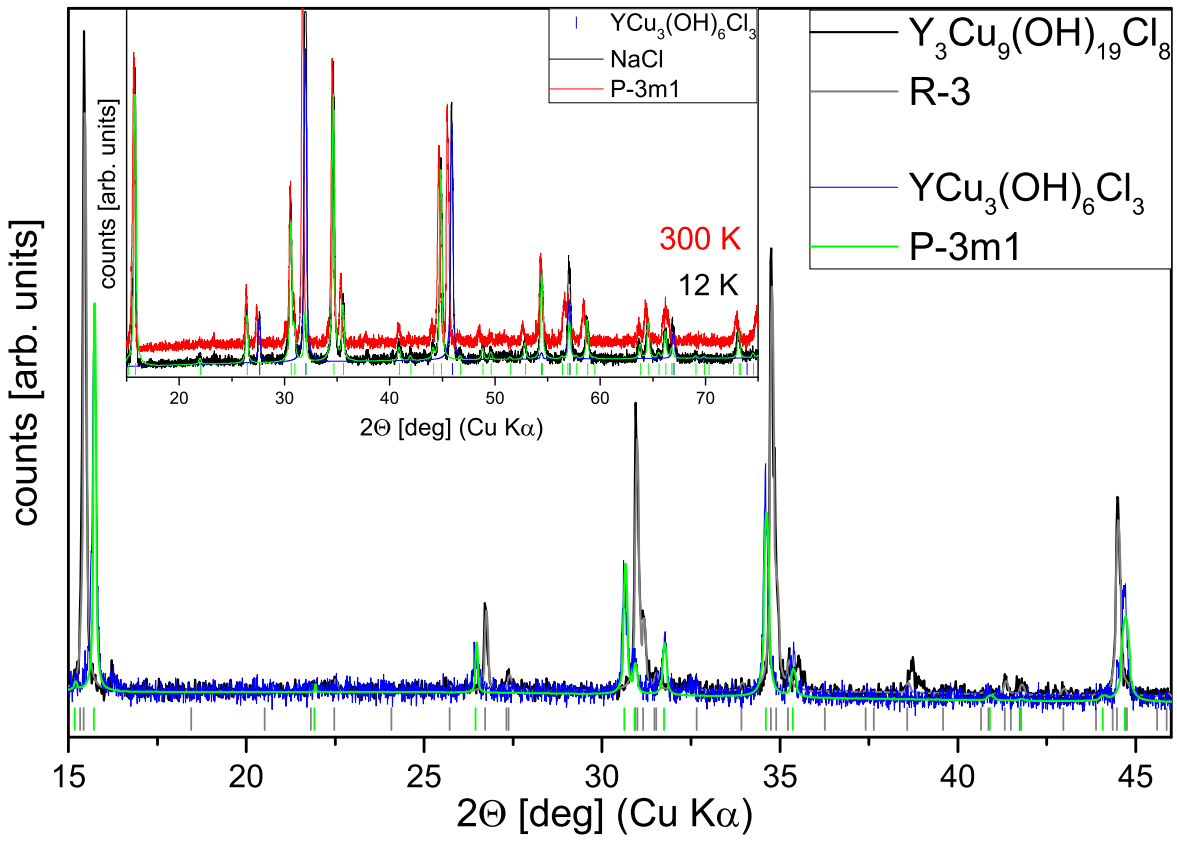

Figure 5.18: Powder X-ray diffraction data of the hydrothermally grown $Y_3Cu_9(OH)_{19}Cl_8$ (black) with an underlying refinement of the R$\bar{3}$ structure (gray) compared to the diffraction of a $YCu_3(OH)_6Cl_3$ sample (blue) with the P$\bar{3}$m1 structure refinement (green). The inset shows a comparison of powder X-ray diffraction data of the $YCu_3(OH)_6Cl_3$ sample (red) at room temperature and 12 K (black) with the P$\bar{3}$m1 structure refinement (green) and NaCl (blue).

$YCu_3(OH)_6Cl_3$ shows no structural phase transition at least down to 12 K as we observed with low temperature PXRD the same P$\bar{3}$m1 structure. The inset of figure 5.18 shows both the room temperature as well as the low temperature diffraction, with a underlying refinement for the latter. The sample was not sufficiently washed with ethanol and thus still contains some NaCl from the flux. Note the strong thermal expansion difference between NaCl and $YCu_3(OH)_6Cl_3$ seen in the position change of the corresponding reflexes (e.g 30.5 and 32°) between 300 and 12 K.

Deuterated powder samples of $Y_3Cu_9(OH)_{19}Cl_8$ were prepared using 1.1g YCl_3, 0.787g CuO and 4 ml D_2O heated to 220 °C for seven days in a reaction vessel shown in figure 1.4 for a neutron diffraction experiment to clear the doubts about the H1 atom. The neutron diffraction data reveals less background noise as expected for deuterium instead of hydrogen, resulting in an improved refinement. We measured with long counting rates both at 1.7 and 298 K. The refinement of this data shown in figure 5.19 proves that there is no deuterium next to O1 resulting in the effective sum formula $Y_3Cu_9O(OH)_{18}Cl_8$. For a simple ionic crystal $Y_3^{3+}Cu_9^{2+}O^{-2}(OH)_{18}^{-1}Cl_8^{-1}$ this would mean a negative oxidation number and thus a negative charge. But a possible explanation lies within the failure to describe a partially covalently bound crystal with the perfect ionic bonding image, also known in the yttrium barium cuprates [67]. Due to consistency with the published results and since it has no influence on the magnetism of the compound in this thesis it will still be referred to as $Y_3Cu_9(OH)_{19}Cl_8$.

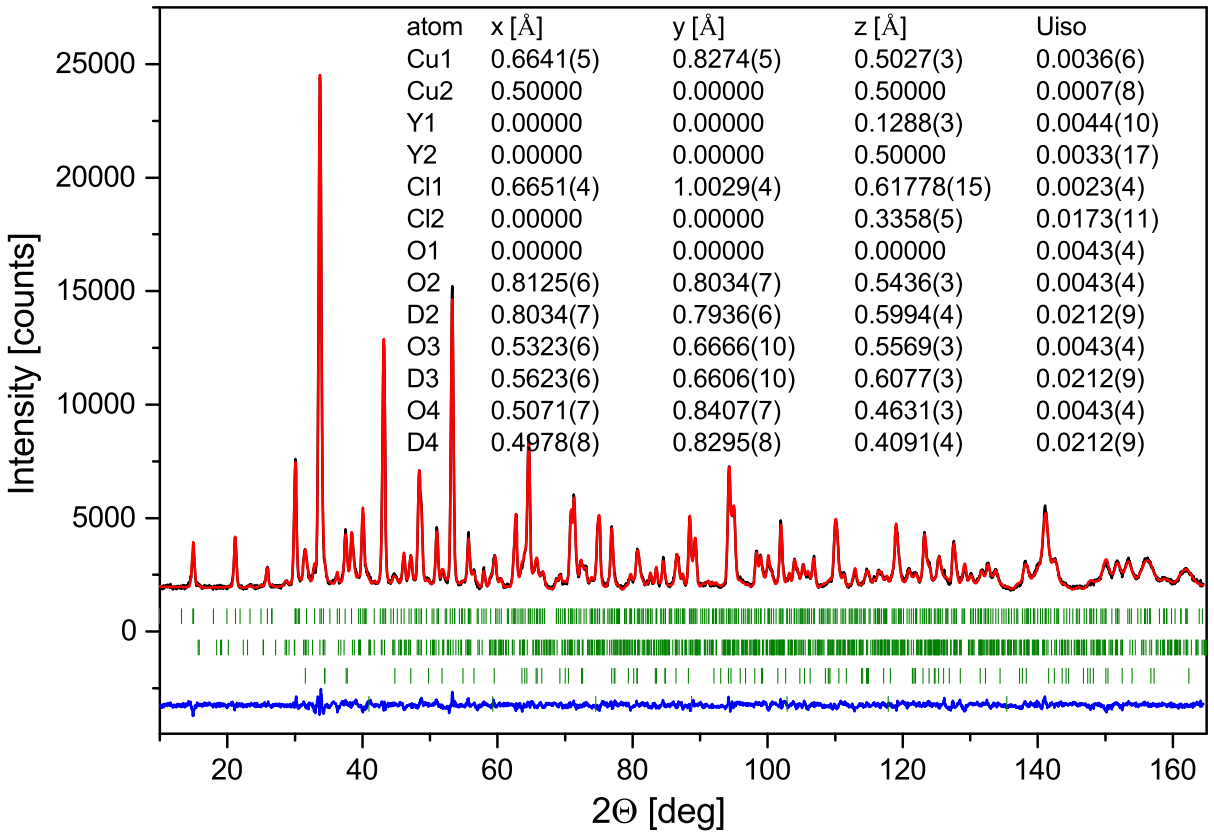

Figure 5.19: Rietveld refinement of the crystal structure parameters from neutron powder diffraction data measured by Denis Sheptyakov at $T = 1.7\,\mathrm{K}$ with a wavelength of $\lambda = 1.494$Å at HRPT. The observed intensity (black), calculated profile (red), and difference curve (blue) are shown of a powder sample. The rows of ticks at the bottom correspond to the calculated diffraction peak positions of the phases (from top to bottom): $Y_3Cu_9(OH)_{19}Cl_8$, $Cu_2(OH)_3Cl$ 6.8(2) wt%, CuO 14.9(1) wt% and . Inset: structural table of the obtained atomic positions and thermal expansion parameters.

5.2.4 Magnetic susceptibility

In Fig. 5.20, we present the inverse susceptibility of $Y_3Cu_9(OH)_{19}Cl_8$ measured on a single crystal for two different directions of the magnetic field. In the temperature range 100-300 K, a clear Curie-Weiss behaviour is observed with a large negative Weiss temperature of $\Theta_W = -100\,\mathrm{K}$ for fields perpendicular to the kagome plane indicating a strongly antiferromagnetic mean-exchange field. The effective moment for a magnetic field applied perpendicular to the kagome plane is $\mu_{eff} \approx 2.07\,\mu_B/\mathrm{Cu}$ resulting in a Landé factor of $g \approx 2.39$, assuming a simple $J = S = 1/2$ coupling system, typical for Cu^{2+}. For fields in the kagome plane, the Curie-Weiss fit yields: $\mu_{eff} \approx 1.89\,\mu_B/\mathrm{Cu}$, $\Theta_W = -86\,\mathrm{K}$ and $g \approx 2.18$. The leading exchange coupling is most likely within the kagome plane, as the interplane-Cu-Cu distances are much longer compared to the inplane distances. The Weiss temperatures of $Y_3Cu_9(OH)_{19}Cl_8$ are quite similar to the results of W. Sun et al. for magnetic measurements on powders of $YCu_3(OH)_6Cl_3$ with $\Theta_W = -99.2\,\mathrm{K}$ [56] indicating, that the leading exchange couplings in the two Y-Cu-OH-Cl kagome systems are rather similar.

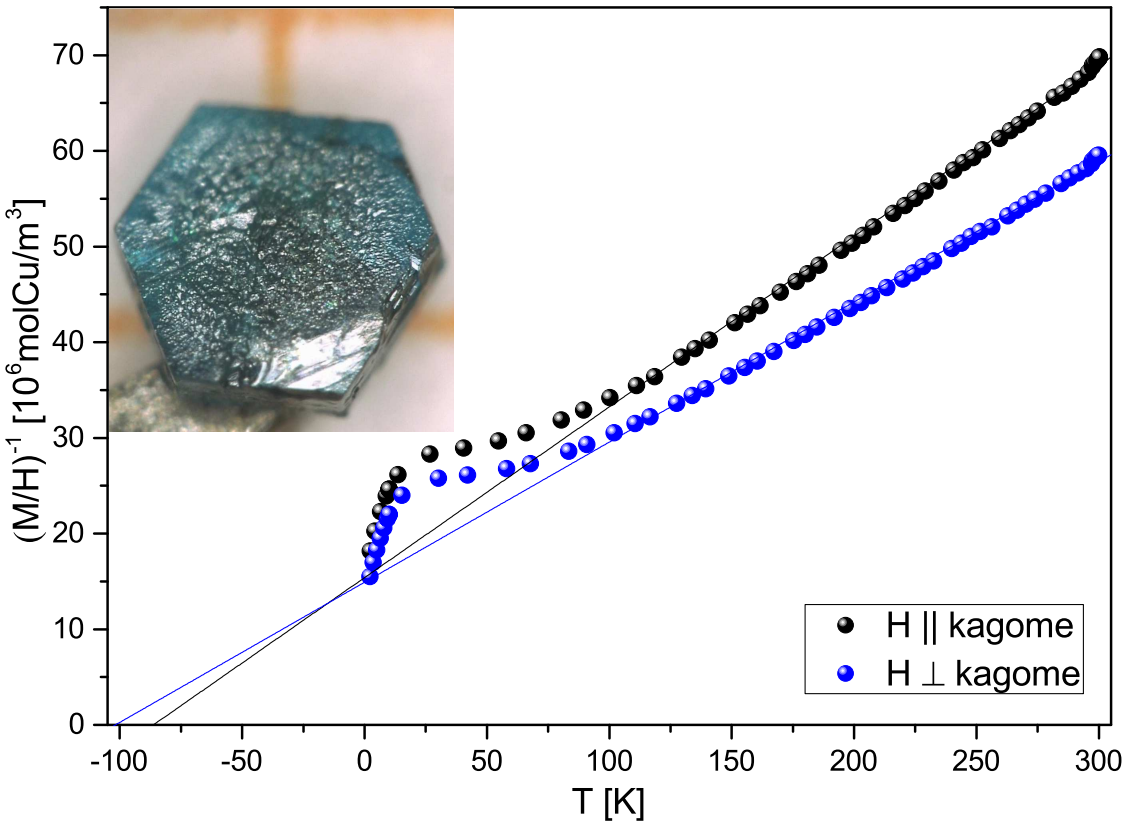

Figure 5.20: Inverse magnetization of a $Y_3Cu_9(OH)_{19}Cl_8$ single crystal ($m = 1.34$ mg) in SI units for the two field-directions, parallel and perpendicular to the kagome layers at $H = 1$ T from 300 to 1.8 K. A linear Curie-Weiss fit was done at high temperatures (lines). The image in the inset shows a picture of a 1 x 1 x 0.15 mm^3 sized crystal with a mass of 1 mg.

We observe a magnetic transition in phase pure crystals in a broad maximum at 2.5 K (see Fig. 5.21). This broad transition is in contrast to the well-defined anomaly in the specific-heat measurements (see figure 5.22) and might be due to a large magnetic background because of enhanced spin-fluctuations of that material. The magnetization is larger for magnetic fields applied perpendicular to the kagome planes, but the overall magnetic anisotropy is weak. The $M(H)$ curve perpendicular to the field (inset of Fig.

5.21) shows a nearly linear increase, while the parallel one has a small kink above 2 T. This might be related to the field induced shoulder observed in the specific heat data. Both $M(H)$ curves show no saturation up to 9 T. In comparison with herbertsmithite, the magnetic anisotropy in $Y_3Cu_9(OH)_{19}Cl_8$ is stronger but also favors the c-direction as the easy magnetic axis [4]. The value of 0.029/ 0.035 μ_B per Cu^{2+} for fields of 5 T parrallel/perpendicular to the kagome plane can be compared to that of $YCu_3(OH)_6Cl_3$ with 0.051 μ_B per Cu^{2+} indicating less free PM spins of Cu ions in our single crystals.

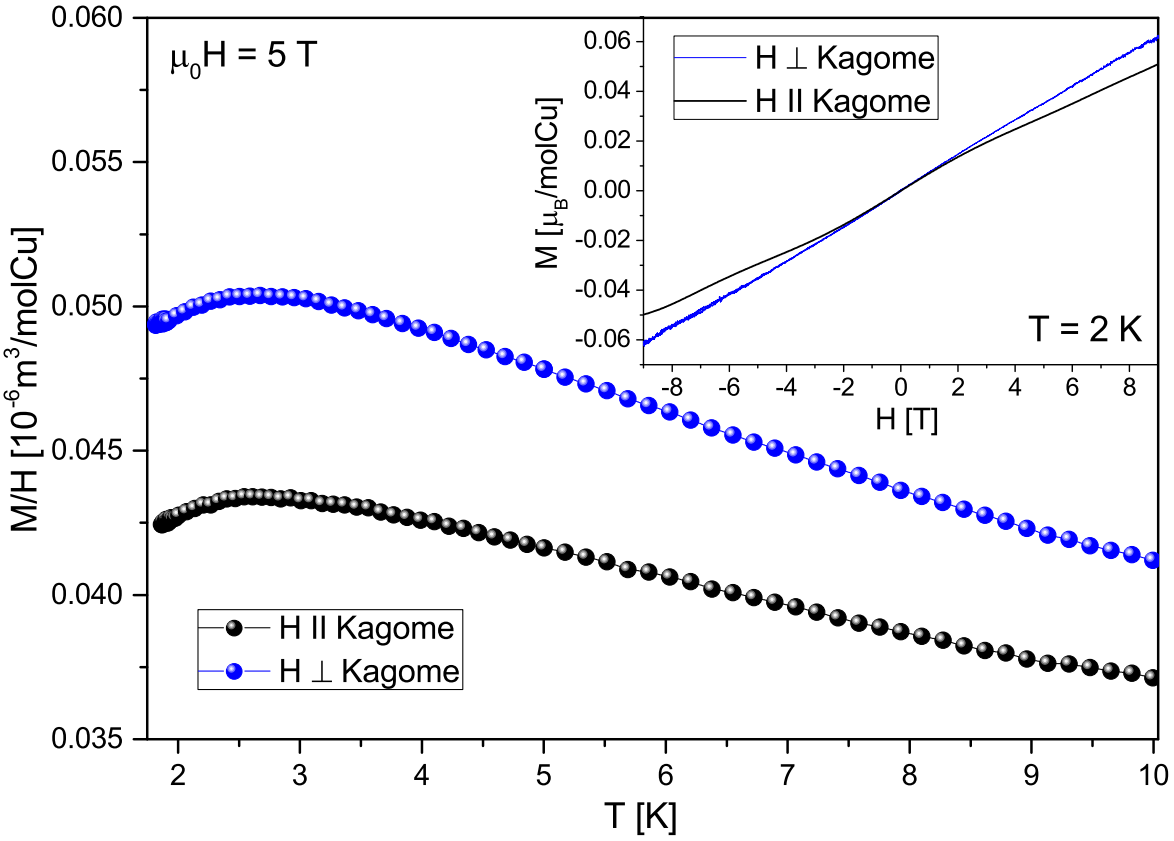

Figure 5.21: Molar susceptibility of a $Y_3Cu_9(OH)_{19}Cl_8$ single crystal measured at 5 T from T = 10 K to 1.8 K. Inset: the magnetization versus field curve measured at 2 K along and perpendicular to the kagome layers.

5.2.5 Specific heat

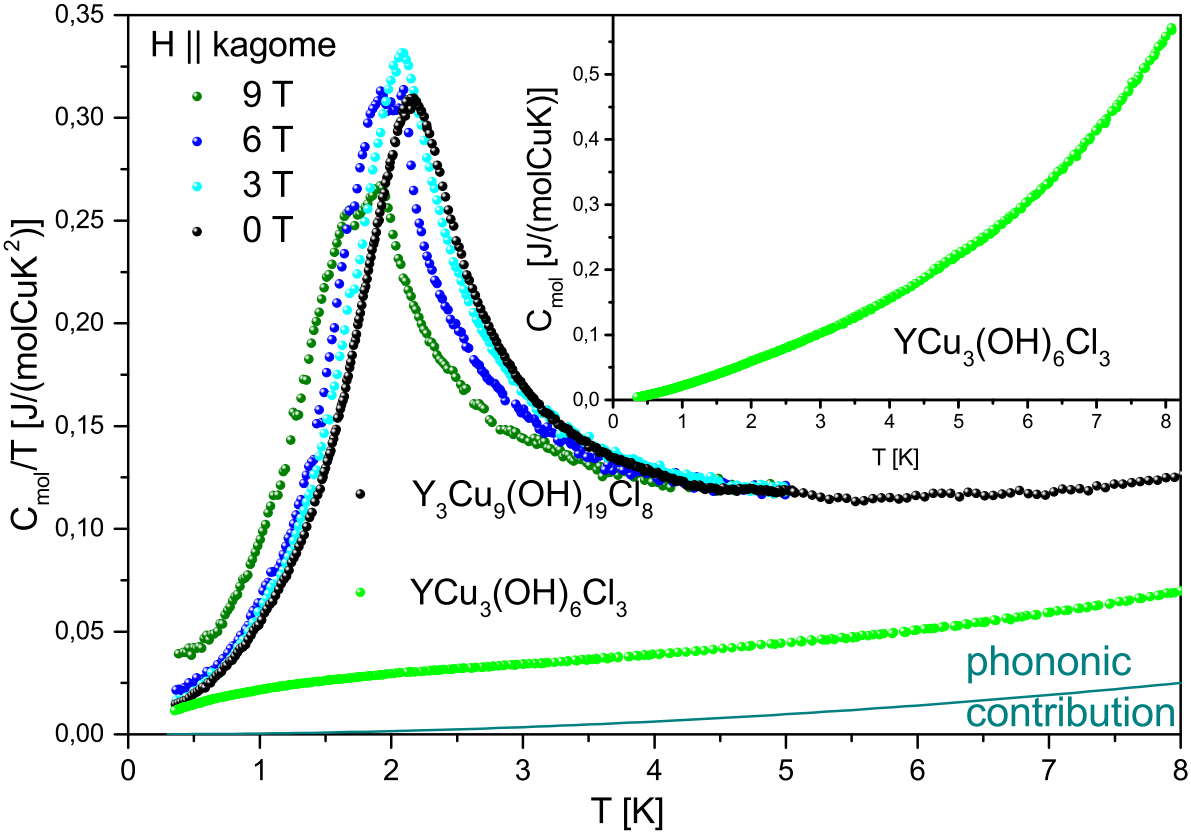

Figure 5.22: Specific-heat divided by temperature at various magnetic fields of an clinoatacamite-free $Y_3Cu_9(OH)_{19}Cl_8$ single crystal and an $YCu_3(OH)_6Cl_3$ powder sample with the $P\bar{3}m1$ structure. In the inset, the zero field curve of $YCu_3(OH)_6Cl_3$ is enlarged and it is apparent, that no long-range magnetic order occurs in the investigated temperature range.

Michael Baenitz measured specific-heat on $Y_3Cu_9(OH)_{19}Cl_8$ single crystals in the temperature range from 0.35 to 270 K on a ^{3}He PPMS. While all powder samples contain small amounts of clinoatacamite only some crystals have clinoatacamite twinnings on their surface leading to an anomaly at 6.5 K from the magnetic ordering of this impurity phase [68, 50]. The phase stability of $Y_3Cu_9(OH)_{19}Cl_8$ is close to that of clinoatacamite and always both phases are formed if the hydrothermal growth conditions are applied that are described above. In magnetic measurements, the impurity contribution can even dominate the signal and we have taken great care to select a crystal without this impurity phase. In Fig. 5.22, the temperature and magnetic-field dependent specific heat of a single crystal without any impurity phase is shown. In zero field (black curve) a maximum is apparent at around 2.2 K. This maximum is slightly shifted to lower temperatures with increasing field approaching ~ 2.0 K at $\mu_0 H = 9$ T, for H parallel to the kagome layer. A small shoulder appears at the low temperature side for fields larger than 3 T. The entropy gain within the maximum in the specific heat at zero field is $S = \int_{0.3}^{4.5} \frac{C_{mol}}{T} dT \approx 0.59 \frac{J}{mol \cdot K} \approx 0.1R \cdot \ln 2$. This shows that the ordered moment of $Y_3Cu_9(OH)_{19}Cl_8$ is strongly reduced and a large portion of the spin degrees of freedom remain fluctuating. We have not subtracted any phononic contribution for the entropy analysis, because at 4 K the estimated contribution of the phonons amounts to only 5%. The phononic contribution was estimated in the range of 8 K to 26 K. The result of a linear fit (see figure 5.23) of C_{mol}/T vs T^2 gives $\gamma_0 = 0.67(2)$ J/(molK^2) and $\beta_0 = 3.38(6)$ mJ/(molK^4). This yields a Debye temperature

of $\vartheta_D \approx 321\,\mathrm{K}$. In addition, we do not observe any phase transition in the temperature range from 8 to 270 K, in agreement with the magnetic measurements and the temperature dependent PXRD. The low ordering temperature together with the large Weiss-temperature gives a frustration parameter $\Theta_W/T_N \approx 50$, proving that $Y_3Cu_9(OH)_{19}Cl_8$ is still a strongly frustrated material. Above T_N, the specific heat of $Y_3Cu_9(OH)_{19}Cl_8$ follows a linear in T-dependence up to 8 K most likely due to the enhanced spin fluctuations.

We have also measured the specific heat of a powder sample of $YCu_3(OH)_6Cl_3$ (orange curves in Fig. 5.22), which clearly shows the absence of magnetic order down to 0.4 K which is in agreement with the proposal of a spin-liquid ground state by W. Sun et al. [56]. Our low-temperature measurements enhance the lower boundary of the frustration parameter of $YCu_3(OH)_6Cl_3$ to $\Theta_W/T_N > 250$ and clearly proves the different magnetic ground states of the two Y-Cu-OH-Cl compounds. The same linear fit procedure was done for a specific heat measurement of $YCu_3(OH)_6Cl_3$ giving $\gamma_0 = 0.27(1)$ J/(molK^2), $\beta_0 = 1.22(3)$ mJ/(molK^4) and $\vartheta_D \approx 312\,\mathrm{K}$, revealing the structural similarity of these systems. Again, no phase transitions were observed up to 250 K.

A highly debated question is, wether the QSL presents a gapped or gapples behaviour in these kagome compounds [45, 69]. The observed low temperature specific heat of the perfect spin liquid candidate $YCu_3(OH)_6Cl_3$ shows a tendency to 0 at 0 K indicating a gappless spin liquid system. However lowest temperetare measurements are necessary to make a clear statement.

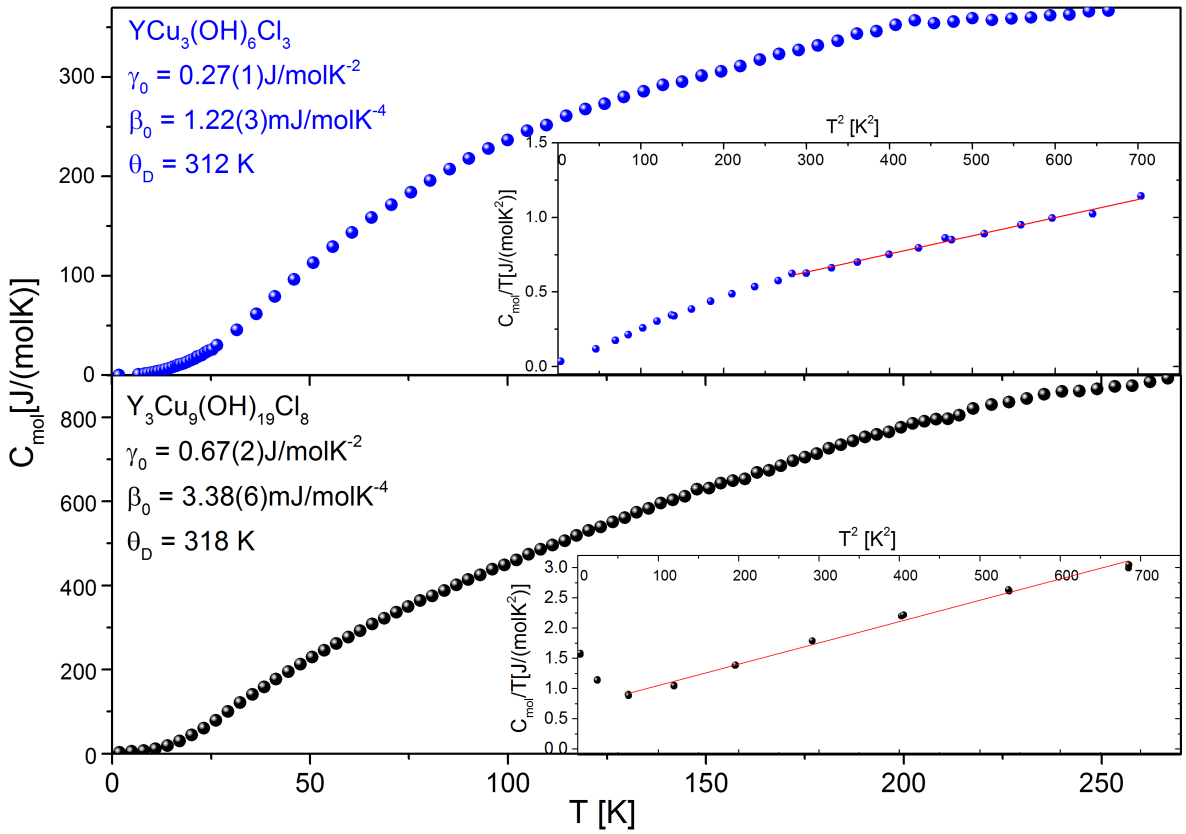

Figure 5.23: Specific-heat of an $YCu_3(OH)_6Cl_3$ powder sample with the P$\bar{3}$m1 structure and an impurity-free $Y_3Cu_9(OH)_{19}Cl_8$ single crystal. In the inset, the C/T vs. T^2 curve is shown used to estimate the phononic contribution.

5.2.6 Conclusion

In conclusion, $Y_3Cu_9(OH)_{19}Cl_8$ is a stoichiometric quantum spin system with well separated kagome layers of localized Cu^{2+} spins. Detailed structural refinements of hydrothermally prepared single crystals revealed a crystal structure with two different copper positions, leading to slightly anisotropic kagome layers. Neutron powder diffraction on deuterated $Y_3Cu_9(OH)_{19}Cl_8$ revealed that the exact stoichiometry is $Y_3Cu_9O(OH)_{18}Cl_8$.

The partial release of magnetic frustration within the kagome layers compared to $YCu_3(OH)_6Cl_3$ is also reflected in the magnetic properties, because we observe weak but clear magnetic order at $T_N = 2.2$ K in magnetization and specific-heat measurements on single crystals of $Y_3Cu_9(OH)_{19}Cl_8$. However, the frustration effects are still very pronounced with a frustration parameter of $\Theta_W/T_N \sim 50$.

Low-temperature specific-heat measurements on a powder sample of $YCu_3(OH)_6Cl_3$ revealed the absence of magnetic order down to 0.4 K, leading to a frustration parameter $\Theta_W/T_N > 250$ and indicating a gappless spin liquid due to a vanishing value for 0 K. Therefore, the two Y-Cu-OH-Cl compounds present an unique setting to investigate the change from a spin-liquid state to a strongly frustrated AFM ordered state, by slightly releasing the frustration in a kagome lattice via structural modification. Unlike for substitution series, as e.g. $Zn_xCu_{4-x}(OH)_6Cl_2$, where we always encounter crystallographic disorder, the magnetic properties of the two stochiometric compounds with fully occupied kagome sites might be much more reliable with ab-initio calculations. Additionally, these two stoichiometric kagome systems might open the way for a systematic understanding of magnetic frustration in kagome materials, which would require further more microscopic measurements of the spin-fluctuation spectrum in these two systems.

5.3 Collaborations & additional measurements

5.3.1 Optical measurements

The optical characterization was done by Andrej Pustogow at the PI1 in Stuttgart with a Bruker Fourier-transform infrared spectrometer and a Woollam spectroscopic ellipsometer. Optical transmission experiments in the mid-infrared range were performed with KBr powder pellets whereas thin flakes were used in the visible/UV range. The discussed features were also observed in single-crystalline samples of different thickness ($d = 15 - 70$ µm) proving them as bulk properties.

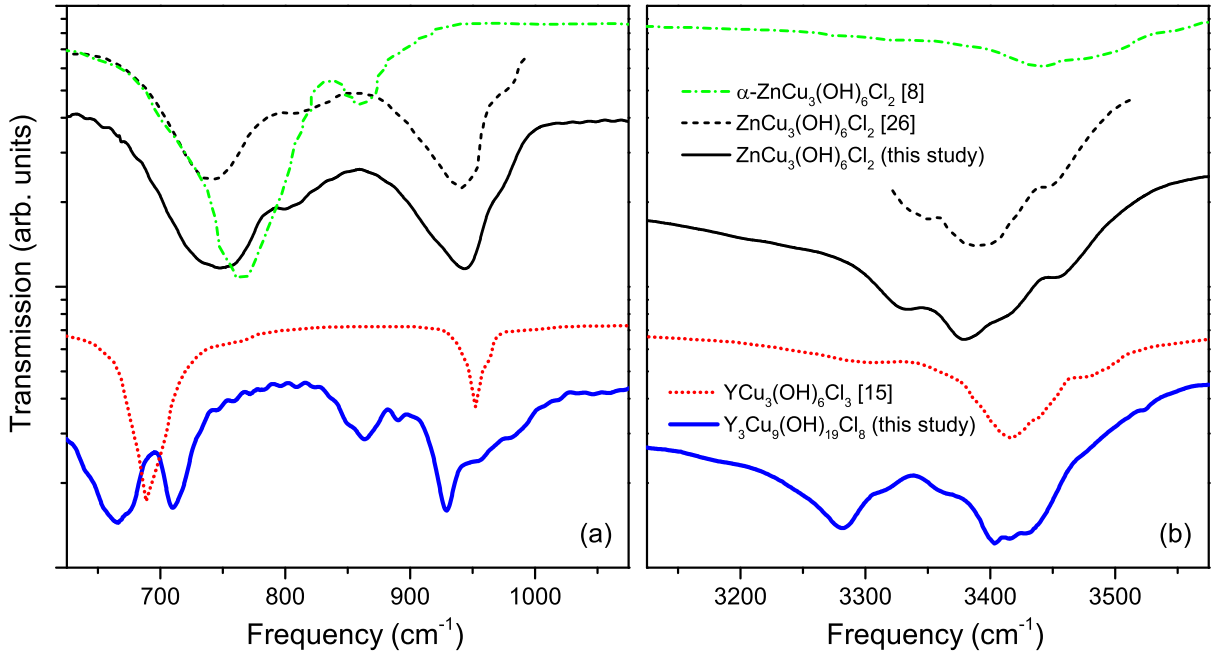

Figure 5.24: Powder transmission measurements in the mid-infrared spectral range reveal pronounced differences between the kagome lattice compounds $YCu_3(OH)_6Cl_3$ (red dotted line), $Y_3Cu_9(OH)_{19}Cl_8$ (blue) , α-$ZnCu_3(OH)_6Cl_2$ (kapellasite, green) and $ZnCu_3(OH)_6Cl_2$ (herbertsmithite, black). For the latter compound, our data (full line) match perfectly with literature (dashed line) [70]. Similar as for the two $ZnCu_3(OH)_6Cl_2$ polymorphs, there are striking differences in the optical response between $YCu_3(OH)_6Cl_3$ from Ref. [56] and $Y_3Cu_9(OH)_{19}Cl_8$ which reflects the structural differences like bond lengths and angles. While the vibrational features in the range 700 – 1000 cm^{-1} are associated with CuO-H deformations (a) and thus give information about the kagome layer, O-H stretching vibrations are observed between 3200 and 3500 cm-1 (b) [70].

As these materials are insulators, the electrodynamic response in the mid-infrared range is dominated by phonons. Following the assignment of previous studies, the features around 700 - 1000 and 3200 - 3500 cm^{-1} are related to CuO-H deformations in the kagome layer and O-H stretching vibrations, respectively [70]. In Fig. 5.24, we plot the optical transmission spectra for the related kagome-lattice compounds $YCu_3(OH)_6Cl_3$ (from Ref. [56]), $Y_3Cu_9(OH)_{19}Cl_8$, α-$ZnCu_3(OH)_6Cl_2$ (kapellasite, Ref. [71]) and $ZnCu_3(OH)_6Cl_2$ (herbertsmithite, our study and Ref. [70]). There are striking differences between the two $ZnCu_3(OH)_6Cl_2$ polymorphs, such as the absence (or strong softening) of the 940 cm^{-1} mode in kapellasite, which reflects the structural differences like bond lengths and angles. Similarly, we clearly observe severe discrepancies between $YCu_3(OH)_6Cl_3$ from Ref. [56] and $Y_3Cu_9(OH)_{19}Cl_8$: Comparing the two we find a shift and splitting of the

modes around 928 cm^{-1} and 700 cm^{-1}, respectively, as well as additional peaks at 860 cm^{-1} and 3280 cm^{-1} , confirming the structural differences in these compounds, which is consistent with the discussed structure details.

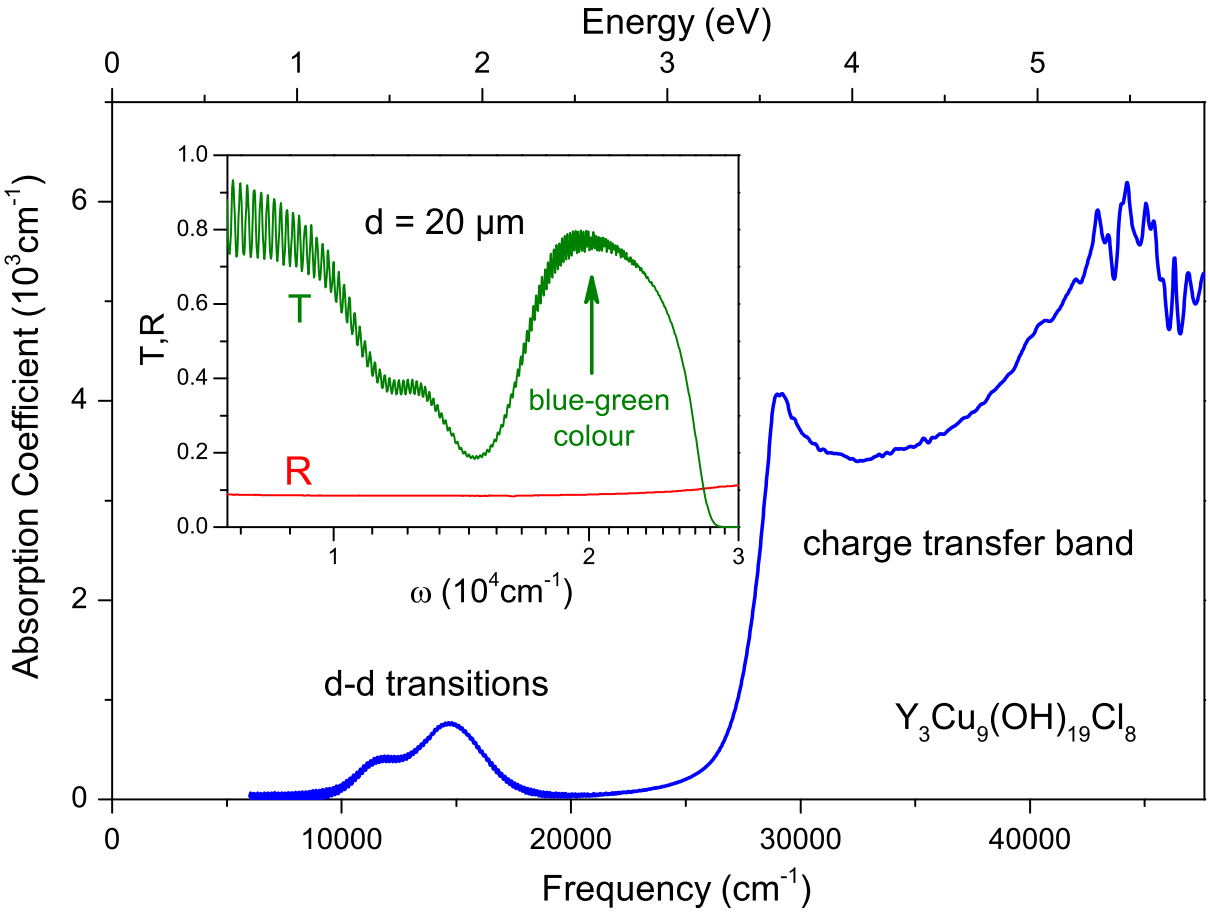

Figure 5.25: The VIS-UV absorption spectrum of $Y_3Cu_9(OH)_{19}Cl_8$ reveals the typical features of transition-metal oxides with d-d transitions in the visible range and the charge-transfer band in the UV. Inset: Pronounced Fabry-Perot fringes occur in the transmission data yielding a refractive index of $n \approx 1.7 - 1.8$ in agreement with the optical reflectivity that is basically flat and featureless in the visible range. As a consequence of the absorption in the long-wavelength range, the largest transmission occurs at around 20,000 cm^{-1} causing the blue-green colour of the crystals.

In addition, we have performed optical transmission experiments on thin single crystals to study the electronic excitations in the visible and ultraviolet spectral ranges. The absorption spectrum shown in Fig. 5.25 reveals the crystal field splitting of Cu *d*-orbitals due to Jahn-Teller distortions in the visible and the charge-transfer band with a van-Hove like peak at 29 100 cm^{-1} (3.6 eV) in the UV. The d-d transitions have maxima at 11 500 and 14 700 cm^{-1} which is in the typical range of copper-oxides. The blue-green colour of the crystals stems from the transmission maximum at 20 000 cm^{-1}. From our optical experiments at lower frequencies we found no indication of the Dirac bands [54]. This agrees with the stoichiometry as the excess charge of the Y^{3+} cations is balanced by Cl^-/OH^- anions and the kagome layer is actually not doped. The corporation will result in a publication of a detailed analysis of Herbertsmithite single crystals and comparison with the new kagome systems presented here.

5.3.2 NMR

Besides the NMR spectra on Han Purple performed in Tallinn, NMR on the kagome systems are done by Michael Baenitz and Ranjith Kumar at MPI-CPfS in Dresden. The sample gives us both a clear ^{69}Ga and a ^{71}Ga line, however without any sidelines. A simple temperature analysis gives no big slope change, but a slight broadening with decreasing temperature caused by the order within the sample. A detailed analysis of the Ga and O NMR will be performed for the deuterated set of samples resulting in a publication by Ranjith Kumar.

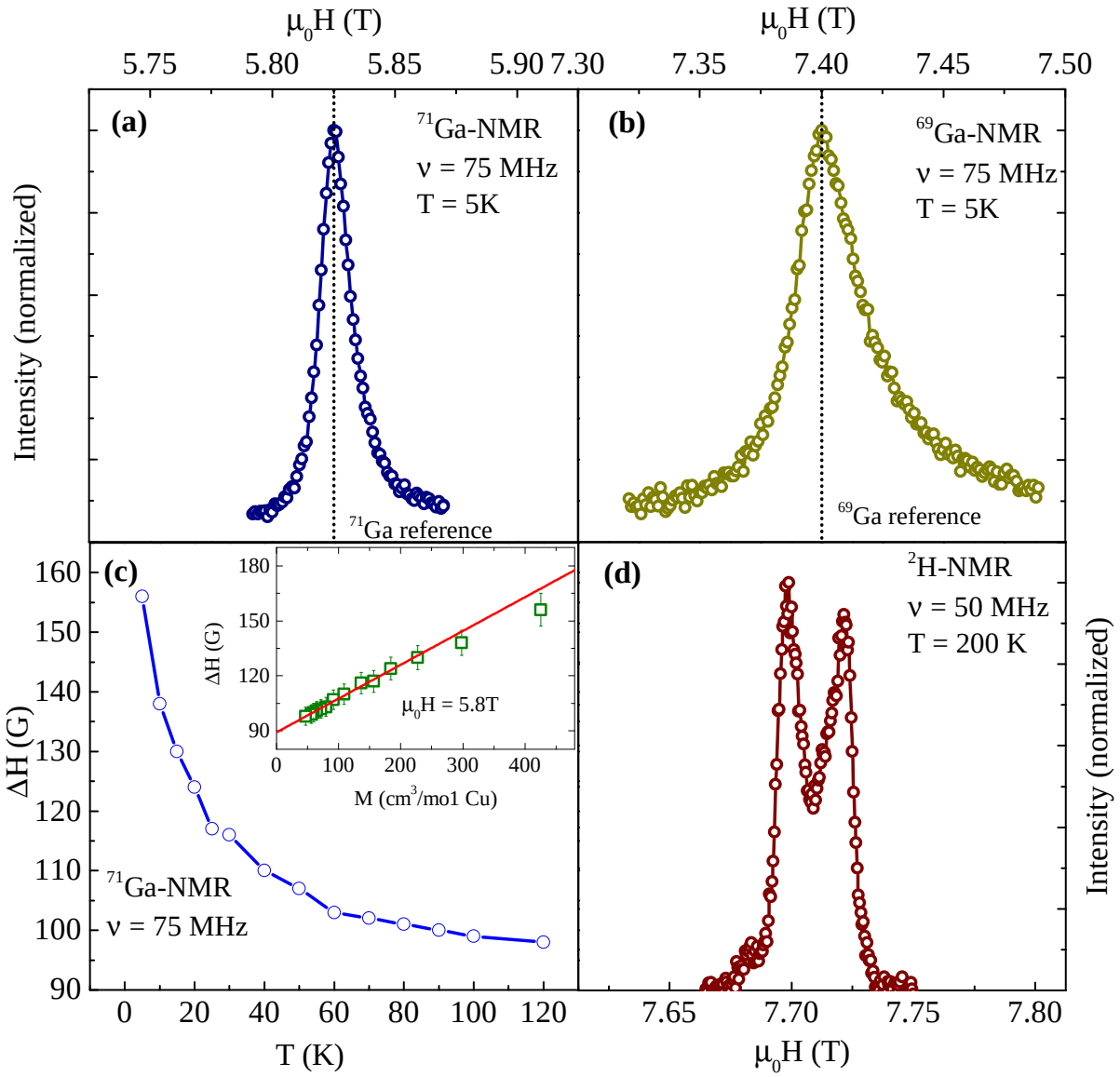

Figure 5.26: (a,b) The two Ga NMR lines on the 1 M $Ga_xCu_{4.-x}(OH)_6Cl_2$ powder sample are shown revealing typical broadness for Ga-Cu based systems. c) gives the ^{71}Ga line knight shift at various temperatures. d) ^{2}H NMR of the 1 M $Ga_xCu_{4.-x}(OH)_6Cl_2$ powder.

6 Summary

Five unique materials from two material classes of highly researched copper based low dimensional magnetic materials have been presented, where novel substitutions led to a great improvement of the so far published results.

The first class of low dimensional dimer systems (2D) presents a condensate of bosonic spin flip quasi particles and the prominent candidate Han Purple $BaCuSi_2O_6$ is researched in detail in this thesis. We reproduced the flux growth from reference [20] of pure $BaCuSi_2O_6$ and examined the reported structural transition from $I4_1/acd$ to Ibam at low temperatures accompanied by an incommensurate modulation [21] on both powder and single crystal samples. We could show that a moderate crawling and evaporation of the $LiBO_2$ flux leads to a crystallization and crystals could be grown at 950°C held for several hours. We managed to introduce both Sr and Ge into the structure by subsequent substitution on the Ba and/or Si place. $\mathbf{Ba_{4-x}Sr_xCuSi_2O_6}$ presents a stable $I4_1/acd$ phase down to lowest temperatures which is stabilized by even the lowest substitution due to microstrains. That the suppression is not from the volume change could be proven by applied external pressure in a diamond cell used in a single crystal diffraction experiment. The external pressure also suppressed the Ibam phase, but lead to a new phase of the satellite reflexes spread to a line, indicating that we are not dealing with an incommensurate modulation but rather twinnings created through slightly misaligned 90° shifted layers growing on top of each other. Furthermore we showed the suppression by detailed diffraction experiments on the substituted samples with neutron and synchrotron radiation down to 1.5 K as well as low temperature MAS-NMR. The NMR experiment further proved an statistical even distribution of the substituent. Generally, the unit cell volume decreases with increasing Sr content and the intradimer magnetic coupling becomes slightly reduced. DFT calculations for $x = 0.1$ for the tetragonal $I4_1/acd$ structures show the presence of strong antiferromagnetic Cu-Cu intradimer couplings and non-negligible antiferromagnetic nearest-neighbor dimer top-bottom antiferromagnetic couplings that avoid any kind of frustration between the dimer layers. The fact that for the germanium substituted sample the phase transition is also suppressed leaves us with a readily tunable system by varying the substitution concentrations. First high-field magnetic measurements on a powder sample with $x = 0.1$ at 2 K reveal clear indications for a field-induced ordered state, similar to the observations reported for the $x = 0$ parent compound. In contrast to the parent compound, however, where the analysis of the critical properties are plagued by uncertainties related to the presence of two sorts of dimers as a consequence of the structural transition, the $x = 0.1$ material is free of this complication. Therefore, detailed high-field measurements on this new material may help to clarify the influence of structural subtleties on the critical behavior of the field-induced order. We want to mention the possibility of growing large single crystals of $Ba_{0.9}Sr_{0.1}CuSi_2O_6$ in a mirror furnace with the zone melting method under oxygen pressure to obtain large enough single crystals for inelastic neutron scattering similar to Ref. [19, 39].

The recently found similar system $\mathbf{Ba_2CuSi_2O_6Cl_2}$ presents the same structure just with additional $BaCl_2$ next to the Ba atomes and has the advantage that the structure is stable down to low temperatures as we could show by PXRD data down to 10 K. Additionally the critical fields of the BEC region are lower [40]. Strontium substitution, which could further reduce the critical fields could not be realised as shown in a sequential DTA

measurement. A successful DTA curve of a flux growth in $BaCl_2$ gives the possibilty to optimize the growth process from [40] to obtain large enough crystals to perform neutron diffraction.

The second class, the frustrated kagome materials present the ideal realizations of a QSL. $GaCu_3(OH)_6Cl_2$ has been promised as the first correlated dirac metal. We could synthesize the first $\mathbf{Ga_xCu_{4-x}(OH)_6Cl_2}$ powder samples and deuterate them, which for $x \leq 0.8$ prove to be insulating. Susceptibility, specific heat and $\mu-$SR measurements show that it is a disordered quantum kagome spin system with similar properties as $Zn_xCu_{4-x}(OD)_6Cl_2$. The phase formation at low temperatures, leaves struggles and prevents the same crystal growth as for herbertsmithite. Powder samples can be obtained by reflux synthesis but no single crystal could be extracted. The green compound is a Mott isolator, so the additional electron of the Ga seems to be compensated. The decrease of the Néel ordering amount observed in $Zn_xCu_{4-x}(OD)_6Cl_2$ is reproduced with Ga, but the general effect of Ga compared to Zn is lower on both the Curie-Weiss temperature as well as the suppression. The highest substitution amount is $x = 0.8$, however locally $x = 1$ substitution amounts could be reached. We observe variations of substitution within one batch in EDX, which indicate varying antisite disorder between the Ga and Cu positions. Summed up $Ga_xCu_{4-x}(OD)_6Cl_2$ proves that electron doping by substitution is not an easy experimental task. Outlook: Resonant X-ray diffraction gives the possibility to resolve the Ga position in this structure, which however requires better sample quality regarding phase purity and crystallinity. Furthermore nuclear magnetic resonance (NQR) measurements will be performed and might exclude/ proof wether there is Cu^{1+} present.

In the attempt to electron dope with Y^{3+} instead of Ga^{3+}we found the new system $\mathbf{Y_3Cu_9(OH)_{19}Cl_8}$, which is a stoichiometric quantum spin system with well separated kagome layers of localized Cu^{2+} spins quite similar to the recently published $YCu_3(OH)_6Cl_3$ [56]. Detailed structural refinements of hydrothermally prepared single crystals revealed a crystal structure with two different copper positions, leading to slightly anisotropic kagome layers. Neutron powder diffraction on deuterated $Y_3Cu_9(OH)_{19}Cl_8$ revealed that the exact stoichiometry is $Y_3Cu_9O(OH)_{18}Cl_8$, so the classical ionic bonding image cannot be applied to this cuprate system similar to $YBa_2Cu_3O_7$ [67]. The partial release of magnetic frustration within the kagome layers compared to $\mathbf{YCu_3(OH)_6Cl_3}$ is also reflected in the magnetic properties, because we observe weak but clear magnetic order at $T_N = 2.2$ K in magnetization and specific-heat measurements on single crystals of $Y_3Cu_9(OH)_{19}Cl_8$. However, the frustration effects are still very pronounced with a frustration parameter of $\Theta_W/T_N \sim 50$. Low-temperature specific-heat measurements on a powder sample of $YCu_3(OH)_6Cl_3$ revealed the absence of magnetic order down to 0.4 K, leading to a frustration parameter $\Theta_W/T_N > 250$ and indicating a gapless spin liquid due to a vanishing value for 0 K. Therefore, the two Y-Cu-OH-Cl compounds present an unique setting to investigate the change from a spin-liquid state to a strongly frustrated AFM ordered state, by slightly releasing the frustration in a kagome lattice via structural modification. Unlike for substitution series, as e.g. $Zn_xCu_{4-x}(OH)_6Cl_2$, where we always encounter crystallographic disorder, the magnetic properties of the two stochiometric compounds with fully occupied kagome sites might be much more reliable with ab-initio calculations. Additionally, these two stoichiometric kagome systems might open the way for a systematic understanding of magnetic frustration in kagome materials, which would require further more microscopic measurements of the spin-fluctuation spectrum in these two systems.

Zusammenfassung

Die Arbeit beschäftigt sich mit der Herstellung sowie der strukturellen und magnetischen Charakterisierung von zwei Materialklassen von kupferbasierten zweidimensionalen Quanten-Spin-Systemen: *Quadratische Gitter von Dimeren* sowie geometrisch frustrierte *Kagomé Gitter*. In beiden Systemen werden Substitutionen vorgestellt die zu verbesserten Eigenschaften führen.

Die Suche nach neuen topologischen Grundzuständen ist zurzeit eines der wichtigsten Themen der Festkörperphysik und wurde daher 2016 mit dem Physik-Nobelpreis gekürt, den Haldane, Kosterlitz und Thouless zur Entdeckung der Theorie zu niedrig-dimensionalen Systemen erhielten. Sie konnten zeigen, dass diese Systeme unkonventionelle Phasenübergänge in Grundzustände haben die mögliche topologische Anregungen aufweisen.

Ein berühmtes Beispiel eines solchen Systems ist das erste untersuchte Material Han Purpur $BaCuSi_2O_6$, ein blau- bis lilafarbenes (durch rote Cu_2O Einschlüsse) Farbpigment, welches schon in der Han Dynastie (200 vor Christus) zur Färbung verwendet wurde. Dieses Material weist ein zweidimensionales Untergitter von sogennanten Cu^{2+} ($[Ar]3d^9$) Dimeren auf, die bei tiefen Temperaturen und hohen Magnetfeldern ein Kondensat von Spinflip-Quasiteilchen erzeugen:

Dimere sind Spin-1/2-Paare, hier Cu^{2+}, welches exakt einen freien Spin trägt. Die Dimere formen einen Singulett Grundzustand und einen angeregten Triplett Zustand. Ab einem kritischen Magnetfeld wird hier bei tiefen Temperaturen durch Zeeman-Aufspaltung der Triplettzustand mit dem Grundzustand überlappen. Eine Skizze des Phasendiagramms ist in Abbildung 2.7 zu sehen. Somit beginnen Spins sich um 180° zu drehen, was einer S = 1-Änderung entspricht. Dies ist also ein Kondensat von bosonischen Quasiteilchen, den Triplonen, auf einem zweidimensionalem Gitter (BKT).

Da ein komplizierter struktureller Phasenübergang bei tiefen Temperaturen zu einer Struktur mit einer inkommensurablen Modulation (nichtperiodische Veränderung) in Han Purpur beobachtet wurde, verloren die Wissenschaftler das Interesse [27, 23]. Wir haben an dieser Verbindung die Flusszucht-Methode aus Referenz [20] reproduziert. Der verwendete $LiBO_2$ Fluss sorgt primär für Kristallisation durch Übersättigung, weil das Flussmittel verdampft und kriecht, was in einer Zucht bei konstanten 950°C gezeigt werden konnte. Der Phasenübergang bei tiefen Temperaturen wurde sowohl an Einkristallen als auch an Pulver Proben von $BaCuSi_2O_6$ genauestens untersucht. Es war uns möglich durch erfolgreiche Substitutionen: $(Ba_{1-x}Sr_x)Cu(Si_{1-y}Ge_y)_2O_6$ eine bei Raumtemperatur stabile Struktur ($I4_1/acd$) herzustellen. Da das übliche Flussmittel $LiBO_2$ mit dem verwendeten $SrCO_3$ reagiert, wurde die eigentliche Verglasung der Schmelze über eine sauerstoffreiche Atmosphäre unterdrückt und Kristalle konnten so direkt aus der Schmelze gezüchtet werden. Die optimale Temperatur und Sauerstoffmenge wurde mithilfe zweier DTA Kurven ermittelt (siehe Abbildung 4.3). Hierzu werden im Vorhinein fast phasenreine (unter 5 % Verunreinigungen) Pulverproben über eine Festkörper-Sinterung bei 1030°C hergestellt und dann anschließend auf einem Platinblech-Tiegel verteilt. In einem Rohrofen werden diese nun einem langsam abkühlenden Temperaturprofil bei 1130°C unter 2 bar strömenden Sauerstoff im Rohr ausgesetzt. Eine Skizze des Aufbaus ist in Abbildung 4.4 dargestellt.

Durch Anlegen eines externen Druckes in einer Diamant-Druckzelle, verwendet in einem Einkristalldiffraktometrie-Aufbau, konnte gezeigt werden, dass die Unterdrückung des strukturellen Phasenübergangs mittels Strontium-Substitution nicht durch die einfache Volumenveränderung verursacht wird, sondern durch Micro-Spannungen. Der volumenverändernde externe Druck unterdrückt zwar auch die Tieftemperatur-Ibam-Struktur, doch stabilisiert er nicht die Raumtemperatur Struktur, sondern führt zu einer neuen aufgezeigten Phase, wie aus Abbildung 4.15 & 4.16 zu entnehmen ist. Während die vier Satelliten gewisser Streu-Reflexe bei der inkommensurablen Struktur um den Hauptreflex angeordnet sind, weist die neue Phase sie zu einer Linie aufgefächert auf. Dies lässt vermuten, dass wir statt einer inkommensurablen Modulation von um 90° verschobenen verwachsenen Schichten reden. Die thermische Ausdehnung sorgt bei tiefen Temperaturen für eine Verkantung und somit Aufspaltung.

Die Unterdrückung des strukturellen Phasenübergangs mittels Strontium Substitution wurde mihilfe von Synchrotron- (Abbildung 4.12) und Neutronen-Diffraktometrie Experimenten sowie spezifischer Wärme (Abbildung 4.14) an Einkristallen und Pulverproben zwischen 300 - 1.5 K gezeigt. Zudem ist in MAS-NMR eine homogene, komplett statistische Verteilung der Strontiumatome auf den Barium-Plätzen zu sehen. Tieftemperatur-NMR-Daten aus Abbildung 4.13 an $(Ba_{1-x}Sr_x)CuSi_2O_6$ zeigen die Abwesenheit der Spaltung der Si-Linie, die durch zwei Kupferpositionen in der Tieftemperatur-Ibam-Struktur in reinem $Ba_{1-x}CuSi_2O_6$ zu beobachten ist.

Detaillierte Rietveldverfeinerungen der temperaturabhängigen Synchrotron-Pulverdiffraktometrie, dargestellt in 4.11 im Bereich von 1.5 bis 750 Kelvin an $BaCuSi_2O_6$, zeigen für das reine System den berichteten Hoch- und Tieftemperatur-Phasenübergang [27] in einem Wendepunkt in den Gitterkonstanten. Der gleiche Vorgang an einer $(Ba_{0.9}Sr_{0.1})CuSi_2O_6$-Probe zeigt auch einen Hochtemperatur-Phasenübergang, jedoch weist dieser eine neue, ungelöste Struktur auf.

Generell führt eine steigende Strontium-Substitution zu einer verkleinerten Elementarzelle, was auch eine sinkende intradimere Kopplung verursacht. Beobachtet wird dies in dem zu tieferen Temperaturen schiebenden Maximum in der Suszeptibilität (Abbildung 4.17). Letztere messen wir indirekt über die vibrierende Probenmagnetometrie (VSM) eines industriell gefertigten Kryostaten (PPMS). Die DFT Rechnungen für $x = 0.1$ ergeben für die $I4_1/acd$ Struktur die Anwesenheit von starken antiferromagnetischen Cu-Cu-intradimeren Kopplungen und nicht vernachlässigbaren antiferromagnetischen Interdimerkopplungen vom oberen zum unteren Kupferatom des nächsten Nachbar-Dimers, welche jegliche Frustration außer Kraft setzen.

Germanium-Substitution unterdrückt ebenfalls den Übergang zur Ibam Struktur und gibt uns somit die Möglichkeit, die Zellparameter und Dimerwechselwirkung unseres Systems weitgehend durch verschiedene Substitutionen zu kontrollieren.

Erste gepulste magnetische Messungen im Hochfeld (Abbildung 4.19) zeigen für die $x = 0.1$-Probe bei 2 K einen feldinduzierten geordneten Zustand, ähnlich wie für die $x = 0$-Ursprungsstruktur. Aber im Gegensatz zu dieser ist für $x = 0.1$ die Analyse der kritischen Parameter nicht durch Unsicherheiten bezüglich zweier Arten von Dimeren als Folge des Phasenüberganges geplagt. Daher könnten Hochfeld Messungen an diesem neuen Material Aufschluss über den Einfluss der strukurellen Feinheiten auf das Verhalten in der feldinduzierten Ordnung geben.

Eine Spiegelofen-Zucht mittels Zonenschmelzen in sauerstoffreicher Atmosphäre könnte zu Einkristall-Proben von $Ba_{0.9}Sr_{0.1}CuSi_2O_6$ führen, die groß genug sind um inelastische Neutronen Experimente, ähnlich zu Ref. [19, 39], durchzuführen.

Als zweites Material mit einem quadratischen Dimer-Gitter untersucht die Arbeit $Ba_2CuSi_2O_6Cl_2$, das vor kurzem publizierte Equivalent zu Han Purpur [40] mit einem

zusätzlichen $BaCl_2$ in der Ba-Zwischenschicht, und eine mögliche Sr-Substitution. Mithilfe einer DTA-Messreihe mit Zwischenschritt-Diffraktogrammen konnte gezeigt werden, dass beim Versuch, $BaCuSi_2O_6$ mit $SrCl_2$ reagieren zu lassen, sich erst bei 820°C anteilig reines $Ba_2CuSi_2O_6Cl_2$ bildet, ab 980°C dieses zu $SrCuO_3$ und Glas zerfällt. Zudem blieben anteilige Sr-Beimischungen erfolglos, somit scheint eine Sr-Substitution nicht möglich. Tieftemperaturdiffraktometrie-Messungen zeigen in Abbildung 4.23 eine stabile Struktur bis 10 K. Mithilfe einer DTA-Messung eines Gemisches aus (6 : 1)-$BaCl_2$- $BaCuSi_2O_6$ konnten Einkristalle in einer Quarzampulle gezüchtet werden, die ein Kristallisationssignal bei 1022°C zeigen. Zudem wird das Salz langsam von der Quarzampulle aufgenommen, was für eine Kristallisation durch Übersättigung sorgen kann. Somit kann das publizierte Ofenprofil aus Referenz [40] optimiert werden, um große Einkristalle zu züchten, denn $Ba_2CuSi_2O_6Cl_2$ präsentiert sich als ein perfekter Kandidat für die Untersuchung der BKT-Phase bei relativ niedrigen kritischen Feldern.

Die zweite Kuprat-Materialklasse sind Verbindungen, die ein sogenanntes *Kagomé-Gitter* aufweisen, in denen die Anordnung der Kupferatome in sternenförmigen Dreier-Paaren bei
antiferromagnetischer Kopplung für Frustration sorgt. Diese Frustration führt dazu, dass diese Systeme nicht langreichweitig magnetisch ordnen können (LRO) und Spinfluktuationen bis zu tieftsten Temperaturen auftreten. Der magnetische Grundzustand hiervon ist die sogennante Quanten-Spin-Flüssigkeit (QSL), die durch das schwingende Valenzbindungsmodell (RVB) von Anderson beschrieben werden kann. Hier treten neuartige topologische Anregungen auf.

Die experimentell bislang beste Realisierung eines solchen Kagomé-Gitters wurde in der Atacamit-Familie gefunden, nämlich Herbertsmithit, $ZnCu_3(OH)_6Cl_3$. In der Bandstruktur-Rechnung von Herbertsmithit liegt ein Dirac-Kreuzungspunkt im unbesetzten oberen Abschnitt. I. Mazin et al. [54] schlägt vor, dass man durch vollständiges Ersetzen des Substitutions-Ions Zn^{2+} durch ein dreiwertiges Ion wie Ga^{3+} die Fermi-Energie in diesen Punkt zu verschieben, was das Material zu einem Dirac Metall machen könnte. Selbst bei Berechnungen mit Korrelationen sollen hierbei die Bänder nicht aufspalten.

In dieser Arbeit wird die Herstellung und Analyse ebendieser Verbindung $GaCu(OH)_6Cl_2$ beschrieben. Mithilfe der Reflux Methode konnten Pulverproben von $Ga_xCu_{4-x}(OH)_6Cl_2$ mit einem Substitutionsgehalt von bis zu $x = 0.8$ hergestellt werden. Die Synthese ist nur bei tieferen Temperaturen bis 90°C möglich und der Substitutionsgehalt von $x = 0 - 0.8$ kann durch die Molarität von 0 bis 1 M $GaCl_3$ in H_2O kontrolliert werden. Die Phase entsteht hierbei auf dem verwendeten CuO, weswegen hiervon immer Reste erhalten bleiben. Der niedrige pH-Wert der Lewis-Säure $GaCl_3$ und die niedrige Synthesetemperatur verhindern bis jetzt die Herstellung von Einkristallen.

Entgegen der Vorhersage für die $x = 1$-Verbindung weisen diese aber eine grüne Farbe und Mott Isolator Eigenschaften mit einem Widerstand im GΩ Bereich auf. Eine Reihe deuterierter Proben verschiedener Substitutionsgehälter wurde hergestellt und im Detail mit Hilfe von Suszeptibilität (Abbildung 5.8), spezifischer Wärme (Abbildung 5.10) und Myon-Spin-Resonanz ($\mu-$SR, Abb. 5.12) analysiert. Alle Messungen zeigen übereinstimmend die langsame Unterdrückung der magnetischen Ordnung mit steigendem Substitutionsgehalt ähnlich wie bei $Zn_xCu_{4-x}(OH)_6Cl_2$. Das durch $\mu-$SR-Daten bestimmte Phasendiagramm aus Abbildung 5.13 zeigt im Vergleich zur Zn-basierten Struktur eine Verschiebung der Unterdrückung zu höheren x-Werten, wobei eine vollständig unterdrückte Ordnung erst bei $x = 0.9$ entstünde.

In EDX Messungen sehen wir starke Substitutionsschwankungen, die Ga-Cu-Positionswechsel andeuten, ähnlich wie in Herbertsmithite. In anderen Systemen dieser Materialklasse

mit dreiwertigen Ionen, wie das gleich diskutierte Y-Beispiel, findet ein Ausgleich des zusätzlichen Elektrons über weitere Chlor-Anionen statt. Doch im Falle von Ga wird die Stöchiometrie $Ga_xCu_{4-x}(OH)_6Cl_2$ durch mehrfache EDX-Messungen an gepressten Pulverpallets aller Batches bestätigt. Das zusätzliche Elektron wird vermutlich durch Ga^{1+} Bildung ausgeglichen, wie es bei Galliumdichlorid Ga(I)Ga(III)Cl_4 zu beobachten ist. Die o.g. Verschiebung des Phasendiagramms kann durch erhöhten Ga-Cu Positions-Austausch erklärt werden. Eine höhere Substitutionsmenge wäre somit nötig, um Cu aus der Zwischenschicht zu vertreiben. Dieses System zeigt also, wie auch schon der Versuch der direkten Elektronen-Dotierung mittels Lithium-Interkalation [55], dass eine experimentelle Realisierung eines elektronendotierten Kagomé-Systems schwierig bis gar nicht realisierbar ist. Denn jegliche anderen dreiwertigen Ionen sorgen für zusätzliche Cl-Anionen, wie das nachfolgende Beispiel zeigt.

Zwei weitere Kagomé-Materialien werden in dieser Arbeit behandelt, welche die ersten Beispiele einer stabilen Kapellasite ähnlichen Struktur mit einem dreiwertigen Ion sind: $Y_3Cu_9(OH)_{19}Cl_8$ und $YCu_3(OH)_6Cl_3$ [56]. Dabei weist vereinfacht $Y_3Cu_9(OH)_{19}Cl_8$ die dreifache Elementarzelle von $YCu_3(OH)_6Cl_3$ mit der Ersetzung eines Cl^- durch $(OH)^-$ auf. Beide Systeme haben den enormen Vorteil, dass sie keinen Y-Cu Austausch zeigen, wie er in dem Ga- und Zn-basierten System zu beobachten ist. Sie existieren auch nur für vollständige Substitution $x = 1$. Die beiden Verbindungen stellen ein einzigartiges Beispiel von zwei fast identischen Strukturen mit dennoch stark unterschiedlichen magnetischen Grundzuständen dar: Einkristalldiffraktometrie-Analysen zeigen im Falle von $Y_3Cu_9(OH)_{19}Cl_8$, dass die Kagomé-Ebene durch zwei unterschiedliche Kupferpositionen leicht uneben ist, was für eine induzierte Ordnung bei 2.2 K sorgt. $YCu_3(OH)_6Cl_3$ hingegen präsentiert sich als ein perfektes Kagomé-Material mit keiner magnetisch langreichweitigen Ordnung bis mindestens 0.35 K.

Das besondere hierbei sind auch die unterschiedlichen Synthesemethoden, da $YCu_3(OH)_6Cl_3$ in Anwesenheit von Wasser zu $Y_3Cu_9(OH)_{19}Cl_8$ und Clinoatacamite ($Cu_2(OH)_3Cl$) zerfällt. Daher kann $YCu_3(OH)_6Cl_3$ nur über eine Festkörper-Sinterung in einer Autoklave hergestellt werden. Hierbei wird die Autoklave lediglich verwendet um das Verdampfen des Kristallwassers zu verhindern. Dies führt zu reinen mikrokristallinen Pulverproben. $Y_3Cu_9(OH)_{19}Cl_8$ hingegen wird über die hydrothermale Methode hergestellt. Die Züchtung erfolgt bei langsamen Kühlen von 270°C in der großen Autoklave Abschnitt 1.4 a) und ergibt 1 x 1 x 0,2 mm^3 große Kristalle. Bei dieser Synthese entsteht immer Clinoatacamite als Nebenphase, welches teilweise sogar mit den Kristallen verwachsen und eingebaut ist. Daher sind diese mithilfe optischer Methoden sorgfältig auszuwählen.

Neutronendiffraktometrie bei 295 K und 1.5 K an deuterierten Proben zeigen, dargestellt in Abbildung 5.19, dass es sich eigentlich um $Y_3Cu_9O(OH)_{18}Cl_8$ handelt und sich somit kein Wasserstoff am Sauerstoff des Cl-Platzes befindet. Dies würde im klassischen Ionenbindungs-Bild eine negative Ladung bedeuten. Folglich greift dieses an dem untersuchten Kuprat System nicht, ähnlich wie bei dem Kuprat-Supraleiter $YBa_2Cu_3O_7$ [67].

Die magnetischen Eigenschaften wurden auch hier mittels Magnetisierung und spezifischer Wärme-Option im PPMS-Kryostaten gemessen, wobei ein Tieftemperatur-Einsatz verwendet wurde um die 0.35 K zu erreichen (^{3}He-Option). Die Curie-Weiß-Konstante liegt für beide Systeme bei sehr ähnlichen Werten, welches die Verwandheit verdeutlicht. Wir beobachten in $Y_3Cu_9(OH)_{19}Cl_8$ ein breites Maximum in der Suszeptibilität (Abbildung 5.21) und einen klaren Peak in der spezifischen Wärme (Abbildung 5.22), welcher durch Integrieren von C/T einer Entropie von $0.1k_B\ln 2$, also 10% Ordnung entspricht. Somit ist dies ein hoch frustriertes System mit einem Frustrationsparameter von $\Theta_W/T_N \sim 50$. Wohingegen $YCu_3(OH)_6Cl_3$ kein solches Maximum zeigt und ungeordnet bis 0.35 K bleibt, was für die Frustration einen Wert von$\Theta_W/T_N > 250$ ergibt.

Die spezifische Wärme zeigt eine Konvergenz gegen $0\,\mathrm{J/(molCuK)}$ für $T \rightarrow 0\,\mathrm{K}$ was für ein System ohne Anregungslücke spricht. In beiden Systemen ist ein lineares Verhalten in der spezifischen Wärme zwischen $3\,\mathrm{K}$ und $10\,\mathrm{K}$ zu beobachten, welches typisch für die Quanten-Spin-Flüssigkeiten ist.

Somit stellen die zwei Kagomé Materialien ein einzigartiges Beispiel von stöchiometrischen voll besetzten eng verwandten Materialien dar, in denen wir den Effekt von leichter Aufhebung der perfekten Frustration eines Kagomé-Gitters beobachten können. Eine genaue Untersuchung der mikroskopischen Eigenschaften des Spin-Fluktuationsspektrums gibt also Einsicht in das magnetische Konzept der Frustration in Kagomé-Materialien, wie es bislang nicht möglich war.

Bibliography

[1] K. Awaga, T. Inabe, Y. Maruyama, T. Nakamura, M. Matsumoto, Chem. Phys. Lett. **195**, 21 (1992).

[2] K.-Th. Wilke, J. Bohm, *Kristall Züchtung*, VEB Deutscher Verlag der Wissenschaften, Berlin 1973.

[3] D. A. Palmer and P. Bénézeth, *Solubility of Copper Oxides in Water and Steam*, 14th International Conference on the Properties of Water and Steam in Kyoto (2008).

[4] T. H. Han, J. S. Helton, S. Chu, A. Prodi, D. K. Singh, Mazzoli, P. Müller, D. G. Nocera, and Y. S. Lee, *Synthesis and characterization of single crystals of the spin-12 kagome-lattice antiferromagnets* $Zn_xCu_{4-x}(OH)_6Cl_2$, Phys. Rev. B **83**, 100402(R) (2011).

[5] J. M. D. Coey, *magnetism and magnetic materials*, Cambridge university press (2009).

[6] S. Blundell, *Magnetism in condensed matter*, Oxford university press (2001).

[7] X. Rocquefelte, K. Schwarz & P. Blaha, *Theoretical Investigation of the Magnetic Exchange Interactions in Copper(II) Oxides under Chemical and Physical Pressures*, Scientific Rep. **2**: 759 (2012)

[8] Anderson, P. W. Mat. Res. Bull. **8**, 153 (1973).

[9] J. M. Kosterlitz and D. J. Thouless, *Ordering, metastability and phase transitions in two-dimensional systems*, J. Phys. C **6** (1973).

[10] A. Bergamaschi et. al, *The MYTHEN detector for X-ray powder diffraction experiments at Swiss Light Source,* Nucl. Inst. Meth. Phys. Res. **A591**, 163-166 (2008).

[11] P. Kraft, A. Bergamaschi, Ch. Broennimann, R. Dinapoli, E. F. Eikenberry, B. Henrich, I. Johnson, A. Mozzanica, C. M. Schlepütz, P.R. Willmott and B. Schmitt, J. Synchrotron Rad. 16, 368–375 (2009).

[12] P. Fischer, G. Frey, M. Koch, M. Koönnecke, V. Pomjakushin, J. Schefer, R. Thut, N. Schlumpf, R. Buürge, U. Greuter, S. Bondt, E. Berruyer, *High-resolution powder diffractometer HRPT for thermal neutrons at SINQ*, Physica B **276-278**, 146 (2000).

[13] http://www.psi.ch/sls/ms/ms.

[14] E. R. Andrew, A. Bradbury, R. G. Eades, Nature 183, 1802 (1959).

[15] R. Stern, I. Heinmaa, E. Joon, A. A. Tsirlin, H. Nakamura, T. Kimura, *Low-Temperature High-Resolution Solid-State (cryoMAS) NMR of Han Purple* $BaCuSi_2O_6$, Appl. Magn. Reson. **45**, 1253 (2014).

[16] P. Puphal, D. Sheptyakov, N. van Well, L. Postulka, I. Heinmaa, F. Ritter, W. Assmus, B. Wolf, M. Lang, H. O. Jeschke, R. Valentí, R. Stern, C. Rüegg, and C. Krellner, *Stabilization of the tetragonal structure in* $(Ba_{1-x}Sr_x)CuSi_2O_6$, Phys. Rev. B **93**, 174121 (2016).

[17] V. Zapf, M. Jaime, and C. D. Batista, *Bose-Einstein condensation in quantum magnets*, Rev. Mod. Phys. **86**, 563 (2014).

[18] T. Giamarchi, C. Rüegg, and O. Tchernyshyov, *Bose-Einstein condensation in magnetic insulators*, Nature Phys. **4**, 198 (2008).

[19] M. Jaime, V. F. Correa, N. Harrison, C. D. Batista, N. Kawashima, Y. Kazuma, G. A. Jorge, R. Stern, I. Heinmaa, S. A. Zvyagin, Y. Sasago, and K. Uchinokura, *Magnetic-Field-Induced Condensation of Triplons in Han Purple Pigment $BaCuSi_2O_6$*, Phys. Rev. Lett. **93**, 087203 (2004).

[20] S. E. Sebastian, N. Harrison, C. D. Batista, L. Balicas, M. Jaime, P. A. Sharma, N. Kawashima, and I. R. Fisher, *Dimensional reduction at a quantum critical point*, Nature **441**, 617 (2006).

[21] E. C. Samulon, Z. Islam, S. E. Sebastian, P. B. Brooks, M. K. McCourt, Jr., J. Ilavsky, and I. R. Fisher, *Low-temperature structural phase transition and incommensurate lattice modulation in the spin-gap compound $BaCuSi_2O_6$*, Phys. Rev. B **73**, 100407 (2006).

[22] S. Krämer, R. Stern, M. Horvatić, C. Berthier, T. Kimura, and I. R. Fisher, *Nuclear magnetic resonance evidence for a strong modulation of the Bose-Einstein condensate in $BaCuSi_2O_6$*, Phys. Rev. B **76**, 100406 (2007).

[23] D. V. Sheptyakov, V. Yu. Pomjakushin, R. Stern, I. Heinmaa, H. Nakamura and T. Kimura, *Two types of adjacent dimer layers in the low-temperature phase of $BaCuSi_2O_6$*, Phys. Rev. B **86**, 014433 (2012).

[24] N. Laflorencie and F. Mila, *Theory of the field-induced BEC in the frustrated spin-$\frac{1}{2}$ dimer compound $BaCuSi_2O_6$*, Phys. Rev. Lett. **102**, 060602 (2009).

[25] S. Krämer, R. Stern, M. Horvatić, C. Berthier, H. Nakamura and T. Kimura, *Spatially Resolved Magnetization in the Bose-Einstein Condensed State of $BaCuSi_2O_6$: Evidence for Imperfect Frustration*, Phys. Rev. B **87**, 180405 (2013).

[26] V. V. Mazurenko, M. V. Valentyuk, R. Stern, and A. A. Tsirlin, *Nonfrustrated interlayer order and its relevance to the Bose-Einstein condensation of magnons in $BaCuSi_2O_6$*, Phys. Rev. Lett. **112**, 107202 (2014).

[27] K. M. Sparta and G. Roth, *Reinvestigation of the structure of $BaCuSi_2O_6$ - evidence for a phase transition at high temperature*, Acta Cryst. B**60**, 491-495 (2004).

[28] H. Berke, *The invention of blue and purple pigments in ancient times*, Chem. Soc. Rev. **36**, 15 (2007).

[29] S. E. Sebastian, P. Tanedo, P. A. Goddard, S.-C. Lee, A. Wilson, S. Kim, S. Cox, R. D. McDonald, S. Hill, N. Harrison, C. D. Batista, and I. R. Fisher, *Role of anisotropy in the spin-dimer compound $BaCuSi_2O_6$*, Phys. Rev. B **74**, 180401R (2006).

[30] N. van Well, P. Puphal, B. Wehinger, M. Kubus, J. Schefer, C. Rüegg, F. Ritter, C. Krellner, and W. Assmus, *Crystal Growth with Oxygen Partial Pressure of the $BaCuSi_2O_6$ and $Ba_{1-x}Sr_xCuSi_2O_6$ Spin Dimer Compounds,* Cryst. Growth Des. **16** (6), pp 3416–3424 (2016).

[31] See Supplemental Material for Selected structure files at http://journals.aps.org/prb/supplemental/10.1103/PhysRevB.93.174121.

[32] J. C. Lashley, M. F. Hundley, A. Migliori, J. L. Sarrao, P. G. Pagliuso, T. W. Darling, M. Jaime, J. C. Cooley, W. L. Hults, L. Morales, D. J. Thoma, J. L. Smith, J. Boerio-Goates, B. F. Woodfield, G. R. Stewart, R. A. Fisher, N. E. Phillips, *Critical examination of heat capacity measurements made on a Quantum Design physical property measurement system*, Cryogenics **43**, 369-378 (2003).

[33] K. Koepernik and H. Eschrig, *Full-potential nonorthogonal local-orbital minimum-basis band-structure scheme*, Phys. Rev. B **59**, 1743 (1999); http://www.FPLO.de.

[34] J. P. Perdew, K. Burke, and M. Ernzerhof, *Generalized Gradient Approximation Made Simple*, Phys. Rev. Lett. **77**, 3865 (1996).

[35] A. I. Liechtenstein, V. I. Anisimov, and J. Zaanen, *Density-functional theory and strong interactions: Orbital ordering in Mott-Hubbard insulators*, Phys. Rev. B **52**, R5467(R) (1995).

[36] U. Tutsch, B. Wolf, S. Wessel, L. Postulka, Y. Tsui, H. O. Jeschke, I. Opahle, T. Saha-Dasgupta, R. Valentí, A. Brühl, K. Remović-Langer, T. Kretz, H.-W. Lerner, M. Wagner, M. Lang, *Evidence of a field-induced Berezinskii-Kosterlitz-Thouless scenario in a two-dimensional spin-dimer system*, Nat. Commun. **5**, 5169 (2014).

[37] H. O. Jeschke, F. Salvat-Pujol, and R. Valentí, *First-principles determination of Heisenberg Hamiltonian parameters for the spin-1/2 kagome antiferromagnet* $ZnCu_3(OH)_6Cl_2$, Phys. Rev. B **88**, 075106 (2013).

[38] H. O. Jeschke, F. Salvat-Pujol, E. Gati, N. H. Hoang, B. Wolf, M. Lang, J. A. Schlueter, and R. Valentí, *Barlowite as a canted antiferromagnet: theory and experiment*, Phys. Rev. B **92**, 094417 (2015).

[39] Y. Sasago, K. Uchinokura, A. Zheludev and G. Shirane, *Temperature-dependent spin gap and singlet ground state in* $BaCuSi_2O_6$, Phys. Rev. B **55**, 8357 (2016)

[40] M. Okada et al., *Quasi-two-dimensional Bose-Einstein condensation of spin triplets in the dimerized quantum magnet* $Ba_2CuSi_2O_6Cl_2$, Phys. Rev. B **94**, 094421 (2016)

[41] L. Balents, *Spin liquids in frustrated magnets*, Nature **464**, 199 (2010).

[42] M. P. Shores, E. A. Nytko, B. M. Barlett, and D. G. Nocera, *A structurally perfect S = (1/2) kagomé antiferromagnet*, J. Am. Chem. Soc. **127**, 13462 (2005).

[43] P. Mendels, F. Bert, M. A. de Vries, A. Olariu, A. Harrison, F. Duc, J. C. Trombe, J. S. Lord, A. Amato, and C. Baines, *Quantum Magnetism in the Paratacamite Family: Towards an Ideal Kagomé Lattice*, Phys. Rev. Lett. **98**, 077204 (2007).

[44] T-H. Han, J. S. Helton, S. Chu, D. G. Nocera, J. A. Rodriguez-Rivera, C. Broholm and Y. S. Lee, *Fractionalized excitations in the spin-liquid state of a kagome-lattice antiferromagnet*, Nature **492**, 406–410 (2012)

[45] J. S. Helton, K. Matan, M. P. Shores, E. A. Nytko, B. M. Bartlett, Y. Yoshida, Y. Takano, A. Suslov, Y. Qiu, J.-H. Chung, D. G. Nocera, and Y. S. Lee, *Spin Dynamics of the Spin-1/2 Kagome Lattice Antiferromagnet* $ZnCu_3(OH)_6Cl_2$, Phys. Rev. Lett. **98**, 107204 (2007).

[46] X. G. Zheng, T. Kawae, Y. Kashitani, C. S. Li, N. Tateiwa, K. Takeda, H. Yamada, C. N. Xu, and Y. Ren, *Unconventional magnetic transitions in the mineral clinoatacamite* $Cu_2Cl(OH)_3$, Phys. Rev. B **71**, 052409 (2005).

[47] T. Malcherek and J. Schlüter, *Structures of the pseudo-trigonal polymorphs of* $Cu_2(OH)_3Cl$, Acta Cryst. B**65**, 334-341 (2009).

[48] M. D. Welch, M. J. Sciberras, P. A. Williams, P. Leverett, J. Schlüter, T. Malcherek, *A temperature-induced reversible transformation between paratacamite and herbertsmithite*, Phys. Chem. Min. **41**, 1, 33–48 (2013)

[49] R. H. Colman, C. Ritter, and A. S. Wills, *Toward Perfection: Kapellasite,* $Cu_3Zn(OH)_6Cl_2$, *a New Model S = 1/2 Kagome Antiferromagnet*, Chem. Mater. **20** (22), 6897–6899 (2008).

[50] M. R. Norman, *Colloquium: herbertsmithite and the search for the quantum spin liquid*, Rev. Mod. Phys. **88**, 041002 (2016).

[51] M. A. de Vries et al., *Extension of the zinc paratacamite phase diagram: Probing the effect of spin vacancies in an S = 1/2 kagome antiferromagnet,* Phys. Rev. B **85**, 014422 (2012)

[52] Tian-Heng Han, M. R. Norman, Wen, Jose A. Rodriguez-Rivera, Joel S. Helton, Collin Broholm, and Young S. Lee, *Correlated impurities and intrinsic spin-liquid physics in the kagome material herbertsmithite*, Phys. Rev. B **94**, 060409(R) (2016)

[53] D. E. Freedman, Tianheng H. Han, Andrea Prodi, Peter Müller, Qing-Zhen Huang, Yu-Sheng Chen, Samuel M. Webb, Young S. Lee, Tyrel M. McQueen, and Daniel G. Nocera, *Site Specific X-ray Anomalous Dispersion of the Geometrically Frustrated Kagomé Magnet, herbertsmithite, $ZnCu_3(OH)_6Cl_2$*, J. Am. Chem. Soc. **132**, 16185–16190 9 16185 (2010).

[54] I. I. Mazin, H. O. Jeschke, F. Lechermann, H. Lee, M. Fink, R. Thomale, and R. Valentí, *Theoretical prediction of a strongly correlated Dirac metal*, Nat. Comm. **5**, 4261 (2014).

[55] Z.A. Kelly, M. J. Gallagher, and T.M. McQueen, *Electron Doping a Kagome Spin Liquid*, Phys. Rev. X **6**, 041007 (2016).

[56] W. Sun, Y. Huang, S. Nokhrin, Y. Pan and J. Mi, *Perfect Kagomé lattices in $YCu_3(OH)_6Cl_3$: a new candidate for the quantum spin liquid state*, J. Mater. Chem. C **4**, 8772-8777 (2016).

[57] D. Guterding, H. O. Jeschke & R. Valentí, *Prospect of quantum anomalous Hall and quantum spin Hall effect in doped kagome lattice Mott insulators*, Sc. Rep. **6**, 25988 (2016).

[58] O. Kondo, M. Ono, E. Sugiura, K. Sugiyama and M. Date, *High field magnetism of CuO*, Journal of the Phys. Soc. of Japan **57**, 3293-3296 (1988).

[59] W. Schnelle, J. Engelhardt, E. Gmelin, *Specific heat capacity of Apiezon N high vacuum grease and of Duran borosilicate glass*, Cryogenic **39**, 271–275 (1999).

[60] P. Puphal, M. Bolte, D. Sheptyakov, A. Pustogow, K. Kliemt, M. Dressel, M. Baenitz, and C. Krellner, *Strong magnetic frustration in $Y_3Cu_9(OH)_{19}Cl_8$: a distorted kagome antiferromagnet*, J. of Mat. Chem. C **5**, 2629-2635 (2017).

[61] R. H. Colman, A. Sinclair, and A. S. Wills, *Comparisons between Haydeeite, α-$Cu_3Mg(OD)_6Cl_2$, and Kapellasite, α-$Cu_3Zn(OD)_6Cl_2$, Isostructural S = 1/2 Kagome Magnets*, Chem. Mater. **23**, 1811–1817 (2011).

[62] T. M. McQueen, T.H. Han, D.E. Freedman, P.W. Stephens, Y.S. Lee, D.G. Nocera, *$CdCu_3(OH)_6Cl_2$: A new layered hydroxide chloride*, J. Solid State Chem. **184**, 3319–3323 (2011).

[63] G. Meyer, *The Ammonium Chloride Route to Anhydrous Rare Earth Chlorides-The Example of YCl_3*, Inorganic Syntheses **25**, 146–150 (1989).

[64] P. Melnikov, V. A. Nascimento, L. Z. Z. Consolo and A. F. Silva, *Mechanism of thermal decomposition of yttrium nitrate hexahydrate, $Y(NO_3)_3{\cdot}6H_2O$ and modeling of intermediate oxynitrates*, J. Therm. Anal. Calorim. **111**, 115-119 (2013).

[65] Stoe and Cie GmbH, X-AREA. Diffractometer control program system (2002).

[66] G. M. Sheldrick, *A short history of SHELX*, Acta Cryst. A **64**, 112-122 (2008).

[67] Yu. M. Baikov, *Intercalated Hydrogen in Yttrium Barium Cuprate: The State and Mobility of a "Guest" and Modification of the "Host" Properties,* Phys. of the Solid State **42**, 6 (2000).

[68] S. Chu, P. Müller, D. G. Nocera, and Y. S. Lee, *Hydrothermal growth of single crystals of the quantum magnets: Clinoatacamite, paratacamite, and herbertsmithite*, Applied Phys. Let. **98**, 092508 (2011).

[69] M. A. de Vries, J. R. Stewart, P. P. Deen, J. O. Piatek, G. J. Nilsen, H. M. Rønnow, and A. Harrison, *Scale-Free Antiferromagnetic Fluctuations in the s = 1/2 Kagome Antiferromagnet Herbertsmithite*, Phys. Rev. Lett. **103**, 237201 (2009)

[70] R. S. W. Braithwaite, K. Mereiter, W. H. Paar and A. M. Clark, herbertsmithite, *$Cu_3Zn(OH)_6Cl_2$, a new species, and the definition of paratacamite*, Mineral. Mag. **68**(3), 527 (2004).

[71] W. Krause, H.-J. Bernhardt, R. S. W. Braithwaite, U. Kolitsch, R. Pritchard, *Restricted access Kapellasite, $Cu_3Zn(OH)_6Cl_2$, a new mineral from Lavrion, Greece, and its crystal structure*, Mineral. Mag. **70**(3), 329 (2006).

Declaration

I, Pascal Puphal confirm that the work presented in this thesis is my own. Where information has been derived from other sources, I confirm that this has been indicated in the thesis.

Acknowledgments

This work and my personal development were only possible due to the constructive, educational and positive worklive of the whole group of Cornelius Krellner.

The greatest support and promotion was given to me by my supervisor Cornelius Krellner who gave me advice just when it was necessary with the complete freedom that was fruitful for my research. His fitting choice of conferences was always a great help for my work, also to break free of the laboratory everyday life. The utmost gratitude for the detailed corrections performed on written publications.

Franz Ritter my bureau donator and thus most suffering victim of questions has to be thanked thousand times. His expertise in DTA, Diffractometry and the general equipment were a help without which this work would have never ended.

My thankfulness also to our technician Klaus-Dieter Luther who as a physicist could give me counsel not only on the instrumental site. Especially I want to thank him for organizing all the necessary chemicals and equipment for my work.

We owe the former group leader Wolf Aßmuss that the group was in the given state with a great asset of equipment and the traditions set up as they are, with common joint coffee breaks including as often as it could be cake and the annual hiking in the alps. Also a thanks for the integration in lecturing at the HSAKA (a student academy) goes to Wolf and Natalija Van-Well my former supervisor during my master thesis who with her strict manner gave me a good start into the group and the work performed here.

The positive mood of the group is mainly driven by the organised and funny way of our secretary Hannah Döring, who ensures that bureaucracy is no hinderance to any member of the group and thus has my greatest gratitude.

A big thank you has to be said also to my doctoral collegues who besides suffering the same throwbacks in the work of crystal growth always helped with positive discussions. Antonia Morherr provided a constant in the work that gave balance to any uncertainties and with her relaxed way was always the best to help especially with the PPMS and the high resistivity measurements on her own setup. As a co-student who started earlier in the group Kristin Kliemt gave me good counsel and had an eye on the safety in the group. Sebastian Witt was a helpful hand with program problems and Christian Klein helped when the chemical knowledge of a physicist failed. Thanks to Mahmoud Abdel-Hafiez who always had an eye on the PPMS and Agnes Adamski for the funny coffee breaks.

Finally I want to thank my students who participated in my work. Such as my bachelor students Kathrin Schütz; Max Müller who did a detailed work on the $GaCu(OH)_6Cl_2$ system. Especially I thank Katharina Zoch who enthusiastically researched more than a basic bachelor thesis demands, finding many new kagome materials. Also thanks to my master student Joy Désor with whom I grew tondiite and haydeeite single crystals.

A great asset of collaborations gave me the opportunity to measure and experience many new methods. I am grateful for: the uncomplicated connection to the theoretical group of Roser Valentí and the connection of Cornelius Krellner to Christian Rüegg establishing a great cooperation with Denis Sheptyakov and Björn Wehinger. Michael Baenitz group from Dresden who not only measured specific heat and NMR himself, but also established a connection to Philippe Mendels group from Orsay for $\mu-$SR measurements. The fruitful work established during the hiking with Andrej Pustogow from the group of Martin Dressel from Stuttgart and Raivo Sterns group from Tallinn who I met at the ICM 2015.

Of course I want to mention also the funding for my position performed by the SFB TR49 in which I found a good environment for scientific discussions and presentation opportunities, as well as many further courses realized in the student retreats.

All my work could not have been realized without the support of my loved ones forging the person I have become.

I dedicate this thesis to my newborn son Raphael Nicholas Puphal.

List of publications

P. Puphal, D. Sheptyakov, N. van Well, L. Postulka, I. Heinmaa, F. Ritter, W. Assmus, B. Wolf, M. Lang, H. O. Jeschke, R. Valentí, R. Stern, C. Rüegg, and C. Krellner, *Stabilization of the tetragonal structure in* $(Ba_{1-x}Sr_x)CuSi_2O_6$, Phys. Rev. B **93**, 174121 (2016).

N. van Well, **P. Puphal**, B. Wehinger, M. Kubus, J. Schefer, C. Rüegg, F. Ritter, C. Krellner, and W. Assmus, *Crystal Growth with Oxygen Partial Pressure of the* $BaCuSi_2O_6$ *and* $Ba_{1-x}Sr_xCuSi_2O_6$ *Spin Dimer Compounds,* Cryst. Growth Des. **16** (6), pp 3416–3424 (2016).

P. Puphal, M. Bolte, D. Sheptyakov, A. Pustogow, K. Kliemt, M. Dressel, M. Baenitz, and C. Krellner, *Strong magnetic frustration in* $Y_3Cu_9(OH)_{19}Cl_8$*: a distorted kagome antiferromagnet*, J. of Mat. Chem. C **5**, 2629-2635 (2017).

A. Pustogow, Y. Li, I. Voloshenko, **P. Puphal**, C. Krellner, I.I. Mazin, M. Dressel, and R. Valentí, *Nature of optical excitations in the frustrated kagome compound Herbertsmithite,* to be published (2017).

P. Puphal, R. Kumar, M. Müller, E. Kermarrec, F. Bert, M. Baenitz, P. Mendels and C. Krellner, $Ga_xCu_{4-x}(OD)_6Cl_2$ *: Insulating ground state in an electron-doped kagome system*, to be published (2018).

HSAKA documentations (in german) ISBN: 978-3-910097-25-4, ISBN: 978-3-910097-27-8, ISBN: 978-3-910097-29-2 and ISBN: 978-3-910097-xx-x (2017).